

1 July 2011 | \$10

Science



cell sciences®

cytokine center

Browse our web site of recombinant proteins, including cytokines, growth factors, chemokines and neurotrophins. Daily shipping and competitive pricing are offered. Bulk quantities of many proteins available. Cell Sciences also carries corresponding antibodies and ELISA kits.



LIST OF PROTEINS

4-1BBL	Caspase-3	sFlt-1 (D3)	IL-2	MEC	sRANK
4-1BB Receptor	Caspase-6	sFlt-1 (D4)	IL-3	Mek-1	sRANKL
6 Ckine	CD4	sFlt-1 (D5)	IL-4	MIA	RANTES
ACAD8	CD14	sFlt-1 (D7)	sIL-4 Receptor	Midkine	RELM- α
ACAT2	CD22	Flt3-Ligand	IL-5	MIG / CXCL9	RELM- β
gAcrp30/Adipolean	CD40 Ligand / TRAP	sFlt-4	IL-6	MIP-1 α / CCL3	Resistin
Activin A	CD95 / sFas Ligand	sFlt-4/ Fc Chimera	sIL-6 Receptor	MIP-1 β / CCL4	RPTP β
ACY1	CD105 / Endoglin	Follistatin	IL-7	MIP-3 / CCL23	RPTP γ
ADAT1	CHIPS	FSH	IL-8 (72 a.a.)	MIP-3 α / CCL20	RPTP μ
Adiponectin	CNTF	Fractalkine/ CX3C	IL-8 (77 a.a.)	MIP-3 β / CCL19	SCF
ADRP	Collagen	G-CSF	IL-9	MIP-4 (PARC) / CCL18	SCGF- α
AITRL	CREB	α -Galactosidase A	IL-10	MIP-5 / CCL15	SCGF- β
Akt1	CTACK/CCL27	Galectin-1	IL-11	MMP-3	SDF-1 α
Alpha-Feto Protein (AFP)	CTGF	Galectin-3	IL-12	MMP-7	SDF-1 β
Alpha-Galactosidase A	CTGFL/WISP-2	Gastrointestinal CA	IL-13	MMP-13	Secretin
Angiopoietin-1 (Ang-1)	CTLA-4/Fc	GCP-2	IL-13 analog	Myostatin	SF20
Angiopoietin-2 (Ang-2)	CXCL16	GDF-3	IL-15	Nanog	SHP-2
Angiostatin K1-3	Cytokeratin 8	GDF-9	IL-16 (121 a.a.)	NAP-2	STAT1
Annexin-V	DEP-1	GDF-11	IL-16 (130 a.a.)	Neurturin	c-Src
apo-SAA	Desmopressin	GDNF	IL-17	NFAT-1	TACI
Apolipoprotein A-1	Disulfide Oxidoreductase	GLP-1	IL-17B	beta-NGF	TARC
Apolipoprotein E2	E-selectin	Glucagon	IL-17D	NOGGIN	TC-PTP
Apolipoprotein E3	ECGF	Goserelin	IL-17E	NOV	TECK
Apolipoprotein E4	EGF	GM-CSF	IL-17F	NP-1	TFF2
APRIL	Elafin/SKALP	GPBB	IL-19	NT-1/BCSF-3	TGF- α
Artemin	EMAP-II	GRO α	IL-20	NT-3	TGF- β 1
ATF2	ENA-78	GRO β	IL-22	NT-4	TGF- β 2
Aurora A	Endostatin	GRO γ	IL-31	Ocreotide	TGF- β 3
Aurora B	Enteropeptidase	GRO/MGSA	Insulin	Oncostatin M	Thymosin α 1
BAFF	Eotaxin	Growth Hormone	IP-10	Osteoprotegerin (OPG)	sTIE-1/Fc Chimera
BAFF Receptor	Eotaxin-2	Growth Hormone BP	JE	OTOR	sTIE-2/Fc Chimera
BCA-1 / BLC / CXCL13	Eotaxin-3 (TSC)	GST-p21/WAF-1	JNK2a1	Oxytocin	TL-1A
BCMA	EPHB2	HB-EGF	JNK2a2	p38- α	TNF- α
BD-1	EPHB4	HCC-1	KC / CXCL1	Parathyroid Hormone	TNF- β
BD-2	Eptifibatide	HGF	KGF	PDGF-AA	sTNFR1
BD-3	Erk-2	Histidyl-tRNA synthetase	L-asparaginase	PDGF-AB	sTNFR2
BDNF	Erythropoietin (EPO)	Histrelin	LAG-1	PDGF-BB	TPO
Bivalirudin	Exodus-2	HRG1- β 1	LALF Peptide	Persephin	TRAIL/Apo2L
BMP-2	Fas Ligand	I-309	LAR-PTP	PF-4	sTRAIL R-1 (DR4)
BMP-4	Fas Receptor	I-TAC	LC-1	PIGF-1	sTRAIL R-2 (DR5)
BMP-7	FGF-1 (acidic)	IFN- α	LBP	PIGF-2	TSH
BMP-13	FGF-2 (basic)	IFN- α A	LD-78 β	PKA α -subunit	TSLP
sBMPR-1A	FGF-4	IFN- α 2a	LDH	PKC- α	TWEAK
Brain Natriuretic Protein	FGF-5	IFN- α 2b	LEC/NCC-4	PKC- γ	TWEAK Receptor
BRAK	FGF-6	IFN- β	Leptin	Pleiotrophin	Urokinase
Breast Tumor Antigen	FGF-7/ KGF	IFN- γ	LIGHT	PLGF-1	VEGF121
C5a	FGF-8	IFN-Omega	LIX	Polymyxin B (PMB)	VEGF145
C5L2 Peptide	FGF-9	IGF-I	LKM	PRAS40	VEGF165
C-10	FGF-10	IGF-II	LL-37	PRL-1	VEGF-C
C-Reactive Protein	FGF-16	proIGF-II	Lymphotactin	PRL-2	VEGF-C I525
C-Src	FGF-17	IGFBP-1	sLYVE-1	PRL-3	EG-VEGF
Calbindin D-9K	FGF-18	IGFBP-2	M-CSF	Prokineticin-2	VEGF-E
Calbindin D-28K	FGF-19	IGFBP-3	MCP-1 (MCAF)	Prolactin	HB-VEGF-E
Calbindin D-29K	FGF-20	IGFBP-4	MCP-2	Protirelin	sVEGFR-1
Calmodulin	sFGFR-1 (IIIc) / Fc Chimera	IGFBP-4	MCP-3	PTHrP	sVEGFR-2
Calcitonin Acetate	sFGFR-2 (IIIc) / Fc Chimera	IGFBP-5	MCP-4	PTP1B	sVEGFR-3
Carbonic Anhydrase III	sFGFR-3 / Fc Chimera	IGFBP-6	MCP-5	PTP-IA2	WISP-1
Carcino-embryonic Antigen	sFGFR-4 / Fc Chimera	IGFBP-7	MDC (67 a.a.)	PTP-MEG2	WISP-2
Cardiotrophin-1	sFlt-1 (native)	IL-1 α	MDC (69 a.a.)	PTP-PEST	WISP-3
		IL-1 β	MDH		WNT-1

CELL SCIENCES INC • 480 NEPONSET STREET, BUILDING 12A, CANTON, MA 02021 • INFO@CELLSCIENCES.COM

TOLL FREE: (888) 769-1246 • TEL: (781) 828-0610 • FAX: (781) 828-0542 • WEB: WWW.CELLSCIENCES.COM

Submission
deadline
August 1

Your name here.



The GE & Science Prize for Young Life Scientists. Because brilliant ideas build better realities.

Imagine standing on the podium at the Grand Hotel in Stockholm, making your acceptance speech for the GE & Science Prize for Young Life Scientists. Imagine having your essay read by your peers around the world. Imagine discussing your work in a seminar with other prize winners and Nobel Laureates. Imagine what you could do with the \$25,000 prize money. Now stop imagining. If you were awarded your Ph.D. in molecular biology in 2010, then submit your 1000-word essay by August 1, and you can make it a reality.

Want to build a better reality? Go to www.gescienceprize.org



* For the purpose of this prize, molecular biology is defined as "that part of biology which attempts to interpret biological events in terms of the physico-chemical properties of molecules in a cell".

(McGraw-Hill Dictionary of Scientific and Technical Terms, 4th Edition).

GE Healthcare Bio-Sciences AB,
Björkgatan 30, 751 84 Uppsala, Sweden.
© 2011 General Electric Company
— All rights reserved.
28-9402-06AB

GE Healthcare
Life Sciences

Confidence comes with the right interactions.

Join leading scientists from academia and industry at Developments in Protein Interaction Analysis (DiPIA), November 12-15, Boston, Massachusetts, USA.

This scientific conference offers opportunities to meet and discuss the latest developments in label-free interaction and stability analysis using Biacore™ Surface Plasmon Resonance (SPR) and MicroCal™ microcalorimetry systems.

Register at www.gelifesciences.com/dipia

© 2011 General Electric Company – All rights reserved.
GE Healthcare Bio-Sciences AB, Björkgatan 30,
751 84 Uppsala, Sweden
K11074. First published May 2011.



WorldMags



EDITORIAL

- 13 **AIDS: Let Science Inform Policy**
Anthony S. Fauci
 >> *Policy Forum p. 42*

NEWS OF THE WEEK

- 18 A roundup of the week's top stories

NEWS & ANALYSIS

- 22 **Underground Lab Would Cost U.S. Billions**
 23 **Antismoking Drive Tries Cigarette Ads, in Reverse**
 24 **Suit Seeks Redress for a Start-Up Package Gone Sour**
 27 **As *E. coli* Outbreak Recedes, New Questions Come to the Fore**

NEWS FOCUS

- 28 **SCIENCE ON THE SHUTTLE**
NASA's Busload of Science
 The Highs and Lows of Shuttle Science
 >> *Science Podcast*

LETTERS

- 35 **Editorial Expression of Concern**
B. Alberts
Not-So-Sunny Outlook for Organic Photovoltaics
E. A. Chandross
An Unorthodox Approach to Forest Restoration
C. J. Kettle et al.
Response
D. J. Merritt and K. W. Dixon
 37 **TECHNICAL COMMENT ABSTRACTS**

BOOKS ET AL.

- 38 **Science Tourism: Some Summer Suggestions**

POLICY FORUM

- 42 **Turning the Tide Against HIV**
R. J. Shattock et al.
 >> *Editorial p. 13*

PERSPECTIVES

- 44 **Fishing in the Nuclear Pore**
R. W. Kriwacki and M.-K. Yoon
 >> *Report p. 90*
 45 **Revealing Virus-Host Interplay**
M. Krupovic and D. H. Bamford
 >> *Research Article p. 58*
 46 **Knot Your Simple Defect Lines?**
R. D. Kamien
 >> *Report p. 62*
 47 **Remember When?**
H. L. Roediger III and K. B. McDermott
 >> *Report p. 108*
 49 **Electrons in Cement**
P. P. Edwards
 >> *Report p. 71*
 50 **Protease Sets Site-1 on Lysosomes**
J. Ye
 >> *Report p. 87*

BREVIA

- 52 **A Biological Screw in a Beetle's Leg**
T. van de Kamp et al.
 Joints on the legs of weevils form a functional screw-and-nut system.

CONTENTS continued >>



page 28



page 38



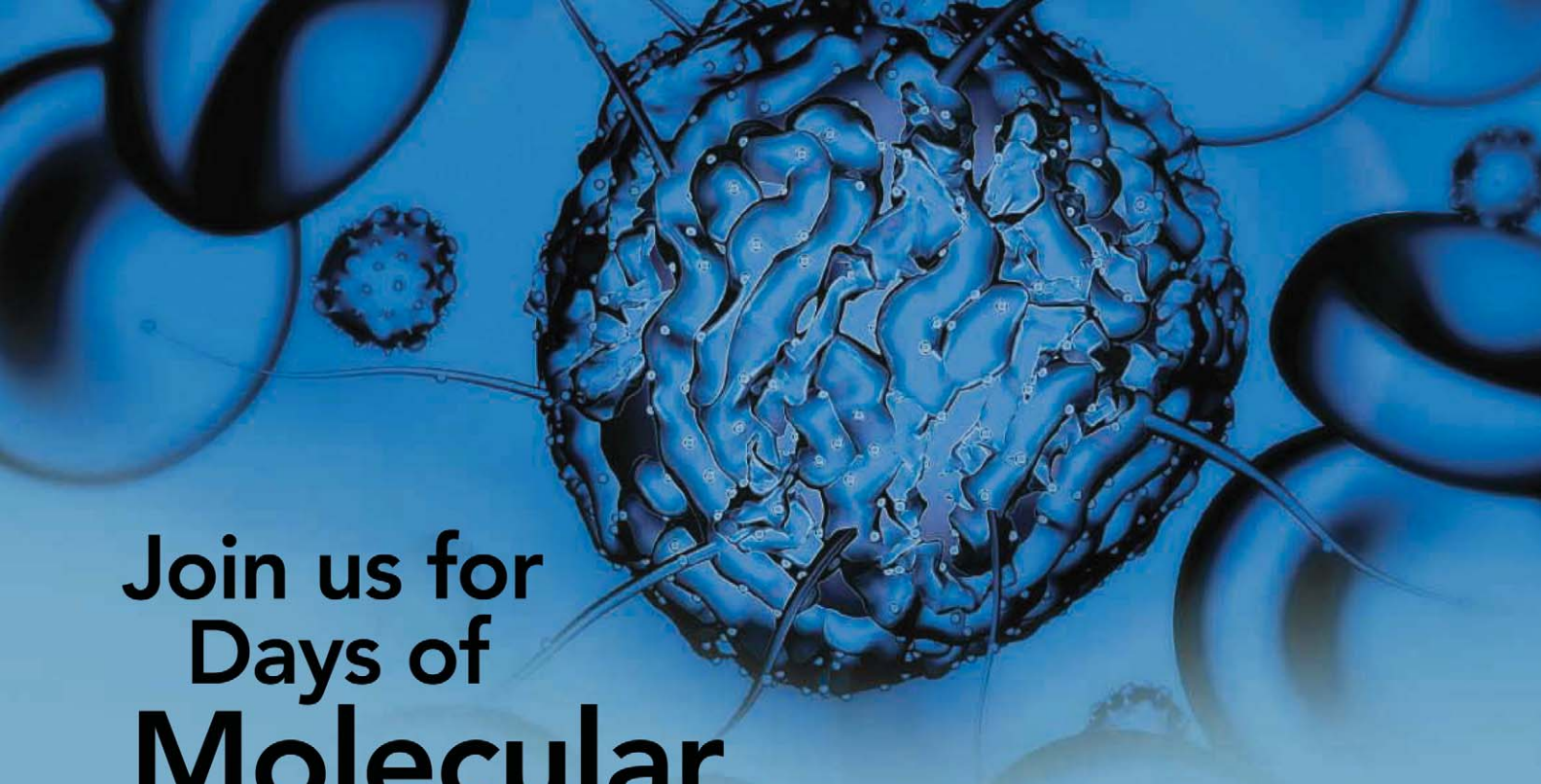
COVER

Differential interference contrast microscopy image showing the gut microbial community of the termite *Reticulitermes tibialis*. Coursing among larger protozoa (ranging in size from 10 to 60 micrometers) are thin, wavy bacteria known as spirochetes, as well as viruses not visible at this magnification. Using a microfluidic digital polymerase chain reaction approach, Tadmor *et al.* examine the interactions between uncultured bacteria and their associated viruses in the termite hindgut. See page 58.

Image: Jared R. Leadbetter, California Institute of Technology

DEPARTMENTS

- 11 **This Week in Science**
 14 **Editors' Choice**
 16 **Science Staff**
 112 **New Products**
 113 **Science Careers**



Join us for Days of Molecular Medicine 2011

Reengineering Regenerative Medicine

November 10-12
Hong Kong

Register today at
dmm.aaas.org

Take advantage of this extraordinary opportunity to learn from, and network with, some of the world's most influential researchers in regenerative medicine.

An international roster of leading tissue engineers and stem cell biologists, headlined by keynote speakers **Anthony Atala, Fiona Watt** and **Molly Stevens**, will discuss how to overcome barriers in translating new research advances into tangible clinical benefits.

Featured topics include:

- New strategies for engineering liver, skin and corneal tissues
- Neural stem cells and nervous system regeneration
- Stem cell therapies for treating heart disease
- Designing better biomaterials for engineering bone, cartilage and muscle

BROUGHT TO YOU BY:



RESEARCH ARTICLES

- 53** **Widespread RNA and DNA Sequence Differences in the Human Transcriptome**
M. Li et al.

All 12 categories of discordances can be observed where the RNA sequence does not match that of the DNA.

- 58** **Probing Individual Environmental Bacteria for Viruses by Using Microfluidic Digital PCR**

A. D. Tadmor et al.

Matching environmental phage with single, uncultured bacterial host cells reveals remarkable species specificity.

>> *Perspective p. 45*

REPORTS

- 62** **Reconfigurable Knots and Links in Chiral Nematic Colloids**

U. Tkalec et al.

Colloidal particles inside a liquid crystalline solvent can be manipulated to create knots of arbitrary shape and complexity.

>> *Perspective p. 46*

- 65** **Rotary Photon Drag Enhanced by a Slow-Light Medium**

S. Franke-Arnold et al.

A spinning slow-light medium (ruby crystal) is used to enhance the rotation of light.

- 68** **Superelastic Effect in Polycrystalline Ferrous Alloys**

T. Omori et al.

A superelastic alloy formed from common elements operates over a wide temperature window.

- 71** **Solvated Electrons in High-Temperature Melts and Glasses of the Room-Temperature Stable Electride $[\text{Ca}_{24}\text{Al}_{28}\text{O}_{64}]^{4+}\cdot 4\text{e}^-$**

S. W. Kim et al.

Solvated electrons persist in high-temperature melts and quenched melts of a calcium aluminum oxide.

>> *Perspective p. 49*

- 74** **Large Sulfur Isotope Fractionation Does Not Require Disproportionation**

M. S. Sim et al.

In the absence of oxygenation, microbial activity can explain the magnitude of sulfur-isotope traces in sediments.

- 77** **Formation and Spread of Aircraft-Induced Holes in Clouds**

A. J. Heymsfield et al.

Aircraft passing through clouds that contain supercooled liquid water can produce holes and canals in those clouds.

- 81** **Pattern in Escalations in Insurgent and Terrorist Activity**

N. Johnson et al.

The escalation of fatal attacks by insurgent groups follows a common pattern.

>> *Science Podcast*

- 84** **Mechanism of RAD51-Dependent DNA Interstrand Cross-Link Repair**

D. T. Long et al.

An in vitro system reveals the steps involved in repairing covalent links between DNA strands of the double helix.

- 87** **A Key Enzyme in the Biogenesis of Lysosomes Is a Protease That Regulates Cholesterol Metabolism**

K. Marschner et al.

Defects in a sterol regulatory pathway also cause defects in lysosome assembly leading to mucopolipidosis and disease.

>> *Perspective p. 50*

- 90** **Long Unfolded Linkers Facilitate Membrane Protein Import Through the Nuclear Pore Complex**

A. C. Meinema et al.

Natively unfolded linkers facilitate nuclear membrane protein import.

>> *Perspective p. 44*

- 94** **No Evidence of Murine-Like Gammaretroviruses in CFS Patients Previously Identified as XMRV-Infected**

K. Knox et al.

Chronic fatigue syndrome patients reported previously to be XMRV-infected show no signs of the virus in an independent evaluation.

- 97** **Recombinant Origin of the Retrovirus XMRV**

T. Paprotka et al.

Analysis of the origin of XMRV suggests that links between the virus and human disease are due to laboratory contamination.

- 101** **Predicting a Human Gut Microbiota's Response to Diet in Gnotobiotic Mice**

J. J. Faith et al.

Model microbial communities in mouse guts respond quickly and predictably to dietary shifts.

- 104** **Oxytocin Selectively Gates Fear Responses Through Distinct Outputs from the Central Amygdala**

D. Viviani et al.

Specific neuronal populations in the amygdala control different behavioral and physiological components of the fear response.

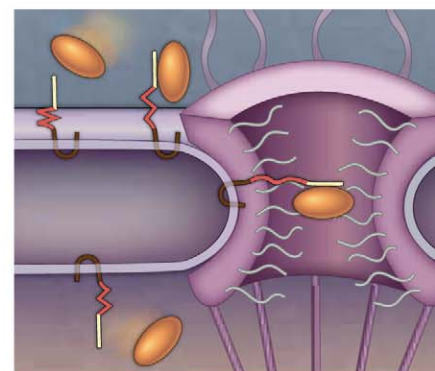
- 108** **Following the Crowd: Brain Substrates of Long-Term Memory Conformity**

M. Edelson et al.

Firmly held memory representations in the brain can be altered by social influence.

>> *Perspective p. 47; Science Podcast*

CONTENTS continued >>



pages 44 & 90



pages 47 & 108



page 65

Go straight to the source of gene expression regulation.

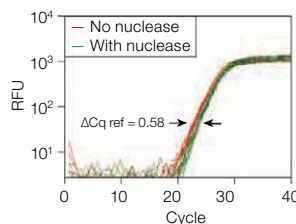
That's **epigenius**.

The EpiQ™ chromatin analysis kit is an innovative epigenetics research tool and real-time PCR assay for the quantitative assessment of chromatin structure using nuclease accessibility in cells. By understanding the chromatin environment around your genes of interest, you'll gain valuable insight into their mode of epigenetic regulation. With the EpiQ kit, you'll also benefit from:

- **Short assay time** — quantitative chromatin structure information in less than 6 hours
- **Small sample requirement** — results with as little as 50,000 cells
- **Valuable results** — strong correlation to gene expression levels

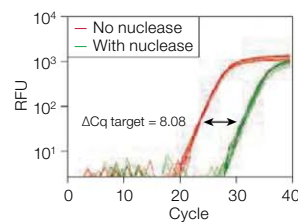
Visit www.bio-rad.com/ad/epigenius to learn more.

Research. Together.



Rhodopsin
Epigenetically silenced

Heterochromatin
0% chromatin accessibility
Minimal Cq shift



GAPDH
Constitutively expressed

Euchromatin
95% chromatin accessibility
Large Cq shift

SCIENCEONLINE

SCIENCEEXPRESS

www.scienceexpress.org

Isolation of Succinivibrionaceae Implicated in Low Methane Emissions from Tamar Wallabies

P. B. Pope et al.

Metagenome sequence predicted the culture conditions required for successful isolation of a marsupial gut bacterium.

10.1126/science.1205760

Structural Basis for Tail-Anchored Membrane Protein Biogenesis by the Get3-Receptor Complex

S. Stefer et al.

Docking of cytoplasmic and membrane receptors facilitates conformational changes that drive protein insertion.

10.1126/science.1207125

Altered Telomeres in Tumors with *ATRX* and *DAXX* Mutations

C. M. Heaphy et al.

Chromosome tips seem to be maintained by an unusual mechanism in tumors that have mutations in chromatin remodeling genes.

10.1126/science.1207313

Trace Metals as Biomarkers for Eumelanin Pigment in the Fossil Record

R. A. Wogelius et al.

X-ray maps of fossil feather pigments reveal color patterning in extinct bird species.

10.1126/science.1205748

Friction Anisotropy-Driven Domain Imaging on Exfoliated Monolayer Graphene

J. S. Choi et al.

Otherwise identical regions of supported graphene can be distinguished by changes in friction with sliding direction.

10.1126/science.1207110

TECHNICALCOMMENTS

Comment on "The Mechanism for Activation of GTP Hydrolysis on the Ribosome"

A. Liljas et al.

Full text at www.sciencemag.org/cgi/content/full/333/6038/37-a

Response to Comment on "The Mechanism for Activation of GTP Hydrolysis on the Ribosome"

R. M. Voorhees et al.

Full text at www.sciencemag.org/cgi/content/full/333/6038/37-b

SCIENCENOW

www.sciencenow.org

Highlights From Our Daily News Coverage

For Conservationists, the (Tasmanian) Devil Is in the Details

The newly sequenced genome of the endangered marsupial could help future generations fight off devastating facial tumor disease.

<http://scim.ag/taz-cancer>

LSD Alleviates 'Suicide Headaches'

Patients taking an analog of a psychedelic drug report fewer and less intense cluster headaches.

<http://scim.ag/lsd-headache>

When the Snake Bites ... Try Ointment

A salve that contains nitroglycerin might delay movement of snake venom.

http://scim.ag/snake_bite

SCIENCE SIGNALING

www.sciencesignaling.org

The Signal Transduction Knowledge Environment
28 June issue: <http://scim.ag/ss062811>

EDITORIAL GUIDE: Focus Issue—Choreographing the Dance of the Mitotic Kinases

N. R. Gough

Research into the phosphoproteome targeted by mitotic kinases reveals insight into the coordination of the activity of these kinases during cell division.

RESEARCH ARTICLE: Spatial Exclusivity Combined with Positive and Negative Selection of Phosphorylation Motifs Is the Basis for Context-Dependent Mitotic Signaling

J. Alexander et al.

RESEARCH RESOURCE: Quantitative Phosphoproteomics Identifies Substrates and Functional Modules of Aurora and Polo-Like Kinase Activities in Mitotic Cells
A. N. Kettenbach et al.

PERSPECTIVE: Substrates of Mitotic Kinases

L. N. Johnson

New research provides insight into how substrate selectivity of the multiple kinases that control mitosis is achieved.

RESEARCH RESOURCE: Mitotic Substrates of the Kinase Aurora with Roles in Chromatin Regulation Identified Through Quantitative Phosphoproteomics of Fission Yeast

A. Koch et al.

The kinase Aurora influences multiple aspects of chromatin architecture and function during mitosis.

PODCAST

S. Hauf et al.

Two studies shed light on cell cycle-dependent protein phosphorylation during mitosis in yeast.

SCIENCE TRANSLATIONAL MEDICINE

www.sciencetranslationalmedicine.org

Integrating Medicine and Science

29 June issue: <http://scim.ag/stm062911>

COMMENTARY: The Fiber of Modern Society

E. R. Edelman and M. B. Leon

COMMENTARY: Repaving the Road to Biomedical Innovation Through Academia

A. R. Marks

COMMENTARY: How to Revive Breakthrough Innovation in the Pharmaceutical Industry

B. H. Munos and W. W. Chin

In a series of articles, diverse experts engage in a critical dialogue on how to spur innovation.

RESEARCH ARTICLE: Human apoE Isoforms Differentially Regulate Brain Amyloid- β Peptide Clearance

J. M. Castellano et al.

Human apoE4 increases the concentration of soluble amyloid- β in the brain by impairing its clearance.

RESEARCH ARTICLE: Rapamycin Reverses Cellular Phenotypes and Enhances Mutant Protein Clearance in Hutchinson-Gilford Progeria Syndrome Cells

K. Cao et al.

Shown previously to extend longevity in animals, the drug rapamycin might serve as a treatment for a human premature aging syndrome.

SCIENCE CAREERS

www.sciencereers.org/career_magazine

Free Career Resources for Scientists

How to Avoid Retirement

L. Laursen

From changing roles to changing institutions, researchers approaching retirement age are finding ways to prolong their scientific careers.

http://scim.ag/avoiding_retirement

Taken for Granted: Creating Opportunities

B. L. Benderly

Two university-based jobs programs are helping to boost opportunities for scientists who are already trained.

http://scim.ag/TFG_Opportunities

Content Collection: Scientific Presentations

Science Careers Staff

Find everything you need to know about delivering oral scientific presentations (except the science), all in one place.

http://scim.ag/collection_presentations

SCIENCEPODCAST

www.sciencemag.org/multimedia/podcast

Free Weekly Show

On the 1 July Science Podcast: social aspects of memory, a look back at NASA's space shuttle program, patterns of insurgent and terrorist attacks, and more.

SCIENCEINSIDER

news.sciencemag.org/scienceinsider

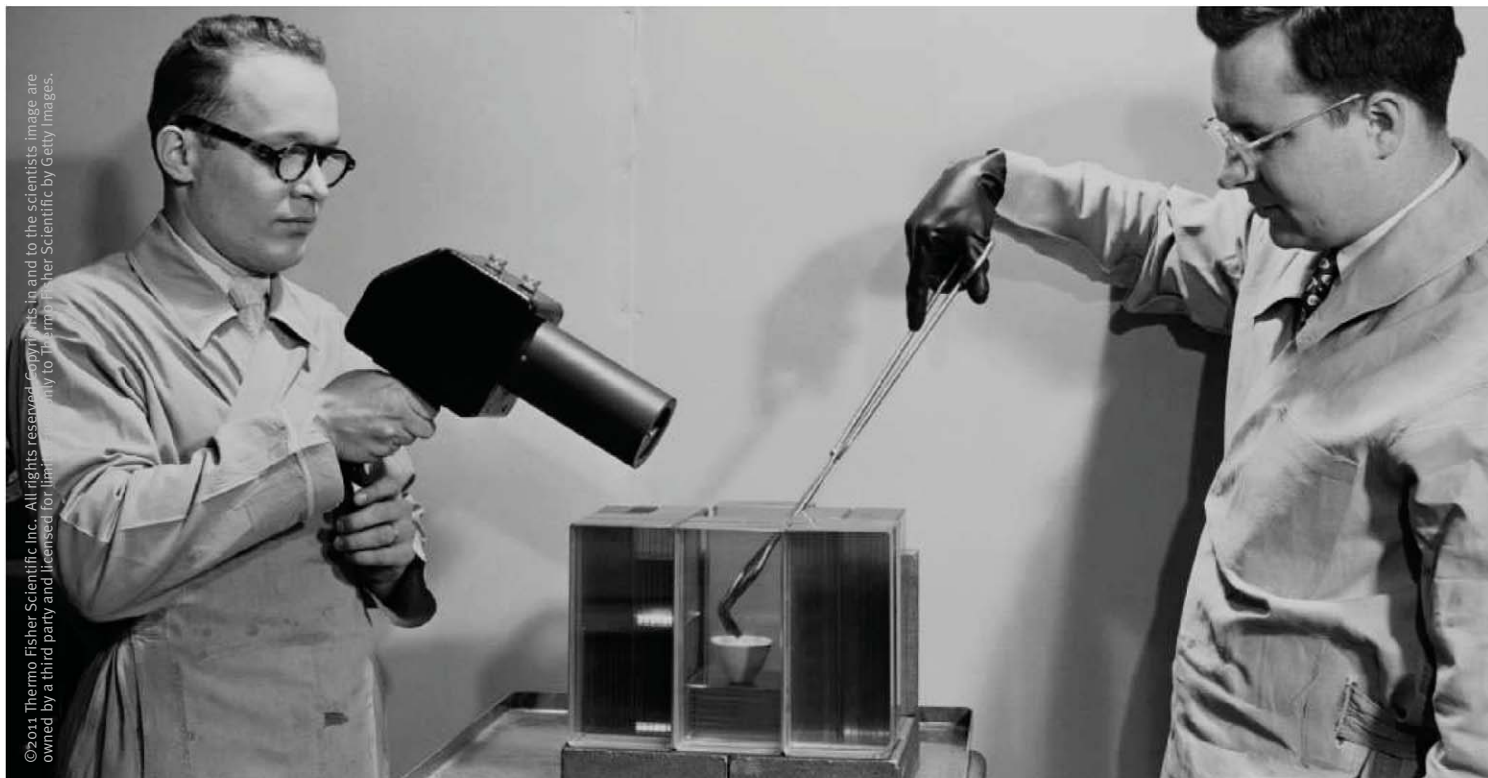
Science Policy News and Analysis

SCIENCE (ISSN 0036-8075) is published weekly on Friday, except the last week in December, by the American Association for the Advancement of Science, 1200 New York Avenue, NW, Washington, DC 20005. Periodicals Mail postage (publication No. 484460) paid at Washington, DC, and additional mailing offices. Copyright © 2011 by the American Association for the Advancement of Science. The title SCIENCE is a registered trademark of the AAAS. Domestic individual membership and subscription (51 issues): \$149 (\$74 allocated to subscription). Domestic institutional subscription (51 issues): \$990; Foreign postage extra: Mexico, Caribbean (surface mail) \$55; other countries (air assist delivery) \$85. First class, airmail, student, and emeritus rates on request. Canadian rates with GST available upon request, GST #1254 88122. Publications Mail Agreement Number 1069624. Printed in the U.S.A.

Change of address: Allow 4 weeks, giving old and new addresses and 8-digit account number. Postmaster: Send change of address to AAAS, P.O. Box 96178, Washington, DC 20090-6178. Single-copy sales: \$10.00 current issue, \$15.00 back issue prepaid includes surface postage; bulk rates on request. Authorization to photocopy material for internal or personal use under circumstances not falling within the fair use provisions of the Copyright Act is granted by AAAS to libraries and other users registered with the Copyright Clearance Center (CCC) Transactional Reporting Service, provided that \$25.00 per article is paid directly to CCC, 222 Rosewood Drive, Danvers, MA 01923. The identification code for Science is 0036-8075. Science is indexed in the Reader's Guide to Periodical Literature and in several specialized indexes.



ADVANCING SCIENCE. SERVING SOCIETY



Limited by an outdated PCR system?

You can run 15 minute PCR protocols and use 50% less consumables and energy by getting away from the old standard. Choose Thermo Scientific Piko Thermal Cyclers, Phusion reagents, and ultra thin wall (UTW) plastic consumables for the most rapid and accurate PCR results. These technologically advanced components can be used individually to improve your current workflow, or as a complete solution for advanced PCR.

- Ultra fast PCR cycling protocols optimized to <15 minutes
- 96-well PCR runs using 50% less plastics, reagents and energy
- PCR kits that allow amplification directly from plant, blood, and tissue samples

Start your PCR experiment today

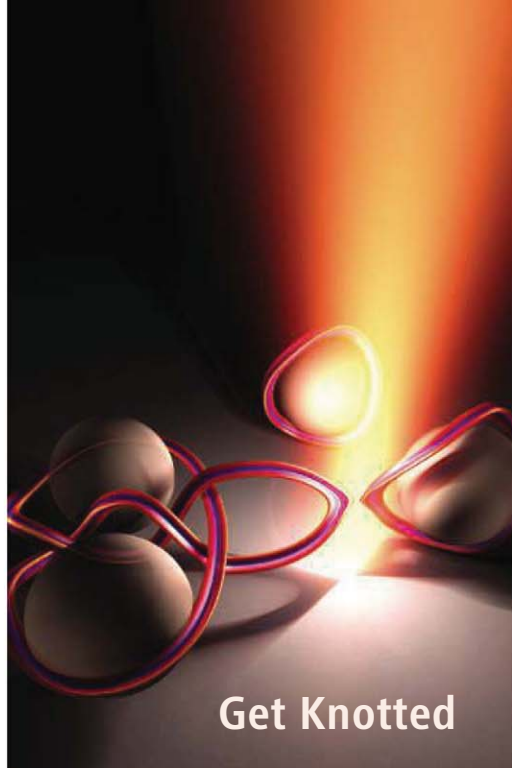
www.thermoscientific.com/advancedpcr



Everything for PCR

Thermo Scientific PCR portfolio has everything you need for successful PCR including industry leading reagents, high-quality instruments and trusted plastic consumables.

Moving science forward



Get Knotted

Topologically, loops and knots cannot be converted one to the other through simple twisting or stretching. These differences make knots and loops interesting objects to study, but it can be difficult to manipulate polymers into predefined shapes. **Tkalec *et al.*** (p. 62; see the Perspective by **Kamien**) immersed surface-treated colloidal particles in a chiral nematic liquid crystal. When the liquid crystal molecules were aligned normal to the surface of the particles, defect lines formed around each particle. By choosing different arrays of colloidal particles that could be manipulated using optical tweezers, structures where neighboring defect loops cross each other were generated allowing the production of knots of arbitrary complexity.

Rotation Can Be Such a Drag

The speed of light is reduced as it passes through a transparent medium, with the extent of the reduction dependent on the refractive index. A spinning window will rotate an image because of photon drag. However, for most materials the effect is minute—typically less than one-millionth of a degree. **Franke-Arnold *et al.*** (p. 65) show that using a spinning slow-light medium—a ruby rod with an optically induced, highly effective refractive index—can enhance the optical drag effect such that it can be visualized by eye or captured on camera.

Superelasticity Set Point

Shape metal alloys can undergo much larger reversible strain deformations than other metals or alloys. This superelasticity is caused by a reversible phase transformation between the parent phase, stable under zero applied stress, and the stress-stabilized martensite phase. A shortcoming of current superelastic alloys is a strong temperature sensitivity to the transformation-inducing stress. **Omori *et al.*** (p. 68) show that the addition of a small amount of Ni to a Fe-Mn-Al alloy leads to an alloy with almost temperature-invariant superelastic properties.

Mobile Electrons in Oxide Melts and Glasses

Electrons often have a short lifetime in solution before they undergo a reaction, but in some

solvents, they dissolve and act like anions. The classic example is sodium dissolved in liquid ammonia, forming Na^+ and a free electron. Some solids, called electrides, can also host free electrons. **Kim *et al.*** (p. 71; see the Perspective by **Edwards**) studied $[\text{Ca}_{24}\text{Al}_{28}\text{O}_{64}]^{4+} \cdot 4e^-$, which has an internal cage structure and forms an electride when oxygen anions are displaced. Metallic conductivity persisted in the melt and in a quenched glass, where the electrons formed a paired state that moved through a hopping mechanism.

Whys and Warfares

Centuries of social and philosophical analysis have been dedicated to the general question of “how will a given war evolve?” **Johnson *et al.*** (p. 81) analyzed publicly available data on fatalities from the wars in Afghanistan and Iraq, suicide bombing data for Hezbollah and Pakistani militants, and fatalities that resulted from global terrorism between 1968 and 2008. The analysis reveals common patterns in the timing of attacks by insurgents in different geographical regions and by global terrorist groups. A linear relationship was observed between the escalation rate for attacks and the time interval between the first 2 days of fatalities in a region.

Bacteria with a Bigger Bias

When sulfate-reducing bacteria use sulfur compounds instead of oxygen during respiration, the chemical reactions that generate energy are biased toward specific natural isotopes of sulfur. The sulfite produced is thus depleted in sulfur isotopes relative to its natural abundance—often

by only a few additional atoms per thousand reactions. **Sim *et al.*** (p. 74) found that a marine bacterium isolated from coastal sediments can produce a remarkably high signal of isotopic fractionation—up to 68 times per thousand reactions. Similar high values that have been observed in sedimentary rocks were thought to require additional cycling of sulfur and oxygen; however, these results suggest that this may not always be the case.

Pros and Contrails

Contrails—the long, thin clouds produced by high-flying aircraft—are a familiar sight in the skies, and most people would think (correctly) that their formation is the primary influence of planes on cloudiness. However, planes can also decrease cloudiness in certain cases. **Heymsfield *et al.*** (p. 77) describe the appearance of aircraft-induced voids in existing clouds, produced by ice particle formation upon passage of an aircraft through a cloud and the resulting convection due to latent heating from ice growth. This phenomenon can also induce local snowfall, and may account for some of the observations previously ascribed to cloud seeding.



Chronic Fatigue

A 2009 report that patients with chronic fatigue syndrome (CFS) are infected with a retrovirus called xenotropic murine leukemia virus (XMRV) (*Science* **326**, 585) attracted considerable interest, but other work has failed to detect XMRV in independent groups of CFS patients. Now, two studies support the view that the purported association between XMRV and CFS is most likely due to contamination of laboratories and research reagents with the virus. **Paprotka *et al.*** (p. 97, published online 2 June) provide evidence that XMRV arose by recombination of two mouse leukemia viruses during laboratory passage of a human prostate tumor xenograft in mice in the 1990s. They conclude that contamination with XMRV produced by a cell line (22Rv1) derived from these early xenograft experiments is the most likely explanation for detection of the virus in patient samples. **Knox *et al.*** (p. 94, published online 2 June) examined blood samples from 61 CFS patients, 43 of whom had been diagnosed

Continued on page 12

NEW PRODUCTS FOR 2011

www.immunodx.com

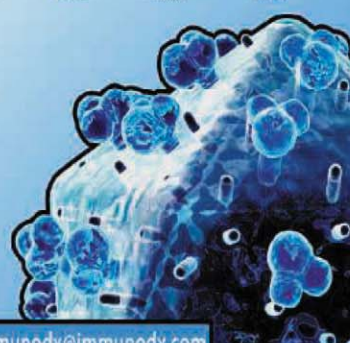
ImmunoDiagnostics, Inc.
1 Presidential Way, Suite 104, Woburn, MA 01801, USA

**Developing and Manufacturing
Quality Biologicals**

Antigens and Antibodies:
(Recombinant) (mAbs/pAbs)

•HIV-1/2	•rhHexim1	•Malaria	•Dengue
•SIV	•rhAdams5	•Toxoplasma	•Influenza
•HBV/HCV	•rhA3G	•Leptospira	•Chikungunya
•EBV	•rhCD4	•Chagas	•Norovirus
+MORE	+MORE	+MORE	+MORE

800.573.1700
immunodx@immunodx.com




Summer Internships Students with Disabilities

To meet the challenge of the competitive economy in the new millennium, AAAS started Entry Point!, a program that offers students with disabilities competitive internship opportunities in science, engineering, mathematics, computer science, and some fields of business. Join us. Together we can make a difference.

To learn more, visit:
aaas.org/plusyou/entrypoint



This Week in *Science*

Continued from page 11

previously as XMRV positive. Sensitive assays for viral nucleic acids, infectious virus, and virus-specific antibodies revealed no evidence of XMRV in any of the samples.

Doing Double Duty

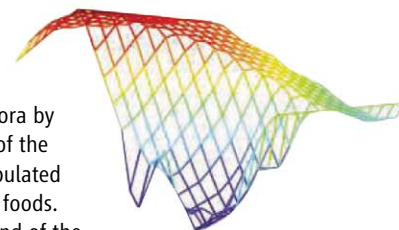
N-acetylglucosamine (GlcNAc)—1-phosphotransferase is the crucial enzyme in the generation of mannose 6-phosphate (M6P) residues on lysosomal enzymes required for their efficient transport to lysosomes. Defects in the GlcNAc-1-phosphotransferase lead to a fatal lysosomal storage disorder. GlcNAc-1-phosphotransferase is synthesized as an inactive precursor protein that is activated by proteolytic cleavage in the Golgi complex. **Marschner *et al.*** (p. 87; see the Perspective by **Ye**) now report that the protease involved in GlcNAc-1-phosphotransferase cleavage is the site-1 protease (S1P), a Golgi-localized protease that plays a central role in cholesterol homeostasis. Loss of S1P resulted in missorting of newly synthesized lysosomal enzymes due to the lack of M6P residues, which may contribute to the defective cartilage phenotype in S1P defective animals.

Nuclear Membrane Protein Sieve

En route from the outer membrane to the inner membrane of the nuclear envelope, nuclear membrane proteins must pass through the nuclear pore complex. **Meinema *et al.*** (p. 90, published online 9 June; see the Perspective by **Kriwacki and Yoon**) found that a natively unfolded linker that spaces the transmembrane domain and the nuclear localization signal, reaches out from the membrane to the central channel of the nuclear pore. During transport, the unfolded linker appears to “slice” through the nuclear pore complex scaffold, allowing the nuclear pore complex to act as a selective gate that regulates intranuclear levels of membrane proteins.

Microbes Are What You Eat

The microbial community within the gut is influenced by dietary constituents. **Faith *et al.*** (p. 101, published online 19 May) attempted to define dietary influences on the microflora by using germ-free mice colonized with 10 sequenced members of the human gut microbiota and fed diets with systematically manipulated concentrations of four ingredients commonly found in human foods. Changes in the absolute abundance of community members and of the community’s meta-transcriptome were monitored and the data were used in a simple linear model. Changes in the proportions of macronutrients explained half of the variation in microbial species abundance and casein intake was highly correlated with total microbial biomass.



Fight, Flee, or Freeze

The medial part of the central amygdala is involved in behavioral and physiological conditioned fear responses. Are the different types of fear responses reflected in different associations between behavioral and physiological components? **Viviani *et al.*** (p. 104) detected separate neuronal populations, with distinct projections to brain stem nuclei, in rats that steer freezing versus cardiovascular function. The neuronal populations in the medial central amygdala also exhibited distinct electrophysiological characteristics and responded differently to oxytocin agonists. In a contextual fear-conditioning paradigm, oxytocin selectively affected freezing, but not heart rate variability, which may explain reduced freezing and increased maternal aggression when rats defend their offspring.

Peer Pressure

Sometimes, firmly held memory representations in the brain are altered by external social influences in a phenomenon called “memory conformity.” **Edelson *et al.*** (p. 108; see the Perspective by **Roediger and McDermott**) used a behavioral paradigm in combination with brain imaging to elucidate the brain mechanisms involved. After watching a documentary and completing a memory task, individuals were presented with fake memories from other participants. Even when their original recollection was correct, a large number of participants conformed to the majority opinion and gave incorrect answers, even after being informed about the original manipulations. Such persistent errors were associated with enhanced activity in the hippocampus, as well as in the amygdala during the test.

CREDIT: FAITH ET AL.



Anthony S. Fauci is director of the National Institute of Allergy and Infectious Diseases, U.S. National Institutes of Health, Bethesda, MD. E-mail: afauci@niaid.nih.gov.

AIDS: Let Science Inform Policy

THIRTY YEARS HAVE PASSED SINCE THE FIRST CASES OF ACQUIRED IMMUNE DEFICIENCY SYNDROME (AIDS) were reported by the U.S. Centers for Disease Control and Prevention. How does this anniversary compare to the 20th or the 10th? The differences are considerable, because we now have an unprecedented opportunity, based on solid scientific data, to control and ultimately end the AIDS pandemic.

More than 60 million people have been infected with human immunodeficiency virus (HIV) worldwide. More than 30 million have died, and 34 million are currently living with HIV infection. In 2009, the most recent year for which data are available, 2.6 million people became newly infected. The burden of HIV/AIDS is overwhelmingly felt in resource-poor countries, especially in sub-Saharan Africa, which are least equipped to deal with the disease. Although the toll is staggering, the scientific progress in HIV/AIDS research over 30 years has been extraordinary, particularly in the development of antiretroviral therapy (ART), which has proven to be life-saving to many millions.

For decades, the idea of ending or even controlling the pandemic was a distant aspiration because we lacked sufficient evidence-based tools to convert the hope to reality. At this 30th anniversary, the situation has dramatically changed: We finally have scientifically validated prevention modalities that clearly work, suggesting that ending the pandemic is feasible. Older, proven prevention tools include the proper use of condoms, needle exchange programs for injection drug users, and antiretroviral treatment of HIV-infected pregnant women to prevent transmission of the virus to their newborn infants. Building on this foundation, recent HIV prevention research also has provided strong scientific evidence that adult male circumcision is highly effective in preventing infection in heterosexual men, that an antiretroviral-based topical gel prevents infection in heterosexual women, and that pre-exposure prophylaxis with ART in men who have sex with men is effective at preventing infection. And in May 2011, a randomized controlled clinical trial demonstrated that early initiation of ART by the infected partner in heterosexual couples, where one partner is HIV-infected and the other not, is highly effective in decreasing transmission of HIV to the uninfected partner.

The fact that treatment of HIV-infected adults is also prevention gives us the wherewithal, even in the absence of an effective vaccine, to begin to control and ultimately end the AIDS pandemic. Of course, the development of an AIDS vaccine would be the ultimate game-changer, and efforts toward this goal are intense. However, the existing armamentarium of scientifically proven interventions immediately offers an unprecedented opportunity to make major gains in the fight against HIV/AIDS. Global implementation of HIV interventions, including scale-up of the delivery of ART, must be accelerated, and this will be costly. Certainly, there are many competing priorities for scarce resources in the global health arena, such as other infectious diseases, maternal and child health, and tobacco control. But if one accepts the tenet that science should inform policy, then the scientific data are speaking loud and clear. Global policy-makers must seriously consider these new data in their priority-setting and decision-making.

Last month, world leaders at the United Nations General Assembly Meeting on AIDS called for providing ART for 15 million people in low- and middle-income countries by 2015, an increase from the 6.6 million currently receiving therapy, plus additional efforts toward universal access to HIV prevention, treatment, and care. An estimated \$22 billion to \$23 billion annually will be needed by 2015; current spending is approximately \$16 billion. Such targeted investments could prevent 12 million infections and 7.4 million AIDS-related deaths by 2020. For the first time in the history of HIV/AIDS, controlling and ending the pandemic are feasible; however, a truly global commitment, including investments by those rich and middle-income countries whose contributions have thus far been limited, is essential. Major investments in implementation now will save even greater expenditures in the future; and in the meantime, countless lives can be saved.

— Anthony S. Fauci

10.1126/science.1209751





ECOLOGY

The Plumage Rainbow

The plumage of birds ranges from the sublime to the (what some might consider) gaudy. Certainly, birds seem to possess a stunning range of colors in their plumage, with the most striking ones often relating to mate choice and social signaling. These colors probably evolved in response to the capabilities of the avian visual system (avian "color space").

Stoddard and Prum determined the range of colors (the color gamut) of 965 plumage samples from a wide range of bird species and showed that they occupied a mere 26 to 30% of the available avian color space. Pigment-based colors (often diet-derived) occupied 6.9% of color space (26.7% of the color gamut), whereas structure-based colors (for example, iridescent barbules) occupied 17.9% of color space (and almost 70% of the color gamut): It is in these latter colors that bird plumage diverges most from plant colors. Over evolutionary time, structural colors have dramatically extended the range of plumage coloration mechanisms available to birds. Still, plumage colors only occupy hue "continents" and "archipelagos" in color space between unoccupied regions, with, for example, few purple and fully saturated green colors. Indeed, bird plumages do not include many of the hues available to flowers, likely because certain colors may be either difficult to create or selectively undesirable. — GR

Behav. Ecol. **22**, 10.1093/beheco/arr088 (2011).

CLIMATE SCIENCE

Dueling Monsoons

Stalagmites recovered from caves in southern and eastern Asia contain a remarkable chronicle of changes in rainfall over the course of the last glacial cycle, including millennial-scale warm intervals and more prolonged episodes of cooling called Heinrich events. The oxygen isotope record of those stalagmites has been interpreted as reflecting mostly the amount of East Asian summer monsoonal rainfall there. Things may not be quite what they seem, however, according to a report by Pausata *et al.*, who use a climate model to assess the causes of the observed oxygen isotopic variations during a simulated Heinrich event. They found that Northern Hemispheric cooling during the event weakens the Indian monsoon and shifts water vapor enriched in ^{18}O from India to China. Therefore, they conclude, Chinese stalagmite oxygen isotopes actually record changes in the Indian monsoon over thousand-year time scales. — HJS

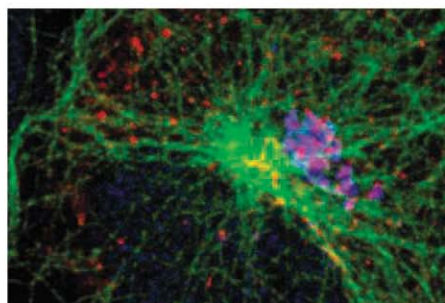
Nat. Geosci. **4**, 10.1038/NGE01169 (2011).

CELL BIOLOGY

Know Your Place

The Golgi apparatus occupies a central position close to the nucleus in mammalian cells. This

localization is determined by the position of the centrosome, the microtubule-organizing center that defines the layout of the cell and is critical for orchestrating mitosis. The importance of Golgi positioning and integrity for a variety of cell polarity-related phenomena has been difficult to distinguish. Hurtado *et al.* dissected the role of a centrosomal protein involved in Golgi positioning, AKAP450. Expression of a fragment of the protein that contains the Golgi targeting domain dissociated endogenous AKAP450 from the Golgi. Under these circumstances, the Golgi fragmented but, instead of scattering throughout the cytoplasm, the fragments collapsed around the centrosome, possibly because of the failure of the Golgi fragments to nucleate microtubules. Another fragment of AKAP450 had a different effect on Golgi positioning: The Golgi became localized in the cell periphery



but reassembled into a ribbon-like morphology reminiscent of its normal unperturbed structure. Although neither fragment significantly perturbed membrane traffic through the Golgi, both fragments inhibited the formation of the primary cilium. Major effects on directional cell migration were observed only when Golgi positioning was disrupted. — SMH

J. Cell Biol. **193**, 917 (2011).

CELL SIGNALING

Keeping Kinases on Target

Modification of proteins by protein kinase-mediated covalent phosphorylation regulates almost every biological process in the cell and especially those related to cell division. But with more than 500 kinases in a human cell phosphorylating tens of thousands of proteins, some at multiple sites, how is order maintained? One explanation is that kinases show specificity toward particular sequences in their substrates. Alexander *et al.* and Kettenbach *et al.* explored such specificity of five kinases with key roles in controlling cell division. Their phosphoproteomic and peptide screening approaches helped to define the preferred sequences of substrates for these kinases and identified previously unrecognized substrates. Furthermore, Alexander *et al.* showed that there are also some sequence

elements that selectively prevent phosphorylation of a particular substrate by certain kinases. Alexander *et al.* further proposed that subcellular localization also contributes to specificity, so that kinases that have overlapping preferred motifs are kept spatially separated. — LBR

Sci. Sig. **4**, rs5; ra42 (2011).

CHEMISTRY

Swimming in Threes

Understanding a liquid at the molecular level is a rather daunting prospect—even small droplets contain a number of molecules too vast for most people to easily imagine, let alone analyze. It turns out, though, that you can get a decent sense of many important properties by thoroughly analyzing the interaction of just a pair of molecules, and then extrapolating that interaction across the whole sample. Pieniazek *et al.* point out one instance where, although this approach falls short, consideration of three molecules' mutual interaction affords a much better match to experimental data. Specifically, they simulate the structure of a water surface and its associated response to a highly surface-selective vibrational probing technique (sum frequency generation). Past experimental studies in this vein, using isotopically labeled HOD-in-D₂O solutions to simplify spectral interpretation, have produced puzzling features attributed to distinct ice-like and bulk liquid-like local arrangements at the interface. The three-body simulations reproduce the experimental data reasonably well and suggest no need to invoke ice-like ordering. — JSY

J. Am. Chem. Soc. **133**, 10.1021/ja2026695 (2011).

ECOLOGY

Diversity Defined

Large life on Earth shows striking gradients of diversity: from the poles to the tropics and from low to high altitude. Whether such large-scale gradients also apply to microorganisms, however, has been controversial. Stomp *et al.* took advantage of a comprehensive data set collected by the U.S. Environmental Protection Agency in 1973–1975. A range of physicochemical data and phytoplankton was sampled from 540 lakes, three times each year. The data were put through regression analysis to identify the most important local environmental variables affecting species richness, as well as a structural equation model to test for links between biodiversity, environmental variables, and geographical location. Although

lake area and depth strongly influenced phytoplankton diversity, there was an overall signal of decreasing diversity as latitude and altitude increased, which reflected the overall topography of the United States. This work, when considered alongside other species richness analyses of microorganisms, suggests that very small organisms are subject to similar constraints governing large-scale distribution as the very large. — CA

Ecology **92**, 10.1890/10-1023.1 (2011).

GEOCHEMISTRY

Iron et Al

Naturally occurring iron-(hydr)oxide particles have a strong influence over nutrient and contaminant transport in Earth's aqueous surface environments. Most phases have stoichiometrically balanced chemical formulas such as FeOOH and Fe₂O₃, but ferrihydrite—an abundant yet metastable, poorly crystalline precursor to more thermodynamically stable phases—is not defined by a simple ordering. Furthermore, all natural iron-(hydr)oxides undoubtedly contain numerous internal and adsorbed impurities that have varying effects on reactivity and stability.

To understand how these impurities get incorporated into growing particles, Bazilevskaya *et al.* used a combined experimental and computational approach to track coprecipitation of ferrihydrite with varying amounts of Al³⁺. When Al³⁺ was present at low levels, it was incorporated into the ferrihydrite structure; at high



Al³⁺ levels, in contrast, two distinct Al- and Fe-rich phases formed. Computations suggest that when Al-rich ferrihydrite transforms into Al-rich FeOOH over time, Al clusters within the new phase are energetically more favorable than isolated substitutions of Al³⁺ for Fe³⁺. In a complementary study, Hansel *et al.* documented the inhibitory effect of Al-substitution on ferrihydrite transformation. Ferrihydrite was more strongly inhibited from transforming into other, more thermodynamically stable phases when Al was adsorbed on the surface than when it was incorporated into the structure. — NW

Geochim. Cosmochim. Acta **75**, 10.1016/j.gca.2011.05.041; 10.1016/j.gca.2011.05.033 (2011).

“A dream told me to do it.”



Carl R. Alving, M.D.
Chief of the Department of Adjuvant & Antigen Research, Division of Retrovirology at the Walter Reed Army Institute of Research
AAAS member

*Dr. Carl Alving
on his inspiration
for inventing
the vaccine patch.*

MemberCentral is the new website that looks at science through the eyes of AAAS members. It celebrates their achievements—like Dr. Alving's vaccine patch—and their shared belief in the transformative power of science. Use MemberCentral to connect with other members, learn about work being done in other fields, and get fresh perspectives on issues ranging from speciation to STEM education.

Visit MemberCentral today and get to know the AAAS member community in a whole new way.



MemberCentral.aaas.org

Blogs | Videos | Webinars
Discounts | Downloads | Community

1200 New York Avenue, NW
Washington, DC 20005

Editorial: 202-326-6550, FAX 202-289-7562

News: 202-326-6581, FAX 202-371-9227

Bateman House, 82-88 Hills Road
Cambridge, UK CB2 1LQ

+44 (0) 1223 326500, FAX +44 (0) 1223 326501

SUBSCRIPTION SERVICES For change of address, missing issues, new orders and renewals, and payment questions: 866-434-AAAS (2227) or 202-326-6417, FAX 202-842-1065. Mailing addresses: AAAS, P.O. Box 96178, Washington, DC 20090-6178 or AAAS Member Services, 1200 New York Avenue, NW, Washington, DC 20005

INSTITUTIONAL SITE LICENSES please call 202-326-6755 for any questions or information

REPRINTS: Author Inquiries 800-635-7181

Commercial Inquiries 803-359-4578

PERMISSIONS 202-326-7074, FAX 202-682-0816

MEMBER BENEFITS AAAS/Barnes&Noble.com bookstore www.aaas.org/bn; AAAS Online Store www.apisource.com/aaas/ code MKB6; AAAS Travels: Betchart Expeditions 800-252-4910; Apple Store www.apple.com/epstore/aaas; Bank of America MasterCard 1-800-833-6262 priority code FAA3YU; Cold Spring Harbor Laboratory Press Publications www.cshlpress.com/affiliates/aaas.htm; GEICO Auto Insurance www.geico.com/landingpage/go51.htm?logo=17624; Hertz 800-654-2200 CDP#343547; Office Depot https://bsd.officedepot.com/portallogin.do; Seabury & Smith Life Insurance 800-424-9883; Subaru VIP Program 202-326-6417; VIP Moving Services www.vipmayflower.com/domestic/index.html; Other Benefits: AAAS Member Services 202-326-6417 or www.aaasmember.org.

science_editors@aaas.org (for general editorial queries)
science_letters@aaas.org (for queries about letters)
science_reviews@aaas.org (for returning manuscript reviews)
science_bookrevs@aaas.org (for book review queries)

Published by the American Association for the Advancement of Science (AAAS), *Science* serves its readers as a forum for the presentation and discussion of important issues related to the advancement of science, including the presentation of minority or conflicting points of view, rather than by publishing only material on which a consensus has been reached. Accordingly, all articles published in *Science*—including editorials, news and comment, and book reviews—are signed and reflect the individual views of the authors and not official points of view adopted by AAAS or the institutions with which the authors are affiliated.

AAAS was founded in 1848 and incorporated in 1874. Its mission is to advance science, engineering, and innovation throughout the world for the benefit of all people. The goals of the association are to: enhance communication among scientists, engineers, and the public; promote and defend the integrity of science and its use; strengthen support for the science and technology enterprise; provide a voice for science on societal issues; promote the responsible use of science in public policy; strengthen and diversify the science and technology workforce; foster education in science and technology for everyone; increase public engagement with science and technology; and advance international cooperation in science.

INFORMATION FOR AUTHORS

See pages 784 and 785 of the 11 February 2011 issue or access www.sciencemag.org/about/authors

EDITOR-IN-CHIEF **Bruce Alberts**
EXECUTIVE EDITOR **Monica M. Bradford**
NEWS EDITOR **Colin Norman**
MANAGING EDITOR, RESEARCH JOURNALS **Katrina L. Kelner**
DEPUTY EDITORS **R. Brooks Hanson, Barbara R. Jasny, Andrew M. Sugden**

EDITORIAL SENIOR EDITORS/COMMENTARY Lisa D. Chong, Brad Wible; **SENIOR EDITORS** Gilbert J. Chin, Pamela J. Hines, Paula A. Kiberstis (Boston), Marc S. Lavine (Toronto), Beverly A. Purnell, L. Bryan Ray, Guy Riddihough, H. Jesse Smith, Phillip D. Szuroni (Tennessee), Valda Vinson, Jake S. Yeston, Laura M. Zahn (San Diego); **ASSOCIATE EDITORS** Kristen L. Mueller, Jelena Stajic, Sacha Vignier, Nicholas S. Wigginton; **BOOK REVIEW EDITOR** Sherman J. Suter; **ASSOCIATE LETTERS EDITOR** Jennifer Sills; **EDITORIAL MANAGER** Cara Tate; **SENIOR COPY EDITORS** Jeffrey E. Cook, Cynthia Howe, Harry Jach, Lauren Kmeck, Barbara P. Ordway, Trista Wagoner; **COPY EDITOR** Chris Filiatreau; **SENIOR EDITORIAL COORDINATORS** Carolyn Kyle, Beverly Shields; **EDITORIAL COORDINATORS** Joi S. Granger, Anita Wynn; **PUBLICATIONS ASSISTANTS** Ramatoulaye Diop, Emily Guise, Jeffrey Hearn, Michael Hicks, Lisa Johnson, Scott Miller, Jerry Richardson, Brian White; **EDITORIAL ASSISTANT** Patricia M. Moore; **EXECUTIVE EDITORIAL ASSISTANT** Yolanda O'Bannon (San Francisco); **EXECUTIVE ASSISTANT** Alison Crawford; **ADMINISTRATIVE SUPPORT** Maryrose Madrid; **EDITORIAL FELLOW** Melissa R. McCartney
EDITORIAL DIRECTOR, WEB AND NEW MEDIA Stewart Willis; **SENIOR WEB EDITOR** Tara S. Marathe; **RESEARCH ASSOCIATE** Corinna Cohn; **WEB DEVELOPMENT MANAGER** Martyn Green; **WEB DEVELOPER** Andrew Whitesell; **INTERNS** Andrew Green, Kerry Klein

NEWS DEPUTY NEWS EDITORS Robert Coontz, David Grimm (Online), Eliot Marshall, Jeffrey Mervis, Leslie Roberts, John Travis; **CONTRIBUTING EDITORS** Elizabeth Culotta, Polly Shulman; **NEWS WRITERS** Yudhijit Bhattacharjee, Adrian Cho, Jennifer Couzin-Frankel, Carolyn Gramling, Jocelyn Kaiser, Richard A. Kerr, Eli Kintisch, Greg Miller, Elizabeth Pennisi, Sara Reardon, Robert F. Service (Pacific NW), Erik Stokstad; **WEB DEVELOPER** Daniel Berger; **INTERNS** Daniel Strain, Yasmin Ogale, Natalie Villacorta; **CONTRIBUTING CORRESPONDENTS** Jon Cohen (San Diego, CA), Daniel Ferber, Ann Gibbons, Sam Jean, Andrew Lawler, Mitchell Leslie, Charles C. Mann, Virginia Morell, Gary Taubes; **COPY EDITORS** Linda B. Felaco, Melvin Gatling, Melissa Raimondo; **ADMINISTRATIVE SUPPORT** Scherraine Mack; **BUREAU** San Diego, CA: 760-942-3252, FAX 760-942-4979; Pacific Northwest: 503-963-1940

PRODUCTION DIRECTOR Wendy K. Shank; **ASSISTANT MANAGER** Rebecca Doshi; **SENIOR SPECIALISTS** Steve Forrester, Chris Redwood, Anthony Rosen; **PREFLIGHT DIRECTOR** David M. Tompkins; **MANAGER** Marcus Spiegler; **SPECIALISTS** Jason Hillman, Tara Kelly

ART DIRECTOR Yale Fitzpatrick; **ASSOCIATE ART DIRECTOR** Laura Creveling; **SENIOR ILLUSTRATORS** Chris Bickel, Katharine Suttill; **ILLUSTRATOR** Yana Hammond; **SENIOR ART ASSOCIATES** Holly Bishop, Preston Huey, Nayomi Kevitayagala, Matthew Twombly; **ART ASSOCIATE** Kay Engman; **PHOTO EDITOR** Leslie Blizard

SCIENCE INTERNATIONAL

EUROPE (science@science-int.co.uk) **EDITORIAL: INTERNATIONAL MANAGING EDITOR** Andrew M. Sugden; **SENIOR EDITOR/COMMENTARY** Julia Fahrenkamp-Uppenbrink; **SENIOR EDITORS** Caroline Ash, Stella M. Hurtle, Ian S. Osborne, Peter Stern; **ASSOCIATE EDITOR** Maria Cruz; **LOCUM EDITOR** Helen Pickersgill; **EDITORIAL SUPPORT** Samantha Hogg, Alice Whaley; **ADMINISTRATIVE SUPPORT** John Cannell, Janet Clements, Louise Hartwell; **NEWS: DEPUTY NEWS EDITOR, U.K.** Daniel Clery; **CONTRIBUTING EDITOR, EUROPE** Martin Enserink; **CONTRIBUTING CORRESPONDENTS** Michael Balter (Paris), John Bohannon (Vienna), Gretchen Vogel (Berlin)

LATIN AMERICA CONTRIBUTING CORRESPONDENT Antonio Regalado

ASIA Japan Office: Asca Corporation, Tomoko Furusawa, Rustic Bldg. 7F, 77 Tenjin-cho, Shinjuku-ku, Tokyo 162-0808, Japan; +81 3 6802 4616, FAX +81 3 6802 4615, inquiry@sciencemag.jp; **ASIA NEWS EDITOR** Richard Stone (Beijing: rstone@aaas.org); **CONTRIBUTING CORRESPONDENTS** Dennis Normile [Japan: +81 (0) 3 3391 0630, FAX +81 (0) 3 5936 3531; dnormile@gol.com]; Hao Xin [China: cindyhao@gmail.com]; Mara Hvistendahl [China: mara@marahvistendahl.com]; Pallava Bagla [South Asia: +91 (0) 11 2271 2896; pbagla@vsnl.com]

EXECUTIVE PUBLISHER **Alan I. Leshner**
PUBLISHER **Beth Rosner**

FULFILLMENT SYSTEMS AND OPERATIONS (membership@aaas.org); **CUSTOMER SERVICE SUPERVISOR** Pat Butler; **SPECIALISTS** Latoya Casteel, LaVonda Crawford, Vicki Linton, April Marshall; **DATA ENTRY SUPERVISOR** Cynthia Johnson; **SPECIALISTS** Shirlene Hall, Tarrika Hill, William Jones

BUSINESS OPERATIONS AND ADMINISTRATION DIRECTOR Deborah Rivera-Wienhold; **BUSINESS SYSTEMS AND FINANCIAL ANALYSIS DIRECTOR** Randy Yi; **MANAGER, FULFILLMENT SYSTEMS** Frits Buningh; **MANAGER, BUSINESS ANALYSIS** Eric Knott; **MANAGER, BUSINESS OPERATIONS** Jessica Tierney; **BUSINESS ANALYSTS** Priti Pamnani, Celeste Troxler; **Christine Wehrli**; **RIGHTS AND PERMISSIONS:** **ADMINISTRATOR** Emilie David; **ASSOCIATE** Elizabeth Sandler; **MARKETING DIRECTOR** Ian King; **MARKETING MANAGERS** Allison Pritchard, Alison Chandler, Julieanne Wiegla, Samantha Smith; **MARKETING ASSOCIATES** Aimee Aponte, Mary Ellen Crowley; **SENIOR MARKETING EXECUTIVE** Jennifer Reeves; **DIRECTOR, SITE LICENSING** Tom Ryan; **DIRECTOR, CORPORATE RELATIONS** Eileen Bernadette Moran; **SENIOR PUBLISHER RELATIONS SPECIALIST** Kiki Forsythe; **PUBLISHER RELATIONS MANAGER** Catherine Holland; **PUBLISHER RELATIONS, EASTERN REGION** Philip Smith; **PUBLISHER RELATIONS, WESTERN REGION** Ryan Rexroth; **CUSTOMER RELATIONS MANAGER** Iqoo Edim; **CUSTOMER RELATIONS COORDINATOR** David Lee; **MARKETING MANAGER** Christina Schlecht; **MARKETING ASSOCIATES** Laura Tutino, Chad Johnson; **ELECTRONIC MEDIA DIRECTOR** Elizabeth Harman; **ASSISTANT MANAGER** Lisa Stanford; **SENIOR PRODUCTION SPECIALIST** Ryan Atkins; **PRODUCTION SPECIALISTS** Antoinette Hodal, Michele Johnston, Kimberly Oster; **DIRECTOR, WEB AND NEW MEDIA** Will Collins; **PROJECT MANAGER** Trista Snyder; **SENIOR PRODUCTION SPECIALIST** Christopher Coleman; **COMPUTER SPECIALISTS** Walter Jones, Kai Zhang

ADVERTISING DIRECTOR, WORLDWIDE AD SALES Bill Moran

COMMERCIAL EDITOR Sean Sanders; 202-326-6430

ASSISTANT COMMERCIAL EDITOR Tianna Hicklin 202-326-6463

PRODUCT (science_advertising@aaas.org); **MIDWEST** Rick Bongiovanni: 330-405-7080, FAX 330-405-7081; **EAST COAST/ E. CANADA** Laurie Faraday: 508-747-9395, FAX 617-507-8189; **WEST COAST/W. CANADA** Lynne Stickrod: 415-931-9782, FAX 415-520-6940; **UK/EUROPE/ASIA** Roger Gonçalves: TEL/FAX +41 43 243 1358; **JAPAN** ASCA Corporation, Makiko Hara: +81 (0) 3 6802 4616, FAX +81 (0) 3 6802 4615; ads@sciencemag.jp; **CHINA/TAIWAN** Ruolei Wu: +86 1367 1015 294 rww@aaas.org

WORLDWIDE ASSOCIATE DIRECTOR OF SCIENCE CAREERS Tracy Holmes: +44 (0) 1223 326525, FAX +44 (0) 1223 326532

CLASSIFIED (advertise@sciencecareers.org); **U.S.:** **MIDWEST/WEST COAST/ SOUTH CENTRAL/CANADA** Tina Burcks: 202-326-6577; **EAST COAST/INDUSTRY** Elizabeth Early: 202-326-6578; **SALES ADMINISTRATOR:** Marci Gallun; **EUROPE/ROW SALES:** Susanne Kharrar, Dan Pennington, Alex Palmer; **SALES ASSISTANT** Lisa Patterson; **JAPAN** ASCA Corporation, Makiko Hara: +81 (0) 3 6802 4616, FAX +81 (0) 3 6802 4615; careers@sciencemag.jp; **CHINA/TAIWAN** Ruolei Wu: +86 1367 1015 294 rww@aaas.org; **ADVERTISING SUPPORT MANAGER** Karen Foote: 202-326-6740; **ADVERTISING PRODUCTION OPERATIONS MANAGER** Deborah Tompkins; **SENIOR PRODUCTION SPECIALIST/GRAPHIC DESIGNER** Amy Hardcastle; **PRODUCTION SPECIALIST** Yuse Lajiminshup; **SENIOR TRAFFIC ASSOCIATE** Christine Hall; **SALES COORDINATOR** Shirley Young

AAAS BOARD OF DIRECTORS RETIRING PRESIDENT, CHAIR Alice Huang; **PRESIDENT** Nina Fedoroff; **PRESIDENT-ELECT** William Press; **TREASURER** David E. Shaw; **CHIEF EXECUTIVE OFFICER** Alan I. Leshner; **BOARD** Nancy Knowlton, Stephen Mayo, Raymond Orbach, Julia M. Phillips, Sue V. Rosser, David D. Sabatini, Inder Verma, Thomas A. Woolsey



ADVANCING SCIENCE, SERVING SOCIETY

SENIOR EDITORIAL BOARD

Cori Bargmann, *The Rockefeller Univ.*
John I. Brauman, *Chair, Stanford Univ.*
Richard Losick, *Harvard Univ.*
Michael S. Turner, *University of Chicago*

BOARD OF REVIEWING EDITORS

Adriano Aguzzi, *Univ. Hospital Zürich*
Takuzo Aida, *Univ. of Tokyo*
Sonia Altizer, *Univ. of Georgia*
Sebastian Amigorena, *Institut Curie*
Angelika Amon, *MIT*
Kathryn Anderson, *Memorial Sloan-Kettering Cancer Center*
Siv G. E. Andersson, *Uppsala Univ.*
Peter Andolfatto, *Princeton Univ.*
Meinrat O. Andreae, *Max Planck Inst., Mainz*
John A. Bargh, *Univ. of Texas, Dallas*
Ben Barres, *Stanford Medical School*
Marisa Bartolomei, *Univ. of Penn. School of Med.*
Jordi Bascompte, *Estación Biológica de Doñana, CSIC*
Facundo Batista, *London Research Inst.*
Ray H. Baughman, *Univ. of Texas, Dallas*
David Baum, *Univ. of Wisconsin*
Yasmine Belkaid, *NIAD, NIH*
Philip Benfey, *Duke Univ.*
Stephen J. Benkovic, *Penn State Univ.*
Gregory C. Berzosa, *Stanford Univ.*
Peer Borik, *EMBL*
Bernard Bourdon, *Ecole Normale Supérieure de Lyon*
Ian Boyd, *Univ. of St. Andrews*
Paul M. Brakefield, *Univ. of Cambridge*
Christian Büchel, *Universitätsklinikum Hamburg-Eppendorf*
Joseph A. Burns, *Cornell Univ.*
William P. Butz, *Population Reference Bureau*
Gyorgy Buzsáki, *Rutgers Univ.*
Mats Carlsson, *Univ. of Oslo*
Mildred Cho, *Stanford Univ.*
David Clapham, *Children's Hospital, Boston*
David Clary, *Univ. of Oxford*
J. M. Claverie, *CNRS, Marseille*
Jonathan D. Cohen, *Princeton Univ.*
Alan Cowman, *Walter & Eliza Hall Inst.*
Robert H. Crabtree, *Yale Univ.*
Wolfgang Cramer, *Potsdam Inst. for Climate Impact Research*
F. Fleming Crim, *Univ. of Wisconsin*
Jeff L. Dangl, *Univ. of North Carolina*
Tom Daniell, *Univ. of Washington*

Stanislas Dehaene, *Collège de France*
Emmanouil I. Dermizakis, *Univ. of Geneva Medical School*
Robert Desimone, *MIT*
Claude Desplan, *New York Univ.*
Ap Dijksterhuis, *Radboud Univ. of Nijmegen*
Neesje Discher, *Univ. of Pennsylvania*
Scott C. Doney, *Woods Hole Oceanographic Inst.*
Jennifer A. Doudna, *Univ. of California, Berkeley*
Julian Downward, *Cancer Research UK*
Bruce Dunn, *Univ. of California, Los Angeles*
Christopher Dye, *WHO*
David Ehrhardt, *Carnegie Inst. of Washington*
Michael B. Elowitz, *Calif. Inst. of Technology*
Tim Elston, *Univ. of North Carolina at Chapel Hill*
Gerhard Ertl, *Fritz-Haber-Institut, Berlin*
Barry Everitt, *Univ. of Cambridge*
Paul G. Falkowski, *Rutgers Univ.*
Ernst Fehr, *Univ. of Zurich*
Tom Fenchel, *Univ. of Copenhagen*
Alain Fischer, *INSERM*
Wulfram Gerstner, *EPFL Lausanne*
Karl-Helmut Glassmeier, *For Geophysics & Extraterrestrial Physics, TU Braunschweig*
Diane Griffin, *Johns Hopkins Bloomberg School of Public Health*
Elizabeth Grove, *Univ. of Chicago*
Tejapraj Ha, *Univ. of Illinois at Urbana-Champaign*
Christian Haas, *Univ. of Tübingen*
Steven Hahn, *Fred Hutchinson Cancer Research Center*
Gregory J. Hannon, *Cold Spring Harbor Lab.*
Martin Heimann, *Max Planck Inst., Jena*
Isaac Held, *NOAA*
James A. Hendler, *Rensselaer Polytechnic Inst.*
Janet G. Hering, *Swiss Fed. Inst. of Aquatic Science & Technology*
Ray Hilborn, *Univ. of Washington*
Michael E. Himmel, *National Renewable Energy Lab.*
Kai-Uwe Hinrichs, *Univ. of Bremen*
Kei Hirose, *Tokyo Inst. of Technology*
David Hodell, *Univ. of Cambridge*
Ove Hoegh-Guldberg, *Univ. of Queensland*
David Holden, *Imperial College*
Lara Hooper, *Univ. of California, Irvine*
Jeffrey A. Hubbell, *EPFL Lausanne*
Steven Jacobsen, *Univ. of California, Los Angeles*
Kai Johnson, *EPFL Lausanne*
Peter Jonas, *Universität Freiburg*
William Kaelin, *Dana-Farber Cancer Inst.*

Barbara B. Kahn, *Harvard Medical School*
Daniel Kahne, *Harvard Univ.*
Bernhard Keimer, *Max-Planck Inst., Stuttgart*
Joel Kingsolver, *Univ. of North Carolina at Chapel Hill*
Robert Kingston, *Harvard Medical School*
Alberto R. Kornblihtt, *Univ. of Buenos Aires*
Leonid Kruglyak, *Princeton Univ.*
Mitchell A. Lazar, *Univ. of Pennsylvania*
David Lazer, *Harvard Univ.*
Virginia Lee, *Univ. of Pennsylvania*
Ottoline Leyser, *Cambridge Univ.*
Olle Lindvall, *Univ. Hospital, Lund*
Marcia C. Linn, *Univ. of California, Berkeley*
John Lis, *Cornell Univ.*
Jianguo Liu, *Michigan State Univ.*
Richard Losick, *Harvard Univ.*
Jonathan Losos, *Harvard Univ.*
Ke Lu, *Chinese Acad. of Sciences*
Laura Machesy, *CRUK Beatson Inst. for Cancer Research*
Andrew P. MacKenzie, *Univ. of St Andrews*
Anne Magurran, *Univ. of St Andrews*
Oscar Marin, *CSIC & Univ. Miguel Hernández*
Charles Marshall, *Univ. of California, Berkeley*
Martin M. Matzuk, *Baylor College of Medicine*
Graham Medley, *Univ. of Warwick*
Yasushi Miyashita, *Univ. of Tokyo*
Richard Morris, *Univ. of Edinburgh*
Edward Moses, *Lawrence Livermore National Laboratory*
Sean Munro, *MRC Lab. of Molecular Biology*
Naoto Nagaosa, *Univ. of Tokyo*
Janes Nelson, *Stanford Univ. School of Med.*
Timothy W. Nilsen, *Case Western Reserve Univ.*
James A. Novak, *Univ. of California, Irvine*
Helga Nowotny, *European Research Advisory Board*
Luke O'Neill, *Trinity College, Dublin*
Stuart H. Orkin, *Dana-Farber Cancer Inst.*
Christine Ortiz, *MIT*
Elinor Ostrom, *Indiana Univ.*
Andrew Oswald, *Univ. of Warwick*
Jane Parker, *Max-Planck Inst. of Plant Breeding Research*
Donald R. Paul, *Univ. of Texas at Austin*
P. David Perini, *Univ. of California, Berkeley*
Lara Hooper, *Univ. of California, Irvine*
John H. J. Petrini, *Memorial Sloan-Kettering Cancer Center*
Simon Philippot, *Univ. of Florida*
Philippe Poulin, *CNRS*
Colin Renfrew, *Univ. of Cambridge*
Trevor Robbins, *Univ. of Cambridge*

Barbara A. Romanowicz, *Univ. of California, Berkeley*
Jens Rostrup-Nielsen, *Aalto Topsoe*
Edward M. Rubin, *Lawrence Berkeley National Lab*
Mike Ryan, *Univ. of Texas, Austin*
Shimon Sakaguchi, *Kyoto Univ.*
Miquel Salmeron, *Lawrence Berkeley National Lab*
Jürgen Sandkühner, *Medical Univ. of Vienna*
Randy Seeley, *Univ. of Cincinnati*
Christine Seidman, *Harvard Medical School*
Vladimir Shalaeu, *Purdue Univ.*
Joseph Silk, *Univ. of Oxford*
Denis Simon, *Univ. of Oregon*
Alison Smith, *John Innes Centre*
Davor Solter, *Inst. of Medical Biology, Singapore*
John Speakman, *Univ. of Aberdeen*
Allan C. Spradling, *Carnegie Institution of Washington*
Jonathan Sprent, *Garvan Inst. of Medical Research*
**Elisbeth Steh, ETH Zürich
Ira Tabas, *Columbia Univ.*
Yoshiko Takahashi, *Nara Inst. of Science and Technology*
John Thomas, *Duke Univ.*
Herbert Virgin, *Washington Univ.*
Bert Vogelstein, *Johns Hopkins Univ.*
Christina Volkert, *Univ. of Göttingen*
Bruce D. Walker, *Harvard Medical School*
Douglas Wallace, *Leibniz Inst. of Marine Sciences*
Ian Walmsley, *Univ. of Oxford*
David A. Wardle, *Swedish Inst. of Agric Sciences*
Detlef Weigel, *Max Planck Inst., Tübingen*
Jonathan Weissman, *Univ. of California, San Francisco*
Sue Wessler, *Univ. of California, Riverside*
Ian A. Wilson, *The Scripps Res. Inst.*
Timothy D. Wilson, *Univ. of Virginia*
Jan Zaanen, *Leiden Univ.*
Mayana Zatz, *University of Sao Paulo*
Jonathan Zehr, *Ocean Sciences*
Huda Zoghbi, *Baylor College of Medicine*
Maria Zuber, *MIT***

BOOK REVIEW BOARD

John Aldrich, *Duke Univ.*
David Bloom, *Univ. of California, Irvine*
Angela Creager, *Princeton Univ.*
Richard Swedner, *Univ. of Chicago*
Ed Wasserman, *DuPont*
Lewis Wolpert, *Univ. College London*

Discover the latest innovation from BD Biosciences.

WELL HELLO HANDSOME.

See more in the insert
(this issue of Science).
bdbiosciences.com/go/verse

BD FACS[®] Universal Loader

What's really exciting is
what's behind it.

The new BD FACSVerse™ flow cytometer is the latest in the family of high-performance analyzers that incorporates the best of our thinking and the very latest advances in technology to simplify your workflow today and tomorrow.

The innovations built into the new BD FACSVerse are on everyone's wish list,

from ingenious automation to unparalleled flexibility, so you can start strong today and grow tomorrow. Take a good look, there's quite a lot to see.

Learn more in the insert bound into this edition or visit bdbiosciences.com/go/verse.

Simply brilliant.



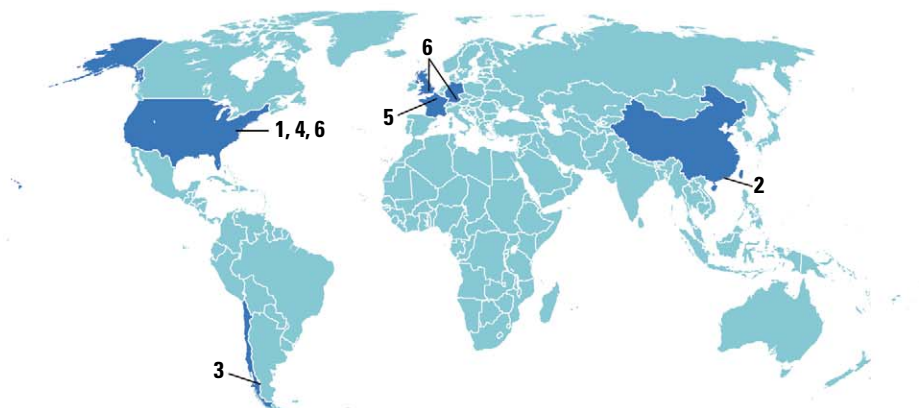
Helping all people
live healthy lives

Class I (1) laser product.
For Research Use Only. Not for use in diagnostic or therapeutic procedures.
BD, BD Logo and all other trademarks are property of Becton, Dickinson and Company. © 2011 BD
23-13306-00

WorldMags

BD Biosciences
2350 Qume Drive
San Jose, CA 95131
bdbiosciences.com

AROUND THE WORLD



Washington, D.C. 1

U.S. on Verge of Patent Reform

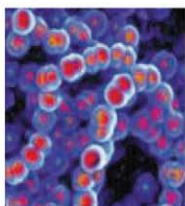
A bill to overhaul the U.S. patent system survived a dispute over funding and passed the House of Representatives last week, 304 to 117. The Senate approved a similar bill in March, 95-5. After 6 years of debate, Congress seems ready to make the first big revision of the U.S. patent system in 60 years.

Both the House and Senate would end the U.S. practice of giving priority to the first person who claims to have invented a new technology; instead, the patent would go to the first to file a valid application. This would bring the U.S. system in line with the rest of the world. Those who favor first-to-file—including large technology firms—say that it is objective, efficient, and likely to reduce lawsuits. But small businesses and independent inventors have argued that the change will favor corporations. House and Senate negotiators will get together this month to work out a final bill.

Hong Kong 2

Mutated Bacteria Drives Scarlet Fever Outbreak

A mutated strain of *Streptococcus* is apparently behind an outbreak of scarlet fever in Hong Kong that has killed two children and sickened more than 600 people so far this year. Over the past decade, Hong Kong has typically recorded 100 to 200 cases annually with no deaths. Young adults, not usually affected by the disease, are now becoming infected. And neighboring parts of southern China and Macao are also seeing more scarlet fever cases, according to



Hong Kong's Department of Health.

University of Hong Kong microbiologist Kwok-Yung Yuen says an analysis of a draft sequence of the genome suggests that the strain acquired greater virulence and drug resistance by picking up one or more genes from bacteria normally found in the human oral and urogenital tracts. He believes the overuse of antibiotics is driving the emergence of drug resistance in these bacteria.

Coyhaique, Chile 3

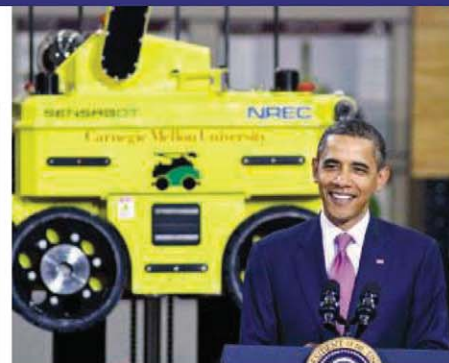
Court Delays Controversial Patagonian Dams

An unexpected decision by an appeals court in Puerto Montt, Chile, has put on hold a proposal to build five dams on the Baker and Pascua rivers in the Patagonian region of Aysén. The court agreed on 20 June to examine claims of irregularities in the environmental review of the \$3.2 billion Hidro-Aysén project, which was approved by the local government on 9 May.

The hydroelectric scheme, backed by the Chilean Colbún and Spanish-Italian Endesa companies, is designed to generate power for central Chile; its reservoirs would flood nearly 6000 hectares of Patagonian land. Long opposed by environmentalists, the project has sparked massive protests throughout Chile since its approval last month.

Opponents, including local entrepreneurs, objected that the review of the dams by the Commission for Environmental Assessment and approval by the government violated their constitutional rights. They also said that critical information, such as data on the risk of landslides and tsunamis around reservoirs, had been ignored in the review. The court has allowed 3 months to resolve the appeal.

<http://scim.ag/chiledams>



Washington, D.C. 4

White House Retools Advanced Manufacturing Efforts

Last week, the Obama Administration gave a shout-out to advanced manufacturing research in an effort to drum up support for an economically important but decidedly unsexy topic. In a visit to Carnegie Mellon University, the president announced that government, academic, and industrial leaders have formed a planned \$500 million public-private partnership to oversee a suite of research investments in the field. In listing the sorts of things the partnership would oversee, Obama mentioned a \$50-million co-robotics initiative being launched by four federal agencies and a proposed \$100-million effort, with the catchy name of the Materials Genome Initiative, to use computing power to improve the discovery, development, and manufacturing of new materials.

The numbers attached to the various efforts are a bit soft. The announced figures represent a combination of money already on the books of various federal agencies, contributions from industry, and spending levels in the president's 2012 budget request that Congress is unlikely to match.

Paris 5

Diabetes Pill Deaths Prompt French Drug Regulation Reform

French health minister Xavier Bertrand unveiled on 23 June what he described as the most important overhaul of the drug regulation system ever undertaken in France. The overhaul was in part driven by a scandal related to the diabetes drug benfluorex, or Médiator. The drug was on the market for 33 years in France and was taken by 5 million people until November 2009 when new research linking it to heart valve damage prompted its withdrawal from the market. Médiator is estimated to have caused 500 to 2000 deaths in France.

The scandal raised questions about the French pharmaceutical industry's closeness

CREDITS (TOP TO BOTTOM): ARCHIE CARPENTER/UP/LANDOV; JAMES CAVALLINI/CUSTOM MEDICAL STOCK PHOTO/NEWS.COM

to politics and the regulators. The reforms will focus on preventing conflicts of interest in the health service, increasing transparency in decision making on drug approvals, and ensuring that drugs offer real benefits. New drugs would be compared with existing ones and not just placebos.

<http://scim.ag/drugreform>

Munich, London, and Washington, D.C. 6

Three Funders Launch Open-Access Biology Journal

Three heavyweight nongovernmental funders of science are launching a free, online biology journal aimed at publishing the very best papers within a few weeks of submission.

The Wellcome Trust in the United Kingdom and the Howard Hughes Medical Institute (HHMI) in the United States are setting up a joint venture with the Max Planck Society in Germany to run the life sciences and biomedical journal. It will “attract the absolute top tier of scientific publications,” said Wellcome Trust Director Mark Walport this week. The journal hopes to review papers within 3 to 4 weeks. “We’re not going to go through endless iterations of nitpicking,” Walport said.

The journal will be open access, meaning that articles will be freely available online the moment they are published. Working scientists, not professional editors, will oversee peer review. The new journal will not charge so-called author fees to cover costs, at least at first. Its founders are also considering whether to pay reviewers. The first issue is to be published in summer 2012.

NEWSMAKERS

California Stem Cell Agency Picks New Chair

The California Institute for Regenerative Medicine (CIRM) has elected southern California bond financier **Jonathan Thomas** to be its next chair. Thomas will succeed Robert Klein, the real estate investor who spearheaded the 2004 ballot initiative to create the publicly funded agency and led it for its first 6 years. Klein’s tenure has generated both praise and controversy, and the process of choosing his successor wasn’t pretty (*Science*, 24 December 2010, p. 1742). But last week the CIRM board opened a new



chapter, picking Thomas over the only other candidate, Frank Litvack, a cardiologist and medical device entrepreneur, by a vote of 14 to 11.

Critics of Klein wanted a chair who’d be less involved in daily operations. Litvack seemed to agree, saying he’d take a part-time salary and play mainly an oversight role. Thomas, however, insisted the chair is a full-time job. He also emphasized his experience in finance. With California in a prolonged fiscal crisis, CIRM may have to find sources of funding other than the state bonds that have sustained it so far, Thomas told the board before the vote.

Studies in Microwaves, Fluids Nab Kyoto Prize

Russian astrophysicist **Rashid Sunyaev** and American chemist **John Cahn** have won the Kyoto Prize from the Japanese Inamori Foundation. The 68-year-old Sunyaev, who is a director of the Max Planck Institute for Astrophysics in Garching, Germany, and chief scientist at the Space Research Institute in Moscow, wins the prize for Lifetime Achievement in the Basic Sciences. And 83-year-old Cahn, an emeritus senior fellow at the U.S. National Institute of Standards and Technology, wins the foundation’s prize in Advanced Technology. Each winner will receive a gold medal and 50 million

THEY SAID IT

“Did he carb load or die from a fight?”

Otzi’s body and burial site provoke speculation of endless duration that makes scientists grin with delight!”

—A limerick composed by a *ScienceNOW* Facebook fan in response to new findings posted about the 5200-year-old Ötzi the Iceman (*Science*, 24 June 2011, p. 1489).

yen—roughly \$625,000.

Sunyaev pioneered the study of fluctuations in the cosmic microwave background (CMB). Working with a tough mentor in the former Soviet Union named Yakov Zel’dovich, Sunyaev showed that the tiny acoustic vibrations in the universe moments after the big bang could be observed as temperature and density variations in CMB radiation, the faint



>>



Fire Threatens Los Alamos

The Los Alamos National Laboratory was shut down on 27 June as a fast-moving wildfire, driven by 100-kilometer-per-hour winds, bore down on the New Mexico facility. The blaze, which started some 20 kilometers southwest of the town of Los Alamos on 26 June, engulfed about 175 square kilometers in 24 hours. This photograph, taken on Sunday night, shows flames cresting over the hills above the lab. On Monday afternoon, authorities ordered a mandatory evacuation of the town. As this issue went to press, the fire continued to rage to the west of the lab, which was scheduled to remain closed at least through Wednesday. Lab officials said the risk to wastes stored at the lab was low.

>>NEWSMAKERS

afterglow of the big bang.

Cahn's work on the behavior of mixtures of different materials has led to the development of several new materials, including better-performing metals, glass, polymers, and thermal materials with unique properties. Cahn's work has also found application in the fields of physics, mathematics, chemistry, engineering, and economics.

<http://scim.ag/KyotoPrize>

Three Q's

Microbiologist **Phillip**

Baker spent years managing the basic research program for Lyme disease at the National Institutes of Health before retiring and joining the American Lyme Disease Foundation (ALDF) in Lyme, Connecticut, as executive director. His latest crusade focuses on the 2008 documentary *Under Our Skin*, which presents the view that Lyme can become a chronic disease, which is at odds with mainstream medicine and treatment guidelines. Baker's been urging PBS affiliate stations not to show the movie, with mixed success—Maryland Public Television aired it 26 June.



Q: Why do you think PBS shouldn't air *Under Our Skin*?

I think it's dishonest to show the film without showing all that background information. There's no evidence for a persistent infection; there's no definition for chronic Lyme disease. I'm afraid that people are going to be terribly misled by a film like this.

Q: How are you fighting back?

I've written to [PBS] headquarters at Arlington, Virginia. They told me that it's up to the individual stations. I contacted a lot of other affiliates. I found out the Boston affiliate decided not to show it. They had an internal review [after Baker wrote to them]. My review of the film is posted on the ALDF Web site. *Microbe* is going to publish my film review in the July issue.

Q: Dozens of PBS stations have already shown the movie, or plan to. What's motivating you to keep fighting it?

I've done all I could do, I think. ... The issue is this: No one is saying that they're not suffering from something. ... It's just that it doesn't have anything to do with chronic Lyme disease. They just won't relent.

Random Sample

Darwin's Library a Click Away

As Charles Darwin finished Charles Lyell's *Principles of Geology*, he scribbled on the last page, "if this were true adios theory." Such comments, which appear in the margins of about half of his 1480 books, reveal an avid, thoughtful reader constantly evaluating his ideas and those of other authors.

Until 20 years ago, Darwin's personal library and his scribbled comments were sequestered away in the Cambridge University Library in the United Kingdom. But now, anyone can peer into those pages to see how Darwin's thinking was evolving as he developed his theory of evolution. The 330 most heavily annotated titles are now digitized and online at the Biodiversity Heritage Library (<http://www.biodiversitylibrary.org/collection/darwinlibrary>).

It's not the first time someone has cataloged Darwin's notes and comments: In the 1990s, two Darwin scholars, Mario A. Di Gregorio and Nick Gill, published the 792-page *Charles Darwin's Marginalia*. But making sense of that catalog required access to the same editions of the books Darwin had, some of which are quite rare, says David Kohn, a historian of science at the American Museum of Natural History in New York City. "What the digitization allowed us to do was bring you into Cambridge University" without having to leave your desk, says Kohn, who started the project 18 months ago in collaboration with the University of Cambridge. A \$290,000 grant from the U.K. Joint Information Systems Committee and the U.S. National Endowment for the Humanities allowed them to digitize about half of the annotated books; they are seeking funding to put the rest online as well.



FINDINGS

Buying Time for Snake Bite Victims

Time is of the essence for people bitten by a poisonous snake. Now, researchers have identified an ointment that might give victims of bites from snakes such as cobras a bit more time to reach a hospital or clinic.

The bulky proteins in some snake venoms don't infiltrate the bloodstream immediately but wend through the lymphatic system to the heart. So physiologist Dirk van Helden of the University of Newcastle in Australia and colleagues went looking for a chemical that might detain the venom. They focused on an ointment for a painful condition called anal fissures that contains nitroglycerin. It releases nitric oxide, causing the lymphatic vessels to clench.

The researchers injected volunteers in the foot with a harmless radioactive mixture that moves through the lymphatic vessels. In control subjects, the mixture took 13 minutes to reach the top of the leg, but required 54 minutes if the researchers immediately smeared the ointment around the injection site,



the team reports online this week in *Nature Medicine*. The researchers then injected the feet of anesthetized rats with venom from the eastern brown snake, one of Australia's deadliest; animals whose limbs were smeared with the cream survived about 50% longer than those left untreated.

The ointment could prove valuable for treating bites from snakes such as cobras, mambas, and kraits that produce neurotoxic venom. But it's unlikely to be effective against bites from U.S. snakes such as rattlesnakes, copperheads, and cottonmouths, which inject a different type of venom.

http://scim.ag/snake_bite

Deciphering Ovarian Cancer

A massive effort to catalog genetic errors in ovarian cancer has found many known cancer genes along with surprising genomic disorders.

The study explored the genetic underpinnings of serous ovarian adenocarcinoma, an aggressive cancer that kills 9700 women in the United States each year. Fifteen teams analyzed nearly 500 patients' tumors for genetic aberrations and sequenced the gene-coding DNA of 316 of the samples. Nearly

all had mutations in P53, a tumor suppressor gene, and some had mutations in other cancer genes. The study also found “enormous structural variation,” including extra copies of many genes, says project leader Paul Spellman of the Lawrence Berkeley National Laboratory in California. Half of the samples had flaws in the cell’s machinery for repairing DNA, suggesting these tumors could be treated with certain drugs.

The study, published this week in *Nature*, is the second cancer completed by The Cancer Genome Atlas, a \$375-million-and-counting project launched by the National Institutes of Health in 2006 that is sequencing more than 20 cancer types.

http://scim.ag/cancer_ovarian



The Mental Hazards of City Living

You can take the person out of the city, but perhaps you really can’t take the city out of the person. City dwellers tend to have higher rates of mental health problems such as schizophrenia, depression, and anxiety disorders than people in rural areas. To understand how city living could predispose people to mental illness, psychiatrist Andreas Meyer-Lindenberg and collaborators at the Central Institute of Mental Health and the University of Heidelberg Medical Faculty in Germany, used functional magnetic resonance imaging (fMRI) on 32 healthy adults from cities, towns, and rural areas. As the subjects solved arithmetic problems, the researchers created social stress by criticizing their performance.

The fMRI scans revealed two differences in how the brains of urban and rural inhabitants respond to social stress: Current city dwellers showed higher activity in the amygdala, which evaluates social threats and tends to be overactive in people with anxiety disorders. But people who’d been raised in a city, regardless of their current home, showed more activation in the perigenual anterior cingulate cortex (pACC), another region involved in emotion and social processing and implicated in some studies of schizo-

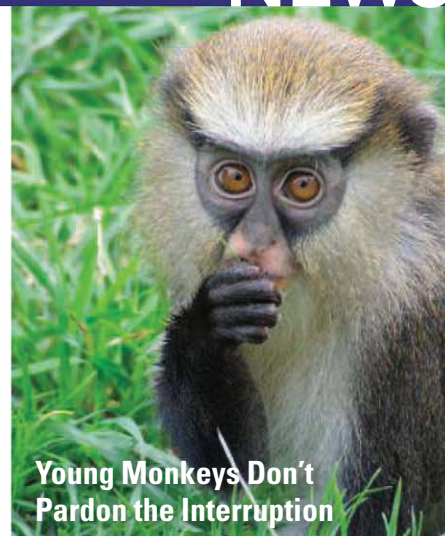
phrenia. Thus, the pACC may be susceptible to lasting effects from one’s environment early in life, whereas the amygdala is more sensitive to one’s current situation, the team hypothesizes in *Nature*.

Sleeping Sickness Drug Shows Promise

African sleeping sickness is one of the most neglected of the neglected diseases. Now, researchers have designed a compound that kills sleeping sickness parasites in the blood and the brain. After promising studies in rodents, the compound will enter human safety trials later this year.

Human African trypanosomiasis, the formal name for the disease, sickens an estimated 30,000 people per year. Injected by the bite of the tsetse fly, the parasites that cause the illness first dwell in the blood and then infiltrate the brain. Treatment can be dangerous and complicated. The drug mainstay kills 1 in 20 people who take it. A newer medicine is less toxic but requires an elaborate treatment regimen.

The new drug candidate emerged from a joint effort between the biotech firm SCYNEXIS of Research Triangle Park, North Carolina, and Anacor Pharmaceuticals of Palo Alto, California. Sponsoring the project was the Drugs for Neglected Diseases *initiative* (DDNi), a nonprofit organization based in Geneva, Switzerland. The compound, which can be taken orally, cures mice even if the parasites have entered the brain, researchers reported this week in *PLoS Neglected Tropical Diseases*. If the drug pans out in further trials, “it will be the first new, orally available treatment for sleeping sickness in the past 30 years,” says medicinal chemist Robert Jacobs of SCYNEXIS. http://scim.ag/sleep_sickness



Young Monkeys Don’t Pardon the Interruption

It can take some parental nagging before human children learn not to interrupt—and monkeys are no different, new research shows. The core of communication in Campbell’s monkeys (*Cercopithecus campbelli*), which are native to western Africa, revolves around alternating vocal calls. Researchers recorded spontaneous utterances of both young and adult monkeys and tallied how often each broke the rules of alternating calls. The adults broke the rules, calling twice in a row instead of letting another monkey take its turn, less than 1% of the time. The juveniles, however, were rule-breakers in 13% of their calls.

Moreover, when played calls that either followed conversational rules or didn’t, adults paid closer attention to alternating conversations, whereas juveniles didn’t seem to differentiate. The findings, which appear 23 June in *Scientific Reports*, could help scientists learn more about how language evolved in humans—as long as no one cuts anyone else off. <http://scim.ag/interruption>

BY THE NUMBERS

£13,481,250 Sale price of Pablo Picasso’s 1935 painting *Jeune Fille Endormie*, sold at auction by the University of Sydney on 22 June. The money will go to medical research on obesity, diabetes, and heart disease.

21 Number of new drugs that entered the global market in 2010, down from 26 in 2009, according to Thomson Reuters’ CMR International.

350 million Adults around the world who have diabetes, according to a study in *The Lancet* that also found diabetes prevalence rose or remained unchanged in virtually every part of the world over the past 3 decades.

PARTICLE PHYSICS

Underground Lab Would Cost U.S. Billions

ROCKVILLE, MARYLAND—The Department of Energy (DOE) would need to spend between \$1.2 billion and \$2.2 billion to build and equip an underground particle physics laboratory, according to a study presented last week to a federal advisory panel. The figures set the price for maintaining a thriving particle physics program on U.S. soil.

“If we want a domestic particle physics program, this is what it’s going to take,” says Milind Diwan, a particle physicist at Brookhaven National Laboratory in Upton, New York. However, some researchers worry that DOE, which is spending \$795 million this year on particle physics, won’t be able to ante up. “Is this going to happen with this price tag?” asks Juan Collar, a physicist at the University of Chicago in Illinois. “I look at the numbers and I go, ‘Oh, my goodness!’”

The cost estimates come from a report to the High Energy Physics Advisory Panel (HEPAP) about converting the abandoned Homestake gold mine in the Black Hills of South Dakota. The numbers aren’t surprising, as they essentially combine the \$875 million that, until recently, scientists had hoped the

National Science Foundation (NSF) would spend to turn Homestake into a Deep Underground Science and Engineering Laboratory (DUSEL) and the money DOE would have spent on experiments in that facility. DUSEL would have housed a suite of physics experiments that must be shielded from cosmic rays, as well as smaller-scale research in geology, microbiology, and engineering (*Science*, 12 November 2010, p. 904).

However, in December, the National Science Board, which sets policy for NSF, declined to fund further development of the laboratory. In particular, the board objected to cost-sharing plans under which NSF would have spent \$480 million on lab infrastructure while DOE built the biggest experiment in DUSEL (*Science*, 17 December 2010, p. 1596). That decision left the project’s fate in the hands of DOE, the primary supporter of U.S. particle physics.

DOE then asked a committee, led by Jay Marx of the California Institute of Technology in Pasadena, to evaluate the costs and risks of different options for the three main experiments slated for Homestake. The largest is a

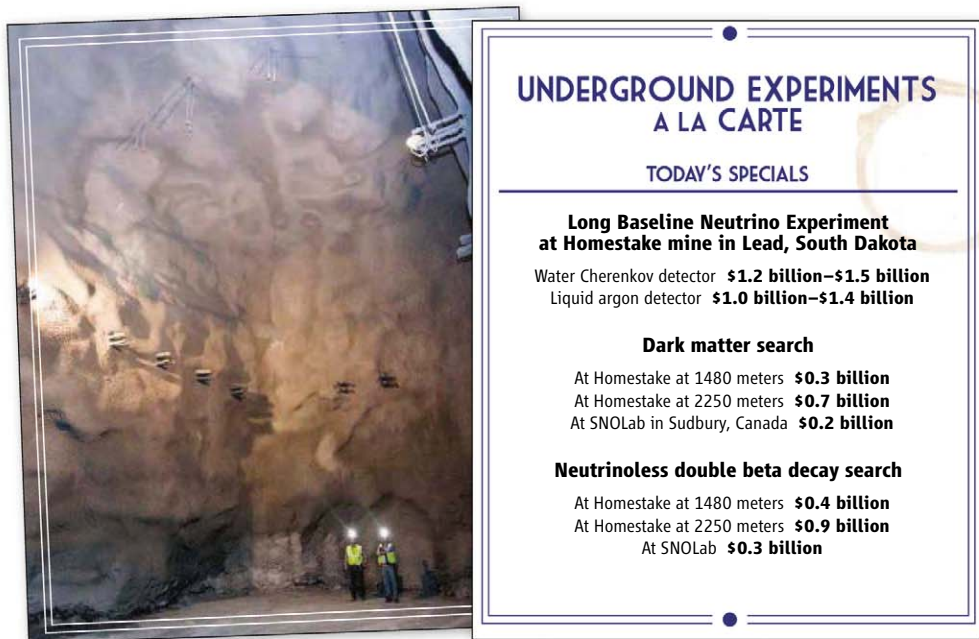
gigantic particle detector, known as the Long Baseline Neutrino Experiment (LBNE), that would snare particles called neutrinos fired from Fermi National Accelerator Laboratory (Fermilab), 1300 kilometers away in Batavia, Illinois. The second is a detector to spot particles of the mysterious dark matter whose gravity appears to bind the galaxies. The third is a detector that would search for a revolutionary form of radioactivity called neutrinoless double beta decay.

LBNE plays a central role in plans for Fermilab’s future. Later this year the lab will shutter its atom smasher, the Tevatron, which has been surpassed by Europe’s higher-energy Large Hadron Collider (LHC). LBNE would serve as the lab’s flagship experiment in the next decade. As neutrinos zing along they can change from one type, or “flavor,” to another, and LBNE would look for a slight difference between the way neutrinos and antineutrinos behave that could ultimately explain how the universe wound up with so much matter and so little antimatter.

Marx’s team considered two technological options for LBNE at Homestake. One is placing a detector filled with water and weighing between 150,000 and 200,000 tons at a depth of 1480 meters. The second would use a more advanced detector, filled with 24,000 to 34,000 tons of liquid argon, at only 240 meters. The water detector would cost between \$1.2 billion and \$1.5 billion, not counting inflation over the decade it would take to build it. At first blush, the liquid argon detector appears cheaper, at \$1 billion to \$1.4 billion in current U.S. dollars. But it’s riskier and would take years longer to build, factors that would likely raise its cost and make it less cost-effective, Marx told HEPAP.

The committee considered three options for the dark matter experiment. Two involve building it at Homestake, at a depth of either 1480 or 2250 meters. The third would make use of the existing SNOLab, which is 2100 meters deep, in Sudbury, Canada. The committee considered the same three options for staging a neutrinoless double beta decay experiment. The dark matter and neutrinoless double beta decay experiments could be built at 1480 meters for \$300 million and \$400 million, respectively, it estimated. Building those two experiments at SNOLab would save about \$100 million, Marx reported, although he added that there were advantages to having all three experiments at the same facility.

Marx emphasized that the committee was not making recommendations. Still, the report clearly puts the kibosh on certain options.



Pricey menu. The options and rough cost estimates for the three major experiments originally slated for a U.S. underground lab at the abandoned Homestake mine (left).

CREDITS: (PHOTO) MATT KAPUST/SANFORD UNDERGROUND LABORATORY; (DATA) J. MARX/BRIEFING TO HEPAP, 23 JUNE 2011

For example, the committee found that it would cost \$700 million and \$900 million, respectively, to build the dark matter and neutrinoless double beta decay experiments 2250 meters down. “We don’t consider it a cost-effective option,” Marx told HEPAP. So plans for operating a very deep level at Homestake, once a selling point because it would provide extremely good shielding, seem dead. Some physicists question whether 1480 meters would be deep enough, especially for neutrinoless double beta decay experiments.

Moreover, without LBNE, it’s likely that nothing else will get built at Homestake. That’s because building the infrastructure for LBNE at 1480 meters would greatly reduce the costs of adding smaller experiments at that level. Without LBNE, staging the dark matter and neutrinoless double beta decay experiments would require investing \$470 million on infrastructure, more than the experiments themselves would cost. That’s “a nonstarter at this point,” says Blas Cabrera, a physicist at Stanford University in Palo Alto, California.

The cost of LBNE may delay Fermilab’s plans for another big project, a high-power proton accelerator called Project-X that could generate neutrinos to shoot at the completed LBNE detector, feed a variety of other experiments, and assure a broader future for Fermilab. The \$1.8 billion machine, which would replace the lab’s current complex of accelerators, could be ready by 2020, says Fermilab Director Pier Oddone. But Fermilab will likely have to slow down development of Project-X to make room for LBNE. “We want to do LBNE with the existing accelerator complex, and Project-X will have to take its lumps in terms of scheduling,” Oddone says.

Of course, DOE officials must first decide if they want to build any of these experiments. Next month, the National Academies’ National Research Council is expected to deliver a report on the lab’s scientific potential, says William Brinkman, head of DOE’s Office of Science. “As soon as that report comes, we’ll be working on the [fiscal year] 2013 budget to figure out what we can do and what we can’t do,” Brinkman says.

DOE’s particle physics budget will need a bump up over the next few years to complete LBNE in a timely manner and make it “scientifically relevant,” says Brookhaven’s Diwan, co-spokesperson for LBNE. However, last month a congressional spending panel urged DOE officials “to further prioritize” between experiments at the LHC and at Fermilab. Increasing the particle physics budget wasn’t an option.

—ADRIAN CHO

SOCIAL PSYCHOLOGY

Antismoking Drive Tries Cigarette Ads, in Reverse

Assuming that a picture is indeed worth a thousand words, the law mandating the U.S. Food and Drug Administration to design graphic health warning labels for cigarette packages gave FDA a chance to show off its creativity. The nine new warning labels revealed last week include a photograph of a cadaver, a man smoking through his tracheotomy hole, and a mother blowing smoke on a baby, among others. As required by the 2009 Family Smoking Prevention and Tobacco Control Act, the images will appear on all cigarette packages sold in the United States by September 2012.

Graphic labels seem to have been quite effective in other nations, many of which use images that are far gorier than those chosen by FDA. But some psychologists argue that the new labels will likely become a joke to the would-be quitters that FDA hopes to reach and white noise in a society accustomed to blood and gore on TV.

The new labels, which are required to take up 50% of the area on the front and back of the package, will enhance the large textual Surgeon General’s warning used since 1985. According to Health and Human Services Secretary Kathleen Sebelius, the labels have two aims: getting smokers to quit and preventing youth from starting. “Anecdotal logic says that [textual] warnings have become white noise,” says FDA spokesperson Jeffrey Ventura. “The new generation of youth at risk are a very visually stimulated group of folks.”

But social psychologist Carol Tavris, co-author of the recent book *Mistakes Were Made (But Not By Me)*, doubts that teenagers will be scared by images of bad things happening to the older strangers and babies on the cartons. “Has anyone been to the movies lately? [HBO’s] *Game of Thrones*, where people’s heads are cut off in front of you? I think people’s tolerance for the ugly and the violent is quite high,” she says.

On the other side, health psychologist Geoffrey Fong of University of Waterloo in Canada argues that it’s the repeated exposure, buoyed by a strong image, that will make the campaign effective. A pack-a-day smoker could be exposed to the images 7300



No glamour.
The ugly side of tobacco use will be displayed in stark images on U.S. cigarette packs.

times per year. “There isn’t any advertising campaign with that much exposure,” he says. To keep the images fresh, the Tobacco Control Act allows them to be changed every few years.

No matter how high the exposure, scary images alone might not get smokers to pay attention, according to Howard Leventhal, a health psychologist at Rutgers University in New Jersey. When people make decisions on smoking, he says, they are influenced at three levels: individual, social, and societal. Powerful imagery can have an impact at the individual level but far less than social and societal pressures. This is particularly true for teenagers, the group FDA most wants to target, for whom peer pressure to smoke could override any image. “It’s inappropriate to think of these behaviors as occurring within the head, between a cigarette and a person,” Leventhal says. What would work better would be a cultural shift where smoking falls out of vogue. “It’s a stronger deterrent if I know everyone out there thinks I’m an idiot,” he says.

Aggressive antismoking campaigns in the United States and other nations have

helped shift cultural attitudes. But it's impossible to tease out exactly how much of that shift is due to warning labels, which have already been instituted in many countries, as opposed to taxation and other methods. To evaluate their effectiveness, in 2010 FDA devised 36 images depicting different health consequences and ran an 18,000-participant survey to determine the best nine. The study looked at factors such as how well people could recall a certain image days later, or what kind of emotional response a subject had. But the study didn't address whether people actually quit as a result of seeing the images.

The particular images chosen by FDA are a mixed bag in terms of how effective they are likely to be, says Linda Cameron, a health psychologist at the University of California, Merced. According to research by her group and others, views of diseased body parts such as a lesion on the lip are the most effective, and a cartoon of a sickly baby may be less so. Although Cameron believes the labels FDA chose

might discourage teens from starting, she says they might not be effective in convincing smokers to quit, given that the vast majority of smokers already say they want to stop.

Fong, who heads a 20-country study of the effectiveness of tobacco-control efforts, says that in countries with graphic labels, smokers do take notice and do quit. His group's surveys have found that graphic warning labels led to a significant increase in the number of smokers who say the labels made them decide to not smoke a cigarette they were about to. Even if just 10% to 20% of the 45 million U.S. smokers are disturbed enough by the labels to want to quit, "you're talking about a huge number of people."

But Tavis argues that smokers who want to quit but have failed are actually the group who are most likely to make a joke out of the new labels. The behavioral phenomenon at play is called cognitive dissonance: a clash between two conflicting beliefs. One way to resolve the tension is to override the disturbing new message by downplaying it.

"Dissonance is a pretty powerful phenomenon," she says. It explains "why people continue to do things they know are harmful but still see themselves as smart." And unless a frightening message is coupled with an action that a person can take, the warning tends to backfire.

The new FDA labels do suggest an action—stop smoking—and they will offer help: "1-800-QUIT-NOW," a hotline to counseling, will be printed on each package. The labels, Fong hopes, may break the "automaticity" of smoking for some addicts. Even better, they might irritate people enough to make them cover up an ugly package or store cigarettes elsewhere, which take time and attention.

One thing all can agree on: After decades of positive images in tobacco advertising, the new labels will be quite a change. "It's leveling the playing field a bit," Fong says. "Tell me, what kind of advertisement would be appropriate for a product that kills half its users?"

—SARA REARDON

SCIENTIFIC WORKFORCE

Suit Seeks Redress for a Start-Up Package Gone Sour

Kelly Suter was nervous about trying to launch her lab with the \$230,000 start-up package that accompanied the offer of a tenure-track position in the biology department at the University of Texas at San Antonio (UTSA). She would be bringing nearly \$1 million in grants from the U.S. National Institutes of Health (NIH) with her from the University of Louisville, Kentucky, proof that she was good. But her work, investigating neurons whose oscillations underlie the release of a hormone that governs sexual reproduction, was expensive.

Still, the electrophysiologist was impressed by UTSA's goal of becoming a top-tier research institution and its promise to give rising stars like Suter, then 41, the resources they would need to be successful. Before making a final decision, Suter managed to bump up her start-up package by negotiating for another \$100,000 from a pot of state money for computational biology. Then, satisfied that she had done the best she could, she accepted the job in June 2006, packed up, and headed west, primed to take the next step in her academic career.

Within weeks of her arrival, however, she found herself instead hurtling down an academic rabbit hole, as her start-up funds were diverted and her research plans



Moving up. Kelly Suter accepting a young investigator award from the American Physiological Society.

delayed. Last summer, after exhausting other options, Suter hit bottom: She sued the university and six UTSA administrators and professors. She claims in her suit that the university failed to honor its commitment to support her research in a timely fashion and that two other male faculty members who arrived after her received money earmarked for her start-up package. She says that the university's actions pushed her small lab—Suter and two technicians—to the brink of

collapse and that when she pushed back by filing a complaint about pay discrimination based on her gender, she was made an outcast in a male-dominated environment.

Suter isn't asking for any money. Instead, she wants the university to apologize for its actions. She says her experience is a cautionary tale for other young academic scientists: "The last 5 years of my life have been a nightmare. And I will not in any way give the impression that this is acceptable."

For its part, the university denies that it has done anything wrong and, therefore, says that no apology is needed. While it acknowledges the bare facts in the case, the university disputes Suter's claims that it misled her or acted improperly. Both sides are awaiting a ruling by a federal district judge in San Antonio on whether the suit can proceed to trial.

Remarkably, for all the bad blood between her and her employer, Suter's scientific career is moving forward. After an initial setback, she won a grant renewal worth \$1 million and, simultaneously, a new \$1.2 million grant to study the action of gonadotropin-releasing hormone on neurons during puberty. Last year, she received a prestigious award for young investigators from the American Physiological Society. And last fall, when she came

CREDIT: COURTESY OF THE PHYSIOLOGIST (AUGUST 2010) © THE AMERICAN PHYSIOLOGICAL SOCIETY

up for tenure, she breezed through the process despite reservations from her department chair.

"Kelly is great," says Charles Wilson, a UTSA professor of neurobiology who served on the original search committee and is not a defendant in the suit. "She's what I want our faculty to be, scientifically. I'm trying to build a successful neuroscience program, and she's as solid as they come." Suter, who says she came to UTSA in part because she knew and admired Wilson's work, was one of seven faculty members hired by the department within 3 years. And Wilson says that, from his perspective, "I think the university has done a great job of supporting all of them."



"I think they assumed that women don't complain. But as a computational biologist with a degree in chemistry, I learned you don't survive if you don't take care of yourself."

—KELLY SUTER, UTSA

Sitting and waiting

How did Suter's dream of working in a supportive, collegial atmosphere at a rapidly growing neuroscience program go so bad, so quickly? At the heart of the dispute is UTSA's promise, in a 30 May 2006 letter, to provide \$200,000 for lab equipment and a further \$30,000 for supplies. Almost half the money would be coming from the faculty development component of a grant from an NIH program, Research Centers in Minority Institutions (RCMI), which targets universities serving a large minority population. The provost's office would provide most of the rest, with the remainder coming from her department.

The offer letter stated that the equipment money must be spent by July 2007. That date corresponds to the end of the fiscal year for the RCMI grant, explained George Perry, dean of the college of arts and sciences, during his deposition.

The first glitch came within a few weeks of Suter's arrival, when Matthew Gdovin, the interim program director, told her that the RCMI funds actually had to be spent by 31 July 2006, not 2007. Given such an impossibly tight schedule, Gdovin said the university would ask NIH for permission to carry forward the money into the 2006–07 cycle.

But that wasn't the end of the matter. In his deposition, Gdovin said that he proposed putting the next \$100,000 allocation from the RCMI grant into a "shell account" for Fidel Santamaria, a new faculty member who was arriving in January 2007. Gdovin explained in his deposition that he "had an understanding" that Suter would get money

from the biology department and that "I would reimburse" the department with the RCMI funds that had been carried forward. And when Todd Troyer was hired in July 2007, UTSA officials tapped the portion of the 2007–08 RCMI grant designated for faculty development to help Troyer set up his lab. In the university's response to the suit, it acknowledged that the offers to Santamaria and Troyer didn't specify the source of their start-up funds but denied that the rest of the events occurred.

Suter says she was "devastated, both personally and professionally," by the delay in getting what she had been promised. She did receive \$100,000 in institutional funds shortly after arriving at UTSA to set up the "wet" side of her research lab. But it was more than 2 years later, in September 2008, that she got the additional \$100,000 in "carry forward" funds from the RCMI grant that she had expected during her first year. "My basic recording setup costs \$197,000. So 100K doesn't go far when one is starting with an empty room," she says. "I'd been submitting equipment orders for months, and then I found out they hadn't been processed because the money wasn't there."

The \$100,000 from the state grant for computational biology, which Suter had negotiated before joining UTSA, arrived in June 2007, triggering a frenzy of lab activity. But her late start contributed to her receiving a very poor score on the first attempt to renew her NIH grant, she says. Reviewers "praised the idea but said the fatal flaw was a lack of timely publications," she says.

Suter kept plugging away, however, and eventually hit pay dirt. "I got the good news [about both grants] on the same day, January 26, 2009, and it was an incredible relief. We came within 3 months of closing," she says. "There's no bridge money [institutional funds used to support researchers between grants] at UTSA. I had also avoided bringing in a graduate student because my money was so unstable."

J. Aaron Cassill, chair of the biology department when Suter was hired and a defendant in the suit, said in his deposition that the uncertainty shouldn't have come as a surprise. The funding "was not a 100% guarantee; ... there had been a history of problems" with allocating the start-up packages of previous hires, he said he told her during her job interview,

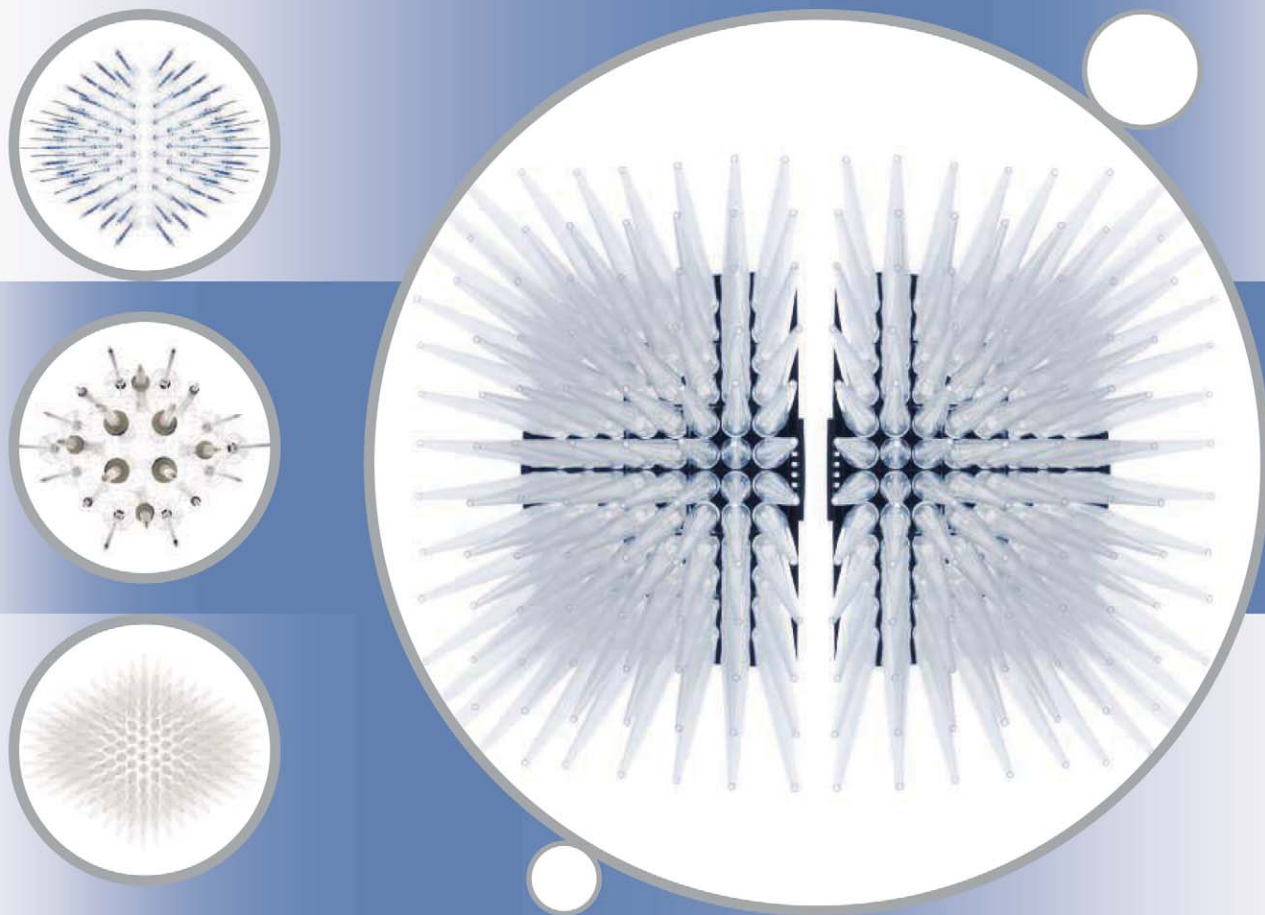
according to his deposition. Those problems stemmed largely from delays in opening buildings that would house the labs of new faculty members. But space allocation is no longer a problem, he added.

Suter says she never would have come to UTSA had she known what lay in store. But Wilson thinks that Suter simply needs "to get over it. Most people have gotten mad at their universities at some point and then moved on," he says. Researchers and universities "put too much emphasis" on start-up packages anyway, he says, to the point that a large one may even be detrimental to a young researcher. "When I was hired in 2000, my start-up was \$10,000," he says. "And when I told my chair that it wasn't enough, he said, 'Instead of complaining to me, you should be writing grant [applications].'"

Suter says she talked with her new department chair about her situation in May 2007. But it went badly. "He wanted to know if we could start over," she says. "So I asked for three things: a written apology, full disclosure to NIH about how the RCMI funding has been managed, and help in digging me out of this hole. He said, 'That's not going to happen.'"

The impasse, she said, prompted her decision to speak out—both as an early-career scientist and as a woman. "These are very proud men," she says of the defendants. "I think they assumed that women don't complain. But as a computational biologist with a degree in chemistry, I learned you don't survive if you don't take care of yourself."

—JEFFREY MERVIS



Go for unaffected assay results!

Choose the right tip for your experiments

Laboratory consumables can affect bioassays!

Consumables for pipetting and dispensing samples should be selected carefully as they can influence the quality and reproducibility of your entire workflow. Eppendorf epT.I.P.S. pipette tips and Combitips plus are made of carefully selected virgin raw material. All materials do not contain metallic dyes or latex and the automated manufacturing under clean-room conditions eliminates human interaction as source for contamination.

We develop tips with your research results in mind!

epT.I.P.S.:

- Certified trace metal release; no slip agents, plasticizers or biocides used during production
- Batch certified purity levels of Biopur and PCR clean
- Also available as epT.I.P.S. LoRetention and ep Dualfilter T.I.P.S. in certified PCR clean, sterile, pyrogen free

Combitips plus:

- Certified trace metal release and no plasticizers or biocides used during production
- Batch certified purity levels of Biopur and sterile
- Nine different sizes allow a wide dispensing range

Experience Eppendorf quality consumables and order your free sample on:

www.eppendorf.com/consumables

eppendorf
In touch with life

Your local distributor www.eppendorf.com/worldwide · Application Support: support@eppendorf.com

Eppendorf AG · Germany · Tel: +49 40 538 01-0 · Eppendorf North America, Inc. · USA · Tel: +1 800 645 3050

Eppendorf Asia Pacific Headquarters · Malaysia · Tel: +60 3 8023 2769

INFECTIOUS DISEASES

As *E. coli* Outbreak Recedes, New Questions Come to the Fore

BERLIN—Germans are breathing a sigh of relief now that the deadliest outbreak of enterohemorrhagic *Escherichia coli* (EHEC) ever recorded appears to be winding down. More than 3900 people have been infected so far and at least 46 have died, but the number of severe cases reported daily has dwindled from more than 60 to a handful.

For researchers, however, the work is just beginning. They are starting new studies and sifting through data gathered so far to figure out how to prevent a repeat and increase the odds of survival for future patients. Indeed, some scientists say the outbreak may have given them study material for years.

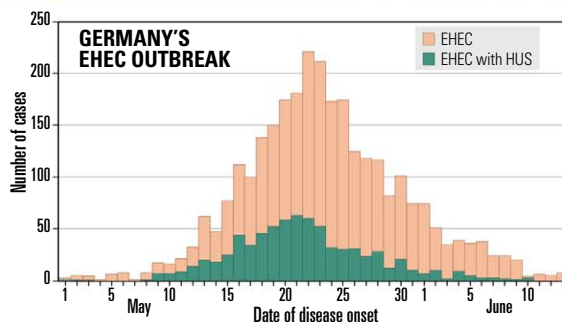
“The first question on everyone’s mind is, ‘Where did this pathogen come from?’” says Lothar Beutin, head of the National Reference Laboratory for *Escherichia coli* at the Federal Institute for Risk Assessment in Berlin. The evidence clearly points to an organic sprouts farm in Lower Saxony as the center of the outbreak, but it’s still not clear how the sprouts—or the seeds from which they were grown—were contaminated in the first place.

Researchers are also looking for the bacterium’s reservoir, because knowing that could help devise measures to prevent a new outbreak. “We need to find out where this pathogen is hiding,” says Tim Eckmanns of the Robert Koch Institute (RKI) in Berlin. EHEC are normally found in the gut of ruminants and are spread with their feces, but genetic analysis of the German strain showed its genes to be derived mostly from a different, usually less dangerous, class of *E. coli*, called enteroaggregative *E. coli* (EAEC), which has been found only in humans. RKI researchers are now screening healthy individuals to see whether some might harbor the pathogen. Others are analyzing samples from animals, soil, and rivers.

Perhaps an even more troubling question is how far the pathogen may have spread and whether it will stick around. “Will this pathogen establish itself and cause more outbreaks in the coming years, or will we be lucky and get rid of it soon?” Eckmanns wonders. Of the new cases still being reported today, some occurred weeks ago and may still be linked to the sprouts. But a considerable number are secondary infections: For instance, 20 of the 65 guests at a party in Hesse appear to have been infected from eating food prepared by an asymptomatic woman who worked for

a catering service. Scientists at the National Reference Laboratory have also detected the bacterium on various objects in homes, such as doorknobs and toys. “The bacterium seems to be quite good at sticking to a variety of surfaces,” Beutin says.

To quantify the secondary infections, RKI epidemiologists have started a follow-up study of families in northern Germany in which at least one case of EHEC was reported. They will take frequent stool samples and monitor whether anybody in these households acquires the pathogen; they’re also hoping to find out how long the microbe remains in the



Past its peak. New patients (*top*) are still trickling in, but case numbers for EHEC and its most severe complication, hemolytic uremic syndrome (HUS), have declined sharply since late May.

human gut. Although most people appear to clear it rapidly as they recover, some shed it in their stool weeks later.

Another remaining question is what makes this particular EHEC so dangerous. More than 20% of those infected went on to develop hemolytic-uremic syndrome (HUS), the most severe complication, which is usually seen in only a few percent of cases. EAEC are better at adhering to the intestinal wall, however, and Helge Karch of the National Consulting Laboratory on HUS in Münster has suggested that this might lead to patients taking up more toxin, causing more severe disease.

Treatment is another area of research. Cur-

rently, HUS patients are treated with plasmapheresis, in which the patients’ blood plasma is replaced with plasma from donors to rid it of the bacterial toxin. But more than 100 German patients have received Eculizumab, an antibody that targets a protein involved in regulating the human immune system. There was not time for a rigorous controlled clinical trial; instead, guidelines for so-called compassionate use of Eculizumab were hastily written up when, just days into the outbreak, *The New England Journal of Medicine* (NEJM) published a study of three children who rapidly recovered from EHEC last year after treatment with the antibody, originally developed for a rare blood disorder.

Doctors are now pooling the data of patients treated with Eculizumab in clinics in Hamburg, Hannover, Lübeck, and Kiel to study its efficacy. “If the data were collected thoroughly, this could be very valuable,” says Phillip Tarr, a gastroenterologist at the Washington University School of Medicine in St. Louis, Missouri, and an expert on HUS. But it’s a daunting task because investigators need to consider a myriad of confounding factors—such as other treatments, lab tests, and prior illnesses—that might have influenced the outcome. “I hope this antibody works,” Tarr says. “But looking at the data in the paper, two of the three patients appear to have been on the way to recovery already before they got it.”

A few physicians have tried another experimental treatment in which they specifically rid the blood of patients with severe neurological symptoms of antibodies. The rationale: So-called autoantibodies that are formed by the immune system as a response to the EHEC infection and attack

a protein on human cells might be leading to clots in brain vessels and eventually to the epileptic seizures seen in a small percentage of cases. This hypothesis, and the treatment, will also be evaluated.

The results of these impromptu trials could have broader ramifications. “There will be a lot of discussions of how we assess novel treatments in a disciplined, ethical, and useful manner in such rare catastrophic emergencies, when no one has a clear idea of what to do,” Tarr says. He is convinced that the German outbreak will turn out to be a “game-changer in many ways.”

—KAI KUPFERSCHMIDT

Kai Kupferschmidt is a writer in Berlin.

NASA's Busload of Science

For 30 years, the shuttle has been the main ticket into space for NASA astronauts. But it has also delivered—and fixed—massive observatories and served as an orbiting laboratory. As the program ends, what is its scientific legacy?



CREDIT: NASA

IN MARCH 1982, PLANT BIOLOGIST JOSEPH COWLES WATCHED the space shuttle's third launch with particular interest. It carried his own experiment: a suitcase-sized apparatus containing seeds from mung beans, oats, and pine trees. His attempt to see how weightlessness affects a plant's growth was one of the first scientific experiments onboard NASA's new flagship. "How often do you get to participate in the space program?" says Cowles, a former associate dean at Virginia Polytechnic Institute and State University, now retired and living in Blacksburg, Virginia.

Next week, a controversial chapter in space science is scheduled to end with the launch of the space shuttle Atlantis. In the 3 decades since Columbia carried Cowles's payload, NASA's five shuttles have flown 134 missions. Although science was never their primary purpose (see timeline, p. 30), the shuttles served as a singular platform from which to observe Earth and the effects of weightlessness. They also launched a half-dozen major scientific satellites and gave new life to the once-crippled Hubble Space Telescope.

Yet the shuttles' accomplishments are haunted by unfulfilled promises. They have flown much less frequently than originally planned and at an enormous cost: roughly \$1.5 billion per launch, in 2010 dollars. "You couldn't justify those expenditures for science," says Charles Kennel, chair of the Space Studies Board of the National Research Council.

The shuttle's name conveys its real purpose. "It was a bus. It was supposed to go to a space station," says Joan Vernikos, former head of research on life sciences at NASA. The station, however, got delayed, so "by the time the shuttle was ready, it had nowhere to go."

Scientists did their best to fill the void. "The bus was going up there. So let's take advantage of it," says Robert Naumann, formerly chief of the microgravity division at NASA's Marshall Space Flight Center in Huntsville, Alabama.

Astronomers jumped at the chance to plant a series of "great observatories" in space. Scientists from other disciplines, however, struggled to make good use of their new opportunity. "The onboard experiments—this was a community that had never existed," says Kennel, who also served as associate administrator of NASA.

At first, there was little room in the shuttle for science. Cowles's experiment, like many others, was tucked into a small storage locker on the shuttle's middeck, where the crew sleeps. The European Space Agency "came to the rescue," Vernikos says. Its Spacelab, a set of pressurized, tube-shaped modules, complete with furnaces and glove boxes, fit inside the shuttle's cargo bay.

Although NASA's calls for proposals were always oversubscribed, Kennel says many top biologists were wary of NASA's pitch, with good reason as it turned out: NASA never managed to fly the shuttle at buslike frequency. Instead of 18 to 24 flights each year, the maximum was nine (in 1985, the year before the Challenger orbiter exploded), and the average was fewer than five. "A scientific career can't depend on flights every 3 years. You'll stay an assistant professor a long time that way," says Raymond Bula, formerly director of the Center for Space Automation and Robotics at the University of Wisconsin, Madison.

Frustration among scientists deepened after Spacelab was lost along with Columbia and its crew in 2003. Experiments were once again relegated to middeck lockers as the bulk of the cargo space was devoted to materials for the international space station. The inability of NASA to keep its promise of frequent research flights "poisoned the relationship between human space flight and the sci-

THE SHUTTLE, BY THE NUMBERS

(All numbers as of 1 July 2011)

134

Number of missions

\$192*

BILLION
Overall program cost

864.4

MILLION km
Total distance traveled

14

In-flight fatalities



THE SHUTTLE ITSELF

2.04 million kg Weight at liftoff

526,126 gallons Amount of fuel in nonreusable external tank

2.5 million Number of moving parts

8.5 minutes Time to orbit

27,875 km/h Orbital velocity

31,440 hours, 59 minutes, 33 seconds Total flight time



THE ASTRONAUTS

355 Total transported

49 Women

16 Number of countries represented

77 years old Oldest passenger, John Glenn

32 years old Youngest astronaut, Sally Ride

1.9 meters tall Tallest astronaut, Jim Wetherbee

1.5 meters tall Shortest astronaut, Nancy (Sherlock) Currie

248 Spacewalks by U.S. astronauts



THE MISSIONS

17.5 days Longest

8 Largest crew

10 Number of defense missions

Over 2,000 Number of experiments

37 Number of missions to ISS

*In 2010 dollars

Online

sciencemag.org



Podcast interview with author Dan Charles.

ence community," Kennel says. He says "things are better now" because NASA has decided to support work on the space station until 2020.

Among some scientists, however, antipathy to the shuttle—or any human space flight—runs deep. "It indulged humankind's impractical space fantasies at a cost that retarded genuine progress," says physicist Robert Park of the University of Maryland, College Park.

Yet even to the end, some scientists have been drawn to the opportunities it offers. A middeck locker on next week's final shuttle flight will carry genetically altered *Salmonella* bacteria from Arizona State University's (ASU's) Biodesign Institute. Previous experiments showed that *Salmonella* bacteria became more virulent in space, says ASU microbiologist Cheryl Nickerson, and she's curious to see how bacteria of the new strain, which have been crippled and altered to act as vaccines against another disease, will behave in microgravity. She's also confident that her research will continue, either on the space station or on commercial space vehicles.

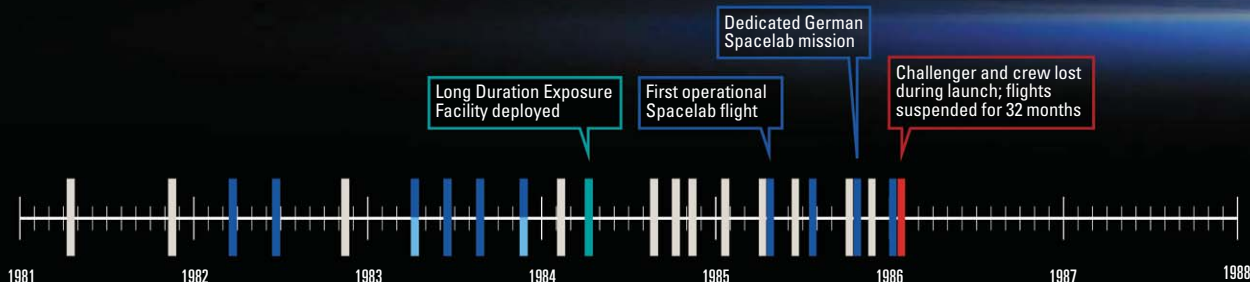
—DAN CHARLES

Dan Charles is a writer in Washington, D.C.

30 YEARS
OF SCIENCE
MISSIONS

KEY

- Launching observatories
- Hubble repairs and upgrades
- Effects of removing gravity
- Observing Earth and sky
- Effects of space environment on exposed materials
- Little or no science
- Crew and mission lost



6 APRIL 1984 Long Duration Exposure Facility deployed



30 OCTOBER 1985 Dedicated German Spacelab mission



28 JANUARY 1986 Challenger and crew lost during launch



The Highs and Lows Of Shuttle Science

For 3 decades, the shuttle has served as NASA's Swiss Army knife. It is capable of performing a remarkable variety of tasks, but it is not always the ideal tool for a particular job.

The above timeline shows that the contributions of the shuttle to science have come in many flavors and at an irregular pace. The timeline oversimplifies the picture, however. During the first 2 decades, many shuttle missions that were devoted to nonscientific tasks also carried small experiments on board. More recently, the shuttle's primary focus has been building the space station, a facility that, among its many purposes, will carry out scientific research.

To tease out the scientific contributions of the shuttle, *Science* has grouped the program's 134 missions into five categories. (The sixth, and largest, category is those missions with little or no scientific activity.) By frequency, the exploration of microgravity leads the way, with a substantial amount of such research aboard 45 missions. In second place are major observations of Earth or the heavens (12 missions), followed by the launching of large scientific instruments (seven missions), repairs and upgrades to the Hubble telescope (five missions), and research on the effects of the external space environment (three missions).

LAUNCHING SCIENTIFIC INSTRUMENTS

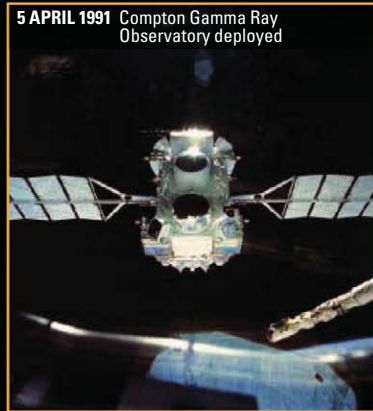
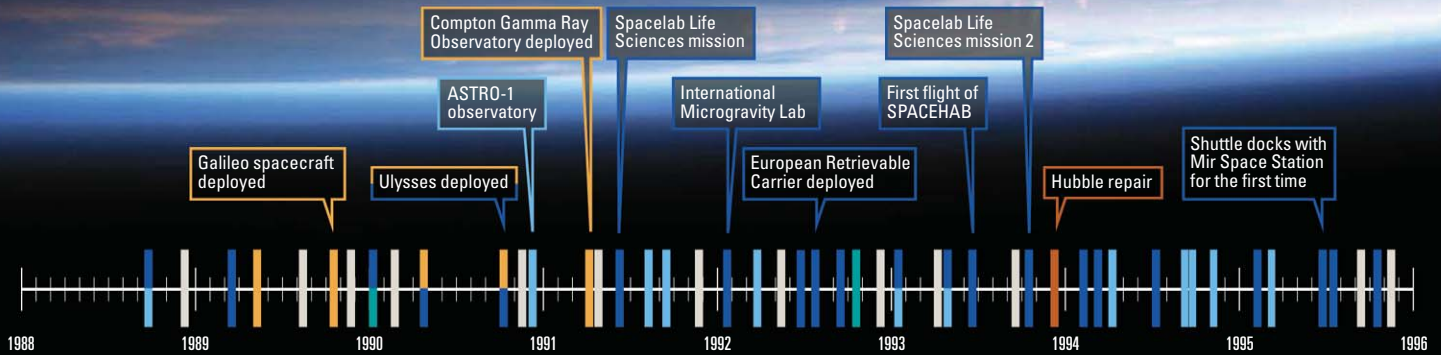
For Charles Kennel, chair of the Space Studies Board at the National Research Council, the shuttle's greatest contribution to science was its "capacity to lift heavy and complex instruments into

space." Three of NASA's four "great observatories"—the Hubble Space Telescope, the Compton Gamma Ray Observatory, and the Chandra X-ray Observatory—soared aloft in the shuttle's cargo bay. (The Spitzer Space Telescope went up in 2003 on a Delta rocket.) So did the Galileo mission to Jupiter, the Magellan spacecraft that mapped Venus, and the European Space Agency's Ulysses mission, which observed the sun from entirely new perspectives, although an additional rocket boosted them into interplanetary space after the shuttle had taken them to low Earth orbit.

All the instruments have led to stunning scientific advances—but all could have been launched on crewless rockets. Other options, however, weren't immediately available. NASA had stopped development of large, expendable rockets in the mistaken belief that the shuttle would prove to be a cheaper route into space. The shuttle is expensive, in part, because it carries people. In addition, it is huge. Its rocket boosters and onboard engines propel 105,000 kg into orbit—but 80,000 kg of that mass is the shuttle orbiter itself, which returns to Earth. There were fewer efficiencies as a result of reusing that orbiter than expected. The shuttle "is not an optimal launch vehicle, and we could have [launched satellites] more cheaply," says Heinz Stoewer, former managing director of the German Space Agency.

Still, "no launch is simple," says Henry Hertzfeld of the Space Policy Institute at George Washington University in Washington, D.C., and the shuttle has managed to deliver the goods. In fact, using a crewless launch vehicle might have left astronomers with a crippled view of high-energy radiation from pulsars and of nova and supernova explosions: When the Compton Gamma Ray Observatory emerged from the shuttle's cargo bay in 1991, its high-gain antenna refused to extend properly. After two long spacewalks and a vigorous tug on the antenna, two astronauts succeeded in fixing the problem.

CREDITS (LEFT TO RIGHT): NASA (2); LANDOV/REUTERS



REPAIRING AND UPGRADING HUBBLE

The embarrassment of faulty optics on the Hubble Space Telescope eventually led to what some consider the shuttle's most spectacular accomplishment.

Hubble's fuzzy vision came to light soon after the telescope's launch in 1990. Three years later, astronauts hauled the telescope back into the shuttle's cargo bay and installed its new "corrective lenses." They did so in the near-vacuum and weightlessness of space, while moving every 90 minutes from sunlight into Earth's night and back again.

With confidence born of that success, NASA kept improving the telescope. In 1997, the shuttle delivered new instruments that allowed Hubble to view infrared light. Two years later, in an emergency repair, astronauts replaced the telescope's failing gyroscopes. Subsequent missions, the most recent in 2009, brought entirely new observing instruments, control systems, and solar panels. All of these upgrades dramatically increased the telescope's power.

Astronaut John Grunsfeld flew on the last three of those missions, earning him the title "Chief Hubble Repairman." Grunsfeld, now deputy director of the Space Telescope Science Institute in Baltimore, Maryland, says these missions "recreated" the telescope and represent the space shuttle's greatest single contribution to science: "Far and away, the Hubble servicing missions top the list."

Critics of crewed space flight point out that NASA could have built and launched an entirely new space telescope for the price of the repair missions. But Grunsfeld says that's unrealistic; it would have taken longer to build and launch a second-generation Hubble, for one thing, and there's no guarantee the project would have been completed.

Shuttle astronauts also carried out another, less famous, repair in 1984. NASA's Solar Maximum satellite, which had been monitoring

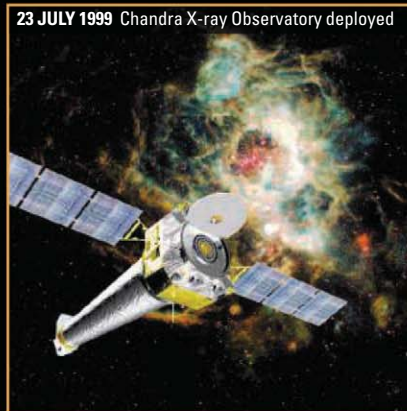
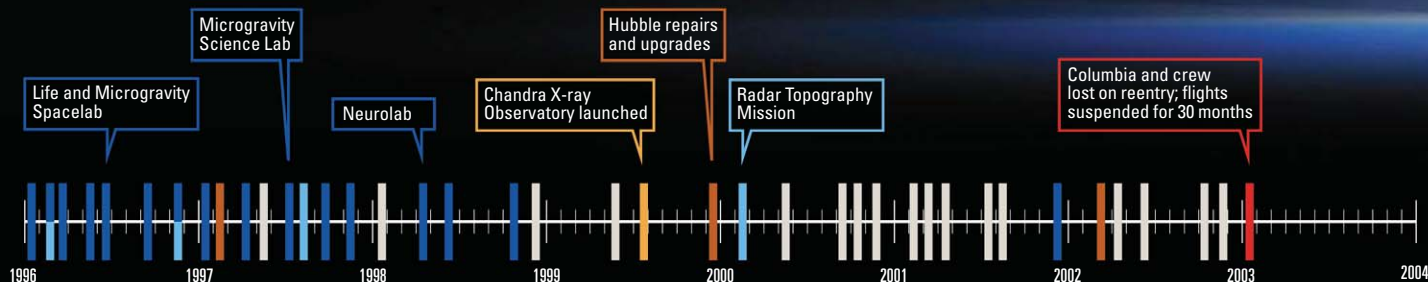
flares and other solar activity since 1980, had lost the ability to point its instruments accurately, rendering some of them useless. Astronauts managed to capture the satellite (on their fourth attempt) and installed a new control system. The rejuvenated "Solarmax" carried on for another 5 years.

SCIENCE ONBOARD: MICROGRAVITY

The space shuttle opened a door into a world in which the effects of gravity almost completely disappear. In fact, because this realm, dubbed microgravity, was so new to human exploration, it was hard at first to know what experiments were worth doing. "Early on, we just mixed things together and threw it up there," says Robert Naumann, former chief of microgravity research at NASA's Marshall Space Flight Center in Huntsville, Alabama.

One group of students launched a colony of honey bees into orbit to see if the insects still created honeycombs. (They did.) Fish, however, lost their orientation and started to tumble in the water, face over fin.

The sheer variety of microgravity research on the shuttle is impressive. In 1999, NASA found that microgravity experiments on Spacelab (first flown on the shuttle in 1983 and reconfigured to fit the requirements of each additional microgravity mission until 2003) had led to more than 1000 journal articles in the fields of biotechnology, materials science, fluid dynamics, and combustion. Scientists tried to create better metal alloys, on the theory that materials with different densities would be less likely to separate in the absence of gravity. Others grew protein crystals, thinking that weightlessness would allow such crystals to grow larger and with a more consistent structure. Combustion researchers found that hot gases don't rise but rather produce flames in the shape of a sphere.



But researchers also discovered the shuttle's limitations as a laboratory of weightlessness. For one thing, "we never got true zero gravity," says Joseph Cowles, a retired biologist from the Virginia Polytechnic Institute and State University in Blacksburg, whose experiments flew on several early shuttle missions. The shuttle's frequent maneuvers, the movements of astronauts, and of course launch and reentry all subjected these experiments to gravitylike forces.

Just creating an apparatus that could work on the shuttle was a complicated job in itself. "This turned out to be quite an experience in hardware development," Cowles says. His own experiment with plant seedlings produced equivocal results because the minigreenhouse on the shuttle didn't control light or carbon dioxide very well. (The equipment was greatly improved on later shuttle missions.) In addition, a 2-week flight wasn't really long enough to study effects on relatively slow-growing plants.

Scientists studying the behavior of fluids on the shuttle were startled to find that convective flows persisted, even when the apparent force of gravity was 1000 times weaker than on Earth. And materials scientists discovered that other forces, such as intermolecular cohesion, came to the fore and drove different materials apart. "In space, there was still massive separation," Naumann says.

Arriving at an overall evaluation of all this work has been difficult and contentious. In 1998, a group assembled by the American Society for Cell Biology asserted that the protein-crystal work on the shuttle had made "no serious contribution" to the field. Two years later, a National Research Council study concluded that those experiments had made "incremental" improvements and that the research remained promising enough to continue on the space station. However, the same report acknowledged that "one cannot point to a single case where space-based crystallization efforts produced a crucial discovery leading to a landmark scientific result."

According to some, the most pathbreaking research on the shuttle has been investigations into the effect of gravity—or its absence—on biological systems, from humans to microbes. Joan Vernikos, formerly director of life sciences research at NASA, says those experiments showed that gravity has surprisingly profound effects. "Muscle synthesis stops immediately when you go into space," she says. There's a "tremendous increase" in bone loss—up to 5% per month—if astronauts don't engage in exercises that simulate gravity.

Weightlessness also appears to affect the nervous system and behavior, she says. Mice born in weightlessness, with no sense of up or down, failed to develop a normal "righting reflex" and didn't gain it fully even after they returned to Earth.

These insights, according to Vernikos, still haven't been fully recognized by the wider scientific community. "Go to any medical textbook, and the term 'gravity' does not appear, to this day," she says.

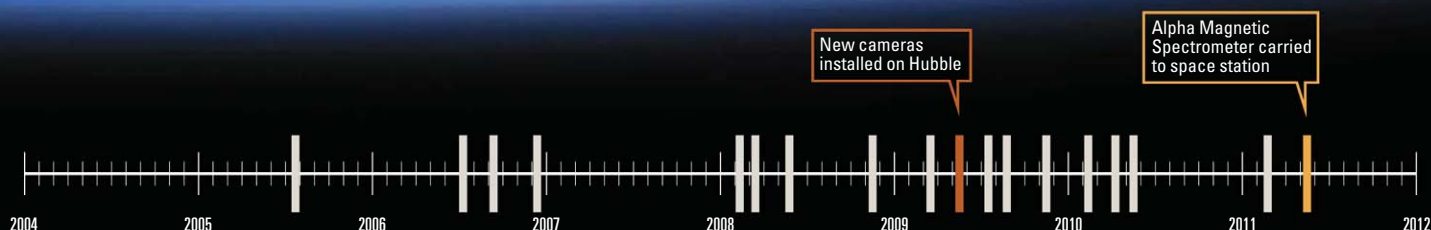
Vernikos's biggest regret is "not having the opportunity to fly a few more" flights that could have deepened that understanding. The fledgling community of microgravity researchers fell on hard times when NASA decided to devote most shuttle missions to building the space station.

OBSERVING EARTH

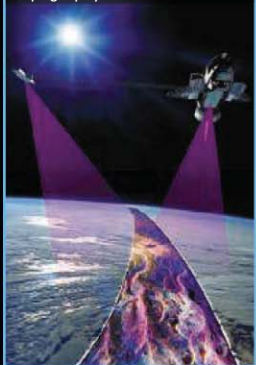
From the beginning, the space shuttle was also a platform from which to look back at humanity's home. On its second flight, crew members took film footage of lightning storms, and another instrument monitored the color of the oceans in search of areas with a lot of photoplankton.

Such efforts intensified during the 1990s as part of NASA's Mission to Planet Earth. A set of instruments called the Atmospheric Laboratory for Applications and Science flew several times in the

CREDITS: NASA



11 FEBRUARY 2000 Radar Topography Mission



16 JANUARY 2003 Columbia and crew lost on reentry



16 MAY 2011 Alpha Magnetic Spectrometer carried to space station



shuttle's payload bay, observing Earth's atmosphere from that vantage point. Even so, says Kennel, who oversaw Mission to Planet Earth as NASA's associate administrator, the shuttle "never served as a very good platform for highly precise instruments." Free-flying satellites offered much "cleaner" observing conditions.

An important exception was a series of radar observations of Earth, culminating in 2000 with the Shuttle Radar Topography Mission. Instruments aboard that mission created the most complete topographical map of Earth's surface. "It could only be done on the shuttle," Kennel says, because the radar was heavy and demanded a lot of power, and the data it produced would have overwhelmed satellite-to-Earth communication links.

Kennel is convinced that the shuttle's low-tech observations of Earth remain its most important legacy, even for earth scientists. The arresting photographs that the astronauts took, he says, "serve as a humanized document of the Earth and how it has changed. That's tremendously important."

EXPERIENCING SPACE

No space vehicle except the shuttle could haul experiments into space, leave them there for a while, and then bring them back to Earth for careful study. The first experiment to test that capability was the Long Duration Exposure Facility (LDEF), a 10,000-kg cylinder, three stories tall, with 86 flat trays covering its surface. Various materials or sensors were placed into those trays to find out how they would survive the stresses of space.

The Challenger orbiter released LDEF into orbit in 1984. For the next 5½ years, it circled the globe, exposed to extreme heat and cold, ionizing radiation, meteoroids and space debris, and reactive oxygen. In January 1990, another shuttle mission brought it back to Earth.

NASA's first glance at the massive cylinder "put a panic into the Hubble people," says William Kinard, a scientist at NASA's Langley Research Center in Hampton, Virginia, who led the LDEF mission.

"Hubble was ready to launch," he recalls, and "it depended on silver-coated Teflon" to reflect the sun's heat. But a sample of that material mounted on LDEF had turned white. Hasty experiments, however, determined that this white Teflon worked just as well as the original silver version, and the Hubble mission proceeded.

The most useful insights from LDEF, Kinard says, were the "synergistic effects" of long exposure to space. Models on Earth could predict how well materials would survive the impact of a particle of dust, for instance, but the effect was completely different after those materials had been exposed to radiation and heat for a few years.

In 1992, the shuttle Atlantis released a similar long-duration experiment, called the European Retrieval Carrier, which stayed in orbit for about a year. More sophisticated than LDEF, the European satellite had its own solar power supply and held a variety of automated materials science experiments. Like LDEF, the European vehicle bore the record of collisions with tiny space particles—small craters on metal walls and holes in Teflon-coated fiberglass blankets. The frequency of such encounters strengthened concerns about the risks posed by such micrometeoroids, as well as by space debris released by human exploration.

Along with hazards, however, the environment of space possessed one potentially valuable quality: a vacuum. A free-flying experiment called the Wake Shield Facility, first deployed from the shuttle in 1994, grew thin films of semiconducting material in vacuum conditions much better than could be achieved on Earth. "It was a very successful experiment," Naumann says. But it never led to any commercial applications: "Technology on Earth has overtaken this."

—D.C.

Science Mobile App Now Available for Android Phones



They say you never know when inspiration will strike. Download the *Science* mobile app for Android devices and be ready the next time you're inspired to read the latest news, research, and career advice from *Science* on your mobile phone.

To download the *Science* mobile app for Android visit content.aaas.org/mobile, visit the Android Market on your phone, or just scan this barcode.



Features include:

- Summaries and abstracts from *Science*, *Science Translational Medicine*, and *Science Signaling*.
- Ability to e-mail full-text links.
- The latest news from *ScienceNOW*.
- Career advice articles from *Science Careers*.
- Access to the *Science* weekly podcast and other multimedia.
- Content caching for reading without wi-fi access.



LETTERS

edited by Jennifer Sills

Editorial Expression of Concern

IN THE ISSUE OF 23 OCTOBER 2009, *SCIENCE* PUBLISHED THE REPORT “Detection of an infectious retrovirus, XMRV, in blood cells of patients with chronic fatigue syndrome,” a study by Lombardi *et al.* purporting to show that a retrovirus called XMRV (xenotropic murine leukemia virus–related virus) was present in the blood of 67% of patients with chronic fatigue syndrome (CFS) compared with 3.7% of healthy controls (1). Since then, at least 10 studies conducted by other investigators and published elsewhere have reported a failure to detect XMRV in independent populations of CFS patients. In this issue, we are publishing two Reports that strongly support the growing view that the association between XMRV and CFS described by Lombardi *et al.* likely reflects contamination of laboratories and research reagents with the virus. In one Report, “Recombinant origin of the retrovirus XMRV” (2), T. Paprotka *et al.* trace the ancestry of XMRV and provide evidence that the virus originated when two mouse leukemia viruses underwent recombination during experimental passage of a human prostate tumor xenograft in mice in the 1990s. A combination of sequencing, phylogenetic, and probability analyses lead Paprotka *et al.* to conclude that laboratory contamination with XMRV produced by a cell line (22Rv1) derived from these early xenograft experiments is the most likely explanation for detection of the virus in patient samples. In the other Report, “No evidence of murine-like gammaretroviruses in CFS patients previously identi-

fied as XMRV-infected” (3), K. Knox *et al.* examined blood samples from 61 CFS patients from the same medical practice that had provided patient samples to Lombardi *et al.* Comprehensive assays by Knox *et al.* for viral nucleic acids, infectious virus, and virus-specific antibodies revealed no evidence of XMRV in any of the samples.

The study by Lombardi *et al.* (1) attracted considerable attention, and its publication in *Science* has had a far-reaching impact on the community of CFS patients and beyond. Because the validity of the study by Lombardi *et al.* is now seriously in question, we are publishing this Expression of Concern and attaching it to *Science*’s 23 October 2009 publication by Lombardi *et al.*

The U.S. National Institutes of Health is sponsoring additional carefully designed studies to ascertain whether the association between XMRV and CFS can be confirmed. *Science* eagerly awaits the outcome of these further studies and will take appropriate action when their results are known.

BRUCE ALBERTS

Editor-in-Chief

References

1. V. C. Lombardi *et al.*, *Science* **326**, 585 (2009); published online 8 October 2009 (10.1126/science.1179052).
2. T. Paprotka *et al.*, *Science* **333**, 97 (2011); published online 31 May 2011 (10.1126/science.1205292).
3. K. Knox *et al.*, *Science* **333**, 94 (2011); published online 31 May 2011 (10.1126/science.1204963).

Published online 31 May 2011; 10.1126/science.1208542

Not-So-Sunny Outlook for Organic Photovoltaics

IN THE NEWS & ANALYSIS PIECE “OUTLOOK brightens for plastic solar cells” (15 April, p. 293), R. F. Service presents a highly optimistic future for organic photovoltaics while disparaging the possibility of cost reductions in current commercial inorganic technologies. The article overlooks the important fact that organic cell efficiencies are generally measured with cells that are less than 1 cm², and larger cells are substantially less efficient. Organic photovoltaics are usually promoted as a low-cost technology because they can be produced by an inexpensive roll-to-roll printing process. However, packaging and installation are major factors in total cost. The big

question is: Will organic photovoltaics be competitive for outdoor applications?

The key numbers to compare are the cost per watt of power and the area required for a given power output.

Using the manufacturer’s data for size and power output to calculate efficiency, First Solar CdTe modules show area-based efficiency of nearly 10% and warranty 80% power for 25 years (1). Grape Solar offers polysilicon modules with 14% efficiency and 80% power warranty for 25 years (2, 3). Many others (such as Suntech) sell similar modules. Konarka’s technical data can be used to obtain total area efficiency at 1 sun (1 sun equals the intensity of the Sun at Earth’s equator at noon) of less than 2% for a typical Power Plastic module, and no warranty information is available (4).

Putting the commercial organic device into perspective, a 1-m² module would deliver less than 20 W of energy at the Equator at noon. In Phoenix, the sunniest U.S. city, that falls to less than 15 W. Recharging a typical cell phone battery (1000 mAh at 4 V) that is half depleted would require a module approximately 30 cm by 45 cm and more than an hour in Phoenix at midday.

Moreover, the News story barely touched on life-span problems. Photooxidation is a well known issue with organic materials, and an affordable oxygen-barrier film for large, flexible devices is yet to be found.

Organic photovoltaics may find some niche applications such as indoor low-power signs, as proposed by Plextronics, but outdoor power is unlikely to be competitive. By only consulting researchers in the area,

Service ran afoul of Greenberg's Law: Don't ask the barber if you need a haircut (5).

EDWIN A. CHANDROSS

Materials Chemistry LLC, 14 Hunterdon Boulevard, Murray Hill, NJ 07974, USA. E-mail: eac@materialschemistry.com

References

1. First Solar (www.firstsolar.com).
2. Grape Solar (www.grapesolar.com).
3. Suntech (<http://am.suntech-power.com>).
4. Konarka (www.konarka.com).
5. D. S. Greenberg, "Don't ask the barber whether you need a haircut," *Saturday Review* (25 November 1972), pp. 58–59.

An Unorthodox Approach to Forest Restoration

IN THEIR POLICY FORUM "RESTORATION SEED BANKS—A matter of scale" (22 April, p. 424), D. J. Merritt and K. W. Dixon highlight the importance of ecological restoration in meeting global conservation goals, and the urgency to scale up seed supplies from seed banks to achieve such endeavors. We support their call, but emphasize that seed banks will only facilitate the restoration of ecosystems dominated by species whose seeds can tolerate drying and long-term storage.

Seeds fall into two storage categories:

orthodox seeds and recalcitrant (or unorthodox) seeds. Orthodox seeds tolerate desiccation without losing viability and germinate upon rehydration, making them highly amenable to storage in seed banks. Recalcitrant seeds have high moisture content and lose viability if moisture drops below a critical amount. The desiccation sensitivity of recalcitrant species means that restoration seed banks are ineffective for many plant species. Other methods, such as cryogenic storage, are unlikely to be scalable for restoration (1).

These limitations are noteworthy, given that many tropical and subtropical tree species have recalcitrant seeds (2). Many such species are ecologically and also economically important, with markets based on global tropical timber valued at nearly US\$100 billion (3). For example, the data that exist on seed behavior in four of the globally most important timber families indicate that, on average, 60% are recalcitrant (4).

Restoration seed banks might contribute to the conservation and restoration of many orthodox plant species, but restoration of tropical forests and many other plant communities will require considerable additional investments in plant nurseries and seedling propa-

gation to maintain the equally numerous, and perhaps ecologically more important, recalcitrant species (5). Expansion of seedling propagation for restoration of tropical forests will require overcoming ecological and financial, rather than technological, constraints (6).

CHRIS J. KETTLE,^{1*} DAVID F. R. P. BURSLEM,² JABOURY GHAZOU¹

¹Institute of Terrestrial Ecosystems, ETH Zürich, Universitätsstrasse 16, Zürich 8092, Switzerland. ²Institute of Biological and Environmental Sciences, University of Aberdeen, Cruickshank Building, St. Machar Drive, Aberdeen AB24 3UU, UK.

*To whom correspondence should be addressed. E-mail: chris.kettle@env.ethz.ch

References

1. P. Berjak, *Science* **307**, 47 (2005).
2. J. Ghazoul, D. Sheil, *Tropical Rain Forest Ecology, Diversity, and Conservation* (Oxford Univ. Press, Oxford, 2010).
3. International Tropical Timber Organisation, "Annual Report" (2009).
4. Kew, Royal Botanic Gardens, Seed Information Database, Version 7.1; <http://data.kew.org/sid/>.
5. C. J. Kettle *et al.*, *Conserv. Lett.* **4**, 184 (2011).
6. C. J. Kettle *et al.*, *Science* **330**, 584 (2010).

Response

KETTLE AND COLLEAGUES ARE CORRECT THAT recalcitrant seeds, many of which grow in tropical climates, cannot be stored long-



1st Biotechnology World Congress
February 14 – 15, 2012; Dubai, U.A.E.

THE PREMIER BIOTECHNOLOGY CONFERENCE

CONFERENCE PRESIDENTS




Prof. Ferid Murad (Nobel Laureate) Prof. Dr. Atta-ur-Rahman FRS

CONFERENCE TRACKS

- **Pharmaceutical Biotechnology:** biopharmaceuticals discovery (CNS, cancer, cardiovascular, endocrine, immune); vaccines; antibodies; protein engineering.
- **Plant and Environmental:** transgenic plants and crops; bioremediation; microbial diversity; bio-monitoring.
- **Industrial and Manufacturing:** bio-fuels; energy crops (cellulosic ethanol industry); industrial enzymes; bioprocess engineering and optimization.
- **Medical Biotechnology:** stem cells; gene therapy; tissue engineering; biopharmaceutical manufacturing; cell based therapy; cell cultivation; diagnostics; imaging; pharmacogenomics (personalized medicine); microarray technology; biomarkers.
- **Business development:** strategic alliances; partnering trends; product opportunities; growth; business models and strategies; licensing; merger and acquisitions; outsourcing; venture capital and financing; intellectual property.

KEY BENEFITS OF ATTENDING

- Explore Cutting-Edge Biotechnology Discoveries
- Gain Networking Opportunities
- Earn CME Accreditation (under application in UAE)
- Commercial Exhibition

PARTICIPATING NOBEL LAUREATES





Harald zur Hausen Peter Agre Michel Hartmut

Deadline for Submissions for a Presentation or Poster Session
31st December 2011

TO KNOW MORE ABOUT

- Registration
- Abstract Submission
- Sponsorship & Exhibition Opportunities

please visit the event website

www.biotechworldcongress.com

Contact: BWC 2012 Secretariat
PO Box 121223, SAIF Zone, Sharjah, U.A.E.
Tel: +971-6-5575783, Fax: +971-6-5575784
E-mail: info@biotechworldcongress.com

INTERNATIONAL ORGANIZER



Eureka Science Ltd.

NATIONAL ORGANIZER



HIGHER COLLEGES OF TECHNOLOGY

term in seed banks. However, the bulk of the world's disturbed landscapes fall outside of tropical forest areas (1), and less than 10% of the world's flora is estimated to produce truly recalcitrant seeds (2, 3). Restoration seed banks (4, 5) can effectively store the seeds of most of the world's plants.

Moreover, as we discussed in our Policy Forum, restoration seed banks are more than just seed vaults, and their wider applications can address the conservation needs of recalcitrant seeds and tropical forests. They can store all kinds of seeds for use within a relatively short time frame (months rather than years) (6). They can work to create vibrant centers of integrated seed science linked through adaptive management to restoration practice. They could also extend current seed farming infrastructure and plant husbandry to incorporate nursery-based seedling production for recalcitrant species.

DAVID J. MERRITT^{1,2*} AND KINGSLEY W. DIXON^{1,2}

¹Kings Park and Botanic Garden, Fraser Avenue, West Perth, WA 6005, Australia. ²School of Plant Biology, Faculty of Natural and Agricultural Sciences, The University of Western Australia, Crawley, WA 6009, Australia.

*To whom correspondence should be addressed. E-mail: david.merritt@bgpa.wa.gov.au

References

1. Millennium Ecosystem Assessment, *Ecosystems and Human Well-Being: Biodiversity Synthesis* (World Resources Institute, Washington, DC, 2005).
2. J. B. Dickie, H. W. Pritchard, in *Desiccation and Survival in Plants: Drying Without Dying*, M. Black, H. W. Pritchard, Eds. (CAB International, UK, 2002), chap. 8.
3. P. Berjak, N. W. Pammenter, *Ann. Bot. London* **101**, 213 (2008).
4. Food and Agricultural Organization of the United Nations/International Plant Genetic Resources Institute, *Genebank Standards* (FAO and IPGRI, Rome, 1994).
5. N. K. Rao *et al.*, *Manual of Seed Handling in Genebanks: Handbooks for Genebanks No. 8* (Bioversity International, Rome, 2006).
6. L. E. Commander *et al.*, *Bot. J. Linn. Soc.* **161**, 411 (2009).

TECHNICAL COMMENT ABSTRACTS

Comment on "The Mechanism for Activation of GTP Hydrolysis on the Ribosome"

Anders Liljas, Måns Ehrenberg, Johan Åqvist

Voorhees *et al.* (Reports, 5 November 2010, p. 835) determined the structure of elongation factor Tu (EF-Tu) and aminoacyl-transfer RNA bound to the ribosome with a guanosine triphosphate (GTP) analog. However, their identification of histidine-84 of EF-Tu as deprotonating the catalytic water molecule is problematic in relation to their atomic structure; the terminal phosphate of GTP is more likely to be the proper proton acceptor.

Full text at www.sciencemag.org/cgi/content/full/333/6038/37-a

Response to Comment on "The Mechanism for Activation of GTP Hydrolysis on the Ribosome"

Rebecca M. Voorhees, T. Martin Schmeing, Ann C. Kelley, V. Ramakrishnan

Our report of the crystal structure of elongation factor Tu (EF-Tu) and aminoacyl-transfer RNA bound to the ribosome with a guanosine triphosphate (GTP) analog included a proposed mechanism of GTP hydrolysis by EF-Tu involving histidine-84. Liljas *et al.* summarize experimental evidence against this mechanism and propose a substrate-assisted catalytic model. However, these experiments and the model are also problematic. Further study is required to definitively determine the mechanism of GTP hydrolysis by EF-Tu.

Full text at www.sciencemag.org/cgi/content/full/333/6038/37-b

Letters to the Editor

Letters (~300 words) discuss material published in *Science* in the past 3 months or matters of general interest. Letters are not acknowledged upon receipt. Whether published in full or in part, Letters are subject to editing for clarity and space. Letters submitted, published, or posted elsewhere, in print or online, will be disqualified. To submit a Letter, go to www.submit2science.org.

Learn how current events are impacting your work.

ScienceInsider, the new policy blog from the journal *Science*, is your source for breaking news and instant analysis from the nexus of politics and science.

Produced by an international team of science journalists, *ScienceInsider* offers hard-hitting coverage on a range of issues including climate change, bioterrorism, research funding, and more.

Before research happens at the bench, science policy is formulated in the halls of government. Make sure you understand how current events are impacting your work. Read *ScienceInsider* today.

www.ScienceInsider.org

ScienceInsider

Breaking news and analysis from the world of science policy



SCIENCE TOURISM

Some Summer Suggestions

Are you planning to escape from the lab and office this summer but still wish to take in some science while on vacation? Again this year, we offer a very small sample of stops for the science-minded traveler. Some might take only a couple of hours, while others could fill a day, a week, or more. And in case you won't be able to get away until much later in the year, we have even included one winter destination.

—Sherman J. Suter

Evolution on Display on the Banks of the Seine

Galleries de Paléontologie et d'Anatomie Comparée and Grande Galerie de l'Évolution. Jardin des Plantes, Muséum National d'Histoire Naturelle, Paris. www.mnhn.fr

Paris's Jardin des Plantes offers visitors botany and much more. Entering from the Gare d'Austerlitz Metro station, you can begin with the Galleries de Paléontologie et d'Anatomie Comparée. Opened for the 1900 World's Fair, this sunlit building houses three floors of anatomical history. Dioramas and handmade educational posters from decades past line the walls, along with case upon case of small fossils. Although nearly every nook and cranny of the museum is filled with paleontological samples, most people come to see the skeletons (of dinosaurs, enormous Ice Age mammals, and even familiar extant species). Many specimens are grouped by evolutionary relationships, emphasizing homologous structures; others, by geologic period. Typed and handwritten signage adds an additional *je ne sais quoi* to the already fascinating displays.

When you're ready to see living organisms, walk down the tree-lined avenue and venture into several hectares of botanical diversity, which include an alpine garden, tropical greenhouses, a rose and rock garden, and a labyrinth. You are also welcome in the ecological garden, an ongoing project maintained by botanists in training at the on-site School of Botany.

Once it's time to cool off, head southwest to the Grande Galerie de l'Évolution. The interior of this impressive, four-story building is primarily dark wood and brass. Opaque skylights diffuse the sun, creating a softly lit atmosphere perfect for wandering leisurely through the museum. I spent quite some time simply admiring the architecture before delving into the exhibits, which

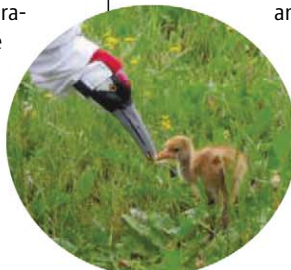
are organized around three topics. On the ground floor, over 7000 preserved specimens (from marine and terrestrial habitats) provide some perspective on biodiversity. Tree diagrams accompany many of the displays, providing a map of phylogenetic relations among different groups. A second component considers the various ways humans affect the natural world, including domestication, pollution, colonization, and extinction (illustrated by the tragedy of the dodo). It ends with a segment on the future of the planet, asking visitors to ponder, "Where do we go from here?" The uppermost (and my favorite) floor offers the opportunity to learn what evolution is and how we reconstruct evolutionary history. From the history of evolutionary thought (in which Lamarck and Cuvier are prominently featured) to Mendel's peas and Darwin's pigeons, ideas and experiments central to understanding evolution are displayed in a thorough and accessible manner. Kiosks peppered throughout the section house interactive tree-thinking games, which will entertain and inform kids and adults alike.

The Grande Galerie de l'Évolution, and the Jardin des Plantes as a whole, succeed admirably at presenting evolution and its results to the public.

—Alison Scott (University of Wisconsin)

Crane Haven

International Crane Foundation. Baraboo, Wisconsin. www.savingcranes.org



About an hour north of Madison and only minutes from the amusements of the Wisconsin Dells, the International Crane Foundation (ICF) has developed into a destination for bird lovers, biologists, and tourists alike. The facility is the only place in the world where visitors can view all 15 extant species of crane. The foundation was established in 1973 by two Cornell University graduate students, George Archibald and Ron Sauey, to study and preserve these tall, elegant wading birds. To help accomplish their goals, Archibald and Sauey began breeding cranes on a horse farm owned by Sauey's parents. Within 10 years, ICF outgrew the farm and moved to its current 225-acre location.

At present, 8 species are classified as vulnerable, 2 as endangered, and 1 as critically endangered. As part of its conservation efforts, ICF has hatched and raised extant species of crane in captivity. The foundation seeks to maintain a "species bank" of crane diversity and to facilitate crane reintroduction into wild populations. An impediment to the latter goal is that crane chicks easily imprint on humans—failing to learn to properly interact with other cranes and becoming too comfortable around humans to be released into the wild. To overcome this problem, ICF researchers pioneered "isolation rearing": all people attending to the captive bred birds are dressed in crane costumes. Shielded from human contact, these cranes can later be safely released to the wild.

The ICF works to protect and restore the wetland and grassland habitats that cranes require, and it is involved in research and conservation efforts around the world. For example, it has collaborated with Russia and China to protect the Amur River, helping preserve an ecosystem that is home to other endangered species, including the Siberian tiger. In the United States, the foundation played an important role in reestablishing a population of whooping cranes through the use of ultralight aircraft to teach novice cranes the migration route from Wisconsin to Florida.

At ICF's headquarters, you can view a captive mating pair of each species. Some wild cranes visit as they see fit—we saw a pair of migratory sandhill cranes taking a break on the grounds. Strolling around the site, you can watch the cranes, read about them, view a video about the loss of their habitat, and explore 5 km of nature paths. Naturalist-led tours offer an engaging way to learn still more about the birds. Overall, the Baraboo facility is a great stop for anyone interested in the biology, behavior, or conservation of these impressive birds.

—Alison Scott and Abigail Mazie (University of Wisconsin)



Fun and Lessons for Do-It-Yourselfers

Maker Faire. San Mateo, CA, 21–22 May; Detroit, MI, 30–31 July; New York, 17–18 September 2011. <http://makerfaire.com>

Maker Faires are gatherings at which innovators, inventors, artists, and craftsmen can show off and show visitors how to do things themselves. Their productions range from home gardening and pyrotechnic art to robots and vehicles of all shapes and sizes. The makers that present at these two-day festivals are brought together by a common love of creating. Attendees can come simply to be entertained, to learn various techniques (such as state-of-the-art 3D printing), or to shop for homemade crafts and gadgets.

Charles Gadeken's *Aperion*



The festivals, associated with *Make* magazine, occur each year in the San Francisco Bay Area and several other cities around the United States. At this May's Maker Faire Bay Area, the exhibition halls were full of hundreds of small displays. Keynote speakers included Adam Savage from Discovery Channel's *MythBusters*, who talked about inspiration. Many of the prominent presentations seamlessly blended science, art, and fun. ArcAttack, led by Joe DiPrima, gave a spectacular—one could say “electrifying”—audiovisual performance using two large homemade “singing” Tesla coils. And the “mad scientists of Eepybird,” Fritz Grobe and Stephen Voltz, offered a live, choreographed Coke Zero and Mentos show, accompanied by an explanation of the science behind the effects.

Fun for children and adults alike, a Maker Faire can be a bit overwhelm-

ing. That is particularly true in the exhibition halls, where people cramped together in a maze of tiny booths show everything from a kit for constructing a model animal cell to a demonstration on how to pick locks. The activity continues outside the exposition buildings, where you might encounter an electric-powered cupcake car or other unique vehicle. In total, there were 750 entries at this year's Bay Area Faire—making it impossible to see everything but fun to try.

There are still two more Maker Faires (Detroit and New York) and a smaller, regional event (Fort Wayne, Indiana) on this year's schedule. Each has its own unique culture of local makers, so the presentations will vary somewhat among them—but they are certain to be creative and innovative.

—Rochelle Urban (University of California, San Francisco)

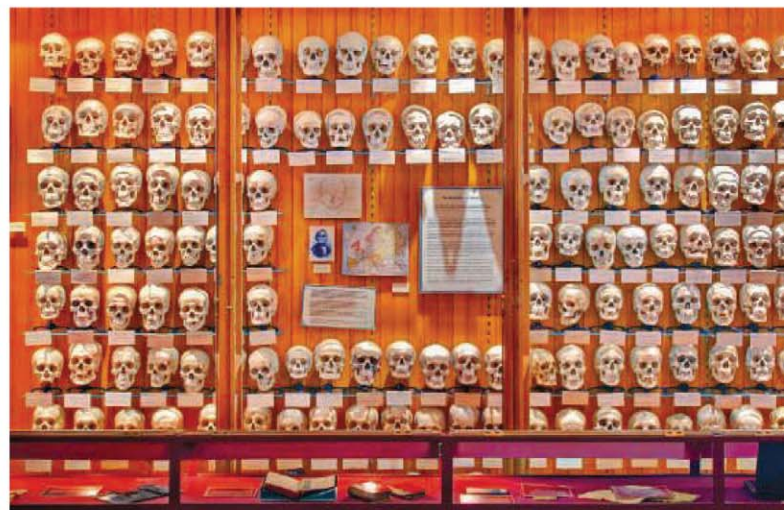
A Medical Miscellany

Mütter Museum. The College of Physicians of Philadelphia, Philadelphia, Pennsylvania. www.collphyphil.org/Site/mutter_museum.html

Occupying parts of two floors in a stately building in downtown Philadelphia, the Mütter Museum is not your average tourist destination. Amid the marble floors, wine-colored carpeting, and light wood paneling, one overhears a little girl in pink sandals ask, “Where did that brain come from?” Her mother answers, “It came from somebody's head.”

The somebody was one John Wilson, who dismembered his former employer, a farmer. Encased in a jar, the brain is part of an exhibit on the “Natural History of Crime,” which displays skulls and brains of various 19th-century felons that were studied for signs of insanity and criminal behavior.

The museum has roots going back to 1858, when Thomas Dent Mütter (pronounced “Mooter”), a Philadelphia surgeon, bequeathed his collection of more than 1700 objects to the College of Physicians. Its current holdings



(more than 25,000 items) encompass a most unusual, sometimes grisly, compilation of artefacts. There's a piece of thorax from John Wilkes Booth, Abraham Lincoln's assassin. One corner is taken up by the extensive ear collection of Adam Politzer, M.D., who is described as having revolutionized the treatment of ear disease in the 19th century. Joseph Hyrtl, a physician who wanted to understand whether sex, occupation, religion, and ethnicity affected cranial development, amassed more than 100 skulls that now gaze out from a wall.

You'll probably stumble upon the giant colon, from a 29-year-old who was found dead in a bathroom. He had a congenital anomaly (likely Hirschsprung's disease) that left him fatally constipated; the colon contained 40 pounds of feces. Along with pickled body parts and bodies—including a two-headed male fetus—you will encounter old forceps and operating instruments. One innocent-looking display of a few books reveals that they belonged to two local doctors, who “occasionally honored the subjects of their anatomical inquiries by tanning their skin for later use in special bindings for their personally prized medical books.”

If this all sounds rather odd, well, it is. But the exhibits cast a spell. They explain how doctors learned from the human body in health and disease and why the specimens—whatever their yuck factor—matter to science. And if you start to feel queasy, step outdoors into a medicinal herb garden (first planted in 1937) that displays more than 60 varieties of medicinal greenery.

—Jennifer Couzin-Frankel

Phenomenal Explorations

Science Storms. Museum of Science and Industry, Chicago. <http://msichicago.org/whats-here/exhibits/science-storms>

As news headlines, horrifying videos, and postings on the Web constantly remind us, catastrophic natural disasters continue to plague people around the world. There is little doubt that if we are to lessen the damage they inflict, we need a better and more fundamental understanding of their nature. Science Storms, at Chicago's Museum of Science and Industry, highlights the physics and chemistry behind seven powerful natural phenomena: atoms in motion, avalanches, fire, lightning, sunlight, tornados, and tsunamis. When visitors to the museum (the largest science museum in the Western Hemisphere) choose from among its thousands of installations and activities, they certainly should give themselves ample time to explore this award-winning permanent exhibition (which opened in March 2010). The exhibition teaches by taking an approach not available in reading books or surfing the Web: helping visitors of all ages “experience” concepts of nature in novel, open-ended, and exciting ways.

As you walk into the 24,000-square-foot exhibit space that towers over two floors, you may feel that you are entering a scientific amusement park. Instead of a spinning carousel, you will be mesmerized by perpetually chang-



where spikes of lightning are generated. A long water tank equipped with a touch-screen monitor demonstrates how different wave patterns can change ordinary ocean waves into a powerful tsunami.

Each phenomenon is accompanied by a number of creative hands-on presentations, video footage that includes explanations from experts and researchers, and numerous historical artefacts. This dynamic, experience-driven approach to the science works better for some phenomena than for others. Nonetheless, the spectacular and memorable *Science Storms* should certainly stir up curiosity about the wonders of nature and leave visitors hungry to dig deeper to learn still more.

—Yuji Ishitsuka (University of Illinois)

Tycho's Island

The Tycho Brahe Museum. Ven, Landskrona, Sweden.

www.tychobrahe.com

Flat and windswept, the Swedish island of Ven is not a place one would associate with state-of-the-art astronomy. However, in the 16th century, before the invention of the telescope, the site was the source of the world's most precise astronomical measurements. In 1576, Ven, then part of Denmark, was given to the young Tycho Brahe, who had become famous for his observations of a new bright star (a supernova) that had appeared in the sky four years earlier. Because the sphere of the stars was supposed to be perfect and immutable, many scholars interpreted the new star as an atmospheric phenomenon. After recording how its apparent position changed over time, Tycho concluded that the star had to be a distant object—well beyond Earth or the Moon.

On Ven, Tycho created more than just a simple observatory or a home. He erected a palace (Uraniborg) specifically designed for astronomical observations. When he found they were not precise enough, he built an underground observatory (Stjärneborg) to shield his instruments (quadrants and sextants)



ing beautiful patterns created by the mixture of brick red- and ivory-colored sand within the 8-ton avalanche disk. In lieu of an undulating roller-coaster ride, you can step into and take control of a 40-foot-tall tornado of water vapor or sample what 80 miles-per-hour winds feel like in a wind tunnel. Among the background sounds, you can hear the thunderous 1.2-million-volt discharge of a 20-foot Tesla coil overhead,

from the disturbances of the weather. He employed assistants to help him with his observations and craftsmen to help construct his instruments. He even put up a printing house, complete with a paper mill and a system of water ponds for power. With the king's support, between 1576 and 1597, Tycho created an entire research infrastructure and carried out astronomical measurements that paved the way for the works of Kepler and Newton—and for the end of the medieval view of the world.

Today, little remains of Tycho's structures apart from Stjärneborg. That was uncovered by excavations during the 1950s and has had its exterior walls reconstructed. Now part of the Tycho Brahe Museum, it is well worth visiting. Inside this unusual building, it is easy to imagine what a night of observations would have been like. The small yet very informative museum, located in a former church, includes replicas of Tycho's instruments. Next door there is a reconstruction of Tycho's Renaissance garden, and a short walk from the compound one can view the site of the vanished paper mill and a replica of one of the lakes that was used to power it. The island of Ven, a beautiful location itself, is easily accessible from both Denmark and Sweden.

—Maria Cruz



Sampling Java's Many Treasures

World Heritage Sites. Java, Indonesia. <http://whc.unesco.org/en/list/592>; <http://whc.unesco.org/en/list/542>; <http://whc.unesco.org/en/list/593>

The region on Java surrounding the beautiful city of Yogyakarta (Yogya) provides an excellent introduction to Indonesia's rich cultural heritage. Borobudur, a colossal Buddhist temple from the 8th and 9th centuries, consists of a pyramid of 5 square terraces, topped by a trio of concentric circular platforms that are surmounted by a monumental stupa. Bas-reliefs carved in the andesite blocks of the walls and balustrades portray phases of the soul's progression toward redemption and scenes from the Buddha's life. Slightly younger, the 10th-century Hindu complex at Prambanan includes 224 temples. At its center are three large temples dedicated to Shiva, Vishnu, and Brahma, which are decorated with reliefs illustrating the epic of the *Ramayana*. Archaeological and geological evidence suggests that the temples were abandoned after a major 10th-century eruption of nearby Mt. Merapi; they were rediscovered by Thomas Raffles in 1815.

The Yogya region holds many other attractions for travelers with interests in anthropology, archaeology, or natural history. Several nearby sites, including the Ratu Boko Temple Complex and the Yogyakarta Palace Complex, have been proposed for World Heritage listing. Diverse flora and fauna can be encountered along the elevational gradient up Mt. Merapi (2900 m), although one must check with the locals about the volcano's status before making the climb. In the tropical montane forests covering the slopes at middle elevations, hikers can observe relatives of popular garden plants (such as aroids, begonias, ginger, and palms). More familiar plants, with north-temperate affinities, will

be encountered at higher elevations. Those interested in birds or other animals will also find the forests a treasure. While the hike to the top may be rigorous, the experience is well worth the effort. For a less tiring trip, one can travel a couple of hours to the Sangiran Early Man World Heritage Site. Researchers working at this location in a teak forest along the Solo River have found some 50 *Homo erectus* fossils as well as a variety of Paleolithic stone tools.

—Scott Hoover (New England Tropical Conservatory)

Code-Crackers' Mecca

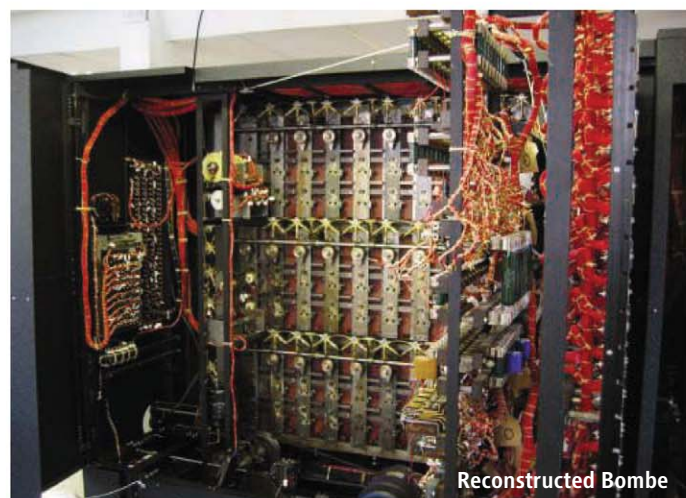
Bletchley Park National Codes Centre. Milton Keynes, UK.

www.bletchleypark.org.uk

Bletchley Park commemorates a moment in history when nerdy types—people who were good at maths and could complete the *Times* crossword in a matter of minutes—became heroes. At the beginning of World War II, such individuals were quietly sought out, recruited, and brought to an unassuming collection of buildings 80 kilometers north of London. There they cracked Germany's "unbreakable" Enigma code with spectacular results for the Allies. Kept secret until the 1970s, their efforts have now been revealed in numerous books. The site has been turned into a museum that attempts to explain the black art of codebreaking while also recording the often bleak living conditions of the time. An architecturally eccentric country house with surrounding wartime huts and blocks, Bletchley Park is now encircled by the postwar new town of Milton Keynes. But it is still possible to imagine the 9000 Oxford and Cambridge dons, computer engineers, and legions of office staff scurrying among buildings or strolling the lawns.

"Station X" opened in 1939, when 200 staff from the Government Code and Cypher School were relocated from bomb-threatened London to Bletchley. With the help of Polish cryptographers who had been studying Germany's Enigma codes for years, the staff had some success decrypting messages using pencil, paper, and brainpower alone. But as Germany's forces upgraded their Enigma cypher machines, faster code-crunching was needed. In response, Alan Turing and others developed an electromechanical device called the Bombe, which was essentially 36 Enigma machines wired together. Given a small piece of encrypted text and its true meaning, the Bombe would grind through all possible variations of the Enigma machine's daily starting settings to find the ones that worked. With those settings, Bletchley could unscramble all the messages sent that day.

Most of the more than 200 Bombes that were built were destroyed after the war. One of the centerpieces of Bletchley today is a working replica of a Bombe, constructed by enthusiasts over 13 years. Another display features a functional reproduction (the product of a similar effort) of Colossus, the world's first semi-programmable computer. The original was developed to crack the Lorenz code used by the German high command.



Reconstructed Bombe

Due to be demolished and redeveloped, the site was saved by local amateur historians, who later formed the Bletchley Park Trust. Although the trust's finances have remained precarious, a bid this year for £4.1 million from the Heritage Lottery Fund may provide much help for restoring and preserving the site. At present, Bletchley Park has the air of a work in progress. Some displays—e.g., ones explaining how Enigma works, how it was broken, and how the Bombe and Colossus were rebuilt—are fascinating and professionally produced. Others are akin to a yard sale of WW2 memorabilia (everything from uniforms to bicycles to toys) that you can wander among and examine. Reconstructions of a wartime kitchen and post office, vintage cars, and a play area reveal a wish to cater to many tastes. But the museum's great strength lies in its enthusiastic volunteers. They will happily explain the intricacies of cryptography and recount anecdotes of the many thousands who labored away here in secret and whose efforts were almost forgotten.

—Daniel Clery



Hot Skies over a Cold Landscape

Aurora Borealis. Fairbanks, Alaska. www.gi.alaska.edu/AuroraForecast

Frozen tundra in the interior of Alaska might seem a most unlikely destination for a winter vacation. Despite the unforgiving weather, science-minded travelers from around the world are drawn to Fairbanks to witness one of nature's most spectacular phenomena—the aurora borealis.

Best described as dynamic displays of glowing arcs and curtains, aurorae light up the dark sky with a full spectrum of visible light, most commonly greens or pinks. They form when charged particles ejected from the Sun's upper atmosphere excite gas molecules in Earth's ionosphere. The charged particles in the solar wind are deflected by Earth's magnetic field and gathered in the sky around the north and south poles.

Witnessing nature's vivid collision experiment requires some luck. The bright side for visitors (especially those who only have time for a brief trip) is that the intensity and frequency of aurorae are predicted to peak in 2011 and 2012, because of the highest expected levels of solar activity in a decade. Aurora tourists probably cannot avoid the cold, as aurorae are amplified in the winter and most visible from October to March. People who cannot tolerate low temperatures might be willing to try indoor viewings from a warm cabin (despite the compromised observation angle). If you decide to head north, I recommend taking a camera with a wide-angle lens, a tripod, extra batteries, and long thermal underwear.

—J. Dongun Kim (Rutgers University)

10.1126/science.1209607

CREDITS: (LEFT) MAGNUS MANSKE/WIKIMEDIA COMMONS; (RIGHT) JOSHUA STRANG/US AIR FORCE

AIDS

Turning the Tide Against HIV

Robin J. Shattock,^{1,2*} Mitchell Warren,³ Sheena McCormack,^{4,1} Catherine A. Hankins⁵

Although the annual number of new HIV infections (incidence) declined from a peak of 3.5 million in 1996 to 2.6 million in 2009, the total number living with HIV continues to rise as more people live longer. While 6.6 million people with HIV are now on antiretroviral treatment (ART), 9 million are waiting to receive it, with two people newly infected for every person starting ART (1). Twenty million more people are predicted to acquire HIV by 2031, which will increase treatment costs up to \$35 billion a year (2). This raises issues of sustainability. Thus, reducing HIV incidence is critical to keeping alive the promise of universal access to HIV prevention, treatment, care, and support.

New biomedical tools with proven effectiveness should be added to individual-level behavioral and population-level structural components, with national policies guided by cost-effectiveness and population impact assessed in randomized controlled trials (RCTs). Sequential implementation of each new biomedical intervention is an inevitable process for unlicensed products. However, we recommend accelerated assessment of potentially beneficial combinations through innovative RCTs that assess more than one biomedical tool against a common control.

RCT Evidence of Success

Combinations of behavioral and structural intervention strategies to reduce vulnerability and risk of HIV infection have been applied for nearly three decades with differing success (3). However, a number of new biomedical tools have demonstrated success in RCTs: medical male circumcision (MMC); daily oral tenofovir (TDF) plus emtricitabine (FTC) used as preexposure prophylaxis (oral-PrEP) by HIV-negative men who have sex with men (MSM); 1% tenofovir gel (microbicide) applied vaginally before and after sex by HIV-negative women as topical PrEP; a

prime-boost HIV vaccine regimen; and, most recently, immediate ART for the HIV-positive partner to prevent onward sexual transmission (4–7) (see the chart).

In contrast, daily oral TDF/FTC used as PrEP by heterosexual women did not appear to provide benefit in the FEM-PrEP trial that is closing early after a planned interim review revealed equal numbers of HIV infections in the active and placebo groups (8). Independent pharmacokinetic studies of oral dosing suggest that TDF drug levels are 10 to 100 times lower in vaginal versus rectal tissues (9). This might provide one explanation for the difference in efficacy of oral TDF/FTC against vaginal (women) and rectal (MSM) HIV transmission.

Recent findings indicate that early use of ART [treatment for prevention (T4P)] by an HIV-infected individual reduced heterosexual transmission to an uninfected partner by 96% when couples also received free condoms, safer-sex counseling, and treatment for sexually transmitted infections (HPTN052) (10). This strengthens previous evidence from a meta-analysis of ART estimating a 92% reduction in transmission (11). Although early ART for serodiscordant couples (where one partner is infected) may be feasible in many settings, offering immediate T4P to all who test HIV-positive is challenging in settings where barely 50% of those medically eligible (based on decline in CD4 T cell count) are receiving ART.

New Approaches to Trial Design

Specific approaches would include focused assessment of MMC combined with microbicide gels for men's female partners. A second combination to evaluate would be T4P with antiretroviral (ARV) PrEP (microbicide for women, oral for MSM) for the HIV-negative partner. At least 7 of the 39 (18%) sexual transmissions in the HPTN052 trial involved virus that was genetically distinct from that of the primary infected partner and were thus presumably acquired from other partners outside the primary relationship (10). Thus, the offer of ARV PrEP for the HIV-negative partner would likely add benefit to treating the positive partner in serodiscordant couples, would facilitate safer conception (12), and may provide a more cost-effective option per infection

Potentially beneficial combinations of prevention options need innovative trials to assess multiple tools against a common control.

averted than early ART alone.

It is, however, widely accepted that a fully efficacious vaccine providing durable (years) protection against HIV would have the biggest impact on HIV incidence. Nevertheless, mounting a protective immune response within hours of exposure is a biological challenge, particularly if viral exposure is high. Positive interactions could be explored by assessing the impact of combining vaccines with other biomedical interventions.

It is plausible that concomitant PrEP might prevent HIV acquisition during the course of immunizations before the full development of vaccine-induced immunity. A second potential positive impact would be seen if combining PrEP and vaccines had additive or synergistic interactions once the course of immunizations were complete. Current understanding is that HIV infection is mostly initiated by a single viral variant that requires local amplification in mucosal tissue before disseminated systemic infection is established (13). When viral exposure is extremely high, as is the case in acute infection, multiple variants capable of establishing many foci of infection may be transmitted. Here, more than one biomedical technology is likely needed to prevent HIV acquisition.

Lessons might be learned from the Thai RV144 vaccine trial, based on a canarypox vector prime (ALVAC)-protein boost, that demonstrated partial protective efficacy in cohorts at low risk of HIV exposure (6). Investigations are under way to try to define the correlates of protection in this trial. It is unclear whether those infected had suboptimal immune responses relative to those protected or if they were exposed to a higher and/or more frequent infectious challenge that was sufficient to overcome the vaccine-induced immunity. If the latter, it is certainly plausible that the implementation of T4P, microbicides, oral PrEP, and/or MMC could reduce both the infectiousness and frequency of viral exposure in a given population, providing conditions that might significantly increase vaccine efficacy. This hypothesis could be explored in the design of the proposed ALVAC-protein prime-boost trials based on the RV144 results currently being discussed in Thailand and South Africa.

Another unexplored possibility is that vaccinated subjects protected from infec-

¹Imperial College, London, London W2 1PG, UK. ²EUROPRISE Network of Excellence on Microbicides and Vaccines (www.europrise.org/). ³AVAC: Global Advocacy for HIV Prevention, New York, NY 10027, USA. ⁴Medical Research Council Clinical Trials Unit, London NW1 2DA, UK. ⁵Office of the Deputy Executive Director, Programme Branch, Joint United Nations Programme on HIV/AIDS, CH-1211 Geneva, Switzerland.

*Author for correspondence. E-mail: r.shattock@imperial.ac.uk

tion by also using ARV-PrEP might display boosted vaccine-induced immune responses (the virus working like a booster vaccination) each time they are exposed to HIV. This might focus vaccine-induced immune responses to better recognize virus from their infected partner(s). Indeed, evidence from nonhuman primate (NHP) studies indicates

that animals exposed to infectious virus when protected by PrEP demonstrate cellular immune responses to the challenge virus (14, 15). Such immune responses in these nonvaccinated animals were insufficient to protect animals from subsequent challenge in the absence of PrEP (15). Studies are now needed to determine whether ARV-protected exposure to infectious virus in vaccinated animals can influence immune responses sufficiently to increase vaccine efficacy.

Dual-delivery technology for concomitant administration of vaccine candidates and vaginal ARV-microbicides is also under development. The simplest approach is the co-formulation of HIV vaccines in a microbicide carrier gel that might be amenable to repeatedly boosting vaginal immune responses, while at the same time delivering topical ARV protection against vaginal HIV acquisition. More sophisticated approaches have been the development of intravaginal ring (IVR) technology that could provide both sustained release of preventive ARV-drug dosing (months) and pulsed exposure of a vaccine (hours to days) (16). Given that IVRs are capable of delivering ARV dosing for up to 3 months, incorporating a pulsed vaccine dose in each ARV-containing IVR could provide regular boosting of vaginal immunity. Another possibility is the combination of vaccine candidates and long-acting (months) injectable PrEP formulations such as the rilpivirine (TMC278) injectable nanosuspension (17). Here, both vaccine and injectable PrEP could be codelivered in a similar fashion to injectable contraception, which would remove the issue of adherence (remembering to take the drug).

However, combinations may also have negative implications. The most important of these is the possibility that individuals who are using condoms consistently may stop doing so in favor of a partially effective technology. Open-label trials (where participants know what they are using) with

biological outcomes (HIV acquisition) are the best way to assess concerns about risk compensation (adjusting behavior based on perceived protection) while learning about implementation. Biomedical combinations may have other negative implications; for example, using the same ARV drugs for treatment and prophylaxis may exacerbate circulating drug resistance if efficacy is only partial. These are complex issues, mandating timely communication about the rationale, design, and results of combination approaches.

Currently, most human clinical trials remain focused on determining safety and efficacy of individual biomedical interventions. Although this remains a priority, we recommend a broadening of focus to accelerate rigorous evaluation of combination approaches. This means a move away from single biomedical interventions to an emphasis on combinations that provide the greatest impact on HIV incidence in diverse epidemic scenarios. A coordinated approach tracked by normative bodies like Joint United Nations Programme on HIV/AIDS (UNAIDS) and World Health Organization is required to advance prevention science efficiently by designing and conducting RCTs to assess the added value of single biomedical interventions or combination strategies (18). In addition, expansion of preclinical studies is needed to assess the biological plausibility of additive or synergistic interactions between ARV prophylaxis and vaccines to create lower-risk conditions that might make partially efficacious vaccines a viable option.

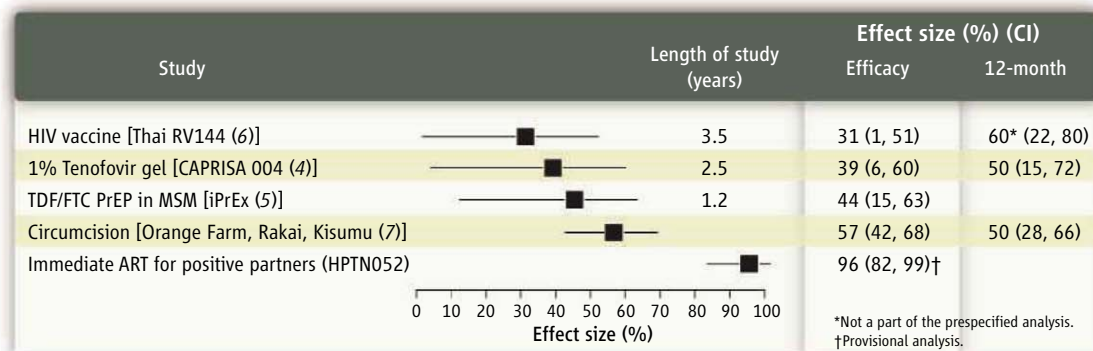
We predict that combining implementation of new biomedical prevention tools to create additive or synergistic effects will stimulate incremental reductions in HIV incidence. This, in turn, will raise the bar of evidence required for evaluation of new approaches, as reduced incidence will necessitate larger, and therefore more costly, tri-

als and place an intrinsic research value on higher-incidence cohorts. For PrEP, this will mean increasing emphasis on surrogate markers of activity, including pharmacokinetics and pharmacodynamics, to demonstrate potential superiority over approaches with proven efficacy in RCTs. For vaccines, it will require proof of efficacy in NHP studies, definition of correlates of immune protection, and demonstration of their induction in early phase I/II clinical trials.

Study of the interactions among, and combinations of, novel HIV biomedical intervention tools represents the next imperative for HIV prevention science—offering hope, at last, for a tangible impact on halting and reversing the HIV pandemic.

References

1. UNAIDS, *AIDS at 30: Nations at the Crossroads* (UNAIDS, Geneva, 2011).
2. R. Hecht *et al.*, *Lancet* **376**, 1254 (2010).
3. C. A. Hankins, B. O. de Zaldondo, *AIDS* **24** (suppl. 4), S70 (2010).
4. Q. Abdool Karim *et al.*, *Science* **329**, 1168 (2010).
5. R. M. Grant *et al.*, *N. Engl. J. Med.* **363**, 2587 (2010).
6. S. Rerks-Ngarm *et al.*, *N. Engl. J. Med.* **361**, 2209 (2009).
7. N. Siegfried, M. Muller, J. J. Deeks, J. Volmink, *Cochrane Database Syst. Rev.* (2): CD003362 (2009).
8. B. Roehr, *BMJ* **342** (3), d2613 (2011).
9. K. B. Patterson *et al.*, 18th International AIDS Conference, Vienna, Austria, 18 to 23 July 2010, abstr. THBS0305 (2010).
10. Initiation of antiretroviral treatment protects uninfected sexual partners from HIV infection (HIV Prevention Trials Network Study 052), "HPTN052PressRelease" at www.hptn.org/.
11. S. Attia, M. Egger, M. Müller, M. Zwahlen, N. Low, *AIDS* **23**, 1397 (2009).
12. L. T. Matthews, J. M. Baeten, C. Celum, D. R. Bangsberg, *AIDS* **24**, 1975 (2010).
13. B. F. Keele, J. D. Estes, *Blood* **9** May 2011 (10.1182/blood-2010-12-325860).
14. M. Cranage *et al.*, *PLoS Med.* **5**, e157 (2008).
15. E. N. Kersh *et al.*, *PLoS ONE* **6**, e19295 (2011).
16. K. J. Whaley, J. Hanes, R. Shattock, R. A. Cone, D. R. Friend, *Antiviral Res.* **88**, (suppl. 1), S55 (2010).
17. G. van't Klooster *et al.*, 15th Conference on Retroviruses and Opportunistic Infections, CROI 2008, Boston, MA, 3 to 6 April 2008, abstr. 134 (2008).
18. J. L. Excler *et al.*, *AIDS Res. Hum. Retroviruses* **27**, 669 (2011).



Effect size of biological intervention strategies to prevent HIV infection. Effect size is the relative reduction in the risk of acquiring HIV between the intervention and control groups. CI, 95% confidence interval. The last column shows the effectiveness 12 months from enrollment and initiation of the intervention.

Fishing in the Nuclear Pore

Richard W. Kriwacki and Mi-Kyung Yoon

Cellular materials pass into and out of the nucleus of a eukaryotic cell through pores in the nuclear membrane. Each nuclear pore is a complex of ~400 modular polypeptide chains [nucleoporins (Nups)] that form a cylindrical structure (1). The pore functions as a semipermeable filter that allows free diffusion of ions, small molecules, and macromolecules <40 kD in mass. Larger, soluble macromolecules that bear a nuclear localization signal (NLS) are ushered through by transport factors (2), but the molecular details of the mechanism remain mysterious. Even more perplexing is how membrane proteins transit from the outer to the inner nuclear membrane. Early models proposed either free diffusion and nuclear retention (3) or energy-dependent transport (4), whereas later results unexpectedly showed that the NLS-dependent transport mechanism for soluble proteins played a role (5). On page 90 of this issue, Meinema *et al.* (6) demonstrate an unprecedented mechanism for the latter model, showing that passage through the pore relies on the energetically unhindered, dynamic features of an intrinsically disordered (ID) domain in the membrane protein and the structural modularity and plasticity of the nuclear pore complex (NPC).

Specific NLSs interact with soluble karyopherins, proteins that bind transiently to Nup proteins bearing phenylalanine-glycine motifs (FG-Nups). The array of FG-Nups in the pore forms a dynamic, gel-like structure (7) that functions as a semipermeable diffusion barrier (8). Karyopherin- α (Kap60 in yeast; Importin- α in human) binds to the so-called classical NLS (a stretch of four or more Arg and/or Lys residues) of cytoplasmic proteins destined for the nucleus (2). This complex further interacts with karyopherin- β 1 (Kap95 in yeast; Importin- β 1 in human) to form a ternary complex. Karyopherin- β 1 then binds weakly and transiently to some of the many different FG-Nups in the pore, causing the ternary complex to stochastically “flow” toward the nucleoplasm (2). Once this destination is reached, the ternary complex disassembles by interactions with Ran (that is bound to guanosine 5'-triphosphate) and a release factor

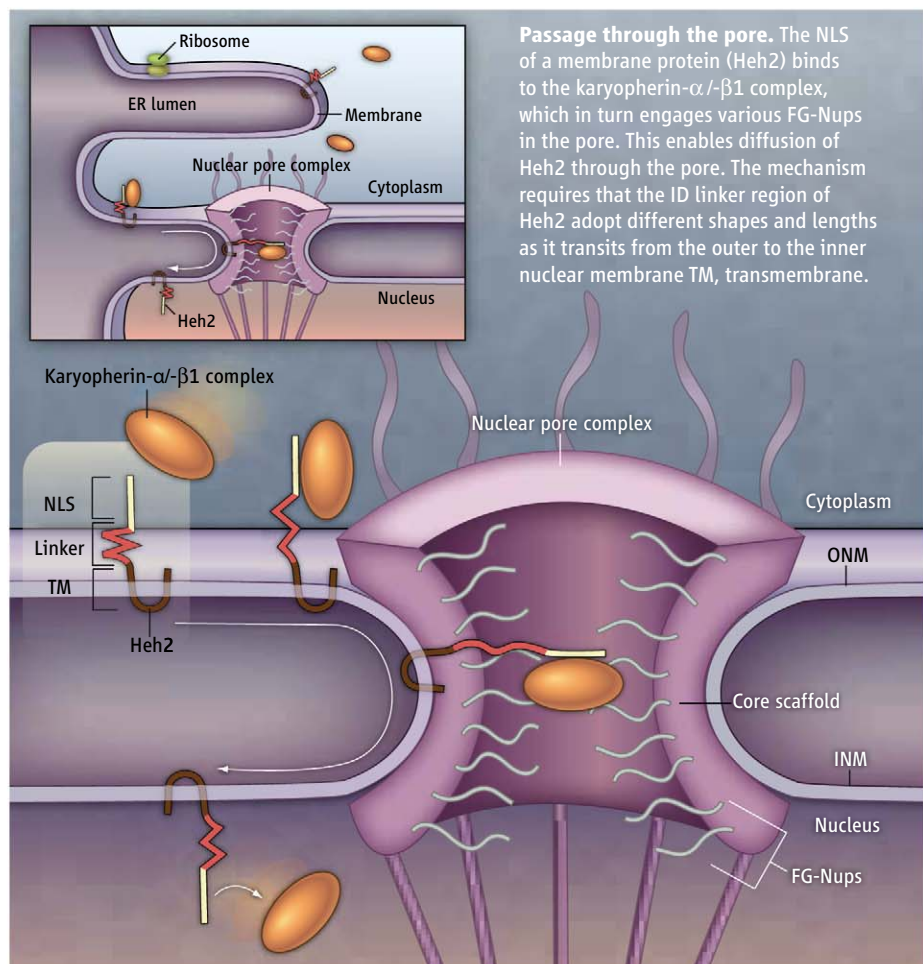
called Nup2. All but the cargo is recycled to the cytoplasm for the transport process to be repeated (9).

Meinema *et al.* show that transport of the yeast protein Heh2 to the inner nuclear membrane (INM) requires three FG-Nups—Nup100, Nup145N, and Nup57, located on the cytoplasmic face, the nucleoplasmic face, and on both faces as well as within the central core of the NPC, respectively. In addition, the authors show that an affinity tag engineered onto the NLS end of Heh2 was captured within the NPC core by the appropriately counter-tagged Nup (Nsp1) located within the core and on the cytoplasmic and nucleoplasmic faces. These results counterintuitively place the end of Heh2 harboring two consecutive NLSs (two hydrophobic transmembrane domains are located at the other end of the protein) within the aqueous NPC core. Mei-

The flexibility of an intrinsically disordered domain of a membrane protein allows it to pass through the nuclear pore.

nema *et al.* used nuclear magnetic resonance spectroscopy and gel filtration chromatography to show that a linker domain of ~180 residues between the NLS region and the first of two transmembrane domains is disordered and exhibits an extended structure. The natural ID linker, or two randomized variants, could still support INM localization when reduced to 120 residues.

ID domains can freely adopt a wide range of disordered shapes and lengths. It may be that like the ID domain of the protein p27^{Kip1} (10), the Heh2 linker domain can stretch up to ~260 Å. This length is sufficient to extend from the lipid bilayer at the periphery of the cytoplasmic face of NPC to the core region of the pore where karyopherins α and β 1 are thought to engage NLS-bearing cargo (see the figure). The minimum linker length (120 residues) that supports INM localiza-



Department of Structural Biology, St. Jude Children's Research Hospital, Memphis, TN 38105, USA. E-mail: richard.kriwacki@stjude.org

tion likely can extend to ~170 Å, which corresponds approximately to the distance from the periphery of the NPC outer rings of Nups to the inner layer of FG-Nups within the NPC central core (1). A requirement of the model of Meinema *et al.* is that the modular structure of the NPC allow passage of the ID linker between the Nup subunits of the outer and inner rings of the pore, from the cytoplasmic to the nucleoplasmic face. This scenario assumes that the transmembrane domains of Heh2 remain associated with the lipid bilayers surrounding the NPC during transit. It is conceivable that the transmembrane domains may interact with one or more of the Nups of the NPC rings during transit to the INM. However, it is energetically implausible that the hydrophobic transmembrane domains are extracted from the lipid periphery or the hydrophobic parts of the outer and inner Nup rings during transport. The disassembly of the

NPC during mitosis and its reassembly after cell division are compatible with the “sub-unit parting” model for linker passage, but these details await elucidation. In addition to Heh2, the ID linker of Heh1 supports nuclear transport of a Heh2 reporter construct. The sequences of several yeast and human INM proteins (9) suggest that the ID-dependent INM transport mechanism is broadly utilized. This utilization may be broader still because the prediction of NLSs within protein sequences is imperfect. However, these suggestions await experimental verification.

Meinema *et al.* illustrate that ID domains can be flexible tethers between membrane-associated cargo and a transport signal during nuclear import of INM proteins. In addition to these tethers, the NPC is replete with other types of disordered domains, with large portions of the FG-Nups serving as flexible linkers or forming the semipermeable core of the

complex (FG-repeat domains) (11). Flexibility and adaptability within the mostly structured importin-β family of karyopherins are critical for their “catch and release” transport mechanism (12). The tethering-transport mechanism elucidated by Meinema *et al.* constitutes a new entry in the growing list of “disorder-function relationships” for ID proteins.

References

1. F. Alber *et al.*, *Nature* **450**, 695 (2007).
2. S. R. Wenthe, M. P. Rout, *Cold Spring Harb. Perspect. Biol.* **2**, a000562 (2010).
3. B. Soullam, H. J. Worman, *J. Cell Biol.* **130**, 15 (1995).
4. T. Ohba *et al.*, *J. Cell Biol.* **167**, 1051 (2004).
5. M. C. King, C. P. Lusk, G. Blobel, *Nature* **442**, 1003 (2006).
6. A. C. Meinema *et al.*, *Science* **333**, 90 (2011); 10.1126/science.1205741.
7. S. Frey, R. P. Richter, D. Görlich, *Science* **314**, 815 (2006).
8. S. S. Patel *et al.*, *Cell* **129**, 83 (2007).
9. C. P. Lusk *et al.*, *Nat. Rev. Mol. Cell Biol.* **8**, 414 (2007).
10. C. A. Galea *et al.*, *J. Mol. Biol.* **376**, 827 (2008).
11. J. Yamada *et al.*, *Mol. Cell. Proteomics* **9**, 2205 (2010).
12. E. Conti *et al.*, *Curr. Opin. Struct. Biol.* **16**, 237 (2006).

10.1126/science.1208568

VIROLOGY

Revealing Virus-Host Interplay

Mart Krupovic¹ and Dennis H. Bamford²

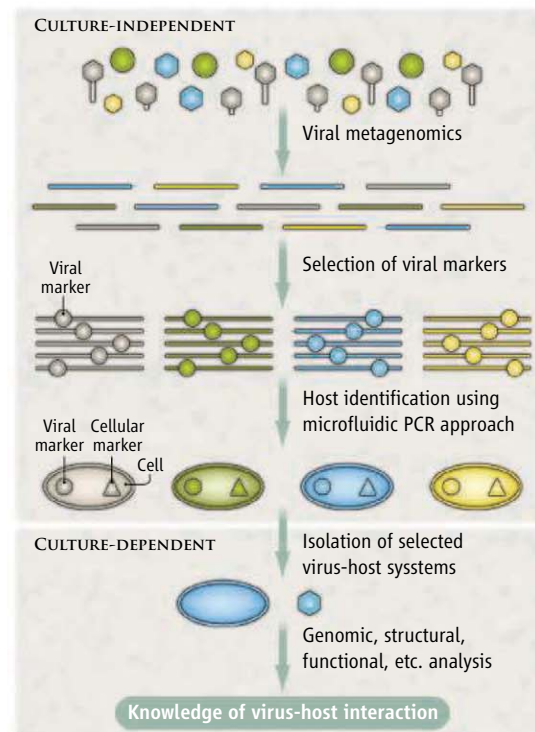
Discoveries made by environmental virologists during the past decade or so have revolutionized our perception of the living world. It has become apparent that viruses are the most abundant living entities on Earth, outnumbering their hosts by an order of magnitude. The vast majority of viruses infect microbes, but many infect humans, making each one of us a platform for a complex microbial community. Researchers now recognize viruses as major players in small- and global-scale ecosystems (1), boosting their interest in studying virus-host interactions (2). Our inability to cultivate the vast majority (>99%) of microbes under laboratory conditions, however, has limited study of these interactions. We still do not know the hosts of most viruses. On page 58 of this issue, Tadmor *et al.* (3) take a considerable step toward overcoming this limitation, reporting on an approach to identifying virus hosts that does not require the culturing of viruses or host microbes. The approach, which features a genetic-analysis technology called microfluidic digital polymerase chain reaction (PCR), adds to recent developments in culture-

independent, high-throughput technologies (4, 5) that promise to provide a revealing picture of dynamic host-virus relationships.

Tadmor *et al.* endeavored to understand the interplay between uncultured viruses

A new microfluidic technique offers a culture-independent method of studying virus-host interactions.

and bacteria that were harvested directly from a natural environment, the hindgut of termites. After harvest, they diluted the bacterial cells and loaded them into a PCR array panel so that each chamber was either empty or contained only a single bacterium. Then, they used microfluidic digital PCR (6) to assess how a selected viral gene marker was associated with a selected microbial gene marker. As bacterial markers, they used genes encoding the small subunit rRNA, a vital component of ribosomes. Based on previous analyses of microbes living in the termite hindgut (7), they chose as the viral marker a gene that encodes the large subunit of terminase (TerL), an enzyme essential for viral particle assembly (8). TerL is found only in certain evolutionarily related “tailed”



Culture-free. Microfluidic digital PCR techniques enable researchers to document virus-host associations without culturing viruses or host microbes. The technology could help reveal virus-host interactions by creating a bridge that links culture-dependent and culture-independent methods.

¹Institut Pasteur, Unité Biologie Moléculaire du Gène chez les Extrêmophiles, 75015 Paris, France. ²Department of Biosciences and Institute of Biotechnology, University of Helsinki, FIN-00014 Helsinki, Finland. E-mail: dennis.bamford@helsinki.fi

bacterial and archaeal viruses, as well as in eukaryotic herpesviruses (8, 9).

Tadmor *et al.* detected 41 “colocalizations” of the viral and bacterial markers. In 28 of these cases, the viral marker was associated with just four microbial phylogenotypes (evolutionarily related hosts); all were members of the spirochetal genus *Treponema*. This identified these bacteria as hosts for the viruses. Tadmor *et al.* also grouped the *Treponema*-infecting viruses into five clades based on phylogenetic analyses of TerL. Analyses of these virus-host systems revealed that certain viral clades are differentially associated with certain bacterial clades, suggesting that neither cross-species transmission of viruses nor horizontal gene transfer between viruses is frequent in these systems.

The greatest merit of the method of Tadmor *et al.* is that it can be employed to examine virus-host interactions in biological samples from virtually any environment, without the need to enrich or cultivate organisms. As the authors note, by itself metagenomics (the analysis of genetic material recovered directly from environmental samples) “has as yet done little to

shed light on the nature of specific viral-host interactions.” However, combining metagenomics with microfluidic digital PCR will undoubtedly advance environmental virology (see the figure). Due to the viral gene marker they selected, Tadmor *et al.* were restricted to studying certain tailed bacteriophages. However, selecting alternative markers could help to finally expose the hosts of other, poorly understood viruses. For example, metagenomic analyses have revealed that uncultured single-stranded DNA viruses of the family *Microviridae* are highly abundant in marine environments and might play an important ecological role (10); microfluidic digital PCR technology could identify their hosts.

So is it time to abandon microbial cultivation? Does the identification of uncultured virus-host systems and infection patterns take us to the frontier of understanding these interactions? Not really. Rather, the new technologies represent essential steps in this quest. The richness of virus-host interplay (11–13) can be unraveled only when the system is experimentally tractable both in nature and in the laboratory, and when researchers are able to apply the full range of genetic,

molecular, and structural biology techniques. High-throughput methods should not carry us away from culture-dependent research; instead, the two approaches should be merged into a continuum.

References and Notes

1. C. A. Suttle, *Nat. Rev. Microbiol.* **5**, 801 (2007).
2. F. Rohwer, R. V. Thurber, *Nature* **459**, 207 (2009).
3. A. D. Tadmor, E. A. Ottesen, J. R. Leadbetter, R. Phillips, *Science* **333**, 58 (2011).
4. E. E. Allen, J. F. Banfield, *Nat. Rev. Microbiol.* **3**, 489 (2005).
5. R. N. Zare, S. Kim, *Annu. Rev. Biomed. Eng.* **12**, 187 (2010).
6. E. A. Ottesen, J. W. Hong, S. R. Quake, J. R. Leadbetter, *Science* **314**, 1464 (2006).
7. F. Warnecke *et al.*, *Nature* **450**, 560 (2007).
8. V. B. Rao, M. Feiss, *Annu. Rev. Genet.* **42**, 647 (2008).
9. M. Krupovic, P. Forterre, D. H. Bamford, *J. Mol. Biol.* **397**, 144 (2010).
10. F. E. Angly *et al.*, *PLoS Biol.* **4**, e368 (2006).
11. M. Frada, I. Probert, M. J. Allen, W. H. Wilson, C. de Vargas, *Proc. Natl. Acad. Sci. U.S.A.* **105**, 15944 (2008).
12. D. Prangishvili, T. E. Quax, *Curr. Opin. Microbiol.* (2011); 10.1016/j.mib.2011.04.006.
13. V. Doceul, M. Hollinshead, L. van der Linden, G. L. Smith, *Science* **327**, 873 (2010).
14. Supported by the European Molecular Biology Organization (ALTF 347-2010 to M.K.) and the Academy of Finland Center of Excellence (grant 11296841 to D.H.B.).

10.1126/science.1208557

APPLIED PHYSICS

Knot Your Simple Defect Lines?

Randall D. Kamien

We owe more to knots in our lives than we might appreciate: Simple bows and knots developed into the practical knots of sailors, decorative braids, and, as we are still learning, into the Khipu records of the Incas (see the figure, panel A). The ancient art of weaving became a driving force in the industrial revolution; the Jacquard loom gave us the first inkling of the modern programmable computer; and ancient embroidery, such as the Bayeux tapestry, imprint the historical record (see the figure, panel B). On page 62 of this issue, Tkalec *et al.* (1) tie knots in a different type of line—the topological defect lines that form when the ordering of a nematic liquid crystal is disrupted by the addition of colloidal particles. When these lines are manipulated with laser tweezers, they can be woven into arbitrarily complex knots and links. Moreover, the for-

mation of these beautiful and stable braided structures is enabled by using a sample cell similar to that commonly used in liquid crystal display technology.

In a nematic liquid crystal phase, anisotropic molecules have a preferred alignment direction, as opposed to a normal or isotropic fluid, where their orientation is random. This anisotropy is responsible for the beautiful images of liquid crystals seen with polarized light. The sample cell Tkalec *et al.* used also imparts a gradual twist to the ordering direction, called the director, and such phases are called chiral nematic phases. The twisting of the chiral nematic can be controlled with electric fields and changes how it transmits light, an effect exploited in display technology. This ordering can be disrupted by heating, which can melt the liquid crystal and form an isotropic fluid, and by defects, such as the colloidal particles added by Tkalec *et al.*, which can locally disrupt ordering and create lines of isotropic fluid.

One way to visualize the ordering of the

The ordering of molecules in a liquid crystal is disrupted by colloidal particles and creates lines of defects, which can be manipulated to form loops and knots.

molecules in the nematic phase that surrounds the defect lines is to consider what happens when the surface of water is disturbed with a paddle. Pulling a paddle through a calm river displaces the water. The flow creates a vortex line in the water ending at two pointlike “whirlpools” on the surface. Eventually, the vortex line shrinks; the two points come together, and the whole loop disappears. The movement of the surrounding fluid is critical—holding a piece of rope in the water displaces a line of water but does not create a vortex. Similarly, the lines in the nematic liquid crystal are vortices in the surrounding nematic—regions where the orientation of the director changes so rapidly that the fluid is forced to be isotropic.

Each colloidal particle is encircled by a defect line, called a Saturn ring (see the figure, panel C). When the particles are brought together with the laser tweezers, the defect lines can merge and tie two particles together with a longer loop. Further manipulations can tie several particles together, and create

Department of Physics and Astronomy, University of Pennsylvania, Philadelphia, PA 19104-6396, USA. E-mail: kamien@physics.upenn.edu



knots. Although the winding of the director is somewhat more subtle than in water flow (because of the symmetries of the nematic phase), the presence of these lines implies an arrangement of molecular orientation in the surrounding space. The tied knots and images indicate only a section of the complexity of the bulk structure. It is not just the vortices that are tangled or the defect lines that are knotted; it is the whole surrounding medium—that is, a knotted field is created. Tkalec *et al.* demonstrate that the knotting of this field can be exquisitely controlled to create all possible knots and links between the colloidal inclusions.

These general structures are apparently only realizable in the twisted-cell geometry. It is an open question whether these knots can be tied and untied by switching the boundary conditions locally, for example, by applying an electric field to change the chiral twist. Not long ago, it was demonstrated (2) that some knots could be tied in light fields through an ingenious method of phase manipulation; in this case, the vortices are lines of complete darkness where the electromagnetic field vanishes.

Compare the links and knots formed by Tkalec *et al.* to the intricate linking of kinetoplast DNA (see the figure, panel D). The link-

A gallery of knots. (A) The bow helps hold the dress together. The braid covers the buttons. (B) Tapestry (actually an embroidery) that encodes information. (C) Loops and knots formed by merging of defect lines created by colloidal particles in liquid crystals. Tkalec *et al.* used laser tweezers to manipulate the particles and lines, which causes the “Saturn ring” defects surrounding the particles to merge and tangle. (D) Catenated DNA minicircles in the mitochondria of *Leishmania tarentolae*. Like defect lines, they too are linked. [Photo in (D) courtesy of L. Simpson (5)]

ing of the minicircles there is certainly not random, but its purpose is still somewhat of a mystery; it has been shown that minicircles play an important role in gene editing (3). Perhaps experimentally controlled particle linking could be used to control catalysis or modify binding sites in nonbiological applications. The tools developed by Tkalec *et al.* pave the path to these sorts of geometric and topological controls. It is intriguing to consider the possibility of marrying the two knotted fields, light and liquid crystals, to develop an entire new set of mathematical constructs (4) and potential devices. Can results in knot theory be discovered experimentally and systematically with these defect arrays? Not if we don’t tie!

References

1. U. Tkalec, M. Ravnik, S. Čopar, S. Žumer, I. Mušević, *Science* **333**, 62 (2011).
2. M. R. Dennis, R. P. King, B. Jack, K. O’Holleran, M. J. Padgett, *Nat. Phys.* **6**, 118 (2010).
3. J. Shlomai, *Curr. Mol. Med.* **4**, 623 (2004).
4. N. A. Baas, *Eur. Phys. J. Spec. Top.* **178**, 25 (2009).
5. L. Simpson, A. Da Silva, *J. Mol. Biol.* **56**, 443 (1971).

10.1126/science.1208526

NEUROSCIENCE

Remember When?

Henry L. Roediger III and Kathleen B. McDermott

Philosophers, psychologists, and neuroscientists usually consider remembering to be a solitary activity. We envision the lone rememberer, lost in contemplation like Rodin’s *Thinker*, recalling his past. In memory experiments, thousands of subjects have sat alone in front of computers or memory drums (older devices designed to present information), or have lain inside giant magnets, duly recollecting events of their lives. We have learned much about remembering

from their efforts. However, this tradition of research fails to capture a prominent characteristic of everyday remembering: its social aspects. That is, people tend to reminisce in groups—whether at family dinners, reunions, or other social engagements. On page 108 of this issue, Edelson *et al.* (1) offer new insight into the social aspects of memory, reporting on the first experiments to examine the neural underpinnings of how memories can change when an individual is exposed to the recollections of others. They show that activity in two brain regions involved in memory—the hippocampus and the amygdala—can vary,

depending on how one person’s memory has been shaped by interacting with others.

Consider a person telling a story to acquaintances at a party. Storytellers routinely (and knowingly) embellish their stories in order to better capture an audience’s interest. Past research, however, has shown that storytellers can readily incorporate these seemingly inconsequential embellishments into their own memory of the original event (2). The situation becomes even more complex when a storyteller recollects an event in the presence of others who were present during the event. In this situation, the vari-

Department of Psychology, Washington University, St. Louis, MO 63130, USA. E-mail: roediger@wustl.edu

ous players contribute to the group recollection. Each can relate events accurately, in turn updating and reinforcing the memories of the storyteller and other group members. But some members of the group may erroneously recall some details, which will tend to infect the storyteller's record of events with distortions (or vice versa); psychologists call this process social contagion (3, 4).

These social aspects of remembering have recently come under renewed scrutiny by cognitive and social psychologists, who have noted both these positive and negative effects (5, 6). Psychologists have tended to note the negative effects more than the positive ones, however, perhaps because errors can have important societal implications, such as erroneous eyewitness testimony in courts of law (7).

Memory conformity is the general term for these positive and negative effects. Psychologists distinguish between private conformity (truly believing the conforming response to be one's own) and public conformity (going along with the group, even if you privately believe the group is wrong). Social psychologists have worked out techniques to distinguish between public and private conformity, and cognitive psychologists have applied them to the study of memory. Edelson *et al.* extend these efforts by using functional magnetic resonance imaging to record the brain activity of 30 adults who viewed a documentary-style movie and then were tested on their memories of the movie over a 2-week period. The researchers intentionally tried to induce memory errors in some subjects by telling them what others recalled about the movie; they exposed other subjects to randomized "recollections."

Their findings offer insight into how social interaction can alter memories. In particular, they provide evidence for separate neural bases for shorter-lived "transient" memory errors, which may reflect public conformity, and longer-lived "persistent" memory errors, which may reveal private conformity. Specifically, the researchers observed greater neural activation in the hippocampus for items that showed persistent memory errors (private conformity) than for items that displayed transient errors (possible public conformity). They were also able to distinguish between conformity elicited by social influences (being exposed to other people, or at least their faces) and conformity produced by nonsocial methods (being exposed to computer-generated responses to questions on a test). The investigators observed robust activation of the amygdala in subjects who displayed social conformity (responding when influenced by



Think again. Memories recalled when alone can change if shared with others. Barry Flanagan's *Thinker on Rock* sits on the campus of Washington University in St. Louis, Missouri.

other people's responses); in contrast, they observed less activation in subjects displaying nonsocial conformity (responding to computer-generated responses). This finding mirrored behavioral data suggesting that greater conformity occurred under social pressure. In addition, a control experiment showed that amygdala activation did not seem to reflect emotional arousal but was instead attributable to the social nature of the influence.

These results are in some ways surprising. For instance, the observation that amygdala activation occurred disproportionately on occasions when social influence consistently changed memory, or changed belief in recently perceived events, suggests a previously unrecognized function for this brain region. But full understanding of this finding awaits future research.

Edelson *et al.* were concerned with memory conformity, but there are also other types of deleterious social influence from remembering in groups. In particular, when people all learn common information and then are tested, either individually or in groups (usually three people), a paradoxical effect called collaborative inhibition emerges (8). The total number of events remembered by the group exceeds that of individuals. However, when researchers compare the recollections of a group that has had collaborative discussions to the recollections of three people acting individually (a nominal group), the actual group recalls fewer events than the nominal group. This outcome is not due to social loafing—the tendency for people in groups to work less hard than they do when individual performance is measured. Rather, the collabor-

ative setting seems to disrupt the retrieval processes that individuals use when they are recalling in isolation (8, 9). To date, the only reported exception to this finding involves collaborative groups made up of experts on a topic; then the groups do better than the individuals (10). A target for future research is to see whether the generally deleterious effect of social remembering has a neural basis similar to that of memory conformity.

Social effects on remembering can be positive as well as negative. Indeed, memory conformity may typically be beneficial. If one individual in a group forgets critical information (about food resources or dangers, for instance), then it is wise to get an updated memory from another group member. In experiments that have examined social influence when others provide accurate information, the effects are strongly positive (11). As with perceptual illusions, most memory illusions probably reveal adaptive processes that can sometimes undermine rather than support accurate remembering (12). Whether the positive effects of social influence have the same neural bases as the negative effects also awaits future investigation. However, we predict that positive memory conformity will have the same bases as the negative effects, because both reflect updating of individual memory by social means.

The study of individual remembering is more than 125 years old, whereas the study of the social aspects of remembering is relatively young. Edelson *et al.* provide a promising first step in delineating the neural underpinnings of memory conformity, an important issue in the social psychology of remembering.

References

1. M. Edelson *et al.*, *Science* **333**, 108 (2011).
2. E. J. Marsh, B. Tversky, *Appl. Cogn. Psychol.* **18**, 491 (2004).
3. F. C. Bartlett, *Remembering: A Study in Experimental and Social Psychology* (Macmillan, New York, 1932).
4. H. L. Roediger 3rd, M. L. Meade, E. T. Bergman, *Psychon. Bull. Rev.* **8**, 365 (2001).
5. M. S. Weldon, in *The Psychology of Learning and Motivation*, D. L. Medin, Ed. (Academic Press, San Diego, CA, 2000), vol. 40, pp. 67–120.
6. M. Ross, C. W. Blatz, E. Schryer, in *Learning and Memory: A Comprehensive Reference*, H. L. Roediger, Ed. (Elsevier, Oxford, 2008), vol. 2, pp. 911–926.
7. E. F. Loftus, *Learn. Mem.* **12**, 361 (2005).
8. M. S. Weldon, K. D. Bellinger, *J. Exp. Psychol. Learn. Mem. Cogn.* **23**, 1160 (1997).
9. S. Rajaram, L. P. Pereira-Pasarin, *Perspect. Psychol. Sci.* **5**, 649 (2010).
10. M. L. Meade *et al.*, *Memory* **17**, 39 (2008).
11. E. F. Loftus, D. G. Miller, H. J. Burns, *J. Exp. Psychol. Hum. Learn.* **4**, 19 (1978).
12. H. L. Roediger, K. B. McDermott, in *The Oxford Handbook of Memory*, E. Tulving, F. I. M. Craik, Eds. (Oxford Univ. Press, Oxford, 2000), pp. 149–162.

CHEMISTRY

Electrons in Cement

Peter P. Edwards

A free or ionized electron introduced into a polar molecular solvent such as water or ammonia can be stabilized or trapped by reorientation of the host solvent molecules, leading to the appearance of “solvated” electrons in the liquid (1, 2). For example, in solutions of alkali metals in liquid ammonia, alkali valence electrons are spontaneously ionized by the dissolving metal and released directly into solution. These systems, first described by Sir Humphry Davy in 1808 (3), are brilliant blue, electrolytic conductors when dilute in metal and spectacular golden-bronze and genuinely metallic in concentrated solutions. Kraus, as early as 1914, described the negative carrier of electric current in dilute metal-ammonia solutions as “the negative electron surrounded with an envelope of solvent molecules” (see the figure, panel A) (4). Two years later, Gibson and Argo (5) introduced the term “solvated electrons” to describe this, the simplest anion in solution. On page 71 of this issue, Kim *et al.* (6) report the synthesis and properties of solvated electrons in an entirely new and highly unusual host solvent—cement. The authors have succeeded in preparing solvated electrons in a high-temperature (1873 K) melt of mayenite, $12\text{CaO} \cdot 7\text{Al}_2\text{O}_3$ (abbreviated to C12A7), a component of alumina cement.

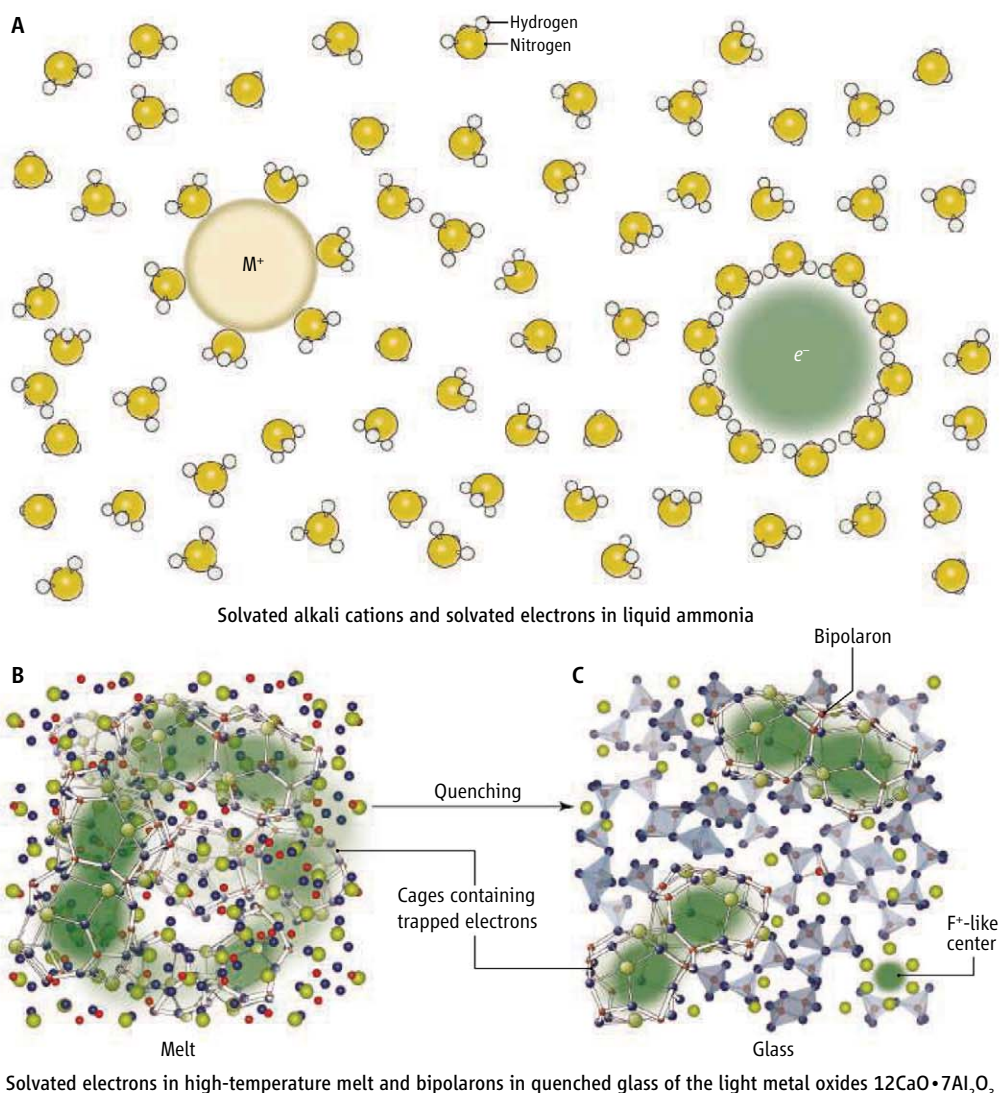
The host material itself is a constituent of slag as a vitreous by-product of the iron smelting process. These stable and recalcitrant light metal oxides are prototype insulators. Therefore, the melt of C12A7 contains no free electrons to carry electric current. On the basis of their earlier single-crystal studies of electron-doped mayenite (7), best considered from a chemical standpoint

as one class of electrides (8), Kim *et al.* wanted to find out whether excess electrons could be introduced and then stabilized as solvated electrons in high-temperature melts of these refractory oxides.

But how can one introduce or dope additional electrons into such unreactive metal oxides so as to turn such a stubbornly resistive insulating material into a conductor of electricity? The innovation reported by Kim *et al.* involves partially replacing mobile oxide ions found in the mayenite lattice by electrons through a high-temperature chemi-

A system of stabilized solvated electrons has been realized in a new type of inorganic electride.

cal reduction with elemental titanium. The introduced electrons are then trapped at oxygen ion vacancies in the melt through solvation (coordination) by calcium ions within the cage structure of the refractory oxide as so-called F^+ -like centers (see the figure, panel B). The transparent, insulating host oxide melt is thereby transformed into a highly colored, electron-doped conducting liquid (abbreviated to $\text{C12A7}:\text{e}^-$). Furthermore, the solvated electrons survive, and indeed thrive, in these high-temperature metal oxide electride melts at temperatures up to 1873 K.



Conduction setting in. Models of solvated electrons in (A) alkali metal–ammonia solution [Adapted from (12)], (B) $\text{C12A7}:\text{e}^-$ melt, and (C) $\text{C12A7}:\text{e}^-$ glass.

CREDIT: (PANEL A) ADAPTED FROM J. L. DYE, SCIENTIFIC AMERICAN, VOL. 237, 92 (1977)

Department of Chemistry, Oxford University, South Parks Road, Oxford OX1 3QR, UK. E-mail: peter.edwards@chem.ox.ac.uk

The three-dimensional connected cages of mayenite and these anionic electrons result in a partially filled conduction band constructed from the accessible, unoccupied orbitals of the cage atoms. Kim *et al.* observed a fundamental change in electrical conduction behavior of the electride melt as the concentration of introduced electrons increases, from that of (thermally activated) electron hopping between centers to recognizable metallic conduction. Above a critical concentration of solvated electrons ($\sim 10^{21}$ electrons/cm³), there is a transition to a highly conducting, genuinely metallic form of liquid cement. This must surely be one of the most unusual and spectacular observations of the transition to the metallic state (9)—turning liquid cement into liquid metal. The characteristic metallic conduction properties then require the extensive delocalization or percolation of the solvated electron wave functions over the entire melt (see the figure, panel B).

This new design concept of doping high densities of electron carriers into insulating light metal oxides has one further, fascinating twist. The rapid quenching of the high-temperature melt leads to C12A7:e⁻ glassy

materials, but here the overwhelming majority (>99%) of the introduced electrons now exist as a diamagnetic (two-electron) spin-paired state. Kim *et al.* speculate that two individual trapped electron states combine to form a peanut-shaped bipolaronic center (see the figure, panel C), again reminiscent of the situation in alkali metal–ammonia solutions (10, 11). In addition, careful studies of the melting process reveal that the glass transition temperature for the highly conducting C12A7:e⁻ electride melt is ~ 160 K lower than that for the parent C12A7 glass. This difference means that the network structure of the electride glass is fundamentally different from that of the parent cement glass, as reflected in the structural model for the melt and glass of C12A7:e⁻ electride (see the figure, panels B and C).

These important advances open the door for new applications for such robust metallic melts and slags and electronically tunable light–metal oxide glasses. In the area of quantum confinement, the work by Kim *et al.* represents a material showing the ultimate confinement of a quantum particle—an electron “set” in cement. Finally, the word “cement” can be traced back to

Roman times where the term “opus caementicium” described the use of burnt lime as a binder with, for example, volcanic ash to produce pure, natural Pozzolan cement. The advance reported by Kim *et al.* binds the quantum physics of excess electrons, correlated electrons, the metal–insulator transition, and the glass transition with the chemistry and engineering of cement. What a natural combination!

References

1. K. R. Siefermann, B. Abel, *Angew. Chem. Int. Ed.* **50**, 5264 (2011).
2. J. C. Thompson, *Electrons in Liquid Ammonia* (Oxford Univ. Press, Oxford, 1976).
3. P. P. Edwards, *Adv. Inorg. Chem. Radiochem.* **25**, 135 (1982).
4. C. A. Kraus, *J. Am. Chem. Soc.* **36**, 864 (1914).
5. G. E. Gibson, W. L. Argo, *Phys. Rev.* **7**, 33 (1916).
6. S. W. Kim, T. Shimoyama, H. Hosono, *Science* **333**, 71 (2011).
7. S. Matsuishi *et al.*, *Science* **301**, 626 (2003).
8. J. L. Dye, *Acc. Chem. Res.* **42**, 1564 (2009).
9. P. P. Edwards, C. N. R. Rao, Eds., *The Metal–Nonmetal Transition Revisited* (Taylor & Francis, London, 1995).
10. Z. Deng, M. L. Klein, G. J. Martyna, *J. Chem. Soc., Faraday Trans.* **90**, 2009 (1994).
11. E. Zurek, P. P. Edwards, R. Hoffmann, *Angew. Chem. Int. Ed.* **48**, 8198 (2009).
12. J. L. Dye, *Sci. Am.* **237**, 92 (July 1977).

10.1126/science.1207837

CELL BIOLOGY

Protease Sets Site-1 on Lysosomes

Jin Ye

One of the defining features of how animal cells maintain cholesterol homeostasis is the complex signaling mechanism that releases transcription factors called sterol regulatory element-binding proteins (SREBPs) from their membrane-bound precursors through proteolysis to control the expression of key metabolic enzymes. One of the proteases that catalyze the cleavage is site-1 protease (S1P), a serine protease that is itself membrane bound. One curious phenotype of cultured mammalian cells lacking S1P has been a defect in lysosomes—instead of being targeted to the organelle, certain lysosomal enzymes are secreted out of the cells. On page 87 of this issue, Marschner *et al.* (1) provide one possible explanation—S1P is required for the biogenesis of lysosomes. The authors show that the protease cleaves a precursor

form of *N*-acetylglucosamine (GlcNAc)-1-phosphotransferase, an enzyme that catalyzes an essential step in forming the mannose 6-phosphate signal that targets many enzymes to lysosomes.

Together with site-2 protease (S2P), a metalloprotease embedded in the Golgi membrane, S1P plays a crucial role in regulating cholesterol metabolism through proteolytic activation of SREBPs (2). When cells are overloaded with cholesterol, SREBP is trapped in the endoplasmic reticulum (ER), preventing its cleavage. Upon cholesterol deprivation, SREBP is transported to the Golgi, where S1P catalyzes the first cleavage in the luminal domain. This allows the membrane-bound amino-terminal fragment of SREBP to be cleaved by S2P in the plane of the membrane (see the figure). The second cleavage releases the amino-terminal domain of SREBP from membranes, allowing it to enter the nucleus where it activates genes required for cholesterol biosynthesis and uptake, thereby

restoring cholesterol homeostasis (3). Because of its role in controlling cholesterol synthesis, S1P has been considered a drug target for treating hypercholesterolemia.

Proteolytic activation of SREBPs provides the first example of a signal transduction pathway called regulated intramembrane proteolysis (4). In addition to SREBPs, S1P and S2P also catalyze regulated intramembrane proteolysis of other mammalian transcription factors in diverse conditions. These proteins include activating transcription factor 6 (ATF6), cAMP response element-binding protein 3-like 1 (CREB3L1, also called OASIS), and CREB3L2 (also called BFB2H7). ATF6 is sequentially cleaved by S1P and S2P in cells in which unfolded proteins accumulate in the ER (5). After cleavage, the amino-terminal domain activates the transcription of genes encoding chaperones that assist the folding of ER proteins, thereby allowing cells to survive ER stress. CREB3L1 and CREB3L2 are involved in bone development. The former

Department of Molecular Genetics, University of Texas Southwestern Medical Center, Dallas, TX 75390, USA.
E-mail: jin.ye@utsouthwestern.edu

S1P cleavage (mammalian proteins)	SREBP	ATF6	CREB3L1	CREB3L2	S1P	GlcNAc-1- phospho- transferase precursor
Regulator of cleavage	Cholesterol	ER stress	ER stress; osteoblast differentiation	ER stress; chondrocyte differentiation	Constitutive	Constitutive
S2P cleavage	Yes	Yes	Yes	Yes	No	?
Consequences	Cholesterol biosynthesis	ER chaperone synthesis	Collagen synthesis	Increased secretion capacity	S1P activation	Mature enzyme
Sites of cleavage						

Mammalian membrane proteins cleaved by S1P. The cleaved functional fragments are highlighted in red. Proteins are not drawn to scale.

is predominately expressed in osteoblasts, and during osteoblast differentiation, it is cleaved by S1P and S2P. The cleaved amino-terminal fragment drives the expression of a gene encoding collagen, a major constituent of bone (6). CREB3L2 is expressed most abundantly in the proliferating zone of cartilage in developing long bones. During chondrocyte differentiation, CREB3L2 is cleaved by S1P and S2P, whereupon it activates transcription of *Sec23a* to increase the secretory capacity of the cells (7).

There are also proteins cleaved only by S1P but not S2P. This was first recognized in S1P itself. The protease self-activates by cleaving away the amino-terminal propeptide that inhibits its activity (8). Marschner *et al.* report a new function of S1P in processing an α/β -subunit precursor of GlcNAc-1-phosphotransferase into a mature form of the enzyme. The phosphotransferase catalyzes an essential step in the addition of mannose 6-phosphate groups onto lysosomal hydrolases. This modification serves as a signal that targets many lysosomal enzymes to the organelle. In cells deficient in S1P, lysosomal enzymes are incorrectly sorted. This phenotype was also observed in cells obtained from patients of a lysosomal storage disorder

called mucopolipidosis II (also called I-cell disease) that contain mutations in GlcNAc-1-phosphotransferase. The authors show that S1P is essential for lysosomal enzyme sorting. However, the study does not address whether the α/β -subunit precursor is a direct target of S1P or whether lack of the cleavage in S1P-deficient cells is an indirect consequence of disruption in regulated intramembrane proteolysis. This question can be studied in cells deficient in S2P. If cleavage of the α/β -subunit precursor is unrelated to regulated intramembrane proteolysis, this cleavage and lysosomal function should not be affected in cells lacking S2P.

Unlike the clear results from S1P-deficient cultured mammalian cells, a requirement for S1P in the biogenesis of lysosomes in vivo remains to be demonstrated. No obvious defect in lysosomes was reported in mice in which the gene encoding S1P was conditionally inactivated in the liver (9). For example, these mice did not accumulate cholesterol in liver as observed in mice lacking the Niemann Pick disease type C2 protein (10), which is targeted to lysosomes by mannose 6-phosphate. However, S1P in these mice was conditionally inactivated for 14 days, which may not be

long enough to produce the lysosomal phenotype.

Marschner *et al.* also observed that chondrocyte morphogenesis was severely disrupted in mice in which the α/β -subunit precursor of GlcNAc-1-phosphotransferase was inactivated. A similar phenotype was observed in mice lacking S1P expression specifically in cartilage (11), supporting the hypothesis that S1P is essential for processing the phosphotransferase in vivo. However, a similar phenotype was also observed in mice deficient in CREB3L2, a substrate for S1P (7). Thus, it remains unclear whether lysosomal dysfunction is responsible for the phenotype observed in cartilage-specific S1P-deficient mice.

In addition to consideration as a treatment for hypercholesterolemia, S1P inhibition has been explored as a method for treating infection by certain viruses whose life cycle depends on the protease. S1P cleaves protein precursors of Lassa virus and Crimean-

Congo hemorrhagic fever virus to produce mature viral surface glycoproteins that are required for viral infection (12, 13). Given the findings of Marschner *et al.*, before further explorations into S1P inhibition-based therapies, it will be important to determine whether S1P inhibition will disrupt lysosomal function in vivo, thereby producing unacceptable toxicity.

References

1. K. Marschner, K. Kollmann, M. Schweizer, T. Bräulke, S. Pohl, *Science* **333**, 87 (2011).
2. J. Sakai *et al.*, *Mol. Cell* **2**, 505 (1998).
3. M. S. Brown, J. L. Goldstein, *Proc. Natl. Acad. Sci. U.S.A.* **96**, 11041 (1999).
4. M. S. Brown, J. Ye, R. B. Rawson, J. L. Goldstein, *Cell* **100**, 391 (2000).
5. J. Ye *et al.*, *Mol. Cell* **6**, 1355 (2000).
6. T. Murakami *et al.*, *Nat. Cell Biol.* **11**, 1205 (2009).
7. A. Saito *et al.*, *Nat. Cell Biol.* **11**, 1197 (2009).
8. P. J. Espenshade, D. Cheng, J. L. Goldstein, M. S. Brown, *J. Biol. Chem.* **274**, 22795 (1999).
9. J. Yang *et al.*, *Proc. Natl. Acad. Sci. U.S.A.* **98**, 13607 (2001).
10. D. E. Sleat *et al.*, *Proc. Natl. Acad. Sci. U.S.A.* **101**, 5886 (2004).
11. D. Patra *et al.*, *J. Cell Biol.* **179**, 687 (2007).
12. O. Lenz, J. ter Meulen, H. D. Klenk, N. G. Seidath, W. Garten, *Proc. Natl. Acad. Sci. U.S.A.* **98**, 12701 (2001).
13. M. J. Vincent *et al.*, *J. Virol.* **77**, 8640 (2003).

A Biological Screw in a Beetle's Leg

Thomas van de Kamp,^{1,2,3} Patrik Vagovič,¹ Tilo Baumbach,¹ Alexander Riedel^{2*}

In many animals, movement relies on joints between skeletal features, analogous to joints between moving parts of mechanical machines. Some, such as ball-and-socket joints, are readily found in both living organism and mechanical engineering (1), whereas others are restricted to one of these realms. We report the finding of a functional screw-and-nut system in the coxa-trochanteral joints of the legs of the Papuan weevil *Trigonopterus oblongus* (Pascos) (2). We reveal the system's structure and function through interactive three-dimensional (3D) reconstructions created from synchrotron-based x-ray microtomography (μ CT) (3) of museum specimens. These reconstructions allow the simulation of movements in this articulation (Fig. 1 and figs. S3 to S5).

The three major joints of an insect leg, the coxa-trochanteral, trochantero-femoral and femoro-tibial articulations, are usually considered as hinges (4). However, in the species of hyperdiverse *Trigonopterus* weevils studied here, the coxa-trochanteral joint is highly modified and allows rotational movement combined with a single-axis translation.

The pro- and mesocoxae of *T. oblongus* are subspherical in shape, the metacoxae bulging somewhat forward. Their apical opening (fig. S1, A and B) is wide and circular and mesially shows a notch marking the start of a well-defined inner thread that continues internally for 345°. Thus, the apical portions of the coxae closely resemble engineered screw nuts. The trochanters (fig. S1, C and D) of all of the weevil's legs are similar, carry external spiral threads that cover 410°, and are perfectly compatible with the threads in the respective coxal openings. Proximally, each trochanter is produced into a thorn that spears the entire coxa; when the hind leg is depressed, the thorn's tip penetrates the opposite coxal wall through a small opening, thus stabilizing the joint along the rotational axis and securing it against jamming.

Three muscles attach to the trochanter between the screw thread and the proximal thorn. The composition of muscles (fig. S2) conforms with that previously described for weevils and most other polyphagan beetles (5). Outward rotation is accomplished by a muscle that originates at the coxal wall and attaches directly to the trochanter; inward rotation is by two muscles attaching to the trochanter via a tendon, one originating from the coxal wall, the other from

an apophysis differing between the fore, mid, and hind legs. The maximum rotation achieved by the muscles is 90° (protrochanter) and 130° (meso- and metatrochanter), respectively. The rotational axes of the trochanters are positioned at approximate right angles to the femoral axes. The overall translation along the axes of rotation ranges from 31.5 μ m (0.35 μ m/°) to 65.0 μ m (0.50 μ m/°). The diameter of the threaded part of the trochanter decreases toward its proximal end.

Our preliminary microscopic examination of other weevil genera [listed in (6)] showed similarities with the coxa-trochanteral joint as revealed here for *Trigonopterus*. The screw-and-nut system appears to be widespread among weevils and may indeed represent a basic character of the family. In other families of beetles, coxa-trochanteral joints that perform a rotation accompanied by a translatory movement along the axis have been observed in Scarabaeoidea (7) and Chrysomelidae (3, 8). However, their constructions [supporting online material (SOM) text] are markedly different. A continuous screw thread is either absent (in Scarabaeoidea) or incomplete (a "spiral ridge of trochanter" covers 210° and the inner thread of the coxa 180° in the chrysomelid genus *Cryptocephalus*); instead, a process of the coxa is interlocked with a pit in the trochanter. This mechanism, securing the joint, has disappeared in the weevils examined.

It is remarkable that in the case of the weevil leg a rotary movement is accomplished by a screw-and-nut system. In engineering, such systems are mainly used for fixing connections, whereas an axle would be used for a simple rotation. The possible advantages and disadvantages of a screw-and-nut system over an axle in a leg joint may be most apparent at its end points. In ventral position, when fully tightened, the joint comes to a dead stop.

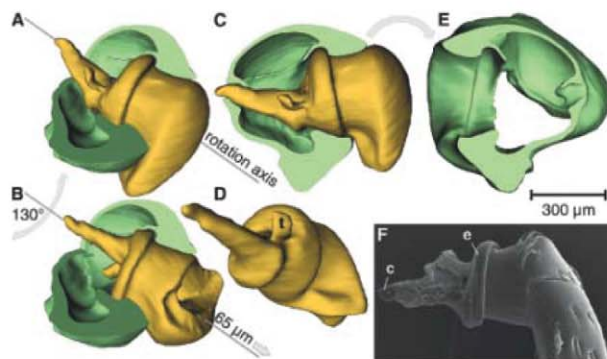


Fig. 1. The 3D reconstruction [(A) to (E)] of coxa (green) and trochanter (yellow) of left hind leg of *T. oblongus*. (A) Depressed position. (B) Elevated position. (C) Coxa cut horizontally along rotation axis; dorsal aspect of trochanter while leg depressed. (D). Isolated trochanter showing external spiral thread and tendon (t). (E) Dorsal portion of coxa corresponding to ventral portion of (C). (F) Scanning electron microscope photograph of the right metatrochanter showing posterior condyle (c) and external spiral thread (e).

One possible disadvantage, the danger of overwinding the thread, then is negligible, because the depressor muscles are already fully contracted at that point. We suggest that an advantage of this construction is that the leg comes to a stable resting position, preventing passive straining of leg muscles, which would not be accomplished by an axle construction. If the weevil's leg is pulled in the opposite direction over its back, the muscles are torn off, and the trochanter can be neatly dislodged from the coxal nut. Such dislocation can be produced with the help of delicate forceps. Under natural circumstances, this is a highly unlikely event, because the beetle's natural defensive reflex is to bring the legs into a ventral position if attacked by a predator.

The presumably primitive coxa-trochanteral joint in ground beetles (Carabidae) possesses a symmetrical pair of condyles and works as a hinge. In Chrysomeloidea and in Curculionoidea, one condyle is reduced (in the foreleg, the posterior condyle; in the mid and hind legs, the anterior condyle) and the other is produced into a thorn. These joints possess a greater dorsoventral mobility, which is better suited for a life on twigs and foliage. Many weevil species depend on tibial spines to provide strong foothold while the rostrum is pushed into the substrate. Possibly, the forces acting on the leg joints during this feeding process unique to weevils have driven the transformation from the chrysomeloid joint type to the more robust one in weevils.

References and Notes

- G. Bögelsack *et al.*, *Theory Biosci.* **119**, 104 (2000).
- A. Riedel, D. Daawia, M. Balke, *Zool. Scr.* **39**, 63 (2010).
- O. Betz *et al.*, *J. Microsc.* **227**, 51 (2007).
- L. Frantsevich, W. Wang, *Arthropod Struct. Dev.* **38**, 16 (2009).
- O. Larsén, *Opusc. Entomol.* **30** (suppl.), 1 (1966).
- Materials and methods are available as supporting material on Science Online.
- F. Reuleaux, in *Lehrbuch der Kinematik*, F. Reuleaux, Ed. (Friedrich Vieweg und Sohn, Braunschweig, Germany, 1900), vol. 2, pp. 723–777.
- M. L. Chamorro-Lacayo, A. S. Konstantinov, *Zootaxa* **676**, 1 (2004).

Acknowledgments: We are grateful to F. Glaw encouraging us to prepare the initial manuscript, to S. Scharf for performing the segmentation of μ CT scans, and to D. Pelliccia for his assistance during the scans. M. Balke, O. Betz, and M. Spies kindly revised earlier drafts. The specimens examined are deposited at SMNK. The image data are stored at www.morphdbase.de?A_Riedel_20110523-M-4.1. This work was supported by grant RI 1817/3-1 from the German Research Foundation.

Supporting Online Material

www.sciencemag.org/cgi/content/full/333/6038/52/DC1

Materials and Methods

SOM Text

Figs. S1 to S5

References

14 February 2011; accepted 13 May 2011

10.1126/science.1204245

¹ANKA - Institute for Synchrotron Radiation, Karlsruhe Institute of Technology, D-76344 Eggenstein-Leopoldshafen, Germany.

²State Museum of Natural History (SMNK), D-76133 Karlsruhe, Germany. ³Institute for Zoology II, Heinrich Heine University, D-40225 Düsseldorf, Germany.

*To whom correspondence should be addressed. E-mail: riedel@smnk.de

Widespread RNA and DNA Sequence Differences in the Human Transcriptome

Mingyao Li,^{1*} Isabel X. Wang,^{2*} Yun Li,^{3,4} Alan Bruzel,² Allison L. Richards,⁵ Jonathan M. Toung,⁶ Vivian G. Cheung^{2,7,8†}

The transmission of information from DNA to RNA is a critical process. We compared RNA sequences from human B cells of 27 individuals to the corresponding DNA sequences from the same individuals and uncovered more than 10,000 exonic sites where the RNA sequences do not match that of the DNA. All 12 possible categories of discordances were observed. These differences were nonrandom as many sites were found in multiple individuals and in different cell types, including primary skin cells and brain tissues. Using mass spectrometry, we detected peptides that are translated from the discordant RNA sequences and thus do not correspond exactly to the DNA sequences. These widespread RNA-DNA differences in the human transcriptome provide a yet unexplored aspect of genome variation.

DNA carries genetic information that is passed onto mRNA and proteins that perform cellular functions, and it is assumed that the sequence of mRNA reflects that of the DNA. This assumed precision is important because mRNA serves as the template for protein synthesis. Hence, genetic studies have mostly focused on DNA sequence polymorphism as the basis of individual differences in disease susceptibility. Studies of mRNA and proteins analyze their expression and not sequence differences among individuals.

There are, however, known exceptions to the one-to-one relationship between DNA and mRNA sequences. These include errors in transcription (1, 2) and RNA-DNA differences that result from RNA editing (3–7). Errors are rare because proof-reading and repair mechanisms ensure the fidelity of transcription (8–10). RNA editing is carried out by enzymes that target mRNA posttranscriptionally: ADARs (adenosine deaminases that act on RNA) that deaminate adenosine to inosine, which is then recognized by the translation machineries as a guanosine (A-to-G), and APOBECs (apolipoprotein B mRNA editing enzymes, cat-

alytic polypeptide-like), which edit cytidine to uridine (C-to-U). Previously, sequence comparisons and computational predictions have identified many A-to-G editing sites (6, 7, 11–13). By contrast, C-to-U changes are rare; apolipoprotein B is one of the few known target genes of human APOBEC1 (14, 15).

We obtained sequences of DNA and RNA samples from immortalized B cells of 27 unrelated Centre d'Etude du Polymorphisme Humain (CEPH) (16) individuals, who are part of the International HapMap (17, 18) and the 1000 Genomes (19) projects. When we compared the DNA and RNA sequences of the same individuals, we found 28,766 events at over 10,000 exonic sites that differ between the RNA and the corresponding DNA sequences. Each of these differences was observed in at least two individuals; many of these were seen in B cells, as well as in primary skin cells and brain tissues from a separate set of individuals and in expressed sequence tags (ESTs) from cDNA libraries of various cell types. About 43% of the differences are transversions and therefore cannot be the result of typical deaminase-mediated RNA editing. By mass spectrometry, we also found peptide sequences that correspond to the RNA variant sequences, but not the DNA sequences, suggesting that the RNA forms are translated into proteins.

Samples. We compared the DNA and RNA sequences from B cells of 27 unrelated CEPH individuals (table S1). We chose these samples because much information is available on them, including dense DNA genotypes obtained using different technologies (20, 21). The genomes of B cells from the CEPH collection are stable as evidenced by Mendelian inheritance of genetic loci that allowed the construction of microsatellite- to single-nucleotide polymorphism (SNP)-based human genetic maps (20, 21). More recently, the International HapMap Consortium (17, 18) obtained millions of SNP genotypes, and the 1000

Genomes Project (19) sequenced the DNA of these individuals. Comparison of sequence data from these two projects showed high concordance (~99%). Here, we used the DNA genotypes and sequences from the two projects for our analyses. First, we considered sites that are monomorphic in the human genome. A monomorphic site is one where there is no evidence for sequence variation at that locus in dbSNP, the HapMap, and the 1000 Genomes Project. Different studies have analyzed these 27 and hundreds of additional individuals for DNA variants; thus, if a site has not been identified as polymorphic, most likely all individuals have the same sequences at these sites. But to be certain, for these sites in the 27 individuals, we compared their DNA sequences from the 1000 Genomes Project with the sequences of the human reference genome and carried out traditional Sanger sequencing (22). To be included in our analysis, we required that each site be covered by at least four reads in the 1000 Genomes Project and that the sequences from 1000 Genomes should be the same as those of the reference genome. To ensure the integrity of the aliquots of B cells that we used for analyses, we carried out Sanger sequencing of their DNA and found perfect concordance of sequences with data from the 1000 Genomes (thus also the reference genome sequences) (table S2). Second, we considered SNPs. For each individual, a SNP locus was included only if it was homozygous and the HapMap, as well as the 1000 Genomes Project, reported the same sequence. We have high confidence in those sequences because despite using different technologies (microarray-based genotyping in HapMap and high-throughput sequencing in 1000 Genomes), we obtained identical sequences in the two projects.

We sequenced the RNA of B cells from the same 27 individuals using high-throughput sequencing technology from Illumina (23). The resulting RNA sequence reads were mapped to the Gencode genes (24) in the reference human genome. In total, we generated ~1.1 billion reads of 50 base pairs (bp) (~41 million reads and 2 Gb of sequence per individual), of which ~69% of the reads mapped uniquely to the transcriptome [see Methods in (25)]. To be confident of the base calls, for each individual, we focused our analysis on high-quality reads (quality score ≥25) and sites that were covered by at least 10 uniquely mapped reads. Another study (26) had carried out RNA sequencing of the same individuals but at a lower coverage; at these sites we compared our sequences with those from their study, and found that the concordance rate of the sequences is >99.5%. This is reassuring given that the samples were prepared and sequenced in different laboratories.

Differences between RNA and corresponding DNA sequences. For each of the 27 individuals, we compared the mRNA sequences from B cells with the corresponding DNA sequences (fig. S1). The comparison revealed many sites where the

¹Departments of Biostatistics and Epidemiology, University of Pennsylvania School of Medicine, Philadelphia, PA 19104, USA. ²Howard Hughes Medical Institute, Chevy Chase, MD 20815, USA. ³Department of Genetics, University of North Carolina School of Medicine, Chapel Hill, NC 27599, USA. ⁴Department of Biostatistics, University of North Carolina School of Medicine, Chapel Hill, NC 27599, USA. ⁵Cell and Molecular Biology Graduate Program, University of Pennsylvania School of Medicine, Philadelphia, PA 19104, USA. ⁶Genomics and Computational Biology Graduate Program, University of Pennsylvania School of Medicine, Philadelphia, PA 19104, USA. ⁷Department of Genetics, University of Pennsylvania School of Medicine, Philadelphia, PA 19104, USA. ⁸Department of Pediatrics, University of Pennsylvania School of Medicine, Philadelphia, PA 19104, USA.

*These authors contributed equally to this work.

†To whom correspondence should be addressed. E-mail: vcheung@mail.med.upenn.edu

mRNA sequences differ from the corresponding DNA sequences of the same individual. To ensure that these are actual differences and to minimize the chance of sequencing errors, we required that at least 10% of the reads covering a site differ from the DNA sequence and at least two individuals show the same RNA-DNA difference at the site. We call each occurrence of a difference between RNA and DNA sequences an “event” and the chromosomal location where such a difference occurs a “site.” Each person can contribute an event to the site; thus, there could be multiple events at a site.

Among our 27 subjects, we identified 28,766 events where the RNA sequences do not match those of the corresponding DNA sequences. These events are found in 10,210 exonic sites (table S10) in the human genome and reside in 4741 known genes [36% of 13,214 genes that are covered by

10 or more RNA sequencing (RNA-Seq) reads in at least one part of the gene, in two or more individuals]. With gene orientation information in Gencode, we observed all 12 possible categories of base differences between RNA and its corresponding DNA (Fig. 1A). All 12 types of differences were found in each of the 27 samples; the relative proportion of each type is similar across individuals. There are 6698 A-to-G events, which can be the result of deamination by ADAR. There are 1220 C-to-T differences, which can also be mediated by a deaminase. However, it is notable that APOBEC1 and its complementation factor AICF that deaminate cytidine are not expressed in our B cells [fragments per kilobase of exon per million fragments mapped (FPKM) (27) ~ 0 for both genes]; thus, it is likely that an unknown deaminase or other mechanism is involved. Even for relatively well-characterized proteins such as

APOBEC1, a recent RNA-Seq study of *Apobec1*^{−/−} mice uncovered many previously unknown targets (28). In addition, we found 12,507 transversions (43%), which cannot result from classic deaminase-mediated editing. Because we do not know the mechanism by which these differences between RNA and DNA sequences arise, we refer to them as RNA-DNA differences (RDD). An example of an RDD is a C-to-A difference on chromosome 12 (at position 54,841,626 bp) in the myosin light chain gene *MYL6*, where 16 of our subjects have C/C in their DNA but A/C in their RNA sequences. Another example is an A-to-C difference on chromosome 6 (at position 44,328,823 bp) in the gene *HSP90AB1* that encodes a heat shock protein, where eight individuals have homozygous A/A DNA genotype but have A/C in their RNA. Additional examples are shown in Table 1. These sites where RNA

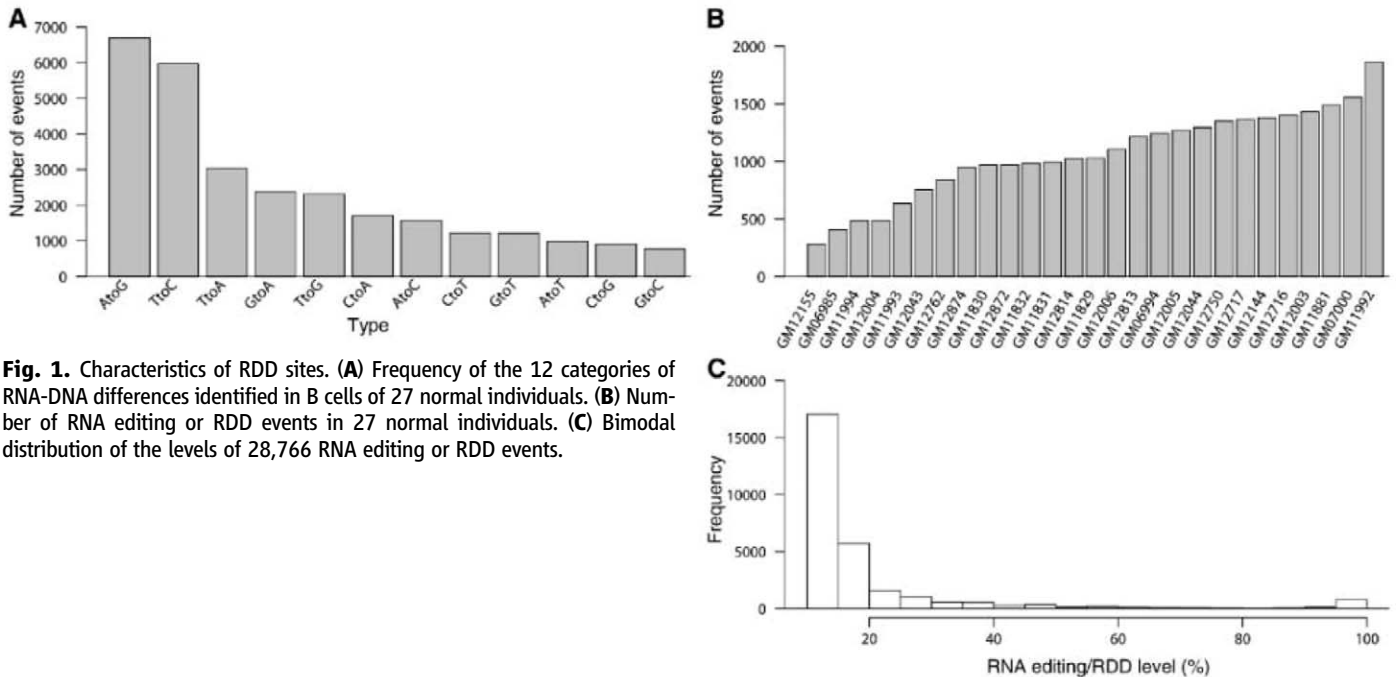


Fig. 1. Characteristics of RDD sites. **(A)** Frequency of the 12 categories of RNA-DNA differences identified in B cells of 27 normal individuals. **(B)** Number of RNA editing or RDD events in 27 normal individuals. **(C)** Bimodal distribution of the levels of 28,766 RNA editing or RDD events.

Table 1. Selected examples of sites that show RNA-DNA differences in B cells and EST clones.

Gene	Chr.	Position (bp)*	Type	No. of informative individuals†‡	No. of individuals with RDD‡	Average level§ [range]	EST
<i>HSP90AB1</i>	6	44,328,823	A-to-C	11	8	0.39 [0.15, 0.79]	BQ355193 (head, neck), BX413896 (B cell)
<i>AZIN1</i>	8	103,910,812	A-to-G	17	10	0.22 [0.12, 0.37]	CD359333 (testis), BF475970 (prostate)
<i>CNBP</i>	3	130,372,812	A-to-T	18	16	0.13 [0.10, 0.21]	EL955109 (eye), BJ995106 (hepatoblastoma)
<i>MYL6</i>	12	54,841,626	C-to-A	16	16	0.35 [0.12, 0.60]	EC496428 (prostate), BG030232 (breast adenocarcinoma)
<i>RBM23</i>	14	22,440,217	C-to-G	11	5	0.18 [0.11, 0.35]	BQ232763 (testis, embryonic)
<i>RPL23</i>	17	34,263,515	C-to-T	12	8	0.16 [0.10, 0.22]	BP206252 (smooth muscle), CK128791 (embryonic stem cell)
<i>BLNK</i>	10	97,957,645	G-to-A	14	7	0.14 [0.11, 0.17]	BF972964 (leiomyosarcoma), BE881159 (lung carcinoma)
<i>C17orf70</i>	17	77,117,583	G-to-C	2	2	0.26 [0.24, 0.28]	AA625546 (melanocyte), AA564879 (prostate)
<i>HMG2</i>	1	26,674,349	G-to-T	7	4	0.22 [0.14, 0.43]	BX388386 (neuroblastoma), BE091398 (breast)
<i>CANX</i>	5	179,090,533	T-to-A	9	8	0.20 [0.13, 0.30]	EL950052, DB558106
<i>EIF3K</i>	19	43,819,430	T-to-C	19	14	0.16 [0.10, 0.27]	AI250201 (ovarian carcinoma), AI345393 (lung carcinoma)
<i>RPL37</i>	5	40,871,072	T-to-G	6	6	0.27 [0.16, 0.45]	CF124792 (T cell), DW459229 (liver)

*hg18 build of the human genome. †RNA-Seq ≥ 10 reads, DNA-Seq ≥ 4 reads. ‡B cells. §Calculated by tallying RNA-Seq reads that contain RDDs and those that do not.

sequences differ from the corresponding DNA sequences appear to be nonrandom because the identical differences were found in multiple individuals: 8163 (80.0%) of the sites were found in at least 50% of the informative individuals (i.e. with RNA-Seq coverage ≥ 10 and DNA-Seq coverage ≥ 4 at the site). Some sites were found in all or nearly all informative individuals. For example, the DNA sequences of all 19 informative individuals at position 49,369,615 bp of chromosome 3 in the *GPXI* gene are G/G, whereas their RNA sequences are G/A. (The remaining individuals were not included because available data did not meet our inclusion criteria although the data suggest the same RDD in all remaining individuals: G/G in DNA, and G/A in RNA.)

RDD in expressed sequence tags. Computational and experimental validations also upheld

these observed RNA-DNA differences. First, for 120 sites (10 sites per RDD type; randomly selected and all examples cited in this paper; see Table 1 and table S3), we looked for evidence of RDD in the human EST database by BLAST alignment (29) and manual inspection of each result. For 81 of the 120 sites, we found EST clones that contain the RDD alleles. The numbers of sites found in human ESTs are similar across different RDD types (average 67.5%; range: 60 to 90%). Second, we examined previously identified A-to-G editing sites (6). Fourteen of the A-to-G sites that we identified were found in their data even though different cell types were studied. Even the levels of editing at these sites are similar between the two studies (fig. S2). Twelve additional sites were found in both studies but were filtered out because they did not meet our selection criteria.

Sanger sequencing of B cells, skin, and brain.

Next, we validated our findings experimentally by Sanger sequencing of both DNA and RNA at 12 randomly selected sites in B cells (2 to 9 individuals per site), primary skin (foreskin; 8 to 10 individuals per site), and brain cortex (6 to 10 individuals per site). We regrew the B cells from our subjects and extracted DNA and mRNA from the same aliquots of cells. By sequencing the paired DNA and RNA samples and analysis of each chromatogram by two individuals independently, we confirmed 57 events in 11 sites (Table 2 and fig. S3). In *EIF2AK2*, in all of the eight individuals whose samples were sequenced, three sites were found within 10 nucleotides (nt) (see below). RDD was not found in one site in *NDUFC2*. Sanger sequencing is not very sensitive or quantitative; thus, we do

Table 2. Sanger sequencing of RDD sites.

Gene	Chr.	Position (bp)*	Type	Location	Amino acid change	B cell†		Primary skin fibroblast†		Brain (cortex)†	
						No. of informative individuals	No. of individuals showing RDD	No. of informative individuals	No. of individuals showing RDD	No. of informative individuals	No. of individuals showing RDD
<i>EIF2AK2</i>	2	37,181,512	A-to-G	3' UTR	Not applicable	8	8	8	0	10	10
	2	37,181,517	A-to-G	3' UTR	Not applicable	8	8	8	3	10	10
	2	37,181,520	A-to-G	3' UTR	Not applicable	8	8	8	3	10	10
	2	37,181,538	A-to-G	3' UTR	Not applicable	8	8	8	6	10	10
<i>AZIN1‡</i>	8	103,910,812	A-to-G	Coding, exonic	S to G	2	2	10	0	9	8
<i>DPP7</i>	9	139,128,755	C-to-T	Coding, exonic	Synonymous (P)	9	2	8	1	10	0
<i>PPWD1</i>	5	64,894,960	G-to-A	Coding, exonic	E to K	2	2	8	8	8	8
<i>HLA-DQB2</i>	6	32,833,537	G-to-A	Coding exonic	G to S	2	2	10	10	NE§	NE
	6	32,833,545	G-to-A	Coding, exonic	R to H	2	2	10	10	NE	NE
	6	32,833,550	C-to-T	Coding, exonic	Synonymous (I)	2	2	10	10	NE	NE
<i>BLCAP#</i>	20	35,580,977	A-to-G	Coding, exonic	Q to R	6	4	10	4	6	6
<i>NDUFC2</i>	11	77,468,303	C-to-G	Coding, exonic	L to V	10	0	10	0	10	0

*hg18 build of the human genome. †In all cases, matched DNA and RNA samples from the same individuals were sequenced. ‡Also reported by Li *et al.* (6). §NE, not expressed. #Known site that we used as a positive control.

Table 3. Peptides encoded by both DNA and RNA forms of mRNA at RDD sites.

Protein	Position (bp)*	RDD	Amino acid change	DNA form†	RNA form†
AP2A2	Chr 11: 976,858	T-to-G	Y-to-D	<u>Y</u> LALES <u>M</u> CTLASSEFSHEAVK	<u>D</u> LALES <u>M</u> CTLASSEFSHEAVK
DFNA5‡	Chr 7: 24,705,225	T-to-A	L-to-Q	<u>V</u> FPLL <u>C</u> ITLNGLCALGR	<u>V</u> FPLL <u>C</u> ITLNGLCALGR
ENO1	Chr 1: 8,848,125	T-to-C	L-to-P	<u>E</u> GLELLK	<u>E</u> GPELLK
ENO3	Chr 17: 4,800,624	T-to-G	V-to-G	<u>L</u> AQSN <u>G</u> WGVMSVSHR	<u>L</u> AQSN <u>G</u> WGVMSVSHR
FABP3	Chr 1: 31,618,424	T-to-A	W-to-R	<u>M</u> VDAFL <u>G</u> TWK	<u>M</u> VDAFL <u>G</u> TR
FH‡	Chr 1: 239,747,217	T-to-A	I-to-K	<u>I</u> EYDT <u>F</u> GELK	<u>K</u> EYDT <u>F</u> GELK
HMGB1	Chr 13: 29,935,772	T-to-A	Y-to-N	<u>M</u> SSYA <u>F</u> VFQTCR	<u>M</u> SSNA <u>F</u> VFQTCR
NACA	Chr 12: 55,392,932	G-to-A	D-to-N	<u>D</u> IELV <u>M</u> SQANVSR	<u>N</u> IELV <u>M</u> SQANVSR
NSF	Chr 17: 42,161,411	T-to-C	V-to-A	<u>L</u> LDYV <u>P</u> IGPR	<u>L</u> LDYA <u>P</u> IGPR
POLR2B	Chr 4: 57,567,852	T-to-A	L-to-Q	<u>I</u> ISD <u>G</u> LK	<u>I</u> ISD <u>G</u> QK
RAD50‡	Chr 5: 131,979,610	T-to-G	L-to-R	<u>W</u> LQDN <u>L</u> TLR	<u>W</u> RQDN <u>L</u> TLR
RPL12	Chr 9: 129,250,509	A-to-G	N-to-D	<u>H</u> SGN <u>I</u> TFDEIVNIAR	<u>H</u> SGD <u>I</u> TFDEIVNIAR
RPL32‡	Chr 3: 12,852,658	G-to-T	A-to-S	<u>A</u> AQLA <u>I</u> R	<u>S</u> AQLA <u>I</u> R
RPS3AP47‡	Chr 4: 152,243,651	C-to-A	T-to-K	<u>E</u> VQT <u>N</u> DLK	<u>E</u> VQK <u>N</u> DLK
SLC25A17	Chr 22: 39,520,485	A-to-G	E-to-G	<u>T</u> THM <u>V</u> LL <u>E</u> IK	<u>T</u> THM <u>V</u> LL <u>G</u> IK
TUBA1‡	Chr 2: 219,823,379	A-to-G	E-to-G	<u>E</u> DMAA <u>L</u> EK	<u>E</u> DMAA <u>L</u> GK
TUBB2C	Chr 9: 139,257,297	G-to-A	G-to-D	<u>L</u> HFFMP <u>G</u> FAPLTSR	<u>L</u> HFFMP <u>D</u> FAPLTSR

*hg 18 build of the human genome. †For each peptide, the amino acid that differs between the DNA and RNA forms are underlined. Abbreviations for the amino acid residues are as follows: A, Ala; C, Cys; D, Asp; E, Glu; F, Phe; G, Gly; H, His; I, Ile; K, Lys; L, Leu; M, Met; N, Asn; P, Pro; Q, Gln; R, Arg; S, Ser; T, Thr; V, Val; W, Trp; and Y, Tyr. ‡DNA sequences of these and other proteins were verified by Sanger sequencing (table S2).

not expect to validate all sites, especially those with low levels of RDD.

To assess whether RDD shows cell type specificity, we looked for evidence of RNA-DNA sequence differences using primary human cells. We studied the same sites as above by Sanger sequencing of DNA and RNA samples from primary skin fibroblasts and brain (cortex) of a separate set of normal individuals (for each site, we examined the DNA and RNA of 6 to 10 samples per cell type). We identified 55 RDD events in primary skin cells and 62 events in brain cortex (Table 2). The results suggest that most sites are shared across cell types (Table 2), although there are exceptions, for example, an A-to-G difference in *EIF2AK2* (chromosome 2: 37,181,512), which was only found in B cells and brain cortex but not in primary skin cells. We also queried the EST database for evidence of RDD (Table 1 and table S3). The RNA alleles are seen in a wide range of tissues from embryonic stem cells to brain and testis; they are also found in tumors such as lung carcinoma and neuroblastoma.

Proteomic evidence for RDD. Validation at the sequence level is important but does not address concerns such as the difficulty in aligning sequences that are highly similar and errors introduced by enzymes in reverse transcription steps. We believe that such artifacts are unlikely considering the consistent patterns across sequencing methods and that we observed all 12 types of nucleotide differences. An alternative and independent validation would be to ask whether the RNA variants in RDD sites are translated to proteins. To do so, first we searched mass spectrometry data from human ovarian cancer cells (30) and leukemic cells for putative RDD sites. Because the levels of most RDDs are less than 100%, both DNA and the RDD forms of the mRNAs should be available to be translated (hereafter, we refer to mRNAs that correspond identically to the DNA sequences as DNA forms and those that contain an RDD as RNA forms). In the ovarian cancer and leukemic cells, we indeed found examples of proteins with peptides encoded by both DNA and RNA forms of mRNA (table S4). Encouraged by the search results and cognizant of possible genome instability and thus DNA mutations in cancer cells, we carried out mass spectrometry analysis of our B cells.

We analyzed the proteome of our B cells using liquid chromatography–tandem mass spectrometry and detected peptides for 3217 proteins. Despite advances in mass spectrometry, far less than 50% of peptides can be detected in most studies (31, 32). We identified 327 peptides that cover RDD sites: 299 of them are encoded by the DNA forms and 28 by RNA forms of RDD-containing mRNAs [false discovery rate (FDR) <1%; tables S5 and S9]. For 17 RDD sites, peptides that correspond to both DNA and RNA forms were identified (Table 3). By BLAST alignment, we ensured that these 28 peptides were unique to the genes that contain the RDD sites. In

addition, we sequenced the DNA of the B cells used for mass spectrometry and validated that the DNA sequences were the same as those of the reference genome but differed from the RNA sequences and thus did not encode the RNA forms of the peptides (table S2). It is easier to detect more abundant proteins by mass spectrometry; for most RDD sites, the unaltered DNA forms are more abundant than variant RNA forms of mRNA (see below). Thus, it is not surprising to find more peptides that correspond to the DNA than to the RNA sequences. However, the counts of peptides corresponding to the DNA and RNA forms of RDD sites should not be taken as a measure of the proportions of DNA versus RNA forms of mRNA that are translated because differences in the amino acid sequences of the DNA and RNA forms of the peptides affect the ability of mass spectrometry to detect them. In addition,

when a peptide is not detected, it does not mean that it is absent from the proteome; it could be a result of sampling.

The proteomic data provide an independent validation that mRNA sequences are not always identical to DNA sequences and demonstrate that RNA forms of genes are translated to proteins. They also show that there are peptides in human cells that are not exactly encoded by the DNA sequences. An example of a protein variant that results from RDD is RPL28 (T-to-A; chromosome 19: 60,590,467). The RDD led to a loss of a stop codon. We identified peptides corresponding to the 55–amino acid extension of RPL28 protein in the ovarian cancer cells and in our B cells (Fig. 2). Previously identified cases of RNA editing leading to proteins not encoded by genomic DNA, such as apolipoprotein B (3, 4), serotonin and glutamate receptors (33–35) in

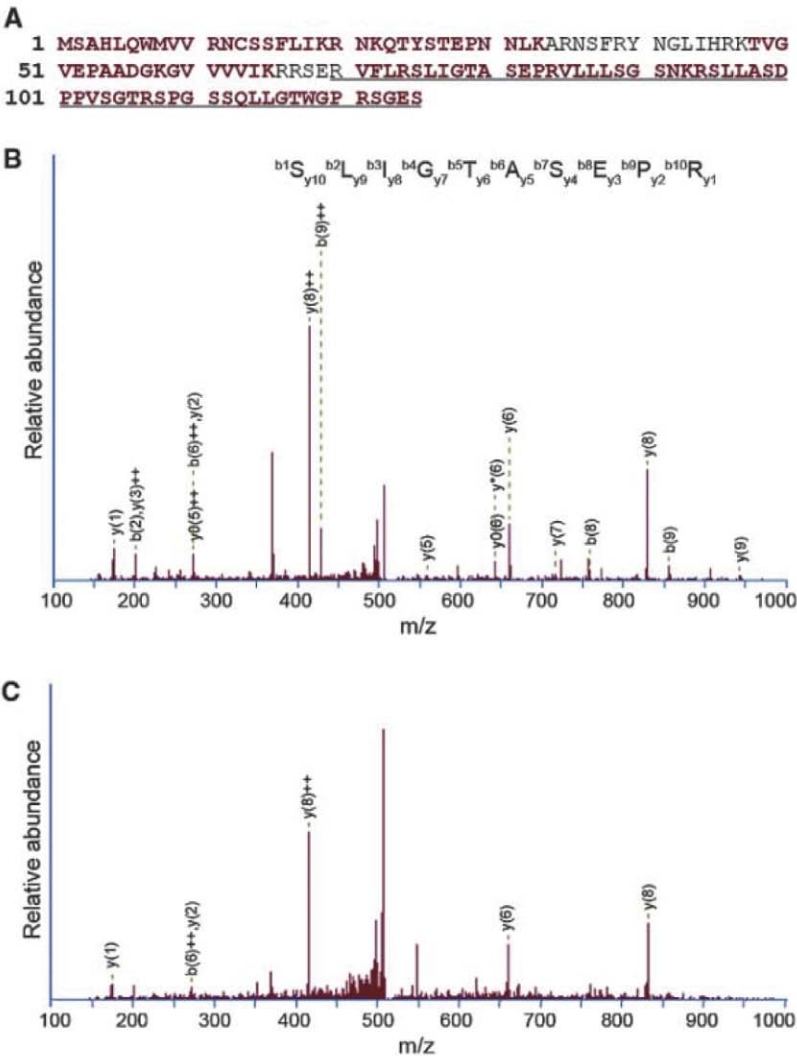


Fig. 2. Identification of peptides coded by both RNA and DNA sequences. (A) The RNA form of a RDD leads to loss of a stop codon in RPL28 and extension of 55 amino acids. Peptides detected by mass spectrometry are shown in red. Extended protein sequence due to RDD is underlined. (B and C) Tandem mass spectrometry (MS-MS) data confirm the detection of peptides encoded by the RDD-containing *RPL28* mRNA. The representative spectra of one peptide (SLIGTASEPR) from ovarian cancer cells (B) and cultured B cells (C) are shown.

humans, and plant ribosomal protein S12 (36), also support our hypothesis that RDD leads to protein isoforms that do not correspond to the DNA sequences of the encoding genes.

Individual variation in abundance of RDD.

Using our selection criteria, we found that in each person among the Gencode genes, there are on average 1065 exonic events that differ in the RNA and DNA sequences. But the number of events varied among individuals (range: 282 to 1863) by up to sixfold across our 27 subjects (Fig. 1B). The degree of sequence coverage and sequencing errors in DNA or RNA samples do not explain these individual differences (25). Thus, there is likely a biological basis for the individual variation in the number of editing and RDD events. We found no significant correlation between *ADAR* expression and the number of RDDs or the numbers of A-to-G events ($P > 0.5$). Thus, either *ADAR* expression does not affect the number of editing or RDD events, or our sample size is not sufficient to detect the correlation.

Characteristics of RDD sites. The 10,210 sites that showed RNA and DNA sequence differences are not evenly distributed across the genome: Chromosome 19 has the most sites, whereas chromosome 13 has the fewest. This pattern is observed after correction for differences in size and gene density among chromosomes. RDD sites are significantly ($P < 10^{-10}$) enriched in genes that play a role in helicase activity, and in protein and nucleotide binding (table S6).

The 10,210 sites that showed RNA and DNA sequence differences are not evenly distributed within genes. About 44% (4453 sites) of them are located in coding exons (10% were found in the last exons), 4% (386 sites) are in the 5' untranslated regions (UTRs), and 39% (3977 sites) are in the 3' UTRs (table S7; those remaining cannot be classified because of differences in gene structures across isoforms). The results suggest that

there are more sites in the 3' ends than in the 5' ends of genes; a pattern that was also observed in deamination-mediated RNA editing (28, 37). Seventy-one percent of the coding sites result in nonsynonymous amino acid changes, including 2.1% that lead to the gain or loss of a stop codon if translated into proteins. Relative to other structural features in genes, we found that 4% of RDD sites are within 2 nt of exon borders and 5% are within 30 nt of polyadenylate [poly(A)] signals (table S7). Among RDD types, the numbers of sites near splice junctions are quite similar, but the numbers near poly(A) sites are more different. C-to-A and G-to-A differences are found more often near poly(A) sites.

Sites also tended to cluster; for example, 2613 sites (26%) are within 25 bp, and 1059 sites (10%) are adjacent to each other. Statistical analysis using a runs test supports the nonrandom locations of the sites (median $P = 0.22$). We did not find obvious patterns or associations with motifs shared across the sites, except for the A-to-G and A-to-C differences that show a preference for a cytidine 5' to the adenosine, as previously observed in *ADAR*-mediated A-to-G changes (7, 35).

RDD levels. We examined the percentage of mRNAs that differ in sequence from the corresponding DNA. For each site, to determine the RDD level, we counted the number of reads with a different nucleotide from that in the corresponding DNA sequence. The distribution of the level is bimodal (Fig. 1C); the average level is 20% (median = 13%). However, for some sites, RDD was detected in nearly 100% of the RNA sequences such as the A-to-C difference in the gene that encodes an mRNA decapping enzyme, *DCP1A* (chromosome 3: 53,297,343). This level is correlated with the frequency and types of RNA-DNA differences. Sites found in more than 50% of the informative individuals tend to have higher levels of RNA editing or RDD than other sites ($P < 10^{-5}$; fig. S5). The levels also differ across individuals.

For example, at a G-to-A site in the gene *RHOT1*, which encodes a RAS protein that plays a role in mitochondrial trafficking (chromosome 17: 27,526,465), in one person, the level was 90% while in another person, it was only 18%. We identified 437 sites with 10 or more informative individuals where the individuals with the highest levels and the lowest levels differed by twofold or more (range: 2- to 8.6-fold).

Conclusions. We have uncovered thousands of exonic sites where the RNA sequences do not match those of the DNA sequences, including transitions and transversions. These findings challenge the long-standing belief that in the same individuals, DNA and RNA sequences are nearly identical. To increase the confidence in our results, we obtained the DNA, RNA, and protein sequences from different individuals and cell types using a range of technologies (fig. S1B). The samples included cell lines and primary cells from healthy individuals and tumors. We used data from public resources such as EST databases, the HapMap, and 1000 Genomes Project, as well as those that we generated with traditional Sanger sequencing, high-throughput sequencing technologies, and mass spectrometry. Table 4 shows the DNA, RNA, and peptide sequences at 15 confirmed sites, which illustrate that the RNA and peptide sequences are the same but differ from the corresponding DNA sequences. The results support our observation that in an individual, DNA and RNA sequences from the same cells are not always identical and some of the variant RNA sequences are translated into proteins. The consistent pattern of the observations suggests that the RDDs have biological significance and are not just "noise." At nearly all RDD sites, we observed only one RDD type across cell types and in different individuals. If the DNA sequence is A/A, and the RNA is A/C in one sample, in other samples, we see the same A-to-C difference, but not other types of differences. These results

Table 4. Corresponding DNA, RNA, and peptide sequences at selected sites.

RDD	Gene	Location	DNA*†	RNA†	Peptide (DNA form, LC-MS/MS)‡	Peptide (RNA form, LC-MS/MS)
T-to-G	<i>CD22</i>	Chr 19: 40,514,815	CTG	CGG	ND§	MHLGPWLLLR
T-to-A	<i>DFNA5</i>	Chr 7: 24,705,225	CTG	CAG	VFPLLCTITLNGLCALGR	VFPQLCTITLNGLCALGR
T-to-C	<i>ENO1</i>	Chr 1: 8,848,125	CTG	CCG	EGLELLK	EGPELLK
T-to-A	<i>FH</i>	Chr 1: 239,747,217	ATA	AAA	IEYDTFGELK	KEYDTFGELK
T-to-A	<i>HMGB1</i>	Chr 13: 29,935,772	TAT	AAT	MSSYAFFVQTCR	MSSNAFFVQTCR
A-to-C	<i>HMGB1</i>	Chr 13: 29,935,469	AAA	AAC	ND	TMSAKEN
A-to-C	<i>ITPR3</i>	Chr 6: 33,755,773	GAC	GCC	ND	DGVEDHSPLMYHISLVALLAACAEKG
T-to-G	<i>RAD50</i>	Chr 5: 131,979,610	CTA	CGA	WLQDNLTLR	WRQDNLTLR
G-to-T	<i>ROD1</i>	Chr 9: 114,026,264	GGA	GTA	ND	NLFIEAVCSVK
G-to-T	<i>RPL32</i>	Chr 3: 12,852,658	GCT	TCT	AAQLAIR	SAQLAIR
A-to-G	<i>RPS25P8</i>	Chr 11: 118,393,375	AAC	GAC	ND	EVPDYK
C-to-A	<i>RPS3AP47</i>	Chr 4: 152,243,651	ACA	AAA	EVQTNDLK	EVQKNDLK
G-to-T	<i>SUPT5H</i>	Chr 19: 44,655,806	CAG	CAT	ND	TPMYGSQTPLHDGSR
T-to-C	<i>TOR1AIP1</i>	Chr 1: 178,144,365	TCA	CCA	ND	QPSVLSPGYQK
A-to-G	<i>TUBA1</i>	Chr 2: 219,823,379	GAG	GGG	EDMAALEK	EDMAALGK

*DNA sequences are monomorphic according to dbSNP, 1000 Genomes, and HapMap projects; all individuals should have the reference allele. We verified this by Sanger sequencing of the B cells used for mass spectrometry. †RDD sites are underlined. ‡LC-MS/MS: liquid chromatography and tandem mass spectrometry. §ND: not detected by mass spectrometry; however, this does not mean that the peptides are absent from the B cell proteome. It is likely a result of sampling.

suggest that there are unknown aspects of transcription and/or posttranscriptional processing of RNA. These differences may now be studied along with those in other genomes and organisms such as the mitochondrial genomes of trypanosomes and chloroplasts of plants, where RNA editing and modifications are relatively common (36, 37).

The underlying mechanisms for these events are largely unknown. For most of the cases, we do not know yet whether a different base was incorporated into the RNA during transcription or if these events occur posttranscriptionally. About 23% of the sites are A-to-G differences; some of these are likely mediated by ADAR, but other, currently unknown, mechanisms can be involved. If it is a cotranscriptional process, then the signal can be in the DNA or the RNA such as secondary structures or modified nucleotides. In addition, as some of the RDDs are found near splice and poly(A) sites, it is possible that this may be a facet of systematic RNA processing steps such as splicing and cleavage (38, 39).

Our findings supplement previous studies demonstrating RNA-DNA differences in the human genome and show that these differences go beyond A-to-G transition. These findings affect our understanding of genetic variation; in addition to DNA sequence variation, we identify individual variation in RNA sequences. For monomorphic DNA sequences that show RDD, there is an overall increase in genetic variation. Thus, this variation not only contributes to individual variation in gene expression, but also diversifies the proteome because some identified sites lead to nonsynonymous amino acid changes. We speculate that this RNA sequence variation likely affects disease susceptibility and manifestations. To date, mapping studies have focused on identifying DNA variants as disease suscep-

tibility alleles. Our results suggest that the search may need to include RNA sequence variants that are not in the DNA sequences.

References and Notes

1. R. T. Libby, J. A. Gallant, *Mol. Microbiol.* **5**, 999 (1991).
2. J. F. Sydow, P. Cramer, *Curr. Opin. Struct. Biol.* **19**, 732 (2009).
3. S. H. Chen *et al.*, *Science* **238**, 363 (1987).
4. L. M. Powell *et al.*, *Cell* **50**, 831 (1987).
5. B. L. Bass, H. Weintraub, *Cell* **55**, 1089 (1988).
6. J. B. Li *et al.*, *Science* **324**, 1210 (2009).
7. A. Athanasiadis, A. Rich, S. Maas, *PLoS Biol.* **2**, e391 (2004).
8. M. J. Thomas, A. A. Platas, D. K. Hawley, *Cell* **93**, 627 (1998).
9. D. Wang *et al.*, *Science* **324**, 1203 (2009).
10. N. Zenkin, Y. Yuzenkova, K. Severinov, *Science* **313**, 518 (2006).
11. M. Sakurai, T. Yano, H. Kawabata, H. Ueda, T. Suzuki, *Nat. Chem. Biol.* **6**, 733 (2010).
12. K. Nishikura, *Annu. Rev. Biochem.* **79**, 321 (2010).
13. E. Y. Levanon *et al.*, *Nat. Biotechnol.* **22**, 1001 (2004).
14. S. G. Conticello, *Genome Biol.* **9**, 229 (2008).
15. A. Chester, J. Scott, S. Anant, N. Navaratnam, *Biochim. Biophys. Acta-Gene Struct. Expression* **1494**, 1 (2000).
16. J. Dausset *et al.*, *Genomics* **6**, 575 (1990).
17. International HapMap Consortium, *Nature* **426**, 789 (2003).
18. International HapMap Consortium, *Nature* **437**, 1299 (2005).
19. The 1000 Genomes Project Consortium, *Nature* **467**, 1061 (2010).
20. H. M. Cann, *Curr. Opin. Genet. Dev.* **2**, 393 (1992).
21. T. C. Matise *et al.*, *Am. J. Hum. Genet.* **73**, 271 (2003).
22. F. Sanger, S. Nicklen, A. R. Coulson, *Proc. Natl. Acad. Sci. U.S.A.* **74**, 5463 (1977).
23. D. R. Bentley *et al.*, *Nature* **456**, 53 (2008).
24. J. Harrow *et al.*, *Genome Biol.* **7** (suppl. 1), S4 (2006).
25. Supporting material is available on Science Online.
26. S. B. Montgomery *et al.*, *Nature* **464**, 773 (2010).
27. C. Trapnell *et al.*, *Nat. Biotechnol.* **28**, 511 (2010).
28. B. R. Rosenberg, C. E. Hamilton, M. M. Mwangi, S. Dewell, F. N. Papavasiliou, *Nat. Struct. Mol. Biol.* **18**, 230 (2011).
29. S. F. Altschul, W. Gish, W. Miller, E. W. Myers, D. J. Lipman, *J. Mol. Biol.* **215**, 403 (1990).
30. K. L. Sodek *et al.*, *Mol. Biosyst.* **4**, 762 (2008).
31. A. Michalski, J. Cox, M. Mann, *J. Proteome Res.* **10**, 1785 (2011).
32. L. M. de Godoy *et al.*, *Genome Biol.* **7**, R50 (2006).
33. C. M. Burns *et al.*, *Nature* **387**, 303 (1997).
34. H. Lomeli *et al.*, *Science* **266**, 1709 (1994).
35. S. Maas, S. Patt, M. Schrey, A. Rich, *Proc. Natl. Acad. Sci. U.S.A.* **98**, 14687 (2001).
36. C. G. Phreaner, M. A. Williams, R. M. Mulligan, *Plant Cell* **8**, 107 (1996).
37. H. A. Hundley, A. A. Krauchuk, B. L. Bass, *RNA* **14**, 2050 (2008).
38. S. M. Rueter, C. M. Burns, S. A. Coode, P. Mookherjee, R. B. Emeson, *Science* **267**, 1491 (1995).
39. S. M. Rueter, T. R. Dawson, R. B. Emeson, *Nature* **399**, 75 (1999).

Acknowledgments: Dedicated to the memory of Dr. Tom Kadesch who gave us important suggestions, taught us salient and subtle points on gene expression, and inspired us with his enthusiasm. Dr. Kadesch died during the preparation of this manuscript. We thank D. Epstein, H. Kazazian, D. Puppione, and L. Simpson for suggestions and discussions. We thank C. Gunter, R. Nussbaum, and J. Puck for comments on the manuscript, M. Morley for help with data analysis, W. Ankener for sample processing, and J. Devlin and CHOP NAP core for results on Sanger sequencing. The mass spectrometry analysis was carried out at the Wistar Proteomic Facility; we thank K. Speicher for help and suggestions. Funded by grants from the National Institutes of Health (to V.G.C. and M.L.) and support from the Howard Hughes Medical Institute. The RNA-Seq data have been deposited in the National Center for Biotechnology Information's Gene Expression Omnibus under the accession no. GSE25840.

Supporting Online Material

www.sciencemag.org/cgi/content/full/science.1207018/DC1
Materials and Methods
Figs. S1 to S5
Tables S1 to S10
References (40–44)

3 March 2011; accepted 10 May 2011

Published online 19 May 2011;

10.1126/science.1207018

Probing Individual Environmental Bacteria for Viruses by Using Microfluidic Digital PCR

Arbel D. Tadmor,^{1*} Elizabeth A. Ottesen,² Jared R. Leadbetter,³ Rob Phillips^{4*}

Viruses may very well be the most abundant biological entities on the planet. Yet neither metagenomic studies nor classical phage isolation techniques have shed much light on the identity of the hosts of most viruses. We used a microfluidic digital polymerase chain reaction (PCR) approach to physically link single bacterial cells harvested from a natural environment with a viral marker gene. When we implemented this technique on the microbial community residing in the termite hindgut, we found genus-wide infection patterns displaying remarkable intragenus selectivity. Viral marker allelic diversity revealed restricted mixing of alleles between hosts, indicating limited lateral gene transfer of these alleles despite host proximity. Our approach does not require culturing hosts or viruses and provides a method for examining virus-bacterium interactions in many environments.

Despite the pervasiveness of bacteriophages in nature and their postulated impact on diverse ecosystems (1), we have a poor

grasp of the biology of these viruses and their host specificity in the wild. Although substantial progress has been made with certain host-

virus systems such as cyanophages (2–5), this is the exception rather than the rule. Conventional plaque assays used to isolate environmental viruses are not applicable to >99% of microbes in nature because the vast preponderance of the microbial diversity on Earth has yet to be cultured in vitro (6). Given the magnitude of the problem, the development of high-throughput, massively parallel sequencing approaches that do not rely on cultivation to identify specific virus-host relations are required. Although metagenomics has revolutionized our understanding of viral diversity on Earth (7–9), that approach

¹Department of Biochemistry and Molecular Biophysics, California Institute of Technology, Pasadena, CA 91125, USA. ²Department of Civil and Environmental Engineering, Massachusetts Institute of Technology, Cambridge, MA 02139, USA. ³Ronald and Maxine Linde Center for Global Environmental Science, California Institute of Technology, Pasadena, CA 91125, USA. ⁴Departments of Applied Physics and Bioengineering, California Institute of Technology, Pasadena, CA 91125, USA.

*To whom correspondence should be addressed. E-mail: arbel@caltech.edu (A.D.T.); phillips@pboc.caltech.edu (R.P.)

has as yet done little to shed light on the nature of specific viral-host interactions, except in restricted cases (10).

Recent advances in microfluidic technology have enabled the isolation and analysis of single cells from nature (11–13). We present an alter-

native to the classical phage enrichment technique where we use an uncultured virus to capture its hosts from the environment with a microfluidic polymerase chain reaction (PCR) approach called digital multiplex PCR (12, 14). To this end, microbial cells were harvested directly from the environment, diluted, and loaded onto a digital PCR array panel containing 765 PCR chambers operating at single-molecule sensitivity. Samples were diluted such that the majority of chambers were ideally either empty or contained a single bacterium (Fig. 1), achieving a Poisson distribution (15). Because there is no universally conserved gene in viruses (7, 16), we designed degenerate primers (17) to target a subgroup of diverse phagelike elements (18). Concurrently, the small subunit ribosomal RNA (SSU rRNA) gene encoded by each bacterial cell was amplified by using universal “all bacterial” primers (see fig. S1 for experimental design). Possible genuine host-virus associations detectable by this assay are depicted in Fig. 1C. Free phages may also colocalize with hosts; however, these events are not expected to lead to statistically significant colocalizations because of the random nature of these associations (19).

Hunting for phages in the termite hindgut.

The system we chose to investigate was the termite hindgut. This microliter-in-scale environment contains $\sim 10^7$ prokaryotic cells per μl (20) with over 250 different species of bacteria (21), making it ideally suited to explore many potential, diverse phage-host interactions. To find a viral marker gene relevant to such an environment, we examined the more abundant candidate viral marker genes present in the sequenced metagenome from a hindgut of a higher termite from Costa Rica collected in 2005 (22) [table S1;

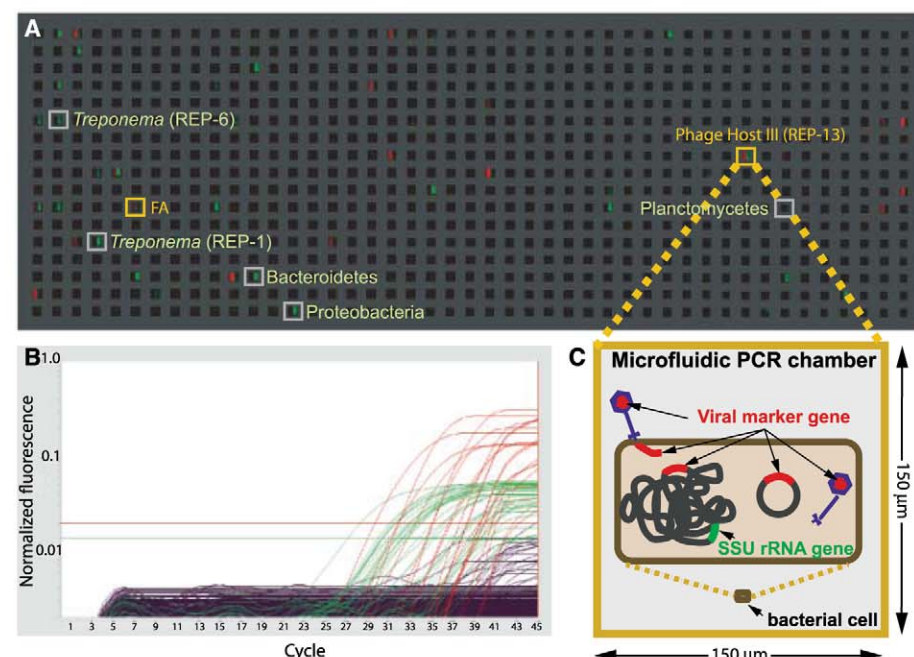
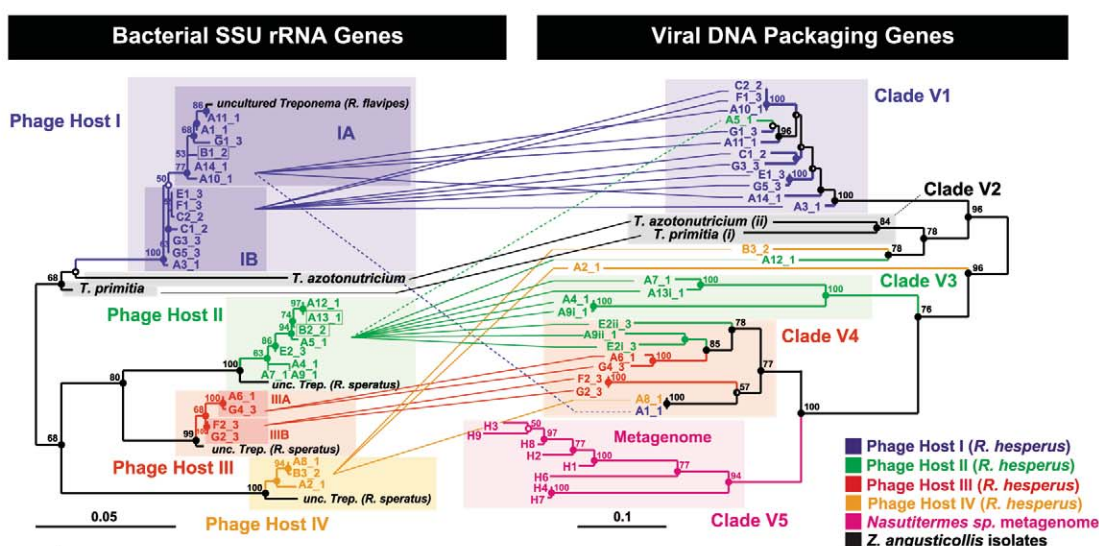


Fig. 1. End-point fluorescence measured in a panel of a microfluidic digital PCR array. (A) The measured end-point fluorescence from the rRNA channel (right half of each chamber, with the left half masked) and the terminase channel (left half of each chamber, with the right half masked) in a microfluidic array panel. Each panel in the array (1 of 12) consists of 765 reaction chambers 150 μm by 150 μm by 270 μm (6 nL). Retrieved colocalizations are outlined in orange, and positive rRNA chambers randomly selected for retrieval are outlined in gray. FA indicates false alarm (a probable terminase primer-dimer). (B) Normalized amplification curves of all chambers in (A) after linear derivative baseline correction (red, viral; green, rRNA). (C) Specific physical associations between a bacterial cell and the viral marker gene resulting in colocalization include, for example, an attached or assembling virion, injected DNA, an integrated prophage, or a plasmid containing the viral marker gene.

Fig. 2. Phylogenetic relationship between cultured and uncultured bacterial host rRNA genes and their associated viral DNA packaging genes. (Left) Maximum likelihood (ML) tree of 898 unambiguous nucleotides of the SSU rRNA gene of ribotypes that repeatedly colocalized with the terminase gene, including the two isolated spirochetes *Treponema primitia* and *Treponema azotonutricium*. Shorter sequences (A7, 780 bp, and A9, 806 bp) were added by parsimony (dashed branches). (Right) ML tree of 705 unambiguous nucleotides of the large terminase subunit gene. Connecting lines represent colocalized pairs, revealing restricted mixing of terminase alleles between different bacterial hosts. For association of three additional recombinant sequences (boxed on the left), see fig. S5. Statistically, we estimate that an average of 0.6 colocalizations are false [$\sim 2\%$ error (19)]. The sequence error rates (40) for the rRNA and terminase genes were measured to be 0 ($n = 8$) and $<0.6 \pm 0.3\%$ SD ($n = 9$),



respectively (18). Alleles are named by array (A to G) and retrieval index followed by an underscore and the colony number (colony 1 being sampled 6 months before colonies 2 and 3). Lowercase roman numerals indicate multiple terminases per chromosome. Scale bars represent substitutions per alignment. For interpretation of node support, refer to (18), and for accession numbers, table S10.

search algorithm described in (18)]. We then checked whether any of these viral genes had homologous counterparts in the sequenced genomes of two spirochetes isolated in 1997 from a laboratory colony of genetically and geographically distant termites originally collected in 1986 from Northern California (23, 24). We identified two such genes encoding a large terminase subunit protein (homologous to the T4-associated pfam03237 Terminase_6) and a portal protein (homologous to pfam04860 Phage_portal) exhibiting about 70 to 78% amino acid identity to their closest homologs in the higher termite gut metagenome (table S2). This finding is unexpected given that typically, across biology, portal proteins and terminase proteins from different phages exhibit little overall sequence similarity (25–28). Further analysis revealed that the spirochete viral genes were part of a larger prophage-like element, with the majority of recognizable genes most closely related to *Siphoviridae* phage genes (19). The association of these genes with prophage-like elements is consistent with the fact that both the Terminase_6 pfam and the Phage_portal pfam describe proteins in known lysogenic and lytic phages.

As a viral marker gene for this prophage-like element, we chose the large terminase subunit gene. This gene is a component of the DNA packaging and cleaving mechanism present in numerous double-stranded DNA phages (26) and is considered to be a signature of phages (29). We consequently designed degenerate primers on the basis of the collection of 50 metagenome and *Treponema*-isolate alleles of this gene. The ~820–base pair (bp) amplicon spanned by these primers covered about two-thirds of this gene and about 77% of the predicted N-terminal domain containing the conserved adenosine triphosphatase (ATPase) center (26, 30), the “engine” of this DNA packaging motor (31) (see alignments in figs. S2 and S3). Testing these primers against the RefSeq viral database (32) did not yield any hits (fig. S2). Indeed, the closest homolog of this gene in the RefSeq viral database displayed only 25% amino acid identity (table S2). Thus, although this terminase gene was associated with the Terminase_6 pfam, the termite-related alleles appear to be part of a novel assemblage of terminase genes in this environment and not closely related to previously sequenced phages (fig. S2).

Given that terminase genes of different phages often exhibit less sequence similarity (see above), the fact that we found such closely related terminase genes from such distantly related termites collected from well-separated geographical locations (California and Costa Rica) and from specimens collected almost two decades apart led us to speculate that this family of viral genes and prophage-like elements might be ubiquitous in termites. Indeed, to date we have identified close homologs of the large terminase subunit gene in the gut communities of nine termite species belonging to four families collected from

five different geographical locations. We therefore wished to identify the bacterial hosts associated with this viral marker gene. To this end, we collected representatives of a third previously unexamined termite family (Rhinothertidae; *Reticulitermes hesperus*, from a third geographical location in Southern California) over a span of 6 months (table S3). We then performed seven independent experiments, where in each case the hindgut contents of three worker termites were pooled, diluted, and loaded onto a digital PCR array, screening in total ~3000 individual hindgut particles (i.e., individual cells or possibly clumps of cells positive for the SSU rRNA gene).

Identification of previously unknown uncultured bacterial hosts. Of the 41 retrieved colocalizations, 28 were associated with just four phylotypes designated phage hosts I, II, III, and

IV (compare Fig. 2, Table 1, and the phylogenetic analysis in fig. S4 and tables S4 and S5). Statistically, the reproducible coamplifications were significant and cannot be explained by random colocalization of two unassociated genes (Table 1). Furthermore, these associations were independently reproduced in specimens from different colonies collected 6 months apart (Fig. 2), indicative that relations between specific host bacteria and viral markers were being revealed.

All four of the phylotypes were members of the spirochetal genus *Treponema* and exhibited substantial diversity within this genus (table S4). No reproducible or statistically robust associations involving other bacteria were observed. The terminase alleles that associated with these cells shared ≥69.8% identity (average $81.9 \pm 8.3\%$ standard deviation, SD) (33) and were divergent

Table 1. Statistics of repeatedly colocalized SSU rRNA genes. The number of repeated colocalizations and occurrences in the reference library are based on a DOTUR analysis (tables S4 and S5). Reference library frequencies are roughly one-third of the colocalization frequencies, indicating that sampling was unbiased. The statistical test to determine the *P* value is explained in (19).

Host	No. of repeated colocalizations (n = 41)	Occurrence in reference library (n = 118)	P value (one-tailed, n = 41)
Host I	13	5	5.4×10^{-18}
Host II	8	2	7.6×10^{-13}
Host III	4	1	5.7×10^{-7}
Host IV	3	1	3.8×10^{-5}

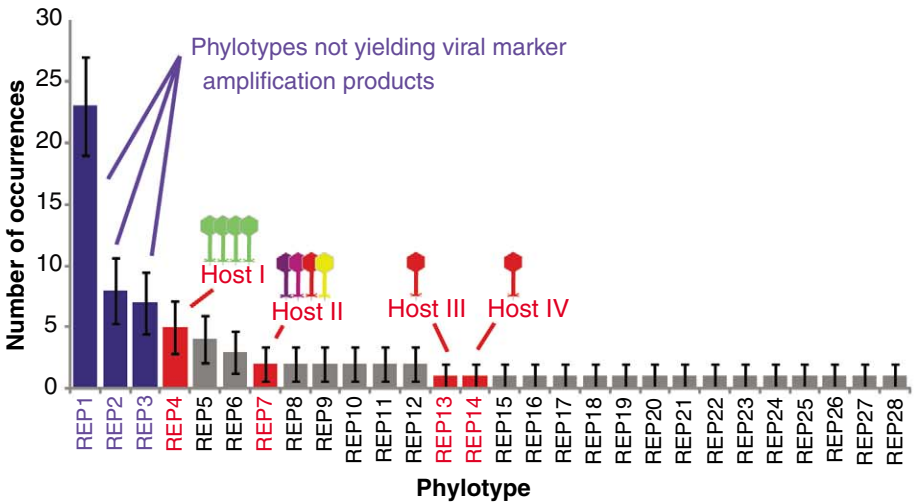


Fig. 3. Rank abundance curve of free-living *Treponema* spirochetes in *R. hesperus* termites identifying putative phage hosts. A library of 118 random chambers positive for the rRNA gene were retrieved, postamplified, and sequenced. Of these, *n* = 78 were related to the *Treponema* genus, corresponding to 28 different phylotypes based on an operational taxonomical unit, OTU, cut-off set by DOTUR (41) at 3.1%. We show these 28 phylotypes, designated as REPs, ordered by their abundance. Phylotype abundance is expected to reflect true relative abundances in the gut because single-cell amplification is not susceptible to primer bias or rRNA copy number bias. Phylotypes identified as phage hosts are marked by red bars (with the highly clonal marker associated with host I depicted by green viruses and the divergent marker associated with host II depicted by colored viruses). The most abundant free-living *Treponema* in the gut—REPs 1, 2, and 3 (blue bars)—were not associated with the viral marker. Remaining bars are gray. Error bars are estimated by the binomial SD. See table S5 for OTU assignment. Note that the isolated spirochetes were not spanned by these REPs (fig. S4).

from other currently known terminases (fig. S2), suggesting that the primer set amplifies elements exclusively found associated with termite gut treponemes. Analysis of the retrieved terminase gene sequences revealed that they are under substantial negative selection pressure with $\omega = \beta/\alpha = 0.079$, where ω is the relative rate of nonsynonymous, β , and synonymous, α , substitutions (18) (see table S6 for additional estimates for individual hosts). Furthermore, none of the terminase sequences in Fig. 2 appeared to encode either errant stop codons or obvious frame shift mutations, and functional motifs appeared to be conserved (fig. S2). Together, the sequence data suggest that these genes have been active in recent evolutionary history and are not degenerating pseudogenes (19).

Because the viral marker gene was present in hosts spanning a swath of species of termite gut treponemes, we were interested to see whether this viral marker exhibited any selectivity within this genus. The relative frequency of free-living *Treponema* phylotypes was determined by randomly sampling chambers positive for the rRNA gene (18) (Fig. 3 and fig. S4). We found that hosts I through IV were relatively infrequent, comprising 1.3% to 6.4% of the sampled *Treponema* cells (Table 1) and collectively about 9.8% of the sampled bacterial cells (correcting for reagent contaminants). Interestingly, the three most abundant *Treponema* phylotypes in the survey, constituting ~30, 10, and 9% of the free-swimming spirochetal cells [*Reticulitermes* environmental phylotypes (REPs) 1, 2, and 3 in Fig. 3; see also fig. S4 and table S5], were never co-retrieved with the viral marker gene to the extent that this target was spanned by our degenerate primers. Given that the degenerate core region (17) of each primer targets residues that were strictly conserved in gut microbes of highly divergent termite specimens (fig. S2) and that these primers successfully amplified this gene from the guts of many different termite species (see above), it appears that these strains are most likely either insensitive to this virus or that only a small percentage are infected (19). Therefore, we conclude that ~50% of the free-swimming spirochetal cells in the gut were likely not infected with an element encoding the targeted viral marker gene, whereas ~12% were potentially infected hosts (Fig. 3).

Phage-host cophylogeny. To elucidate the evolutionary relations between the terminase alleles and their hosts, we examined the phylogeny of the terminase genes associated with each bacterial host. Terminase alleles from *R. hesperus* formed separate clades from the clades of the two other termite species investigated in this study (clades V2 and V5 in Fig. 2). Within *R. hesperus*, different bacterial hosts exhibited different patterns of viral allelic diversity. Terminase sequences associated with host I, for example, were highly clonal, with 11 out of 13 terminase alleles sharing $96.7 \pm 1.7\%$ SD identity ($n = 11$, clade V1) (33). Conversely, terminase alleles associated with host II displayed marked diversity ($79.1 \pm 6.2\%$ identity, $n = 11$) (33), deep branches, and

divergent multiple alleles per bacterium for three out of eight repetitions (with 15 to 31% divergence). The unique features of the terminase alleles associated with host II compared with host I may reflect a more ancient infection or possibly an infection by a phage replicating with a lower fidelity. Alternatively, host II may be a more sensitive bacterial host susceptible to a wider range of phages. Overall, phage terminase alleles associated with different bacterial hosts were significantly divergent with only three exceptions (table S7).

The tandem trees in Fig. 2 reveal multiple possible relations between bacterial hosts and terminase alleles: Whereas host I was associated almost exclusively with a single terminase clade (V1), host II was associated with multiple terminase clades (primarily V3 and V4). Conversely, terminase clade V1 was associated almost exclusively with host I, whereas terminase clade V4 was associated with all bacterial hosts. Overall, the terminase tree was highly structured and displayed specific bacterial host-associated clades (e.g., clades V1 and V3, compare with fig. S5A). Applying the P Test (34) implemented in Fast UniFrac (35) to terminase alleles grouped by bacterial host indeed revealed significant differences between alleles associated with most pairs of hosts (table S8). Grouping terminase alleles by colony, however, did not reveal significant differences between alleles (table S9), indicating that sampling was not a factor in determining the observed host-associated heterogeneity in terminase alleles. The highly nonrandom distribution of host-associated terminase alleles therefore suggests that lateral gene transfer and/or host switching is limited in this system. This result, however, could also reflect the fact that the terminase gene does not appear to shuffle randomly among phages, possibly indicating a connection between DNA packaging and other characteristics of the phage (36). It remains to be seen whether other viral genes follow similar patterns.

The fact that there was little mixing between terminase alleles associated with host I (V1) and the more distantly related hosts II (V3 and V4) and III (V4), whereas alleles of the more closely related hosts II and III (table S4) exhibited a certain degree of mixing (V4), supports the notion that the probability of cross-species transmission or lateral gene transfer decreases with the phylogenetic distance of the hosts (37). The rRNA gene of hosts I through IV also exhibited patterns of microdiversity that may have physiological relevance (38, 39). These patterns, however, were mirrored only by the terminase alleles of host III. Host I and II terminase alleles appeared to be indifferent to the bacterial host at the subspecies level.

Our results show that, in a marked departure from classical phage enrichment techniques, specific viral-host relations can be revealed in uncultivated cells harvested straight from the environment. We found that variants of a viral packaging gene appear to have infected bacterial hosts across an entire genus of bacteria. Further-

more, despite the substantial potential for lateral gene transfer and/or host switching in this well-mixed, small-volume system, the terminase tree was highly structured and displayed specific bacterial host-associated clades. It will be interesting to continue to monitor the host-virus interactions within this ecosystem as a function of space and time and across the termite community at large, shedding further light on host-virus coevolution in this unique ecosystem. More broadly, the method we have developed enables a highly parallel analysis of host-virus interactions in environmental samples from nearly any environment in nature.

References and Notes

1. C. A. Suttle, *Nat. Rev. Microbiol.* **5**, 801 (2007).
2. M. B. Sullivan *et al.*, *Environ. Microbiol.* **12**, 3035 (2010).
3. D. Lindell *et al.*, *Nature* **449**, 83 (2007).
4. F. E. Angly *et al.*, *PLoS Biol.* **4**, e368 (2006).
5. S. J. Williamson *et al.*, *PLoS ONE* **3**, e1456 (2008).
6. P. Hugenoltz, *Genome Biol.* **3**, reviews0003 (2002).
7. R. A. Edwards, F. Rohwer, *Nat. Rev. Microbiol.* **3**, 504 (2005).
8. E. A. Dinsdale *et al.*, *Nature* **452**, 629 (2008).
9. D. M. Kristensen, A. R. Mushegian, V. V. Dolja, E. V. Koonin, *Trends Microbiol.* **18**, 11 (2010).
10. A. F. Andersson, J. F. Banfield, *Science* **320**, 1047 (2008).
11. R. N. Zare, S. Kim, *Annu. Rev. Biomed. Eng.* **12**, 187 (2010).
12. E. A. Ottesen, J. W. Hong, S. R. Quake, J. R. Leadbetter, *Science* **314**, 1464 (2006).
13. Y. Marcy *et al.*, *Proc. Natl. Acad. Sci. U.S.A.* **104**, 11889 (2007).
14. L. Warren, D. Bryder, I. L. Weissman, S. R. Quake, *Proc. Natl. Acad. Sci. U.S.A.* **103**, 17807 (2006).
15. S. Dube, J. Qin, R. Ramakrishnan, *PLoS ONE* **3**, e2876 (2008).
16. F. Rohwer, R. Edwards, *J. Bacteriol.* **184**, 4529 (2002).
17. T. M. Rose *et al.*, *Nucleic Acids Res.* **26**, 1628 (1998).
18. Materials and methods are available as supporting material on Science Online.
19. Supporting text is available as supporting material on Science Online.
20. A. Tholen, B. Schink, A. Brune, *FEMS Microbiol. Ecol.* **24**, 137 (1997).
21. Y. Hongoh, M. Ohkuma, T. Kudo, *FEMS Microbiol. Ecol.* **44**, 231 (2003).
22. F. Warnecke *et al.*, *Nature* **450**, 560 (2007).
23. J. R. Leadbetter, T. M. Schmidt, J. R. Gruber, J. A. Breznak, *Science* **283**, 686 (1999).
24. T. G. Lilburn *et al.*, *Science* **292**, 2495 (2001).
25. S. D. Moore, P. E. Prevelige Jr., *Curr. Biol.* **12**, R96 (2002).
26. V. B. Rao, M. Feiss, *Annu. Rev. Genet.* **42**, 647 (2008).
27. S. Chai *et al.*, *J. Mol. Biol.* **224**, 87 (1992).
28. K. Eppler, E. Wyckoff, J. Goates, R. Parr, S. Casjens, *Virology* **183**, 519 (1991).
29. S. Casjens, *Mol. Microbiol.* **49**, 277 (2003).
30. M. S. Mitchell, S. Matsuzaki, S. Imai, V. B. Rao, *Nucleic Acids Res.* **30**, 4009 (2002).
31. S. Sun *et al.*, *Cell* **135**, 1251 (2008).
32. K. D. Pruitt, T. Tatusova, D. R. Maglott, *Nucleic Acids Res.* **33**, D501 (2005).
33. Percent identity was measured across 235 unambiguous aligned amino acids.
34. A. P. Martin, *Appl. Environ. Microbiol.* **68**, 3673 (2002).
35. M. Hamady, C. Lozupone, R. Knight, *ISME J.* **4**, 17 (2010).
36. S. R. Casjens *et al.*, *J. Bacteriol.* **187**, 1091 (2005).
37. N. Wolfe *et al.*, *Glob. Change Hum. Health* **1**, 10 (2000).
38. L. Moore, G. Rocap, S. Chisholm, *Nature* **393**, 465 (1998).

39. J. R. Thompson *et al.*, *Appl. Environ. Microbiol.* **70**, 4103 (2004).
 40. S. G. Acinas, R. Sarma-Rupavtarm, V. Klepac-Ceraj, M. F. Polz, *Appl. Environ. Microbiol.* **71**, 8966 (2005).
 41. P. D. Schloss, J. Handelsman, *Appl. Environ. Microbiol.* **71**, 1501 (2005).

Acknowledgments: We wish to thank D. Baltimore, S. Casjens, D. S. Fisher, R. W. Hendrix, H. J. Lee, M. Lindén, E. G. Matson, R. Milo, V. J. Orphan, S. R. Quake, A. Z. Rosenthal, E. M. Rubin and colleagues at JGI, D. Z. Soghoian, N. D. Wolfe, D. Wu,

X. Zhang, and the anonymous referees for their advice and feedback. We also wish to thank E.G.M. and A.Z.R. for their assistance in collection of specimens and E.G.M. for ZAS genomic DNA. This project was supported by the NIH Director's Pioneer Award, NIH American Recovery and Reinvestment Act grant number R01 GM085286-01S, U.S. Department of Energy grant no. DE-FG02-07ER64484, and NSF grant nos. EF-0523267 and CMMI-0758343 and by the Davidow Family Research Fund. GenBank accession numbers are given in table S10.

Supporting Online Material

www.sciencemag.org/cgi/content/full/333/6038/58/DC1
 Materials and Methods
 SOM Text
 Figs. S1 to S5
 Tables S1 to S10
 References

22 November 2010; accepted 16 May 2011
 10.1126/science.1200758

REPORTS

Reconfigurable Knots and Links in Chiral Nematic Colloids

Uroš Tkalec,^{1*†} Miha Ravnik,^{2,3} Simon Čopar,³ Slobodan Žumer,^{1,3} Igor Muševič^{1,3*}

Tying knots and linking microscopic loops of polymers, macromolecules, or defect lines in complex materials is a challenging task for material scientists. We demonstrate the knotting of microscopic topological defect lines in chiral nematic liquid-crystal colloids into knots and links of arbitrary complexity by using laser tweezers as a micromanipulation tool. All knots and links with up to six crossings, including the Hopf link, the Star of David, and the Borromean rings, are demonstrated, stabilizing colloidal particles into an unusual soft matter. The knots in chiral nematic colloids are classified by the quantized self-linking number, a direct measure of the geometric, or Berry's, phase. Forming arbitrary microscopic knots and links in chiral nematic colloids is a demonstration of how relevant the topology can be for the material engineering of soft matter.

Knots are fascinating topological objects and symbols of complexity that have fascinated the human mind since the dawn of our history. Although they are treated within the mathematical discipline of topology (1), knots and links have always played a prominent role in physical and life sciences (2). In supramolecular chemistry, complex links were demonstrated as interlinked molecular rings—catenanes—and interlocked molecules—rotaxanes (3–5). Knotting and the entanglement of polymer molecules were proved to be essential for the crystallization and rheological properties of polymers (6). Knotted structures have also been predicted in classical field theory (7), and it was recently demonstrated that the lines of zero intensity in interfering light beams can be knotted and linked as well (8, 9). In biological systems, molecular knots and links are particularly important because the entanglement of DNA molecules plays the crucial role in vital processes of replication, transcription, and recombination (10, 11). Knot-like topological defects have been

observed in the chiral nematic liquid crystal (NLC) (12) but have remained unexplored because of the difficulty associated with control. The smallness of the length scales involved and the inherent lack of precise control and means of manipulating the knots and links are major obstacles in studying the structure, properties, and mechanisms of their formation.

We demonstrate knotted and linked microscopic loops of topological defects of arbitrary complexity in chiral nematic colloids. The loops are responsible for the stabilization of colloidal microparticle structures in a chiral NLC, thus forming an unusual colloidal soft matter (13–16). We performed knot and link manipulation by cutting, fusing, and reversibly reconnecting individual defect loops into knots and links of arbitrary complexity using the highly focused light of laser tweezers, which gives us full control over the knot and link formation.

The medium that supports our knots and links is a NLC with colloidal inclusions, and the strings used to tie knots and links are closed defect loops in the NLC. When spherical particles that promote alignment of NLC molecules normal to the surface are dispersed in the NLC, the direction of molecular alignment—the director—is forced to align normal to the curved and closed surface of each inclusion. Because the spherical surface makes it impossible for the molecules to fill the space uniformly, defects in the form of singular points—and in our case, closed defect loops—

are created. Each particle is encircled by its own micro-loop, also called a Saturn's ring, in which the degree of molecular order is reduced in the ~10-nm-thick core, and the director exhibits fast spatial variations, making the rings visible under an optical microscope (16). The Saturn's ring behaves as an elastic strip that can be stretched and deformed with laser tweezers (17–20). More importantly, several Saturn's rings can be fused together by using the laser tweezers to entangle a pair or multiple colloidal particles (21, 22). Here, the particles and defect loops are topologically and energetically interlinked because the loops must compensate for the topological charge of the particles (16) and tend to be as short as possible in order to reduce the total free energy. Although in nematic colloids with a generally homogeneous director alignment only linear entangled objects were successfully created (22), the defect loops in chiral NLC colloids can be optically knotted into knots and links of arbitrary complexity.

A dispersion of 4.72-μm-diameter silica microspheres in a pentylicyanobiphenyl (5CB) NLC is used in all of the experiments. The surface of the microspheres is chemically functionalized to induce a strong perpendicular alignment of the NLC molecules. The colloidal dispersion is confined to a thin glass cell, made of glass plates, coated with transparent indium tin oxide and rubbed polyimide alignment layers, spaced by a 5.5-μm-thick mylar foil (23). The alignment directions at the top and bottom of the cell are set perpendicular to ensure a 90° twist of the director, thus creating either left- or right-twisted chiral liquid-crystal profiles. Using twisted director structure is essential for the stability of nematic knots and links because the cell-imposed twist energetically favors effectively longer and out-of-plane deformed defect loops (Fig. 1A), which can more easily interlink.

An individual colloidal particle in the chiral nematic cell acquires a single-defect loop shown in Fig. 1A, known as a Saturn's ring (16). The ring is tilted at 45° with respect to the molecular alignment at the cell walls and is clearly visible because its core scatters light. In terms of topology, a closed loop without a knot in it is an unknot (1, 24). We used laser tweezers to bring together several particles and observed either spontaneous or laser-assisted fusion of their rings,

¹Condensed Matter Physics Department, Jožef Stefan Institute, Jamova 39, 1000 Ljubljana, Slovenia. ²Rudolf Peierls Centre for Theoretical Physics, University of Oxford, Oxford OX1 3NP, UK.

³Faculty of Mathematics and Physics, University of Ljubljana, Jadranska 19, 1000 Ljubljana, Slovenia.

*To whom correspondence should be addressed. E-mail: uros.tkalec@ijs.si (U.T.); igor.musevic@ijs.si (I.M.)

†Present address: Max Planck Institute for Dynamics and Self-Organization, Bunsenstrasse 10, 37073 Göttingen, Germany.

leading to the formation of longer loops that entangle two or more particles (fig. S1 and movies S1 to S3). In small colloidal clusters, presented in Fig. 1, B to E, all the loop conformations are likewise topologically equivalent to the unknot.

The simplest nontrivial topological configuration that is created by a sequence of local, isotropic-to-nematic, temperature, and optically induced micro-quenches is the Hopf link (Fig. 1F).

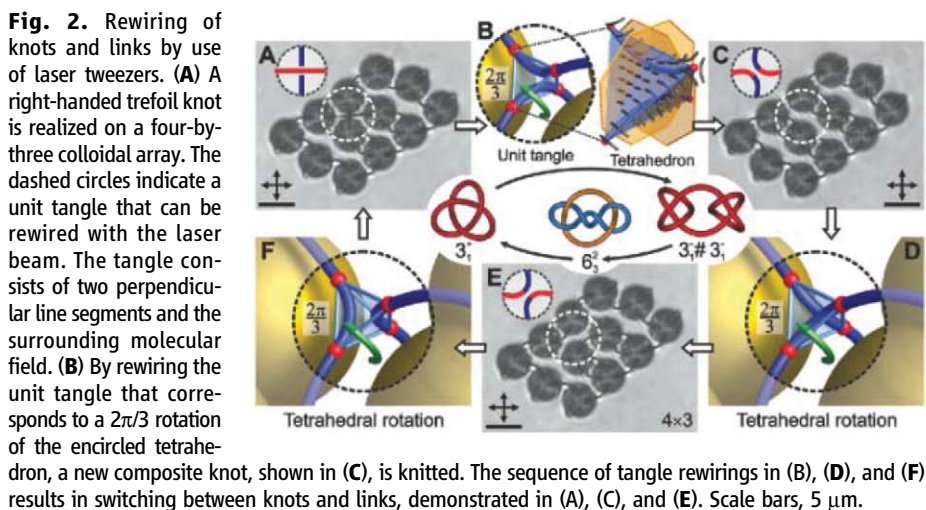
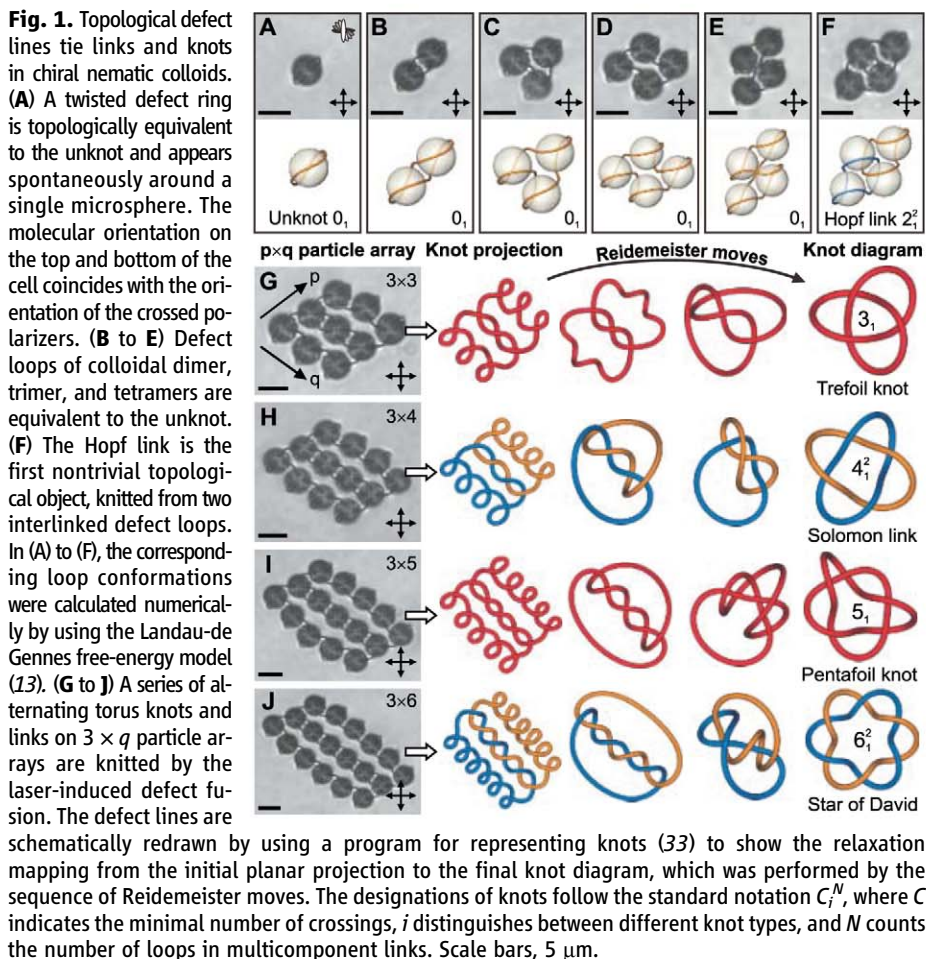
Two interlinked loops, entangled around four neighboring particles, are visible in both the polarizing optical micrograph and the numerically calculated structure.

However, the true richness of the knots and links is revealed when the colloidal clusters are extended to arrays of $p \times q$ particles (Fig. 1G). The laser-assisted knitting technique was applied at multiple knitting sites so as to connect the

neighboring defect rings. A series of nematic braids, realized on $3 \times q$ particle arrays is shown in Fig. 1, G to J (left). To identify the topology of the entangled loops, we performed a sequence of topology-preserving Reidemeister moves (*I*), which virtually transform the real physical conformation of the loops into its planar projection with the minimum number of crossings. Negative or left-handed crossings (*I*) are favored in a left-twisted nematic profile because of the geometric constraint of the cell. The relaxation mappings, illustrated in Fig. 1, G to J (right), reveal a surprising result. There is a series of alternating torus knots and links (*I*): the trefoil knot, the Solomon link, the pentafoil knot, and the Star of David. This generically knotted series of knots and links shows that the confining lattice of colloidal particles allows for the production of torus links and knots of arbitrary complexity, simply by adding and interweaving additional rows of particles—that is, by increasing q .

The knots and links can also be reversibly retied. Topologically, this corresponds to locally changing the mutual contact—the unit tangle (*I*)—between the two segments of the knotted line, which can either cross or bypass one another in two perpendicular directions. We were able to reknit the disclination lines in the region of the selected tangle by applying the laser-induced micro-quench, as shown in Fig. 2, thus transforming the unit tangles one into another and consequently changing the topology of the presented conformations. Starting from a tangle inside the encircled region in Fig. 2A, the laser beam initially cut the tangle, and then by using precise positioning and intensity tuning of the beam, the line segments were reknotted into a distinct tangle (Fig. 2C). Further, we reknotted a tangle (Fig. 2C) into another distinct tangle (Fig. 2E). We can make exactly three tangles by reversibly transforming them one into another. These local transformations change the topology and the handedness (right, +; left, −) of the chiral knots and links, which in a given example corresponds to conversions between the right-handed trefoil knot 3_1^+ (Fig. 2A), the left-handed composite knot $3_1^+ \# 3_1^-$ (Fig. 2C), and the two-component link 6_2^2 (Fig. 2E). Eventually, the reknitting of knots and links can be performed for any desired knotting sequence of unit tangles at any specific position in a colloidal array. More specifically, the $p \times q$ array of particles generates a template of $(p-1) \times (q-1)$ unit tangles—for example, six tangles on a four-by-three particle array, which can all be individually switched, thus inducing site-specific transformations between various knots and links.

The optical retying of knots and links is directly related to the changes in the orientational field of the nematic host. Each tangle has four free ends of two-defect line segments (Fig. 2, A, C, and E, insets), which in our system form the corners of an approximate tetrahedron (Fig. 2B). The director field inside the tetrahedron has an intrinsic dihedral symmetry, with two perpendicular mirror symmetry planes and a full tetrahedral



symmetry on its surface. Therefore, when enclosing any of the three unit tangles with such tetrahedrons the orientational profiles within the tetrahedrons prove to be equivalent, and the only difference is the relative orientation of the tetrahedrons. Consequently, the rewiring of the tangles corresponds to a solid rotation of the director field inside the tetrahedron (25), as schematically illustrated in Fig. 2, B, D, and F. By symmetry, these rotations preserve the continuity of the nematic orientational profile and position the two line segments exactly in one of the three distinct

configurations, which were recognized as unit tangles.

The defect loops that we used to knit the knots and links are not only structureless strings but are dressed by the surrounding director field. For this reason, they possess a threefold rotational symmetry of the hyperbolic molecular orientational profile in the plane perpendicular to the defect line (Fig. 3A, inset). This threefold symmetric pattern can twist along the disclination and makes the defect lines the three-sided strips, which are analogous to the well-known Moebius strip

(24). Because our three-sided strips are always closed into loops, only fractional values of the internal twist are allowed by the continuity of the director field, corresponding to the integer multiples of a $2\pi/3$ rotation. This property can be described by a topological invariant called the self-linking number SL that counts the turns of the binormal around the curve tangent for algebraic curves (26) and can be generalized to count the turns of the director field around the defect loop (25). For multiple loops, the summation of SL over all the loops can be used as a natural

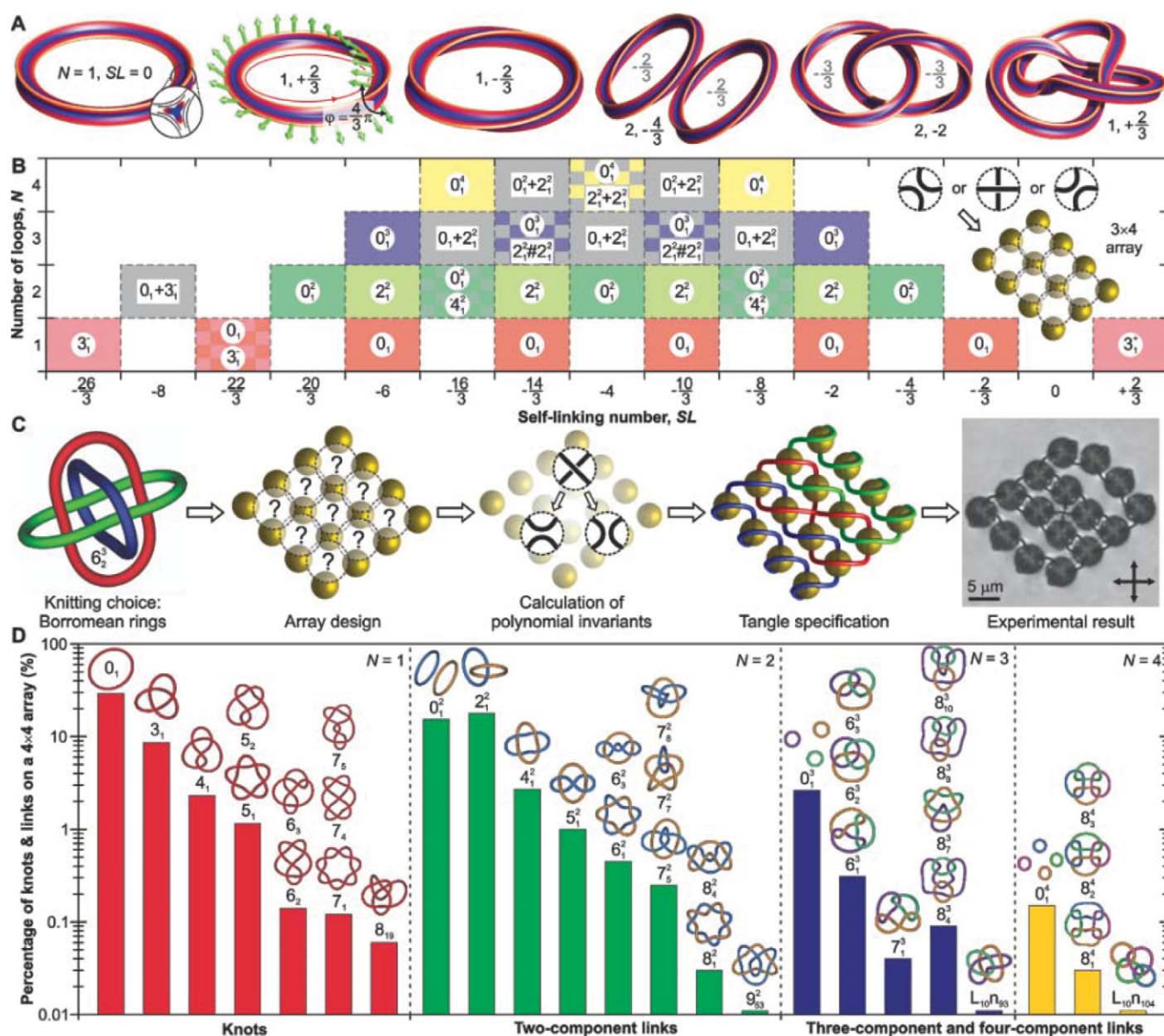


Fig. 3. Topological classification and made-to-order assembly of linked and knotted nematic braids. **(A)** The defect loops have a local threefold rotational symmetry of the hyperbolic cross section and correspond to three-sided strips, analogous to the Moebius strip. They can be distinctly characterized by the number of loops N and the self-linking number SL of fractional values. **(B)** The classification of all possible knots and links on a three-by-four particle array by SL and N . The hierarchical ordering of knots and links, depicted by distinct colors and standard knot symbols, are shown. **(C)** Made-to-order assembly of Borromean rings on a particular $p \times q$ particle array.

The feasible tangle combinations were tested with the numerical algorithm based on the Jones polynomials and Kauffman bracket approach (24, 28). The selected configuration was identified by direct comparison with polynomials in the enumerated *Table of Knot Invariants* (29) and then assembled by using laser tweezers. **(D)** The distribution of prime knots and links on a four-by-four particle array shows a large diversity of topological conformations with minimum crossing numbers up to 10. The probability of occurrence of a particular knot or link decreases with its complexity, as measured by the minimum crossing number.

generalization of this invariant. The quantization of the self-linking number is directly related to the geometric, or Berry's, phase (27). For nematic braids, the geometric phase corresponds to the angular shift φ that is acquired upon the parallel transport of a surface normal traveling along one surface of the characteristic three-sided strip. More specifically, the angular shift is equivalent to $\varphi = 2\pi SL$ (Fig. 3A). Eventually, the SL and the number of loops N can be used for a unique classification of all possible loop conformations—that is, all the available knot types on a given $p \times q$ particle array. Figure 3B shows the classification of the topological objects on a three-by-four particle array, determined by testing all the possible combinations of unit tangles. Using SL and N as the characteristic invariants, the knots and links arrange hierarchically and regularly alternate between the knotted/unknotted and linked/unlinked structures (25), which is promising for predicting the complexity of the knots and links that can be realized on a specific $p \times q$ particle array.

Having experimental control over the knotting and having theoretical tools for finding all possible conformations of nematic braids, we were able to perform a made-to-order assembly of knots and links, illustrated in Fig. 3C. First, we selected Borromean rings (23) as an example of a complex interwoven structure, which we attempted to weave. Next, we specified the size of the particle array to be four by four, the smallest array required for the chosen link. By using a computer algorithm that is based on calculating the polynomial invariants from knot theory (fig. S2) (23, 28, 29), the tangle configuration that corresponds to the chosen link was identified. The site-specific pattern of tangles shown in Fig. 3C (fourth frame) was needed. Lastly, we experimentally assembled the Borromean rings using laser tweezers. To show the reach of our assembly method, we present all of the prime knots and links that can be made to order on a four-by-four particle array in Fig. 3D. Almost 40 dif-

ferent knot and link types are discerned among $3^{(p-1)(q-1)} = 3^9$ tangle combinations with minimum crossing numbers up to 10. Out of all the loop conformations, 35% are prime knots or links, 29% are unknots, 18% are unlinks, and 18% are more complex composite links (table S1). Such a large diversity of topological objects suggests that it is possible to design any knot or link on a sufficiently large colloidal array.

We have shown that chiral nematic colloids are stabilized by defect knots and links of fascinating complexity, which can be fully controlled and rewired by light. This unusual colloidal soft-matter system provides a robust made-to-order assembly of an arbitrary knot or link on a microscopic scale and is a new route to the fabrication of soft matter with special topological features. We believe that the strategy presented here offers guidance to further progress in our understanding of the knotting of topologically nontrivial entities, such as DNA (5), skyrmion lattices in chiral magnets (30) and confined blue phases (31), and entangled vortices in superconductors (32).

References and Notes

1. C. C. Adams, *The Knot Book* (American Mathematical Society, Providence, 2004).
2. L. H. Kauffman, *Knots and Physics* (World Scientific Publishing, Singapore, ed. 3, 2000).
3. J. P. Sauvage, C. Dietrich-Buchecker, Eds., *Molecular Catenanes, Rotaxanes and Knots: A Journey Through the World of Molecular Topology* (Wiley, Weinheim, 1999).
4. K. S. Chichak et al., *Science* **304**, 1308 (2004).
5. D. Han, S. Pal, Y. Liu, H. Yan, *Nat. Nanotechnol.* **5**, 712 (2010).
6. P. G. de Gennes, *Scaling Concepts in Polymer Physics* (Cornell Univ. Press, New York, 1979).
7. L. Faddeev, A. J. Niemi, *Nature* **387**, 58 (1997).
8. W. T. M. Irvine, D. Bouwmeester, *Nat. Phys.* **4**, 716 (2008).
9. M. R. Dennis, R. P. King, B. Jack, K. O'Holleran, M. J. Padgett, *Nat. Phys.* **6**, 118 (2010).
10. A. D. Bates, A. Maxwell, *DNA Topology* (Oxford Univ. Press, Oxford, ed. 2, 2005).
11. D. Meluzzi, D. E. Smith, G. Arya, *Annu. Rev. Biophys.* **39**, 349 (2010).
12. Y. Bouligand, *J. Phys. (Paris)* **35**, 215 (1974).
13. P. G. de Gennes, J. Prost, *The Physics of Liquid Crystals* (Oxford Science Publications, Oxford, 1993).
14. N. D. Mermin, *Rev. Mod. Phys.* **51**, 591 (1979).
15. P. Poulin, H. Stark, T. C. Lubensky, D. A. Weitz, *Science* **275**, 1770 (1997).
16. H. Stark, *Phys. Rep.* **351**, 387 (2001).
17. D. G. Grier, *Nature* **424**, 810 (2003).
18. M. Yada, J. Yamamoto, H. Yokoyama, *Phys. Rev. Lett.* **92**, 185501 (2004).
19. I. Mušević et al., *Phys. Rev. Lett.* **93**, 187801 (2004).
20. I. Mušević, M. Škarabot, U. Tkalec, M. Ravnik, S. Žumer, *Science* **313**, 954 (2006).
21. T. Araki, H. Tanaka, *Phys. Rev. Lett.* **97**, 127801 (2006).
22. M. Ravnik et al., *Phys. Rev. Lett.* **99**, 247801 (2007).
23. Materials and methods are available as supporting material on Science Online.
24. V. V. Prasolov, A. B. Sossinsky, *Knots, Links, Braids and 3-Manifolds* (American Mathematical Society, Providence, RI, 1997).
25. S. Čopar, S. Žumer, *Phys. Rev. Lett.* **106**, 177801 (2011).
26. J. H. White, *Am. J. Math.* **91**, 693 (1969).
27. F. Wilczek, A. Shapere, Eds., *Geometric Phases in Physics* (World Scientific Publishing, Singapore, 1988).
28. D. M. Raymer, D. E. Smith, *Proc. Natl. Acad. Sci. U.S.A.* **104**, 16432 (2007).
29. J. C. Cha, C. Livingston, *KnotInfo: Table of Knot Invariants*; <http://www.indiana.edu/~knotinfo> (2011).
30. S. Mühlbauer et al., *Science* **323**, 915 (2009).
31. J. Fukuda, S. Žumer, *Nat. Commun.* **2**, 246 (2011).
32. D. R. Nelson, *Nature* **430**, 839 (2004).
33. R. G. Sharein, thesis, University of British Columbia (1998).

Acknowledgments: U.T. thanks S. Herminghaus, S. Kralj, and S. Vrtnik for discussions and kindly acknowledges support of the Max Planck Society. M.R. acknowledges support of the European Commission (EC) under the Marie Curie Program Active Liquid Crystal Colloids (ACTOIDS); content reflects only the authors' views and not the views of the EC. The research was funded by Slovenian Research Agency under the contracts P1-0099, PR-00182, and J1-9728 and in part by the NAMASTE Center of Excellence.

Supporting Online Material

www.sciencemag.org/cgi/content/full/333/6038/62/DC1

Materials and Methods

Figs. S1 and S2

Table S1

References (34–43)

Movies S1 to S3

16 March 2011; accepted 12 May 2011

10.1126/science.1205705

Rotary Photon Drag Enhanced by a Slow-Light Medium

Sonja Franke-Arnold,^{1*} Graham Gibson,¹ Robert W. Boyd,^{2,3} Miles J. Padgett¹

Transmission through a spinning window slightly rotates the polarization of the light, typically by a microradian. It has been predicted that the same mechanism should also rotate an image. Because this rotary photon drag has a contribution that is inversely proportional to the group velocity, the image rotation is expected to increase in a slow-light medium. Using a ruby window under conditions for coherent population oscillations, we induced an effective group index of about 1 million. The resulting rotation angle was large enough to be observed by the eye. This result shows that rotary photon drag applies to images as well as polarization. The possibility of switching between different rotation states may offer new opportunities for controlled image coding.

The speed of light is independent of the choice of reference frame only in a vacuum. Once light enters a moving medium, it can be dragged in either the transverse or lon-

gitudinal direction. This phenomenon was first considered by Fresnel in 1818 (1) and then, for the longitudinal case, verified by Fizeau (1859), who used water flowing along the light paths

within an interferometer as a means of introducing a phase shift (2). Over 100 years later, the transverse displacement of a beam transmitted near the edge of a spinning glass disk was observed (3). A similar setup allowed the study of a closely related effect for light traveling along the rotation axis of a spinning medium, which results in the rotation of the optical polarization state (4, 5), the mechanical Faraday effect (6).

The rotation of a linear polarization state originates from a phase difference between the right- and left-handed circular polarization states,

¹School of Physics and Astronomy (SUPA), University of Glasgow, Glasgow G12 8QQ, Scotland. ²Department of Physics, University of Ottawa, Ottawa, ON K1N 6N5, Canada. ³The Institute of Optics and Department of Physics and Astronomy, University of Rochester, Rochester, NY 14627, USA.

*To whom correspondence should be addressed. E-mail: sonja.franke-arnold@glasgow.ac.uk

which are the spin angular momentum states of light. However, light can also carry orbital angular momentum (OAM) arising from helical phase fronts and the associated azimuthal component of the Poynting vector (7). For a transverse phase profile given by $\exp(i\ell\phi)$, where ϕ describes the azimuthal angle, the OAM corresponds to $\ell\hbar$ per photon.

Whereas a phase shift between the spin angular momentum states leads to a rotation of the linear polarization state, a phase shift between the components with positive and negative OAM is manifested as a rotation of the transmitted intensity profile (8). A mechanical rotation of a medium is predicted to induce a rotational photon drag (9, 10), rotating the transmitted polarization state and the transmitted image through the same angle

$$\Delta\phi = \left(n_g - \frac{1}{n_\phi}\right) \frac{\Omega L}{c} \quad (1)$$

Here, n_g and n_ϕ are the group and phase refractive index, respectively; Ω is the angular frequency at which the medium rotates, L is the length of the medium, and c is the speed of light in a vacuum.

For a typical dielectric material with a window thickness of a few tens of millimeters and a rotation rate of ~ 1000 rpm, the resulting angle is on the order of a microradian. Although the rotation of polarization has been observed (4), the corresponding image rotation has not.

The small rotation angle makes a measurement very difficult, and as an alternative, we previously examined a rapidly spinning image incident upon a stationary window, where a megahertz rotation rate gave a delay in the spinning of the image by ~ 1 rad (11). A spinning image is just a superposition of beams at different frequencies that can be treated separately in a linear medium. In that experiment, however, the effect was complicated by the Galilean transformation of the frame that modified the incident angle of the light upon the interfaces and, through Snell's law, the angular displacement of the transmitted light. Because of this transformation, the lag in rotation arose simply from the delay in arrival time of the light due to the thickness of the optical medium, i.e., $(n_g - 1)\Omega L/c$ (12).

Rather than measuring the rotational lag between two images, our present experiment directly observes the rotation of the image, which becomes feasible when the angle of the rotation is enhanced by use of a slow-light medium. We used a ruby rod as the spinning medium and a stationary elliptical laser beam at 532 nm to act as the image. Ruby is an unusual material in that, by illuminating it with green light, one can probe an absorption that acts as a near perfect two-level system with a long (≈ 20 ms) upper-state lifetime. If the incident beam is subject to a slight temporal intensity modulation, the resulting modulation in the lower-state population leads to a modulation of the absorption that is, due to the long upper-state lifetime, slightly out of phase with the mod-

ulation of the incident intensity. This phase lag in the absorption distorts the intensity modulation of the transmitted light, resulting in an optical delay that is interpreted as a large group index.

The effective group index depends upon many factors, including the intensity and modulation amplitude of the light compared to the saturation intensity, and the modulation frequency compared to the inverse of the upper-state lifetime. Previously it had been shown that group indices of $\approx 10^6$ may be obtained from coherent population modulations (13–15).

When viewed in a rotating frame, the right- and left-handed helical states are subject to a rotational frequency shift (16, 17), which, because of the dispersion of the ruby, means that their phase indices differ. A phase shift therefore accumulates between the states upon propagation through the medium, leading to a rotation of the resulting image.

An image rotation is defined only if the incident light is not rotationally symmetric; for simplicity we have chosen an elliptical beam profile. This beam profile also provides the intensity modulation that causes a large group index in ruby. Even for a beam with constant intensity, the off-axis atoms in the spinning ruby rod experi-

ence an intensity modulation. The resulting delay and associated group index in general is a function of radius, intensity, and modulation rate and must be evaluated numerically (see supporting online material). For rotation speeds that are slow compared to the inverse of the upper-state lifetime, the group index is large. At higher speeds, the effect saturates and the group index decreases. Consequently, for rotation rates below that corresponding to the inverse of the upper-state lifetime, we anticipate a large effective group index, leading to substantial rotational drag of the transmitted beam profile.

In a preliminary experiment, we used a highly elliptical 2-W laser beam at 532 nm, focused through a 100-mm-long ruby rod. By focusing the beam into the ruby, it is possible to reach a high intensity, albeit with a complicated beam profile that changes upon propagation and makes the configuration hard to model. After transmission through the rod, the beam cross section is a single line that is readily observed on a viewing screen. Spinning the ruby rod at ≈ 30 Hz drags the orientation of the line by $\sim 5^\circ$. Figure 1 shows two images of the line for clockwise and anti-clockwise rotation, respectively (also see movie

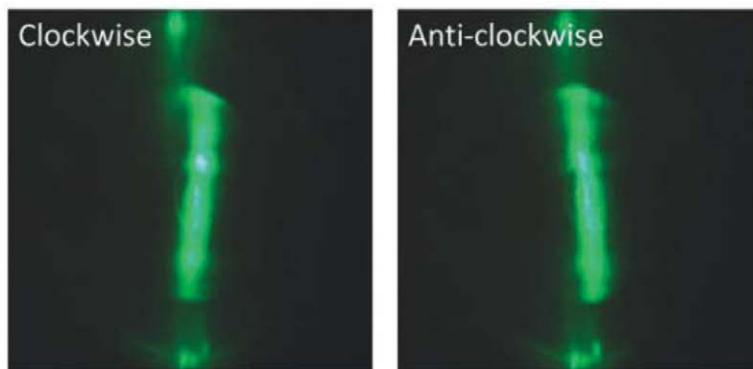


Fig. 1. An intense line of laser light is focused through a 100-mm-long ruby rod. The images show the transmitted intensity as recorded on a screen positioned ~ 500 mm behind the rod spinning at ± 30 Hz. The difference in line orientation between the two directions is $\sim 10^\circ$. The fixed light at the top and bottom of the images is transmitted around the sides of the ruby and hence not subject to any rotation.

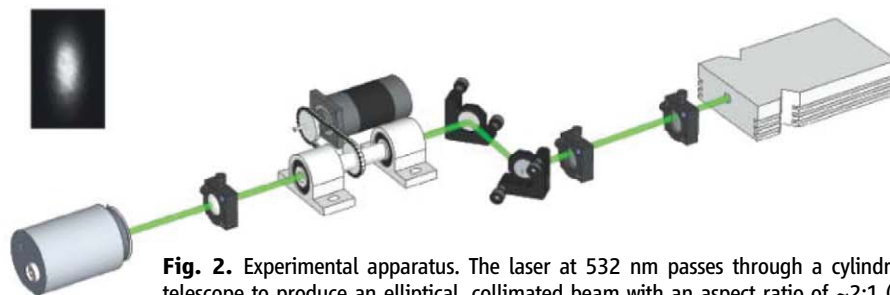


Fig. 2. Experimental apparatus. The laser at 532 nm passes through a cylindrical telescope to produce an elliptical, collimated beam with an aspect ratio of $\sim 2:1$ (see inset). The light is transmitted axially through a rotating ruby rod and monitored on a CCD camera. The ruby rod is mounted within a hollow cylinder, itself mounted within a standard engineering high-speed bearing. The rotation of the ruby rod is controlled by a servo-controlled, programmable stepper motor at up to ± 30 Hz.

S1). We attribute this rotation of the beam to the rotary image drag, enhanced by the high group index in the ruby. Within the limits of experimental observation, the resulting transmitted intensity pattern appears as a rotated line, as one would expect from a simple interpretation of rotary image drag in Eq. 1.

To quantitatively investigate the effect of rotary image drag in a self-pumped slow-light medium, we instead propagated a collimated elliptical beam through a 6-mm length of ruby rod spinning at up to 30 Hz, observing rotations of the intensity profile of some tenths of a degree.

The experimental setup is shown in Fig. 2. The collimated elliptical laser beam with major and minor axes of 2 mm and 0.9 mm, respectively (see inset of Fig. 2), was incident on the ruby rod, colinear with its rotation axis. The exit face of the rod was imaged with unity magnification to a low-noise charge-coupled device (CCD) detector array. The orientation of the elliptical intensity cross section was then analyzed from the CCD image with respect to its center in terms of its second-order moments to determine the angle between the major axis of the elliptical profile and the camera horizontal. For each rotation speed, the sense of rotation was switched several times over a period of a few seconds, and the

average difference in orientation of the major axis was recorded (Fig. 3 shows a typical recording). The process was repeated for each rotation speed and for two different levels of laser power (Fig. 4). For a constant group index of the medium, the rotation of the transmitted beam would simply be proportional to the rotational speed. However, in our case, the group index and hence the phase delay is itself a function of that speed (fig. S2), resulting in a leveling-off of the orientation angle for higher rotation speeds.

The vertical scaling of the data depends upon the saturation intensity and precise beam size, and therefore the total power of the beam was set as a free parameter within a 30% range of its measured value. The level of agreement between observations and predicted forms of the data is good, both with respect to the lower-speed linear growth of the image rotation and the higher-speed saturation that occurs when the rotation period is less than the upper-state lifetime of the ruby.

Our results show that the phenomenon of rotary photon drag applies not just to linear motion and image displacement, but also to rotational motion and image rotation. The Faraday effect arising from the mechanically induced difference in phase velocity for right- and left-handed cir-

cularly polarized light has an equivalent effect for orbital angular momentum. For orbital angular momentum, the difference in phase velocity results in a phase shift between right- and left-handed helical phase fronts, giving an image rotation. The observed rotation is compatible with the two rotation angles for polarization and image being the same.

References and Notes

1. A. Fresnel, *Ann. Chim. Physique* **9**, 57 (1818).
2. M. H. Fizeau, *Ann. Chim. Physique* **57**, 385 (1859); *Philos. Mag.* **19**, 245 (1860).
3. R. V. Jones, *Proc. R. Soc. London A Math. Phys. Sci.* **328**, 337 (1972).
4. R. V. Jones, *Proc. R. Soc. London A Math. Phys. Sci.* **349**, 423 (1976).
5. M. A. Player, *Proc. R. Soc. London A Math. Phys. Sci.* **349**, 441 (1976).
6. G. Nienhuis, J. P. Woerdman, I. Kuscser, *Phys. Rev. A* **46**, 7079 (1992).
7. L. Allen, M. W. Beijersbergen, R. J. C. Spreeuw, J. P. Woerdman, *Phys. Rev. A* **45**, 8185 (1992).
8. L. Allen, M. Padgett, *J. Mod. Opt.* **54**, 487 (2007).
9. M. Padgett *et al.*, *Opt. Lett.* **31**, 2205 (2006).
10. J. B. Götte, S. M. Barnett, M. Padgett, *Proc. R. Soc. London A* **463**, 2185 (2007).
11. J. Leach *et al.*, *Phys. Rev. Lett.* **100**, 153902 (2008).
12. The functional dependence with regard to the phase index differs between the propagation of a spinning image through a stationary rod and a stationary image through a spinning medium (Eq. 1). However, this difference becomes experimentally negligible in a slow-light medium where the large group index dominates.
13. M. S. Bigelow, N. N. Lepeshkin, R. W. Boyd, *Phys. Rev. Lett.* **90**, 113903 (2003).
14. M. S. Bigelow, N. N. Lepeshkin, R. W. Boyd, *Science* **301**, 200 (2003).
15. A. Schweinsberg, N. N. Lepeshkin, M. S. Bigelow, R. W. Boyd, S. Jarabo, *Europhys. Lett.* **73**, 218 (2006).
16. B. A. Garetz, *J. Opt. Soc. Am.* **71**, 609 (1981).
17. J. Courtial, D. A. Robertson, K. Dholakia, L. Allen, M. J. Padgett, *Phys. Rev. Lett.* **81**, 4828 (1998).
18. G. Piredda, R. W. Boyd, *J. Eur. Opt. Soc.* **2**, 07004 (2007).

Acknowledgments: This work is supported by the UK Engineering and Physical Sciences Research Council. M.J.P. thanks the Royal Society and the Wolfson Foundation. We acknowledge the financial support of the Future and Emerging Technologies (FET) program for Research of the European Commission, under the FET Open grant agreement PHORBITECH number FP7-ICT-255914. R.W.B. acknowledges support from the Defense Advanced Research Projects Agency (DARPA)—DSO Slow Light Program and from the Defense Threat Reduction Agency—Joint Science and Technology Office for Chemical and Biological Defense (grant HDTRA1-10-1-0025). The enhancement of image rotation in a slow-light medium was proposed by S.F.-A. and R.W.B., based on the spinning window for image drag previously investigated by M.J.P. The theoretical analysis was devised by S.F.-A. and R.B. and performed by S.F.-A. The experiment was designed by G.G. and M.J.P. and performed by G.G. All authors contributed to the writing of the manuscript.

Supporting Online Material

www.sciencemag.org/content/full/333/6038/65/DC1
Materials and Methods
Figs. S1 to S3
References
Movie S1

8 February 2011; accepted 27 April 2011
10.1126/science.1203984

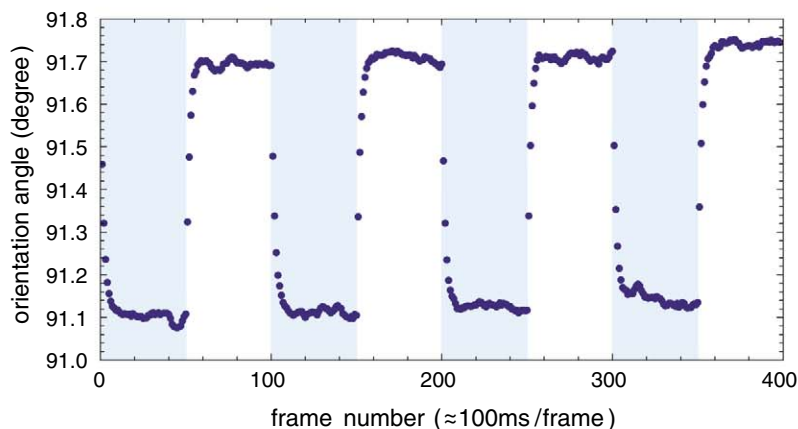
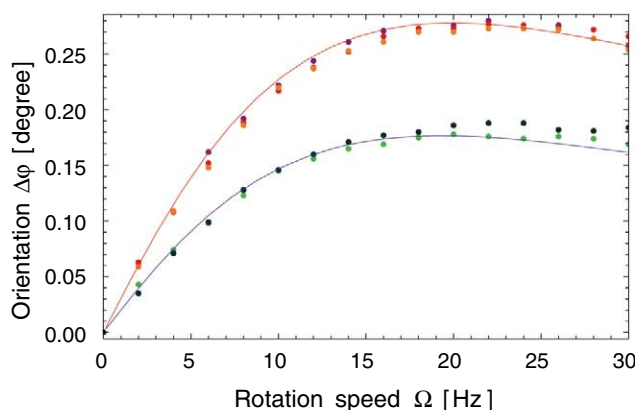


Fig. 3. Typical data of the orientation of the major axis of the elliptical beam profile for rotation speeds switched between ± 14 Hz.

Fig. 4. Rotation angle of the elliptical laser beam upon passage through a 6-mm-long ruby rod for a beam power of 1 W (blue, green) and 2 W (red, orange, purple). The solid lines are theoretical predictions of the model described in the supporting online material. The rotation angle is taken to be half the difference of the measured values for the ruby spinning in the forward and backward directions.



Superelastic Effect in Polycrystalline Ferrous Alloys

T. Omori,* K. Ando, M. Okano, X. Xu, Y. Tanaka, I. Ohnuma, R. Kainuma, K. Ishida

In superelastic alloys, large deformation can revert to a memorized shape after removing the stress. However, the stress increases with increasing temperature, which limits the practical use over a wide temperature range. Polycrystalline Fe-Mn-Al-Ni shape memory alloys show a small temperature dependence of the superelastic stress because of a small transformation entropy change brought about by a magnetic contribution to the Gibbs energies. For one alloy composition, the superelastic stress varies by 0.53 megapascal/°C over a temperature range from −196 to 240°C.

Since shape memory behavior was discovered in Au-Cd alloys (1), many shape memory alloy systems, such as Ti-Ni, Cu-Al-Ni, Ni-Mn-Ga, and Ni-Co-Mn-In alloys, have been reported (2–4). In contrast to metallic materials with elastic limits of about 0.2%, Ti-Ni alloys exhibit a large recoverable strain of up to 8% and are used in engineering and medical fields (5). Superelasticity is caused by a reversible phase transformation between the parent phase, stable under no stress, and the martensite phase, stabilized by stress. The critical stress for stress-induced martensitic transformations, σ_c , hereafter called superelastic stress, which corresponds to an effective yield stress in superelastic behavior, increases with increasing temperature T in agreement with the Clausius-Clapeyron relation (6):

$$\frac{d\sigma_c}{dT} = -\frac{\Delta S}{\epsilon \cdot V_m} \quad (1)$$

where ΔS is the molar entropy difference between the parent and martensite phases, ϵ is the strain caused by the phase transformation, and V_m is the molar volume. The rate of increase in Ti-Ni alloys is about 6 MPa °C^{−1}.

We recently reported that the ternary alloy Fe₄₉Mn₃₆Al₁₅ undergoes a martensitic transformation from the α parent phase with a body-centered cubic (bcc: A2) structure to a γ' martensite phase with a face-centered cubic (fcc: A1) structure (7); the prime in this phase notation represents a martensite phase. The sequence of the phase transformation from the α phase (high-temperature parent phase) to the γ' phase (low-temperature or stress-induced phase) in the Fe-Mn-Al alloy is unusual, because most Fe alloys exhibit a martensitic transformation from a γ phase with the A1 structure to a α' phase with the A2 or body-centered tetragonal (bct) structure. It is known that the superelastic behavior is usually attributed to a thermoelastic martensitic transformation, in which a martensite plate grows and shrinks upon cooling and heating, respectively (2). However, most Fe-based alloys, including the Fe-Mn-Al,

have a nonthermoelastic martensitic transformation with no reversibility in the microstructure and exhibit no superelasticity. Thermoelastic martensitic transformations have been reported in alloy systems with fully or partially ordered structures, such as Ti-Ni with the CsCl-type ordered bcc (B2) structure and Fe-Ni-Co-Ti (8) and Fe-Ni-Co-Al (9) alloys with coherent precipitates, Ni₃Ti and Ni₃Al, having a L1₂ structure in the γ phase. It is known that the B2 phase exists over a wide concentration range in Ni-Mn-Al system (10) and that a phase separation of the A2 and B2 phases occurs by low-temperature aging in Fe-Ni-Al (11). On the basis of the information, we tried adding a range of Ni to the Fe-Mn-Al alloy, and Fe_{43.5}Mn₃₄Al₁₅Ni_{7.5} superelastic alloy with nanosized particles of the B2 ordered phase in the A2 disordered matrix phase (fig. S2) was obtained.

The magnetization versus temperature (M - T) of Fe_{43.5}Mn₃₄Al₁₅Ni_{7.5} measured in a magnetic field of 0.05 T is shown in Fig. 1A for an as-solution-treated specimen and in Fig. 1B for a specimen aged at 200°C for 15 min (12). For both specimens, an abrupt decrease and increase in magnetization because of the martensitic transformation were detected in both cooling and heating cycles. The transformation process in Fig. 1A was found to have a temperature hysteresis, defined as $T_{Af} - T_{Ms}$ or $T_{As} - T_{Mf}$, of 150°C, where T_{Ms} and T_{Mf} are the martensitic transformation starting and finishing temperatures and T_{As} and T_{Af} the reverse transformation starting and finishing temperatures. Although temperature hysteresis in thermoelastic transformations is normally less than ~100°C (2, 13), the martensitic transformation in the Fe_{43.5}Mn₃₄Al₁₅Ni_{7.5} alloy is thermoelastic because growth and shrinkage of martensite plates are observed upon cooling and heating, respectively, as shown in Fig. 1B. The Fe_{43.5}Mn₃₄Al₁₅Ni_{7.5} alloy shows an abnormal magnetic change from a ferromagnetic parent phase to a weak magnetic martensite phase during cooling. Further aging at 200°C for 3 hours causes the martensitic transformation to be suppressed, and the M - T curve for the specimen aged at 200°C for 6 hours is shown in Fig. 1C. From the change of transformation behavior with aging, it is apparent that the martensitic transformation temperatures gradually decrease after aging at 200°C. In order to clarify the magnetic features of

the martensite phase, we measured magnetization of a specimen having a fully martensitic structure. Figure 1D shows the magnetization-versus-temperature curve obtained in a magnetic field of 10 kOe for a specimen with a single martensite phase obtained by a ~80% reduction in thickness

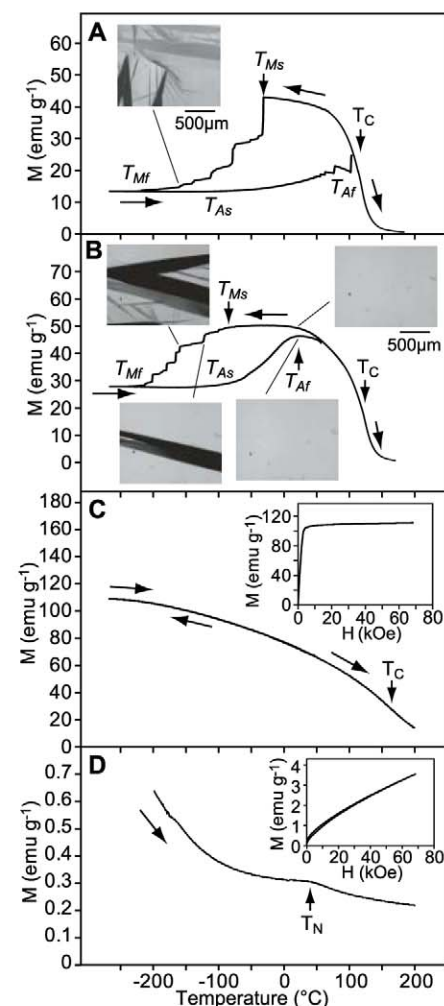
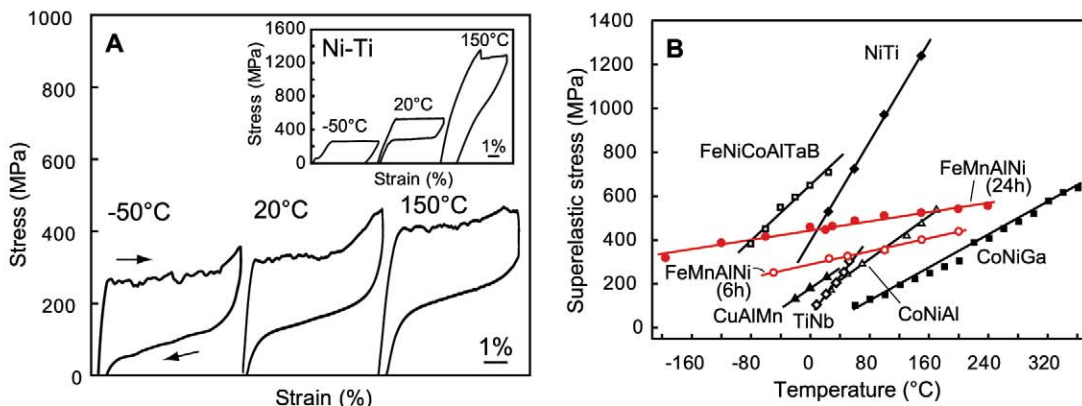


Fig. 1. Thermomagnetization curves of Fe_{43.5}Mn₃₄Al₁₅Ni_{7.5}. (A) Curve of the as-solution-treated sample in a magnetic field of 0.5 kOe. (Inset) Optical micrograph taken at −160°C. emu indicates electromagnetic unit. (B) Curve of the sample aged at 200°C for 15 min in a magnetic field of 0.5 kOe. (Insets) Optical micrographs taken at 20°C, −120°C, and −160°C in the cooling process and at 20°C in the heating process. (C) Curve of the sample aged at 200°C for 6 hours in a magnetic field of 10 kOe. (Inset) The magnetization versus magnetic field measured at 4.2 K. (D) Curve of the sample aged at 200°C for 6 hours and subsequently cold-rolled at a reduction rate of 80%, where the cold rolling was carried out in order to obtain the martensite phase. A magnetic field of 10 kOe was applied. (Inset) The magnetization versus magnetic field at 4.2 K. The Curie temperature of each specimen was determined to be 117°C, 124°C, and 165°C for (A), (B), and (C), respectively, and the Néel temperature is 40°C in (D).

Department of Materials Science, Graduate School of Engineering, Tohoku University, 6-6-02 Aoba-yama, Sendai 980-8579, Japan.

*To whom correspondence should be addressed. E-mail: omori@material.tohoku.ac.jp

Fig. 2. Superelastic properties of Fe-Mn-Al-Ni and its temperature dependence. **(A)** Stress-strain curves of $\text{Fe}_{43.5}\text{Mn}_{34}\text{Al}_{15}\text{Ni}_{7.5}$ aged at 200°C for 6 hours at various temperatures in a tensile test. (Inset) The superelasticity of commercial $\text{Ti}_{49.98}\text{Ni}_{50.02}$. Compared with Ti-Ni, the stress level in Fe-Mn-Al-Ni is insensitive to temperature. **(B)** Superelastic stress as a function of temperature in $\text{Fe}_{43.5}\text{Mn}_{34}\text{Al}_{15}\text{Ni}_{7.5}$ polycrystalline alloy and conventional $\text{Ti}_{49.98}\text{Ni}_{50.02}$, $\text{Fe}_{40.95}\text{Ni}_{28}\text{Co}_{17}\text{Al}_{11.5}\text{Ta}_{2.5}\text{B}_{0.05}$, $\text{Cu}_{71.9}\text{Al}_{16.6}\text{Mn}_{9.3}\text{Ni}_{2}\text{B}_{0.2}$, $\text{Ti}_{74}\text{Nb}_{26}$, and $\text{Co}_{37.6}\text{Ni}_{32.9}\text{Al}_{29.5}$ polycrystalline alloys and $\text{Co}_{49}\text{Ni}_{21}\text{Ga}_{30}$ single crystal. The stresses are in tension except for Co-Ni-Al and Co-Ni-Ga in compression.



after cold rolling. It was found that the martensite phase became antiferromagnetic below a Néel temperature, T_N , of 40°C. This result means that the martensitic transformation occurring at temperatures below 40°C is from a ferromagnetic to an antiferromagnetic state, which is similar to the magnetic transformation reported in FeRh alloy (14). Furthermore, in the as-solution-treated sample a large amount of parent phase remains at -160°C (Fig. 1A, inset), and the martensitic transformation does not apparently complete even by cooling to 4.2 K.

In order to examine ductility and superelasticity of the $\text{Fe}_{43.5}\text{Mn}_{34}\text{Al}_{15}\text{Ni}_{7.5}$ alloy, we carried out tensile tests at several temperatures. The stress-strain curves at -50°C, 20°C, and 150°C for the alloy aged at 200°C for 6 hours are shown in Fig. 2A. The alloy exhibits excellent ductility with a fracture tensile strain of over 8% and pseudoelastic behavior with a recoverable strain of over 5%. This is obtained despite no thermal martensitic transformation on cooling (Fig. 1C). We conducted in situ observation of the microstructure during the tensile testing to decide the origin of this pseudoelastic behavior. It was confirmed that the stress-induced martensite (SIM) plates appear upon loading and disappear upon unloading (fig. S4) and that this pseudoelastic behavior is superelasticity resulting from SIM transformation. The superelasticity depends on the relative grain size d/t and d/w , where d , t , and w are the mean grain diameter, thickness, and width of the sheet specimen, respectively, and the superelastic strain increases with increasing d/t and d/w as shown in fig. S5. The d/w in Fig. 2 is about 3.8.

The stress-strain curves obtained at different temperatures for the $\text{Fe}_{43.5}\text{Mn}_{34}\text{Al}_{15}\text{Ni}_{7.5}$ alloy are very similar to one another in contrast to those for a commercial Ti-Ni alloy (Fig. 2A). The superelastic stresses of the $\text{Fe}_{43.5}\text{Mn}_{34}\text{Al}_{15}\text{Ni}_{7.5}$ alloys are plotted with those of other polycrystalline superelastic alloys in Fig. 2B. The $\text{Fe}_{43.5}\text{Mn}_{34}\text{Al}_{15}\text{Ni}_{7.5}$ alloy exhibits superelasticity over a very wide temperature range from -196° to 240°C (i.e., the temperature window is about 440°C at least) for the one composition with very small temperature de-

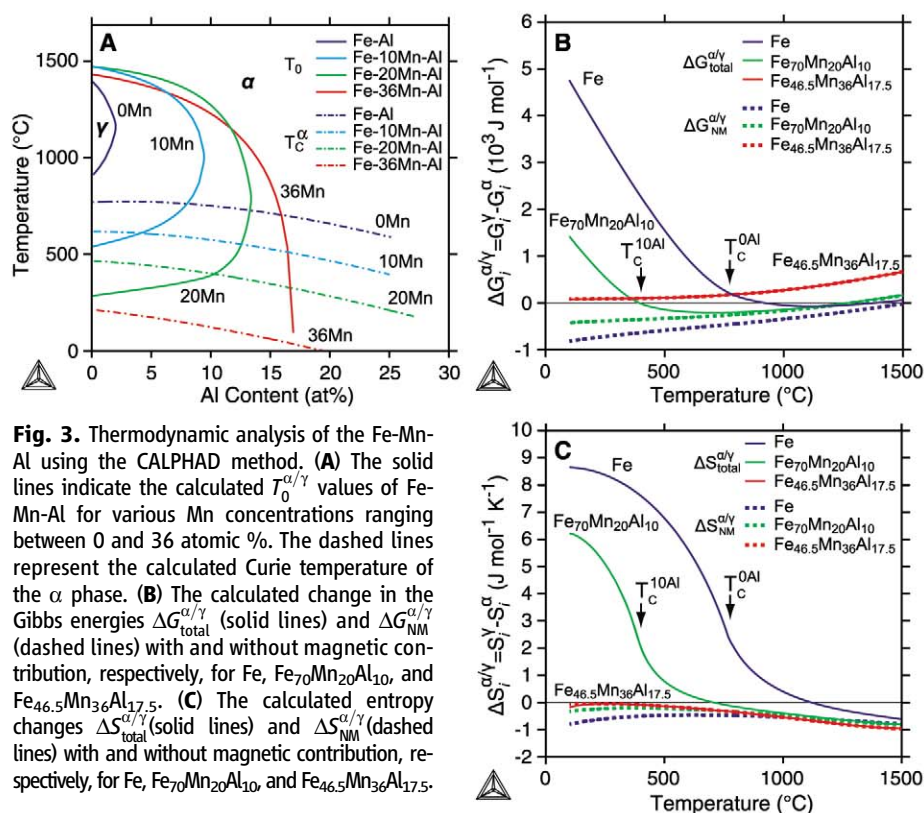


Fig. 3. Thermodynamic analysis of the Fe-Mn-Al using the CALPHAD method. **(A)** The solid lines indicate the calculated $T_0^{\alpha/\gamma}$ values of Fe-Mn-Al for various Mn concentrations ranging between 0 and 36 atomic %. The dashed lines represent the calculated Curie temperature of the α phase. **(B)** The calculated change in the Gibbs energies $\Delta G_{\text{total}}^{\alpha/\gamma}$ (solid lines) and $\Delta G_{\text{NM}}^{\alpha/\gamma}$ (dashed lines) with and without magnetic contribution, respectively, for Fe, $\text{Fe}_{70}\text{Mn}_{20}\text{Al}_{10}$, and $\text{Fe}_{46.5}\text{Mn}_{36}\text{Al}_{17.5}$. **(C)** The calculated entropy changes $\Delta S_{\text{total}}^{\alpha/\gamma}$ (solid lines) and $\Delta S_{\text{NM}}^{\alpha/\gamma}$ (dashed lines) with and without magnetic contribution, respectively, for Fe, $\text{Fe}_{70}\text{Mn}_{20}\text{Al}_{10}$, and $\text{Fe}_{46.5}\text{Mn}_{36}\text{Al}_{17.5}$.

pendence of superelastic stress. It can be seen that the slopes ($=d\sigma_s/dT$) of the plots for the Fe-Mn-Al-Ni specimens aged at 200°C for 6 and 24 hours are 0.74 MPa °C⁻¹ and 0.53 MPa °C⁻¹, respectively. Furthermore the temperature dependences are smaller, roughly by one order of magnitude, than those in conventional superelastic alloys, Ti-Ni (5.7 MPa °C⁻¹), Fe-Ni-Co-Al-Ta-B (3.1 MPa °C⁻¹), Cu-Al-Mn [2.4 MPa °C⁻¹ (15)], Ti-Nb [4.4 MPa °C⁻¹ (16)], Co-Ni-Al [2.5 MPa °C⁻¹ (17)], and Co-Ni-Ga [1.9 MPa °C⁻¹ (17)] (table S1). The temperature-insensitive superelasticity has also been obtained in an $\text{Fe}_{45.5}\text{Mn}_{32}\text{Al}_{15}\text{Ni}_{7.5}$ alloy with higher superelastic stress by about 150 MPa. The ΔS can be calculated by Eq. 1 using the experimental value $d\sigma_s/dT$ and the molar volume V_m when we know the ϵ . However, it is difficult to

determine the ϵ in the polycrystalline specimen in Fig. 2. Therefore, we conducted a tensile test at various temperatures in an $\text{Fe}_{43.5}\text{Mn}_{34}\text{Al}_{15}\text{Ni}_{7.5}$ single crystal, and the ΔS was determined as being -0.43 J mol⁻¹ K⁻¹ by using the experimental results of $d\sigma_s/dT = 0.60$ MPa °C⁻¹ and $\epsilon = 0.097$ (fig. S1) and $V_m = 7.366 \times 10^{-6}$ m³ mol⁻¹.

According to Eq. 1, the temperature dependence of superelastic stress is proportional to ΔS under fixed ϵ and V_m . We discuss the temperature-insensitive superelasticity from a thermodynamic viewpoint by using the phenomenological CALPHAD (calculation of phase diagrams) method. Because the calculation for the quaternary two-phase alloys is complicated and Ni content in the matrix is expected to be low resulting from the precipitation of the B2 (NiAl) phase, we con-

sidered the thermodynamic quantities of the α (A2) and γ (A1) phases for the Fe-Mn-Al ternary system (18) rather than for Fe-Mn-Al-Ni. Figure 3A shows the equilibrium temperature $T_0^{\alpha/\gamma}$ lines calculated for Fe-Mn-Al alloys with various Mn concentrations, together with the Curie temperatures T_C^{α} of the α phase. $T_0^{\alpha/\gamma}$ is the temperature at which the Gibbs energies of the α and γ phases are equal and approximately corresponds to $T_0^{\alpha/\gamma} \approx (T_{Ms} + T_{Af})/2$ in thermoelastic martensitic transformation of a single-crystal specimen (19). From Fig. 3A it can be seen that the α phase is substantially stabilized near T_C^{α} , forming so-called γ loops, up to 30 atomic % Mn, where the conventional γ/α' martensitic transformation takes place on cooling from the γ to the α region. With increasing Mn content and for Al content above 15%, T_C^{α} decreases to near room temperature and the γ loop diminishes, as seen for the ^{36}Mn alloy. In this condition, a diffusionless martensitic transformation can take place from the α to the γ' phase because it can go through the $T_0^{\alpha/\gamma}$ line at low temperatures.

Figure 3, B and C, shows the differences in Gibbs energy, $\Delta G_{\text{total}}^{\alpha/\gamma}$ and $\Delta G_{\text{NM}}^{\alpha/\gamma}$, and the differences in entropy, $\Delta S_{\text{total}}^{\alpha/\gamma}$ and $\Delta S_{\text{NM}}^{\alpha/\gamma}$, between the α and γ phases calculated for pure Fe, $\text{Fe}_{70}\text{Mn}_{20}\text{Al}_{10}$, and $\text{Fe}_{46.5}\text{Mn}_{36}\text{Al}_{17.5}$ alloys, where $\Delta G_{\text{total}}^{\alpha/\gamma}$ and $\Delta S_{\text{total}}^{\alpha/\gamma}$ are defined as

$$\begin{aligned} G_{\text{total}}^{\alpha} &= G_{\text{NM}}^{\alpha} + \Delta G_{\text{mag}}^{\alpha}, \\ G_{\text{total}}^{\gamma} &= G_{\text{NM}}^{\gamma} + \Delta G_{\text{mag}}^{\gamma} \end{aligned} \quad (2)$$

$$\Delta G_{\text{NM}}^{\alpha/\gamma} = G_{\text{NM}}^{\gamma} - G_{\text{NM}}^{\alpha} \quad (3)$$

$$\Delta G_{\text{mag}}^{\alpha/\gamma} = \Delta G_{\text{mag}}^{\gamma} - \Delta G_{\text{mag}}^{\alpha} \quad (4)$$

$$\begin{aligned} \Delta G_{\text{total}}^{\alpha/\gamma} &= G_{\text{total}}^{\gamma} - G_{\text{total}}^{\alpha} \\ &= G_{\text{NM}}^{\gamma} - G_{\text{NM}}^{\alpha} + \Delta G_{\text{mag}}^{\gamma} - \Delta G_{\text{mag}}^{\alpha} \\ &= \Delta G_{\text{NM}}^{\alpha/\gamma} + \Delta G_{\text{mag}}^{\alpha/\gamma} \end{aligned} \quad (5)$$

$$S_{\text{total}}^{\alpha} = S_{\text{NM}}^{\alpha} + \Delta S_{\text{mag}}^{\alpha},$$

$$S_{\text{total}}^{\gamma} = S_{\text{NM}}^{\gamma} + \Delta S_{\text{mag}}^{\gamma} \quad (6)$$

$$\Delta S_{\text{NM}}^{\alpha/\gamma} = S_{\text{NM}}^{\gamma} - S_{\text{NM}}^{\alpha} \quad (7)$$

$$\Delta S_{\text{mag}}^{\alpha/\gamma} = \Delta S_{\text{mag}}^{\gamma} - \Delta S_{\text{mag}}^{\alpha} \quad (8)$$

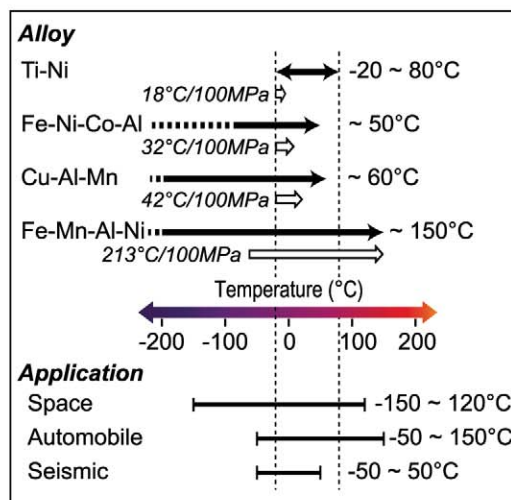
$$\begin{aligned} \Delta S_{\text{total}}^{\alpha/\gamma} &= S_{\text{total}}^{\gamma} - S_{\text{total}}^{\alpha} \\ &= S_{\text{NM}}^{\gamma} - S_{\text{NM}}^{\alpha} + \Delta S_{\text{mag}}^{\gamma} - \Delta S_{\text{mag}}^{\alpha} \\ &= \Delta S_{\text{NM}}^{\alpha/\gamma} + \Delta S_{\text{mag}}^{\alpha/\gamma} \end{aligned} \quad (9)$$

where Gibbs energy, G_i^{ϕ} , and entropy, S_i^{ϕ} , refer to the ϕ phase. Here, the subscript i is either mag or NM and indicates whether in the calculation the magnetic term has been included or excluded, respectively. As shown by the solid lines of Fig. 3B, $\Delta G_{\text{total}}^{\alpha/\gamma}$ of pure Fe and of $\text{Fe}_{70}\text{Mn}_{20}\text{Al}_{10}$ abruptly increases with decreasing temperature in the region below T_C^{α} of the α phase. However, $\Delta G_{\text{NM}}^{\alpha/\gamma}$ monotonically decreases, as demonstrated by the dashed lines of Fig. 3B. This means that the ferromagnetism of the α phase strongly affects phase stability and that the bcc “ferrite” phase never appears unless there is a magnetic contribution, as pointed out by Zener (20). The magnetic contribution to $\Delta S_{\text{total}}^{\alpha/\gamma}$ of pure Fe and $\text{Fe}_{70}\text{Mn}_{20}\text{Al}_{10}$ is very large (Fig. 3C). Decreasing T_C^{α} of the α phase, by adding both Mn and Al, reduces the effect of the magnetic term in $\Delta G_{\text{mag}}^{\alpha/\gamma}$ and $\Delta S_{\text{mag}}^{\alpha/\gamma}$ (Fig. 3, A to C). In $\text{Fe}_{46.5}\text{Mn}_{36}\text{Al}_{17.5}$, which is selected as a ternary alloy with phase stability and magnetic properties similar to those of the $\text{Fe}_{43.5}\text{Mn}_{34}\text{Al}_{15}\text{Ni}_{7.5}$ alloy (Fig. 1), the magnetic contribution is further reduced, the differences between $\Delta G_{\text{total}}^{\alpha/\gamma}$ and $\Delta G_{\text{NM}}^{\alpha/\gamma}$ and between $\Delta S_{\text{total}}^{\alpha/\gamma}$ and $\Delta S_{\text{NM}}^{\alpha/\gamma}$ are hardly observed, and the entropy change $\Delta S_{\text{total}}^{\alpha/\gamma}$ becomes close to zero. Besides

the ferromagnetism of the α phase, the antiferromagnetism of the γ phase is also important, and the magnetic effect of the antiferromagnetism (21, 22) should be taken into account to obtain the small $\Delta S_{\text{total}}^{\alpha/\gamma}$. The result calculated for $\text{Fe}_{46.5}\text{Mn}_{36}\text{Al}_{17.5}$ (Fig. 3C) is comparable to the ΔS ($= -0.43 \text{ J mol}^{-1} \text{ K}^{-1}$) for $\text{Fe}_{43.5}\text{Mn}_{34}\text{Al}_{15}\text{Ni}_{7.5}$ evaluated from Eq. 1. The ΔS of Fe-Mn-Al-Ni is smaller by one order of magnitude than the $-4.37 \text{ J mol}^{-1} \text{ K}^{-1}$ found in Ti-Ni (23), the $-6.28 \text{ J mol}^{-1} \text{ K}^{-1}$ in Fe-Ni (24), and those in other superelastic alloys (table S1). The temperature-insensitive superelastic effect is considered to be strongly related to the magnetic contribution to the thermodynamic quantities. Because the driving force for thermal martensitic transformation ΔG is given with supercooling ΔT by $\Delta G \approx \Delta S \cdot \Delta T$ and thermal hysteresis is inversely proportional to ΔS , the large thermal hysteresis shown in Fig. 1, A and B, is apparently brought about by the small ΔS .

A small temperature dependence of superelasticity over a wide temperature range is very important for practical applications because structural and functional materials are, in most cases, subjected to change in temperature. Figure 4 shows the temperature ranges in which the superelasticity can be obtained and the temperature width giving the change of superelastic stress of 100 MPa for the commercial Ti-Ni, Fe-Ni-Co-Al, and Cu-Al-Mn and the present Fe-Mn-Al-Ni alloy. The temperature of matter in space (Earth's orbit) changes from about -150°C in the shade to about 120°C under sunlight, and for most automotive applications operation at temperatures ranging from about -50 to 150°C is required (Fig. 4). Ti-Ni applications are limited to temperatures lower than about 80°C . This means that Fe-Mn-Al-Ni has potential for use as a superelastic alloy in severe environments, such as high-integrity seals, joints, and controls of a broad variety in automobile, aeroplane, and space systems. Recently, superelastic alloys have attracted much attention for seismic applications because they can exhibit recentering and damping capabilities against strong earthquakes (25, 26). However, high cost because of raw materials and the forming and machining of Ti-Ni is an obstacle for the application of superelastic alloys, and its implementation has been limited to a few historic buildings (27). Because the Fe-Mn-Al-Ni alloy is composed of common metals and has high workability as well as small temperature dependence, it offers great promise as a candidate for large-scale applications such as seismic dampers and isolators.

Fig. 4. Operational temperature range of polycrystalline superelastic alloys. The arrows indicate the temperature regions in which superelasticity can be obtained, and the temperature width over which the superelastic stress changes by 100 MPa is also shown.



References and Notes

1. A. Ölander, *J. Am. Chem. Soc.* **56**, 3819 (1932).
2. K. Otsuka, C. M. Wayman, in *Shape Memory Materials*, K. Otsuka, C. M. Wayman, Eds. (Cambridge Univ. Press, Cambridge, 1998), pp. 1–48.
3. T. Kakeshita, K. Ullakko, *MRS Bull.* **27**, 105 (2002).
4. R. Kainuma *et al.*, *Nature* **439**, 957 (2006).
5. T. W. Duerig, K. N. Melton, D. Stöckel, C. M. Wayman, *Engineering Aspects of Shape Memory Alloys* (Butterworth-Heinemann, London, 1990).

6. P. Wollants, M. De Bonte, J. R. Roos, *Z. Metallk.* **70**, 113 (1979).
7. K. Ando, T. Omori, I. Ohnuma, R. Kainuma, K. Ishida, *Appl. Phys. Lett.* **95**, 212504 (2009).
8. T. Maki, K. Kobayashi, M. Minato, I. Tamura, *Scr. Metall.* **18**, 1105 (1984).
9. Y. Tanaka *et al.*, *Science* **327**, 1488 (2010).
10. R. Kainuma, M. Ise, K. Ishikawa, I. Ohnuma, K. Ishida, *J. Alloy. Comp.* **269**, 173 (1998).
11. S. M. Hao, T. Takayama, K. Ishida, T. Nishizawa, *Metall. Trans.* **15**, 1819 (1984).
12. Materials and methods are available as supporting material on Science Online.
13. T. Maki, in *Shape Memory Materials*, K. Otsuka, C. M. Wayman, Eds. (Cambridge Univ. Press, Cambridge, 1998), pp. 117–132.
14. L. Muldrew, F. de Bergevin, *J. Chem. Phys.* **35**, 1904 (1961).
15. Y. Sutou, N. Koeda, T. Omori, R. Kainuma, K. Ishida, *Acta Mater.* **57**, 5759 (2009).
16. H. Y. Kim, S. Hashimoto, J. I. Kim, H. Hosoda, S. Miyazaki, *Mater. Trans.* **45**, 2443 (2004).
17. J. Ma, I. Karaman, R. D. Noebe, *Int. Mater. Rev.* **55**, 257 (2010).
18. R. Umno *et al.*, *J. Phase Equilibria Diffus.* **27**, 54 (2006).
19. H. C. Tong, C. M. Wayman, *Acta Metall.* **22**, 887 (1974).
20. C. Zener, *J. Met.* **7**, 619 (1955).
21. S. S. Yan *et al.*, *Solid State Commun.* **54**, 831 (1985).
22. G. A. Pérez Alcazar, E. Galvão da Silva, C. Paduani, *Hyperfine Interact.* **66**, 221 (1991).
23. W. Tang, R. Sandström, Z. G. Wei, S. Miyazaki, *Metall. Mater. Trans. A Phys. Metall. Mater. Sci.* **31**, 2423 (2000).
24. C. L. Magee, R. G. Davies, *Acta Metall.* **20**, 1031 (1972).
25. E. J. Graesser, F. A. Cozzarelli, *J. Eng. Mech.* **117**, 2590 (1991).
26. M. Dolce, D. Cardone, R. Marnetto, *Earthquake Eng. Struct. Dynam.* **29**, 945 (2000).
27. A. Abbott, *Nature* **414**, 572 (2001).

Acknowledgments: The authors are grateful to K. R. A Ziebeck, Cavendish Laboratory, University of Cambridge, for help

in critical reading. This work was supported by the Grants-in-Aid for Scientific Research from Japan Society for the Promotion of Science and by the Global Center of Excellence Program "Materials Integration (International Center of Education and Research), Tohoku University," Ministry of Education, Culture, Sports, Science, and Technology. A patent application has been filed on the materials, including the alloy presented herein.

Supporting Online Material

www.sciencemag.org/cgi/content/full/333/6038/68/DC1
Materials and Methods

SOM Text

Figs. S1 to S6

Table S1

References (28–41)

27 December 2010; accepted 13 May 2011
10.1126/science.1202232

Solvated Electrons in High-Temperature Melts and Glasses of the Room-Temperature Stable Electride $[\text{Ca}_{24}\text{Al}_{28}\text{O}_{64}]^{4+} \cdot 4\text{e}^-$

Sung Wng Kim,¹ Terumasa Shimoyama,² Hideo Hosono^{1,2}

Solvated electrons in alkali metal-ammonia solutions have attracted attention as a prototype electronic conductor and chemical reducing agent for over a century. However, solvated electrons have not been realized in a high-temperature melt or glass of an oxide system to date. We demonstrated the formation of persistent solvated electrons in both a high-temperature melt and its glass by using the thermally stable electride $[\text{Ca}_{24}\text{Al}_{28}\text{O}_{64}]^{4+} \cdot 4\text{e}^-$ (C12A7:e⁻) and controlling the partial pressure of oxygen. The electrical and structural properties of the resulting melt and glass differ from those of the conventional C12A7:O²⁻ oxide, exhibiting metallic and hopping conduction, respectively, and a glass transition temperature that is ~160 kelvin lower than that of C12A7:O²⁻ glass. Solvated electrons reside in cage structures in C12A7:e⁻ and form a diamagnetic paired state.

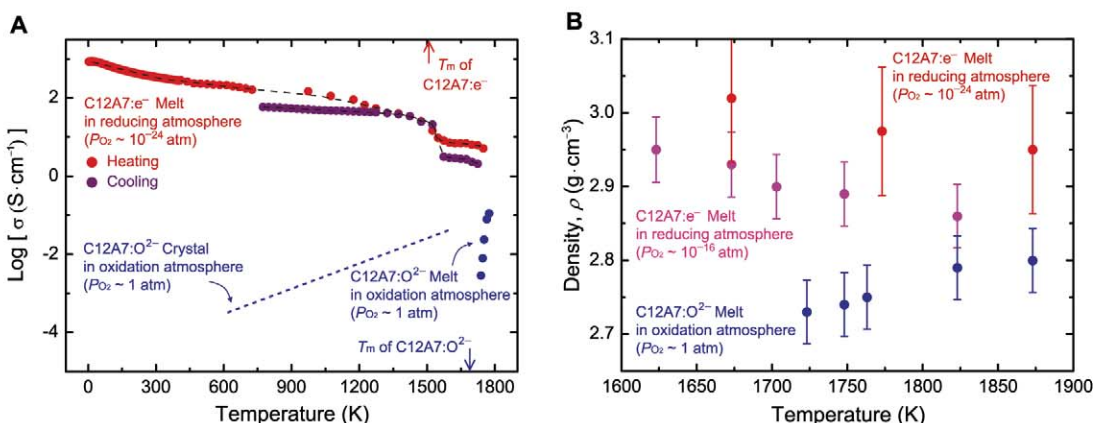
Solvated electrons in alkali metal-ammonia solution have been a diverse stem for scientific and applied researches (1). Furthermore, alkali metal-amine solutions containing solvated electrons can be condensed into ionic solids, known as electrides, in which electrons are

trapped in well-defined structural cavities and/or channels in matrices (2). Organic electrides can be created in which organic complexants, such as crown ethers, bind electrons, but these compounds are thermally unstable (2). This drawback provoked the development of thermally

stable electrides based on inorganic compounds, such as calcium aluminum oxide (12CaO·7Al₂O₃, abbreviated as C12A7:O²⁻). In this compound, O²⁻ is a caged species that compensates for the positive charge of the ~0.4-nm cage, and an electride can be formed by displacing this anion (3, 4). The caged electrons are protected from air and moisture even near room temperature (RT) because of the small size of the windows (diameters of ~0.1 nm) connecting the cages.

C12A7:e⁻ can be synthesized by means of various chemical and physical processes. We reported that strongly reduced C12A7:O²⁻ melt crystallizes to form C12A7:e⁻ and that single crystals of C12A7:e⁻ can be grown from polycrystalline C12A7:e⁻ by the floating zone (FZ) melting method under a strongly reducing atmosphere (5, 6). These findings imply that the electrons persist in the cages just below melting point (*T_m*) under a strongly reducing atmosphere. Because

Fig. 1. (A) The temperature dependence of σ of C12A7:e⁻ and C12A7:O²⁻ melts. The σ of C12A7:e⁻ melt decreases as the temperature increases, showing metallic conduction. In contrast, a melt of the mother compound, C12A7:O²⁻ oxide, shows ionic conduction. Upon melting, the σ of C12A7:e⁻ electride decreases to several siemens, which is an order of magnitude lower than that of the crystalline electride just below *T_m*. The sudden decrease in the σ of C12A7:O²⁻ on melting is ascribed to the disappearance of free O²⁻ ions accommodated in the cages because of the collapse of the three-dimensional network of sub-nanometer-sized cages that serve as the conduction pathway for oxide ions. The activation of ionic conduction in the C12A7:O²⁻ melt (6.3 eV) is related to viscosity (19), implying that dissociation of O²⁻ ions from the polymerized network structures determines both the rate of ionic conduction



and viscous flow. (B) Density of C12A7:e⁻ and C12A7:O²⁻ melts as a function of temperature. All data were acquired during heating. The red and pink circles represent the densities of C12A7:e⁻ melts measured under $P_{\text{O}_2} \sim 10^{-24}$ and $\sim 10^{-16}$ atm, respectively. The error range was $\pm 3\%$ for the red and $\pm 2\%$ for the pink and blue data points.

the excess electrons in alkali metal-molten salt solutions at high temperature have been studied extensively (7), it is of both fundamental and applied interest whether a high concentration of solvated electrons persist in high-temperature melts of typical refractory oxides because the precursor C12A7:O^{2-} , which is a by-product from iron smelting processes, exhibits $T_m \sim 1688$ K (8). Because CaO and Al_2O_3 are both stable oxides and typical electrical insulators, the conventional melt of C12A7:O^{2-} does not contain carrier electrons in the molten state. Thus, the question arises: Do solvated electrons exist in the melt of refractory oxide-based C12A7:e^- —that is, like the solvated electrons in alkali metal-ammonia solutions, but at much higher temperatures? To answer this, we studied the physical properties of the melt of C12A7:e^- electrode under a low-oxygen partial pressure (P_{O_2}). In addition, we examined structural and electrical properties of glasses prepared by rapidly quenching the C12A7:e^- melt so as to obtain structural information about the melt and realize a new type of amorphous semiconducting oxide.

The electrical conductivity (σ) of C12A7:e^- at elevated temperature decreases monotonically as the temperature increases up to 1750 K (Fig. 1A). Although a small decrease in σ is observed around the melting point ($T_m \sim 1500$ K) (fig. S3), the dependence does not change below and above T_m , so the C12A7:e^- melt exhibits metallic conduction. In contrast, σ increases with temperature in a C12A7:O^{2-} melt, like that of a conventional oxide. The C12A7:e^- electrode melt exhibits a higher density (ρ) than that of a C12A7:O^{2-} melt, by $\sim 10\%$ at 1773 K (Fig. 1B).

This difference suggests that there are marked structural differences between the melts of C12A7:e^- and C12A7:O^{2-} . To clarify this possibility, we rapidly quenched the C12A7:e^- melt from ~ 1873 K using a twin-roller at RT and examined the resulting glasses. When the C12A7:e^- melt is quenched, it is imperative to maintain a low P_{O_2} in order to prevent oxidation of the melt (figs. S1, S4, and S5). Thus, we attached a homemade chamber containing a twin-roller to the melting system. The quenched black sample (C12A7:e^- electrode glass) had a thickness of ~ 50 μm (Fig. 2A, inset). The x-ray diffraction (XRD) pattern of the glass shows a broad halo, and we only observed a ring pattern of transmission electron microscopy (TEM) electron diffraction (fig. S2), indicating that the glass was fully amorphous. Figure 2A shows the differential thermal analysis (DTA) of the C12A7:e^- glass, revealing a distinct shift in the base line at ~ 973 K that corresponds to the glass transition temperature (T_g). T_g is ~ 160 K lower than that of the conventional C12A7:O^{2-} glass. This difference strongly suggests that the network structure of C12A7:e^- glass differs substantially from that of C12A7:O^{2-} glass.

Figure 2B shows the temperature dependence of σ of C12A7:e^- glass. The conductivity near RT is $\sim 10^{-7}$ S cm^{-1} and increases with in-

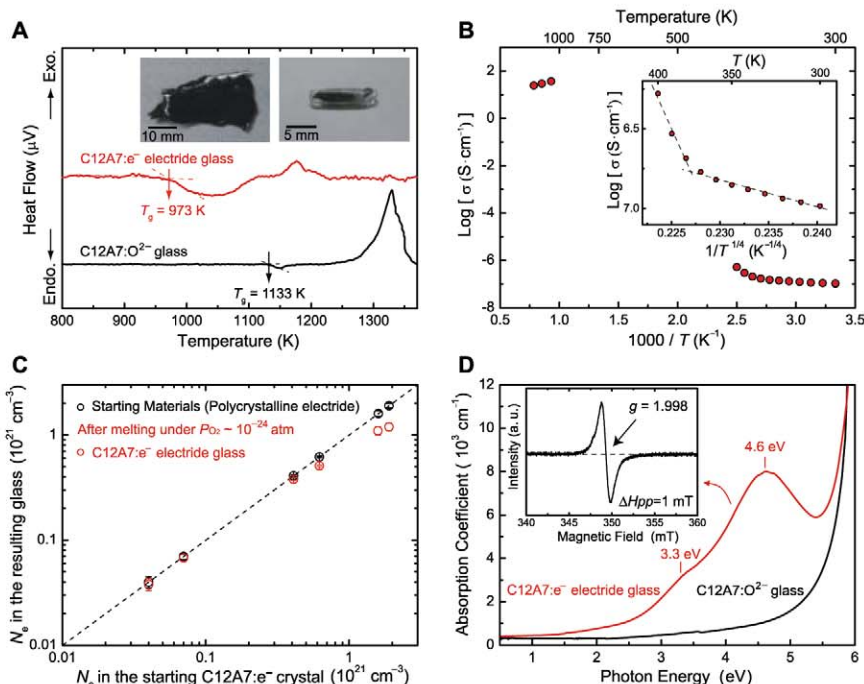
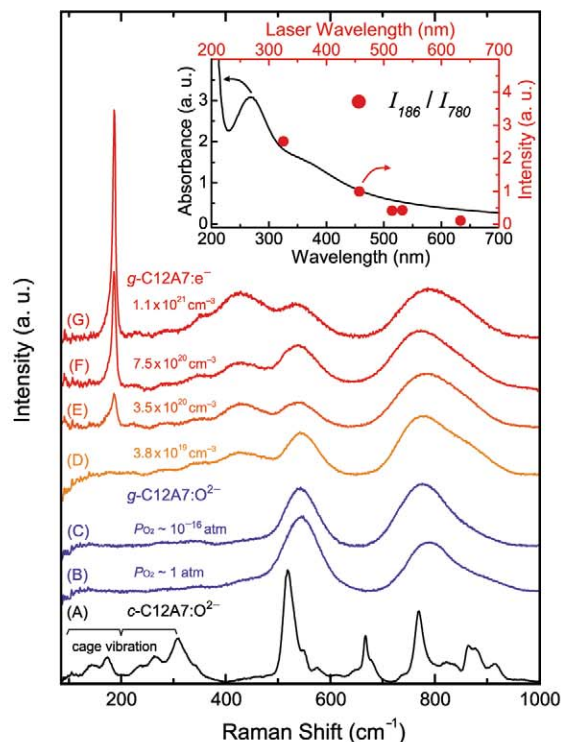


Fig. 2. (A) DTA comparison of the samples obtained by quenching C12A7:e^- (red line) and C12A7:O^{2-} melts (black line). The left inset shows a photograph of the C12A7:e^- glass, which was sealed in a silica capsule (right inset) under a vacuum to avoid oxidation during heating. The combined XRD, TEM (fig. S2), and DTA results reveal that a glass with a T_g of 973 K was obtained. (B) The σ of C12A7:e^- glass. The σ increases as the temperature increases, showing semiconducting behavior following $\log \sigma \propto T^{-1/4}$. When the glass is crystallized under an atmosphere of $P_{\text{O}_2} \sim 10^{-24}$ atm, σ shows the same temperature dependence as that of the parent electrode at high temperature. The σ of C12A7:O^{2-} glass is lower than the detection limit (10^{-10} S cm^{-1}) at RT. (C) Correlation of the N_e in C12A7:e^- glasses and that in the starting C12A7:e^- electrode used for melting. The dashed line shows the value of N_e in the starting C12A7:e^- electrodes. (D) Optical absorption spectra of C12A7:e^- glass (red line) and C12A7:O^{2-} glass (black line). The band at 3.3 eV is assigned to F^+ -like centers containing trapped electrons; their concentration was determined to be $\sim 5 \times 10^{18}$ cm^{-3} from an ESR spectrum (inset).

Fig. 3. Raman spectra of a C12A7:O^{2-} crystal ($c\text{-C12A7:O}^{2-}$), C12A7:O^{2-} glasses ($g\text{-C12A7:O}^{2-}$), and C12A7:e^- glasses ($g\text{-C12A7:e}^-$) with different N_e . The C12A7:O^{2-} glasses (B) and (C) were obtained by quenching a melt of C12A7:O^{2-} oxide under an oxidizing atmosphere of $P_{\text{O}_2} \sim 1$ atm by using an alumina crucible and a reducing atmosphere of $P_{\text{O}_2} \sim 10^{-16}$ atm by using a carbon crucible (11), respectively. The wavelength of the excitation laser was 457 nm. (Inset) The relationship of the Raman intensity ratio (I_{186}/I_{780}) of the 186 cm^{-1} band to the 780 cm^{-1} band measured with excitation lasers of various wavelengths. The optical absorption spectrum of C12A7:e^- glass [sample (G)] is shown to clarify the resonance effect.



creasing temperature. The temperature dependence of $\log \sigma$ is proportional to $T^{-1/4}$ rather than T^{-1} , indicating that electronic conduction is controlled by variable-range hopping (VRH). This temperature dependence implies that the C12A7:e^- glass contains a high concentration of localized electrons. Moreover, this change of conduction mechanism—from metallic conduction in the melt to VRH conduction in the glass—is similar to that reported in an amorphous thin film of metallic sodium-ammonia solution containing solvated electrons (9).

Next, we used iodometry (10) to confirm the presence of electrons and quantify the electron concentration (N_e) in different C12A7:e^- glasses. We prepared glasses by quenching melts of C12A7:e^- containing different N_e under an atmosphere of $\text{PO}_2 \sim 10^{-24}$ atm. The relation between N_e in the polycrystalline C12A7:e^- used to form the melts and N_e in the resulting C12A7:e^- glasses is shown in Fig. 2C. The observed linear relation shows that N_e is retained in C12A7:e^- glasses. That is, C12A7:e^- glasses exhibit a maximum N_e of $1.1 \times 10^{21} \text{ cm}^{-3}$, which is almost the same as that of recrystallized C12A7:e^- from a melt of C12A7:e^- with N_e of $1.7 \times 10^{21} \text{ cm}^{-3}$. We verified N_e values by measuring the weight gain caused by oxidation using thermogravimetry (TG). We checked whether solvated electrons were generated in the preparation of glasses by comparing N_e of a glass obtained from a C12A7:O^{2-} oxide melt under the present PO_2 atmosphere and a

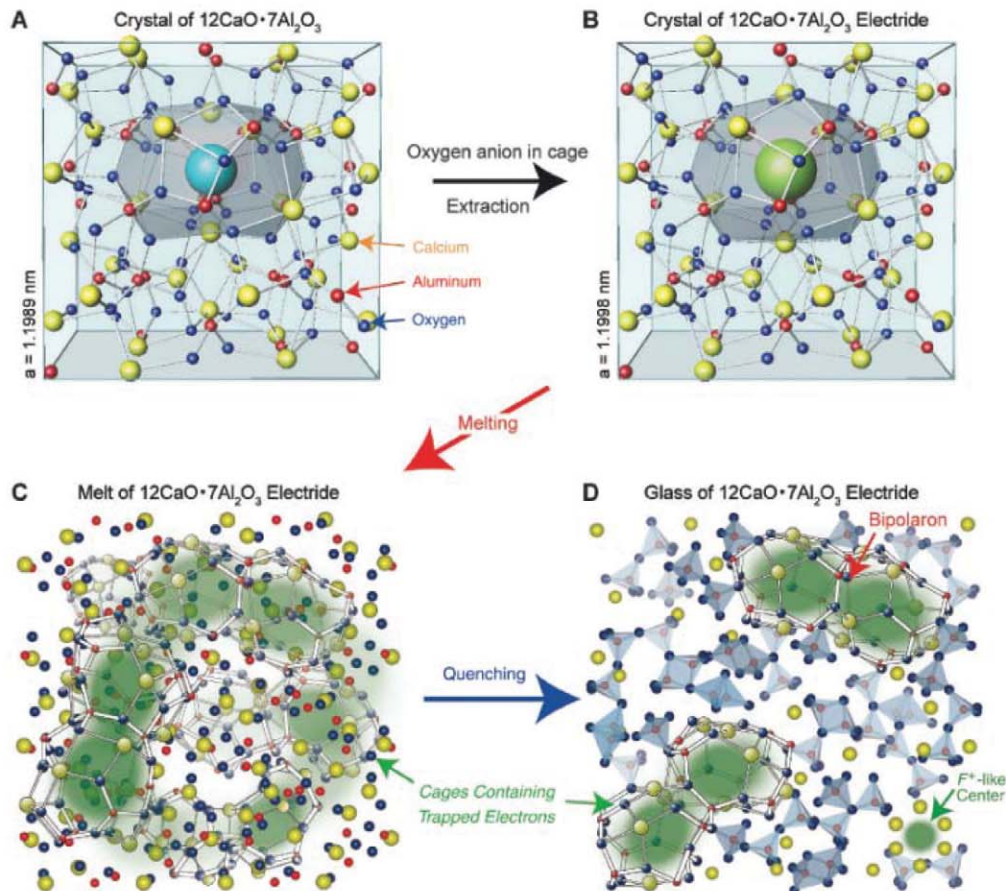
recrystallized sample. However, N_e was negligible in both the glass and crystal of C12A7:O^{2-} . In other words, the electrons present in the electride glasses and recrystallized electrides are not newly generated but come from the electride melt. This result suggests that electrons caged in C12A7:e^- crystals persist in the melt without a severe degradation of N_e if a low PO_2 of $\sim 10^{-24}$ atm is maintained during melting and quenching.

Optical absorption spectra of C12A7:e^- and C12A7:O^{2-} glasses are shown in Fig. 2D. The C12A7:O^{2-} glass shows no distinct absorption band, whereas the C12A7:e^- glass exhibits a broad absorption band at 4.6 eV with a shoulder at 3.3 eV. The band at 3.3 eV is attributed to electrons forming F^+ -like centers, similar to the C12A7:O^{2-} glass obtained by melting C12A7:O^{2-} under a strongly reducing atmosphere in a carbon crucible (11). Electron spin resonance (ESR) measurement (Fig. 2D, inset) of the C12A7:e^- glass reveals a weak signal at $g = 1.998$ that we assigned to the F^+ -like centers where an electron is trapped at an oxygen ion vacancy and is coordinated by Ca^{2+} ions (11). ESR measurements gave an N_e of $\sim 5 \times 10^{18} \text{ cm}^{-3}$, which is just 0.5% of the N_e ($\sim 1.1 \times 10^{21} \text{ cm}^{-3}$) of the C12A7:e^- glass. From these results, we assume that most of the electrons in the C12A7:e^- glasses are responsible for the optical absorption at 4.6 eV, existing in a spin-paired state.

Raman spectra of the C12A7:e^- glasses with different N_e provide structural information to com-

pare with those of C12A7:O^{2-} oxide glasses (Fig. 3). There are three distinct differences: First, a sharp band appears at 186 cm^{-1} in the spectra of the C12A7:e^- glasses, and its intensity increases as N_e increases. Second, the band at 430 cm^{-1} , which is weak in C12A7:O^{2-} glass, becomes distinct, and its intensity relative to the 780 cm^{-1} band increases with N_e . Third, the intensity of the 780 cm^{-1} band, which is assigned to the stretching mode of Al–O of a tetrahedral AlO_4 unit (12), is greater relative to the 560 cm^{-1} band. The sharp band at 186 cm^{-1} in the spectra of the electride glasses should be associated with trapped electrons because this band is observed only for the electride glasses with $N_e > 3 \times 10^{20} \text{ cm}^{-3}$ and its intensity is proportional to N_e . To confirm the relation between the 186 cm^{-1} band and trapped electrons, we measured Raman spectra of the electride glass with a N_e of $1.1 \times 10^{21} \text{ cm}^{-3}$ using several excitation lasers of different wavelengths. As shown in the inset of Fig. 3, the intensity of the 186 cm^{-1} band relative to the 780 cm^{-1} band increases as the excitation photon energy increases, agreeing well with the optical absorption spectrum. This observation strongly suggests that the 186 cm^{-1} band originates from the resonance Raman scattering associated with the absorption band at 4.6 eV. Several bands associated with cage vibration are present at around 200 cm^{-1} in Raman spectrum of a C12A7 crystal (13). Thus, we attribute the sharp band at 186 cm^{-1}

Fig. 4. Model of the melt and glass of C12A7:e^- electride. (A and B) The crystal structures of C12A7:O^{2-} and C12A7:e^- electride. The free oxygen anions [blue sphere in the cage of (A)] of C12A7:O^{2-} can be selectively extracted by several reducing processes, and electrons [green sphere in the cage of (B)] are trapped to maintain charge neutrality, yielding C12A7:e^- electride. (C and D) Feasible structures of the melt and glass of C12A7:e^- electride, respectively. Upon melting, empty cages collapse to form a dense network structure, and the cages containing electrons remain but decrease in size. The wavefunctions of electrons trapped in the cages of the melt percolate to allow metallic conduction. In the glassy state, electrons in cages have different trapping potential because of structural randomness. The majority of electrons in the glass are trapped in cages to form a diamagnetic state (bipolaron) with a nearby electron, whereas a minority of electrons ($\sim 10^{18} \text{ cm}^{-3}$) are trapped at interstitial sites and coordinated with Ca^{2+} ions to form a paramagnetic state similar to an F^+ -like center in CaO .



to vibration associated with the cages containing trapped electrons that generate the absorption band at 4.6 eV. The sharpness of this Raman band may be understood in terms of selective excitation of the cages containing trapped electrons at the specific excitation wavelength of the laser.

Following a previous Raman study on calcium aluminate glasses (12), we assigned the band at 560 cm^{-1} to the transverse motion of bridging oxygen within ${}^4\text{Al}-\text{O}-{}^4\text{Al}$ (superscript denotes oxygen coordination number) linkages. The increase in the intensity of the 780 cm^{-1} band relative to that of the 560 cm^{-1} band is explained by the higher concentration of depolymerized tetrahedral AlO_4 units in C12A7:e^- glasses as compared with C12A7:O^{2-} glass. Such an anion unit is the dominant structure in a CaO-rich composition. The band at 430 cm^{-1} is attributed to edge- or face-sharing AlO_4 units that are present in glasses with Al_2O_3 -rich compositions (12). The presence of these structural units is consistent with the higher density of the C12A7:e^- glass compared with the C12A7:O^{2-} glass. That is, C12A7:e^- glass contains heterogeneous anion structures corresponding to those in CaO- and Al_2O_3 -rich compositions (the fraction of such anion structures is very low in conventional C12A7:O^{2-} glass) in addition to structures with the nominal composition—highly depolymerized structures and a highly polymerized network structure connected by edge- or face-sharing.

On the basis of the above results, we propose a structural model for the melt and glass of C12A7:e^- electride, as shown in Fig. 4. The densities of both electride and oxide melts are greater than the 2.68 g cm^{-3} of the crystal composed of sub-nanometer-sized cages connected in three dimensions, indicating that the crystallographic cages lacking caged species collapse upon melting. Indeed, no cage structure has been observed in many structural analyses of C12A7:O^{2-} melts and glasses (14, 15). However, because the density of the C12A7:e^- melt is $\sim 10\%$ greater than that of the C12A7:O^{2-} melt we need to consider a denser network structure for the electride melt. The appearance of a distinct Raman band from edge- or face-sharing AlO_4 groups in the electride glasses is consistent with the observed difference in density. Edge- or face-sharing AlO_4 groups form a dense network structure that not only leads to a lower T_g of the electride glass than that of C12A7:O^{2-} glass (Fig. 2A) but also facilitates crystallization when the electride melt is quenched. This difference forced us to use a roller-quenching process, even though the viscosity of the C12A7:e^- melt is higher than that of the C12A7:O^{2-} melt (the stable glass formation range for $\text{CaO}-\text{Al}_2\text{O}_3$ systems is restricted to CaO 62 to 65%) (16).

Next, we considered the structure that traps electrons. The absorption peak from electrons trapped in cages of crystalline C12A7 is located at ~ 2.8 eV. Given that a caged electron can be modeled as a “particle in a box” (17), we considered that the cages containing trapped elec-

trons that give rise to the 4.6 eV band are smaller than the cages in the crystal. Observations of the spin-paired state and hopping conduction in the glass indicate that two electrons are trapped at adjacent sites. Because of large Coulombic repulsion, it is unrealistic that a single shrunken cage accommodates two electrons, so it is more probable that two shrunken cages each containing a trapped electron are connected to each other, forming a peanut-shaped structure: a bipolaron, which is reminiscent of solvated electrons in alkali metal-ammonia solutions (18), although this peanut-shaped bipolaronic structure is still speculative. The metallic conduction of the melt suggests that the shrunken cages containing trapped electrons are connected and span the melt, leading to the percolation of the wave functions of the electrons over the melt. Thus, we consider that the melt of C12A7:e^- electride at high temperature adopts a similar state to an alkali metal-ammonia solution containing solvated electrons in which the electron density is delocalized over the liquid by strongly associated bipolaron structures. That is, solvated electrons persist in the high-temperature melt because they are trapped in sub-nanometer-sized cages like those in a C12A7:e^- crystal. The present semiconductive glasses, which were obtained by quenching of C12A7:e^- melts, contain a high concentration of interstitial electrons and may be categorized as a previously unidentified class of amorphous electronic materials.

C12A7:e^- electride is a light metal oxide-based material and is a representative constituent of slag as a vitreous byproduct of the smelting process. The present C12A7:e^- melt exhibiting metallic conductivity—metallic slag—and C12A7:e^- glass displaying electro-conductivity will provide new applications for oxide melts and glasses. We anticipate that our present work will stimulate further research to exploit similar liquids in other

inorganic-based electrides and elemental electrides under high pressure.

References and Notes

1. J. C. Thompson, *Electrons in Liquid Ammonia* (Oxford Univ. Press, Oxford, 1976).
2. J. L. Dye, *Acc. Chem. Res.* **43**, 1564 (2009).
3. S. Matsuishi et al., *Science* **301**, 626 (2003).
4. S. W. Kim et al., *Nano Lett.* **7**, 1138 (2007).
5. S. W. Kim et al., *J. Am. Chem. Soc.* **127**, 1370 (2005).
6. S. G. Yoon, S. W. Kim, D. H. Yoon, M. Hirano, H. Hosono, *J. Nanosci. Nanotechnol.* **9**, 7345 (2009).
7. W. Freyland, in *The Metal-Nonmetal Transition Revisited*, P. P. Edwards, C. N. Rao, Eds. (Taylor & Francis, London, 1995), pp. 167–191.
8. B. J. Hallstedt, *J. Am. Ceram. Soc.* **73**, 15 (1990).
9. N. A. McNeal, A. M. Goldman, *Phys. Rev. Lett.* **38**, 445 (1977).
10. T. Yoshizumi, S. Matsuishi, S.-W. Kim, H. Hosono, K. Hayashi, *J. Phys. Chem. C* **114**, 15354 (2010).
11. H. Hosono, N. Asada, Y. Abe, *J. Appl. Phys.* **67**, 2840 (1990).
12. P. F. McMillan, B. Piriou, *J. Non-Cryst. Solids* **55**, 221 (1983).
13. K. Kajihara, S. Matsuishi, K. Hayashi, M. Hirano, H. Hosono, *J. Phys. Chem. C* **111**, 14855 (2007).
14. P. F. McMillan et al., *J. Non-Cryst. Solids* **195**, 261 (1996).
15. Q. Mei et al., *J. Phys. Condens. Matter* **20**, 245107 (2008).
16. H. Rawson, *Inorganic Glass-Forming Systems* (Academic Press, London, 1967).
17. P. V. Sushko, A. L. Shluger, K. Hayashi, M. Hirano, H. Hosono, *Phys. Rev. Lett.* **91**, 126401 (2003).
18. Z. Deng, G. J. Martyna, M. L. Klein, *Phys. Rev. Lett.* **68**, 2496 (1992).
19. G. Y. Onoda Jr., S. D. Brown, *J. Am. Ceram. Soc.* **53**, 311 (1970).

Acknowledgments: We thank K. Hayashi and T. Yoshizumi of Tokyo Institute of Technology for the help of iodometric titration. S. Matsuishi and S. Ito of Tokyo Institute of Technology are thanked for useful discussions. Help by T. Tomoda for Raman spectra measurements is acknowledged. This study was supported by the Funding Program for World-Leading Innovative R&D on Science and Technology (FIRST), Japan Society for the Promotion of Science, Japan.

Supporting Online Material

www.sciencemag.org/cgi/content/full/333/6038/71/DC1
Materials and Methods

Figs. S1 to S5

Movie S1

16 February 2011; accepted 6 May 2011

10.1126/science.1204394

Large Sulfur Isotope Fractionation Does Not Require Disproportionation

Min Sub Sim,* Tanja Bosak, Shuhei Ono

The composition of sulfur isotopes in sedimentary sulfides and sulfates traces the sulfur cycle throughout Earth's history. In particular, depletions of sulfur-34 (${}^{34}\text{S}$) in sulfide relative to sulfate exceeding 47 per mil (‰) often serve as a proxy for the disproportionation of intermediate sulfur species in addition to sulfate reduction. Here, we demonstrate that a pure, actively growing culture of a marine sulfate-reducing bacterium can deplete ${}^{34}\text{S}$ by up to 66‰ during sulfate reduction alone and in the absence of an extracellular oxidative sulfur cycle. Therefore, similar magnitudes of sulfur isotope fractionation in sedimentary rocks do not unambiguously record the presence of other sulfur-based metabolisms or the stepwise oxygenation of Earth's surface environment during the Proterozoic.

Dissimilatory microbial sulfate reduction (MSR) uses sulfate (SO_4^{2-}) as an electron acceptor and simple organic compounds or hydrogen as electron donors, producing sulfide that is depleted in heavy isotopes of sulfur (${}^{33}\text{S}$, ${}^{34}\text{S}$, and ${}^{36}\text{S}$) relative to the starting sulfate.

For more than 2.5 billion years of Earth history, this biological process has controlled the partitioning of sulfur isotopes between sedimentary sulfides and sulfates, leaving a sedimentary S isotope record that is commonly used to track the geochemical cycling of sulfur, the oceanic budgets of

oxidants, the evolution of microbial metabolisms, and the levels of atmospheric oxygen throughout geologic history (1–3).

All interpretations of this geobiological record have drawn heavily on more than five decades of systematic studies of sulfur isotope effects produced by MSR under controlled laboratory conditions. Although previous environmental studies and models predicted that MSR alone could produce a sulfur isotope offset between sulfides and sulfates ($\delta^{34}\text{S}_{\text{sulfate-sulfide}}$) (4) as large as ~75 per mil (‰) (5–8), growth and chemical conditions that lead toward such large offsets remain poorly understood. On the other hand, laboratory culture studies of MSR have not reported sulfur isotope effects larger than 47‰ under chemically and biologically defined reproducible conditions (Fig. 1). Large $\delta^{34}\text{S}_{\text{sulfate-sulfide}}$ values commonly measured in nature (Fig. 1) were thus attributed to a combination of MSR, extracellular oxidative re-

cycling of sulfur by abiotic or microbial processes, and microbial sulfur disproportionation (MSD) (2, 9). This oxidative recycling model, applied to the temporal record of $\delta^{34}\text{S}_{\text{sulfate-sulfide}}$ values, is used to track the evolution of more oxidized conditions and the progressive oxygenation of Earth's surface environment (2, 10–13).

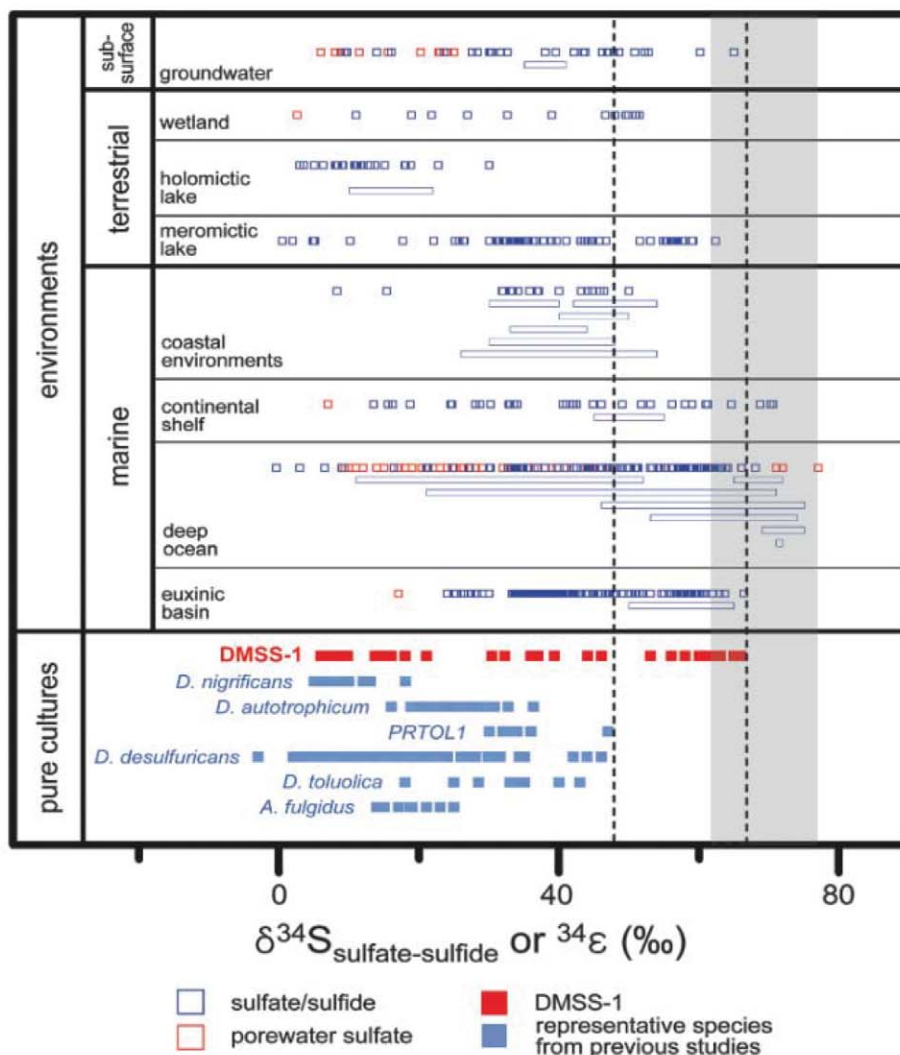
We isolated a sulfate-reducing δ -proteobacterium [*Desulfovibrio* sp., (DMSS-1)] from marine coastal sediments from Cape Cod, Massachusetts (14), where $\delta^{34}\text{S}_{\text{sulfate-sulfide}}$ exceeds 50‰ (15). This microbe couples the reduction of sulfate with the incomplete oxidation of various organic substrates including fructose and glucose (14), producing a wide range of isotope enrichment factors ($^{34}\epsilon$) from 6.1 to 65.6‰ (Fig. 1). Fractionations by DMSS-1 expand the range of $^{34}\epsilon$ and the triple isotope fractionation coefficient for $^{32}\text{S}/^{33}\text{S}/^{34}\text{S}$ ($^{33}\lambda$) (4) values produced by MSR, accommodating most S isotope fractionations observed in modern environments (Figs. 1 and 2 and Table 1). Very slow growth of DMSS-1 in batch cultures grown on glucose as an electron donor and carbon source produces $^{34}\epsilon$ values larger than 47‰ (Table 1) (16): During the early exponential growth,

the $^{34}\epsilon$ values exceed 60‰, decreasing down to 44‰ at the very end of experiment (Table 1). Decreasing $^{34}\epsilon$ values are accompanied by an increasing growth rate and cell yields, as well as a different reaction stoichiometry (16). Because DMSS-1 can ferment glucose in the absence of sulfate, different stoichiometries during the early and the late exponential growth suggest that DMSS-1 ferments some glucose during the early exponential growth (16). Conditions producing large and constant $^{34}\epsilon$ values (>47‰) can be maintained indefinitely in continuous-flow cultures, where sulfate and glucose are the only available oxidant and reductant, respectively (Table 1). The production of large $^{34}\epsilon$ values cannot be attributed to MSD coupled with the extracellular oxidation of sulfide to intermediate sulfur species (for example, thiosulfate, sulfur, or sulfite), because other potential oxidants are absent from the defined culture medium (16). By proving that MSR alone can generate sulfides extremely depleted in ^{34}S , even in the absence of extracellular oxidative recycling, our findings bridge the long-standing discrepancy between the ranges of sulfur isotope effects observed in

Department of Earth, Atmospheric, and Planetary Sciences, Massachusetts Institute of Technology, Cambridge, MA 02139, USA.

*To whom correspondence should be addressed. E-mail: mssim@mit.edu

Fig. 1. Fractionations of ^{34}S reported by studies of environmental samples ($\delta^{34}\text{S}_{\text{sulfate-sulfide}}$ or $^{34}\epsilon$) and pure cultures of 44 different sulfate-reducing microbes ($^{34}\epsilon$). Isotope fractionations in environmental samples were estimated using dissolved sulfate and sedimentary or dissolved sulfide or were calculated from the concentration and the isotope composition of pore water sulfate. Each point in culture studies represents a different growth condition. Dashed black lines indicate the expanded range of ^{34}S fractionations by MSR (this study). The gray shaded area outlines the equilibrium isotope effects between sulfate and sulfide with varying temperatures (0 to ~40°C). Complete lists of references, data, and criteria are available in tables S1 and S2.



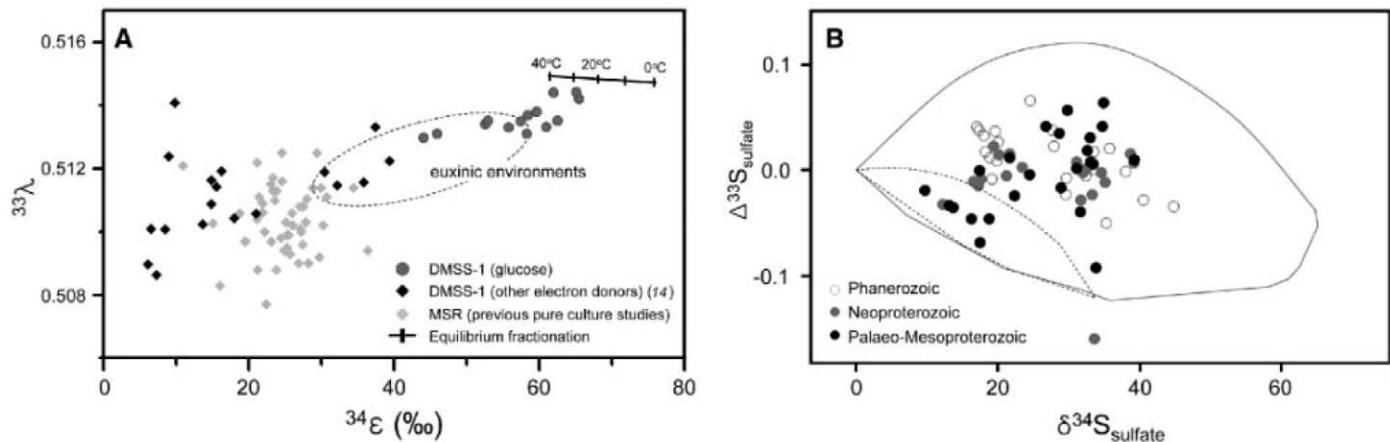


Fig. 2. (A) Comparison of $^{34}\epsilon$ and $^{33}\lambda$ values in this study to the values reported by previous culture studies (23, 34) and to the range ($^{34}\epsilon$, $^{33}\lambda$) from coexisting dissolved sulfide and sulfate in modern euxinic environments [Green Lake (Fayetteville, New York), Lago di Cadagno (Ticino, Switzerland), and Cariaco Basin (Venezuela)] (8, 27, 35). (B) $\delta^{34}\text{S}$ and $\Delta^{33}\text{S}$ (‰) of seawater sulfate proxies (circles)

from 2 to 0.2 billion years ago standardized to the Vienna Canyon Diablo Troilite (11, 32). Shown here is the predicted range of $\delta^{34}\text{S}$ and $\Delta^{33}\text{S}$ values of seawater sulfate based on the steady-state global sulfur-cycle model including only MSR without MSD, constrained by the previous range of $^{34}\epsilon$ and $^{33}\lambda$ values for MSR (11) (dashed outline) or the expanded range reported in this study (solid outline).

Table 1. Sulfur isotope effects during the growth of DMSS-1 on glucose. Solid horizontal lines indicate separate experiments. For 8.5 mM glucose/21 mM sulfate, we carried out the experiment two times using different inocula. Individual numbers within solid lines represent cultures inoculated at the same time and grown simultaneously in identical growth media, but in separate bottles. Calculated $^{34}\epsilon$ values vary depending on the growth stage. The largest and the smallest $^{34}\epsilon$ values were always found during the early and late exponential growth, respectively. Errors were propagated from analytic uncertainties of isotope analysis and sulfide concentration measurement. *f*, fraction of remaining sulfate.

Experiments	<i>f</i>	$^{34}\epsilon$ (‰)	$^{33}\epsilon$ (‰)	$^{33}\lambda$
<i>Batch cultures</i>				
10 mM glucose/ 21 mM sulfate	0.99	62.6 ± 0.3	32.7 ± 0.1	0.5135 ± 0.0002
	0.99	65.6 ± 0.3	34.3 ± 0.1	0.5142 ± 0.0002
	0.99	65.2 ± 0.3	34.1 ± 0.1	0.5144 ± 0.0002
8.5 mM glucose/ 21 mM sulfate	0.91	58.5 ± 0.3	30.5 ± 0.1	0.5137 ± 0.0003
	0.93	59.7 ± 0.4	31.1 ± 0.2	0.5138 ± 0.0002
	0.87	57.6 ± 0.4	30.0 ± 0.2	0.5135 ± 0.0002
	0.81	53.0 ± 0.4	27.6 ± 0.2	0.5135 ± 0.0003
10 mM glucose/ 21 mM sulfate (+ amino acids)	0.96	55.9 ± 0.4	29.1 ± 0.2	0.5133 ± 0.0004
	0.93	62.1 ± 0.3	32.4 ± 0.1	0.5144 ± 0.0002
1 mM glucose/ 21 mM sulfate	0.99	58.4 ± 0.3	30.4 ± 0.1	0.5131 ± 0.0003
10 mM glucose/ 2 mM sulfate	0.85	61.1 ± 0.4	31.9 ± 0.2	0.5133 ± 0.0002
1 mM glucose/ 2 mM sulfate	0.90	45.9 ± 0.4	23.8 ± 0.2	0.5131 ± 0.0003
<i>Chemostat (0.08 day⁻¹)</i>				
10 mM glucose/ 21 mM sulfate		52.6 ± 0.3	27.4 ± 0.1	0.5134 ± 0.0005

*Data from (14).

laboratory cultures and geologic environments (Fig. 1).

One may ask whether large sulfur isotope effects produced by a single sedimentary microbe are truly representative of the natural environment. However, it is similarly unclear whether previous culture studies of MSR are representative of conditions conducive to large isotope fractionations in the environment, because most of these studies investigated MSR during growth on

simple organic acids (e.g., lactate) and hydrogen and only rarely attained very slow growth rates and cell-specific sulfate reduction rates (csSRRs) (16). Here, slow growth rates and csSRRs are attained by growing DMSS-1 on glucose. This is not a conventional substrate for sulfate-reducing microbes, but it is a common building block in the biofilms (17) and storage polymers of some sulfate reducers (18), as well as a common monosaccharide in the ocean (19).

Sulfate-reducing microbes accomplish the eight-electron reduction of sulfate to sulfide in a stepwise and reversible manner (7, 20). The overall isotope effects between sulfate and sulfide thus depend both on the ratio between forward and backward fluxes at each intermediate step and on the isotope effect intrinsic to each transfer flux (20, 21). The largest isotope effect is expected when the sulfate-reduction pathway operates in a highly reversible manner, leading to near equilibrium conditions (7). Accordingly, the largest $^{34}\epsilon$ values produced by MSR should approach the equilibrium isotope effect between dissolved sulfate and sulfide, calculated to 68 ± 2‰ at 20°C (22). This upper boundary is also supported by the relation among multiple isotopes of sulfur. As $^{34}\epsilon$ approaches the equilibrium value, so does $^{33}\lambda$ (Fig. 2A), whereas smaller $^{34}\epsilon$ values are associated with smaller $^{33}\lambda$ values, as expected for the kinetic isotope effects in multiple-isotope systems (23). Our estimate for the largest $^{34}\epsilon$ value is close to the apparent upper boundary for the values of $\delta^{34}\text{S}_{\text{sulfate-sulfide}}$ in nature (Fig. 1). In contrast, models that include oxidative recycling do not necessarily limit the values of $\delta^{34}\text{S}_{\text{sulfate-sulfide}}$ to the equilibrium value [figure 2 in (9)].

Models of S isotope effects produced by a combination of MSR and MSD predict that the largest $\delta^{34}\text{S}_{\text{sulfate-sulfide}}$ should occur in areas of intense sulfur redox cycling and substantial MSD. Although these processes demonstrably occur in modern coastal environments (9, 24), large (>47‰) $\delta^{34}\text{S}_{\text{sulfate-sulfide}}$ values are not reported frequently in these settings (Fig. 1). Large $\delta^{34}\text{S}_{\text{sulfate-sulfide}}$ values are instead commonly reported from deep-sea sediments, where the extremely slow microbial metabolisms are attributed to the limited availability and the poor reactivity of organic substrates (25, 26). The diversity of microbes and growth conditions that generate natural $\delta^{34}\text{S}_{\text{sulfate-sulfide}}$ values larger than 47‰ remains to be determined, but the overall scarcity of sulfides

exhibiting $\delta^{34}\text{S}_{\text{sulfate-sulfide}} > 47\%$ over geologic history (2) thus might simply be related to the lack of preservation of deep-sea sediments. Euxinic basins also exhibit a wide range of $\delta^{34}\text{S}_{\text{sulfate-sulfide}}$ values that commonly exceed 47‰ and $^{33}\lambda$ values larger than those previously attributed to MSR (Fig. 2A). These $\delta^{34}\text{S}_{\text{sulfate-sulfide}}$ and $^{33}\lambda$ values have been used as an indication of the contribution of MSD to the cycling of sulfur in modern euxinic environments (27). However, the combined isotopic signatures of $^{34}\epsilon$ and $^{33}\lambda$ produced by DMSS-1 can explain nearly all observations from modern euxinic settings (Fig. 2A) and demonstrate that neither $^{34}\epsilon$ nor $^{33}\lambda$ unambiguously indicates MSD in modern environments.

The earliest values of $\delta^{34}\text{S}_{\text{sulfate-sulfide}}$ larger than 50‰ occur in a 1.2-billion-year-old non-marine environment (13) and may have become more widespread in marine environments after ~700 million years ago (28) or even later (10, 12). Given the assumption that $^{34}\epsilon$ values larger than 47‰ do not occur during MSR alone, this temporal trend was attributed to various mechanisms including the growth of the marine sulfate reservoir (29), the increasing importance of disproportionation (11), the progressive oxygenation of the oceans (2), and the advent of bioturbating organisms close to the Precambrian/Cambrian boundary (30). However, given that DMSS-1 in the presence of just 2 mM sulfate produces $^{34}\epsilon$ values of 61.1‰ (Table 1) [i.e., outside the limit previously attributed to MSR alone (2, 11)], MSR alone could have produced similar S isotope signatures after a moderate increase in the size of marine sulfate reservoir (2 mM) during the mid-Mesoproterozoic (31).

In addition to ^{34}S (2), the ^{33}S record has been used to show the substantial contribution of MSD to the global sulfur cycle as early as 1300 million years ago (11, 32). This constraint is based on model estimates for sulfur isotope compositions ($\delta^{34}\text{S}$ and $\Delta^{33}\text{S}$) of proxies for seawater sulfate (Fig. 2B). However, the input parameters for this model include the relatively small ranges of $^{34}\epsilon$ and $^{33}\lambda$ values from previous laboratory experiments (11). When the same box model is solved with new expanded ranges of $^{34}\epsilon$ and $^{33}\lambda$ values produced by DMSS-1, all but one sample of Phanerozoic and Proterozoic sedimentary sulfates (11, 32) are consistent with the global sulfur cycle including only MSR without MSD (Fig. 2B). Therefore, ^{33}S isotope signatures in sedimentary records do not clearly indicate sulfur disproportionation in the ancient oceans (2, 9, 11).

Because the fractionation of sulfur isotopes between sulfate and sulfide can exceed 50‰, even if sulfide is not reoxidized outside of the cell and at an environmental scale, more Proterozoic samples exhibiting a large $\delta^{34}\text{S}_{\text{sulfate-sulfide}}$ value may be found. Any temporal changes in the sulfur isotope record during this time could reflect the changing nature of organic material that fueled sulfate reduction, rather than measure the extent of oxygenated areas in oceans. The relative contributions of MSR alone and of the environmental-

scale oxidative recycling toward large present and past natural fractionations of S isotope ratios now remain to be evaluated.

References and Notes

- R. M. Garrels, A. Lerman, *Proc. Natl. Acad. Sci. U.S.A.* **78**, 4652 (1981).
- D. E. Canfield, A. Teske, *Nature* **382**, 127 (1996).
- R. A. Berner, S. T. Petsch, *Science* **282**, 1426 (1998).
- $\delta^{34}\text{S}_{\text{sulfate-sulfide}}$ is the depletion of ^{34}S in sulfide relative to sulfate source (e.g., seawater sulfate for marine environments) ($\approx \delta^{34}\text{S}_{\text{sulfate}} - \delta^{34}\text{S}_{\text{sulfide}}$). $\delta^x\text{S}$ values are defined as $\delta^x\text{S} = 1000 \cdot [(^{x}\text{S}/^{32}\text{S})_{\text{sample}} / (^{x}\text{S}/^{32}\text{S})_{\text{standard}} - 1]$, where x is 33 or 34. $\Delta^{33}\text{S} = \delta^{33}\text{S} - 1000 \cdot [(\delta^{34}\text{S}/1000 + 1)^{0.515} - 1]$. $^{34}\epsilon = 1000 \cdot [1 - (^{34}\text{S}/^{32}\text{S})_{\text{sulfide}} / (^{34}\text{S}/^{32}\text{S})_{\text{sulfate}}]$ and $^{33}\lambda = \ln[(^{33}\text{S}/^{32}\text{S})_{\text{sulfide}} / (^{33}\text{S}/^{32}\text{S})_{\text{sulfate}}] / \ln[(^{34}\text{S}/^{32}\text{S})_{\text{sulfide}} / (^{34}\text{S}/^{32}\text{S})_{\text{sulfate}}]$, where $(^{33}\text{S}/^{32}\text{S})_{\text{sulfide}}$ and $(^{33}\text{S}/^{32}\text{S})_{\text{sulfate}}$ are the instantaneous S isotope ratios of sulfide and the remaining sulfate, respectively.
- M. D. Rudnicki, H. Elderfield, B. Spiro, *Geochim. Cosmochim. Acta* **65**, 777 (2001).
- U. G. Wortmann, S. M. Bernasconi, M. E. Böttcher, *Geology* **29**, 647 (2001).
- B. Brunner, S. M. Bernasconi, *Geochim. Cosmochim. Acta* **69**, 4759 (2005).
- D. E. Canfield, J. Farquhar, A. L. Zerkle, *Geology* **38**, 415 (2010).
- D. E. Canfield, B. Thamdrup, *Science* **266**, 1973 (1994).
- M. T. Hurtgen, M. A. Arthur, G. P. Halverson, *Geology* **33**, 41 (2005).
- D. T. Johnston *et al.*, *Science* **310**, 1477 (2005).
- D. A. Fike, J. P. Grozinger, L. M. Pratt, R. E. Summons, *Nature* **444**, 744 (2006).
- J. Parnell, A. J. Boyce, D. Mark, S. Bowden, S. Spinks, *Nature* **468**, 290 (2010).
- M. S. Sim, S. Ono, K. Donovan, S. P. Templer, T. Bosak, *Geochim. Cosmochim. Acta.*, published online 23 May 2011 (10.1016/j.gca.2011.05.021).
- B. J. Peterson, R. W. Howarth, R. H. Garritt, *Ecology* **67**, 865 (1986).
- Materials and methods are available as supporting material on Science Online.
- B. Vu, M. Chen, R. J. Crawford, E. P. Ivanova, *Molecules* **14**, 2535 (2009).
- J. M. Stams, M. Veenhuis, G. H. Weenk, T. A. Hansen, *Arch. Microbiol.* **136**, 54 (1983).
- K. Mopper *et al.*, *Mar. Chem.* **10**, 55 (1980).
- C. E. Rees, *Geochim. Cosmochim. Acta* **37**, 1141 (1973).
- D. B. Northrop, *Annu. Rev. Biochem.* **50**, 103 (1981).
- The range reflects values derived by either extrapolation from high temperature (>200°C) or theoretical calculations (33), assuming pH = 7. The equilibrium isotope fractionation factor between aqueous H_2S and HS^- is ~6‰.
- J. Farquhar *et al.*, *Geobiology* **1**, 27 (2003).
- B. B. Jørgensen, *Science* **249**, 152 (1990).
- S. D'Hondt, S. Rutherford, A. J. Spivack, *Science* **295**, 2067 (2002).
- B. B. Jørgensen, A. Boetius, *Nat. Rev. Microbiol.* **5**, 770 (2007).
- A. L. Zerkle *et al.*, *Geochim. Cosmochim. Acta* **74**, 4953 (2010).
- G. M. Ross, J. D. Bloch, H. R. Krouse, *Precambrian Res.* **73**, 71 (1995).
- J. M. Hayes, I. B. Lambert, H. Strauss, in *The Proterozoic Biosphere: A Multidisciplinary Study*, J. W. Schopf, C. Klein, Eds. (Cambridge Univ. Press, Cambridge, 1992), pp. 129–132.
- D. E. Canfield, J. Farquhar, *Proc. Natl. Acad. Sci. U.S.A.* **106**, 8123 (2009).
- L. C. Kah, T. W. Lyons, T. D. Frank, *Nature* **431**, 834 (2004).
- N. Wu, J. Farquhar, H. Strauss, S.-T. Kim, D. E. Canfield, *Geochim. Cosmochim. Acta* **74**, 2053 (2010).
- T. Otake, A. C. Lasaga, H. Ohmoto, *Chem. Geol.* **249**, 357 (2008).
- D. T. Johnston, J. Farquhar, D. E. Canfield, *Geochim. Cosmochim. Acta* **71**, 3929 (2007).
- X. Li *et al.*, *Geochim. Cosmochim. Acta* **74**, 6764 (2010).

Acknowledgments: We thank W. Olszewski, K. Donovan, S. Templer, J. Seewald, S. Sylva, B. Weiss, L. Kump, J. Grabenstatter, B. Bannan, P. Hedman, and Y. J. Joo. This work was partially supported by NASA Astrobiology Institute (#NNA08CN84A).

Supporting Online Material

www.sciencemag.org/cgi/content/full/333/6038/74/DC1
Materials and Methods
SOM Text
Fig. S1
Tables S1 to S5
References (36–133)

3 March 2011; accepted 16 May 2011
10.1126/science.1205103

Formation and Spread of Aircraft-Induced Holes in Clouds

Andrew J. Heymsfield,^{1*} Gregory Thompson,¹ Hugh Morrison,¹ Aaron Bansemer,¹ Roy M. Rasmussen,¹ Patrick Minnis,² Zhien Wang,³ Damao Zhang³

Hole-punch and canal clouds have been observed for more than 50 years, but the mechanisms of formation, development, duration, and thus the extent of their effect have largely been ignored. The holes have been associated with inadvertent seeding of clouds with ice particles generated by aircraft, produced through spontaneous freezing of cloud droplets in air cooled as it flows around aircraft propeller tips or over jet aircraft wings. Model simulations indicate that the growth of the ice particles can induce vertical motions with a duration of 1 hour or more, a process that expands the holes and canals in clouds. Global effects are minimal, but regionally near major airports, additional precipitation can be induced.

The passage of aircraft through subfreezing, supercooled liquid water cloud can produce circular and linear voids called

hole-punch and canal clouds on the basis of their distinctive appearance (Fig. 1A).

Ice streamers embedded within or descending from circular holes or elongated channels carved out of mid-level, subfreezing cloud layers were first reported in the meteorological literature in the 1940s (1). In correspondence titled “Man-Made Cirrus?” in *Weather* (2), a large horizontal loop sketched in a midlevel cloud was the first of

¹National Center for Atmospheric Research (NCAR), Boulder, CO 80301, USA. ²NASA Langley Research Center, Hampton, VA 23681, USA. ³Department of Atmospheric Sciences, University of Wyoming, Laramie, WY 82071, USA.

*To whom correspondence should be addressed. E-mail: heyms1@ncar.ucar.edu

such features to be attributed to an aircraft. A photograph published two decades later in “Hole-in-Cloud: A Meteorological Whodunit?” generated considerable interest from the U.S. meteorological community as to its cause (3). In the 1980s, research aircraft studying ice formation in supercooled clouds observed that their propeller aircraft produced copious ice crystals that confounded their observations and interpretations (4, 5). Working from the premise that holes in clouds can indicate inadvertent seeding by aircraft and drawing on a series of images of holes and canals together with modeling of ice injection into a supercooled cloud, we examined aircraft-induced inadvertent seeding effects within supercooled cloud layers.

Ice nuclei such as dust are generally required to freeze supercooled droplets at temperatures above -40°C . Supercooled droplets are not found at temperatures below this point because droplets freeze spontaneously at about -40°C . Once produced in a supercooled cloud, ice grows rapidly at the expense of the droplets. According to the Bergeron-Findeisen (B-F) process, if ice is introduced into a supercooled cloud, the liquid droplets will be at subsaturation relative to the ice; the liquid will evaporate, condensing and freezing onto the ice crystals and causing them to grow larger. This process is the basis for cloud seeding operations that convert supercooled droplets into snow.

The passage of an aircraft through a supercooled cloud can cause cooling sufficient to initiate the formation of ice crystals at cloud temperatures of -10 to -20°C and the subsequent operation of the B-F process (4, 5). Expansion of air behind aircraft propeller tips produces 20 to 30°C of cooling, and flow of air over the wings of jet aircraft at cruise speed produces 20°C of cool-

ing, creating aerodynamic contrails in high relative humidity conditions (6, 7). In both instances, cooling can induce spontaneous droplet freezing.

The operation of the B-F process in the context of inadvertent seeding is illustrated in Fig. 1B. It shows bands of enhanced radar signal embedded in a low-level supercooled cloud layer; a local sounding showed that the layer had a minimum temperature of about -16°C . The enhanced radar signal convert to snowfall-accumulation rates up to about 23 mm hr^{-1} (8), assuming an average 12:1 snowfall-accumulation-to-liquid-precipitation rate in Colorado storms. Snowbands are generally linear, so the curved nature of these bands and their path and proximity to the runways all suggest that it is probable they were induced by aircraft.

If a supercooled cloud is vertically thin or the cloud water is not replenished, snow can develop and fall out, leaving holes and voids in clouds. On 29 January 2007, over Texas and neighboring states a sequence of 20 visible images of an extensive cloud layer with embedded holes and canals was obtained with the Geostationary Operational Environmental Satellite (GOES-12) (Fig. 2, A and B). These images spanned a 4-hour period from 1632 to 2032 UTC, at 15- or 30-min intervals, when the holes and canals were most prevalent.

The characteristics of the cloud layer were identified from local radiosondes, wind profilers, and the sequence of GOES imagery. The cloud altitude was $\sim 7.7\text{ km}$, and cloud top temperature was $\sim -30^{\circ}\text{C}$ (7). From soundings, reanalyzed to correct for humidity sensor time lag indicating a relative humidity of approximately 100% with respect to water in the cloud layer, from satellite imagery indicating an approximately $10\text{-}\mu\text{m}$ radius of the cloud particles (7) characteristic of droplet populations, and the near absence of snow

virga except in localized regions of ice fallout in photographic images taken from the ground (Fig. 3A), we conclude that this cloud layer was primarily liquid. The liquid cloud layer was approximately 150 m deep. Below it, there was a 450-m layer favorable for ice growth with relative humidities above ice saturation conditions at the ambient temperatures. The wind speed in the cloud environment is relevant to the advection speed of the holes: From radiosondes, wind profilers, and tracking of individual holes, the mean horizontal wind velocity in the cloud layer was about 40 m s^{-1} .

We followed a total of 92 features from their first appearance on a satellite image until they were no longer visible or until the end of the time period had been reached (Fig. 2B). Some holes reached lengths of $>100\text{ km}$ and were detected for 4 or more hours.

From the consecutive 15-min satellite images, we measured the hole diameters and fractional increases of the area with time (fig. S2). Over the first 30 min from detection, the holes doubled their area. From 30 to 60 min, identifiable holes increased in area by 25%. After 1 hour from first detection, the holes' areas slowly decreased.

Hole-producing aircraft were identified from Federal Aviation Administration (FAA)-archived track information (9). Candidate aircraft were selected as those that flew within the altitude range of 7 to 8 km and within close proximity in time and $[x, y]$ positions relative to specific features (fig. S1). Not all holes could be attributed definitively to a single aircraft because of a regular succession of aircraft along certain flight corridors. In such an instance, the hole was ignored in the analysis, or if the candidate aircraft were of the same model and manufacturer, the

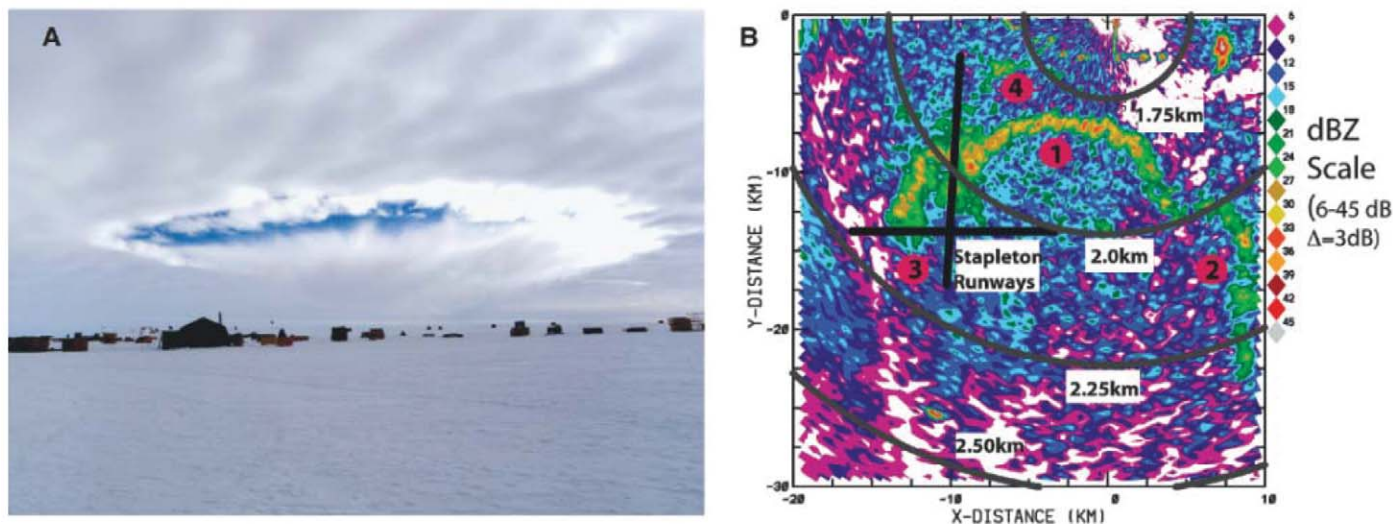


Fig. 1. (A) Aircraft-induced hole observed at the West Antarctic Ice Sheet Divide Camp, Antarctica ($79^{\circ}28.058'\text{S}$ $112^{\circ}05.189'\text{W}$, 1806 m elevation) on 12 Dec 2009, 1400 New Zealand Time. The cloud's bright cumuliiform structure with gray fallstreaks below are visible. The hole first appeared on the horizon and then moved toward the camera. It is likely that a LC130 aircraft produced the ice that formed the hole. [Photo provided by Eric Zrubek and Michael Carmody] (B) Radar reflectivity measurements taken

on 3 December 1992 by the NCAR Mile High Radar near the former Stapleton (Denver, Colorado) Airport. The radar antenna was operating at 1.6 degrees, so that the observed height through the cloud layer increases with distance (shown by the range rings in altitude increments of 250 m). The airport north-south and east-west runways are indicated. Arcs of snow generated by unknown aircraft (labeled 1 to 4) are observed to fall from a higher (left) to lower level.

most likely track among these similar aircraft was chosen.

Three-quarters of the hole-producing aircraft were identified. On this day, a full spectrum of aircraft types was found to produce the holes and canals: large passenger jets, regional jets, private jets, military jets, turboprop, and prop/piston (table S1).

This analysis supports the previous findings that there are at least two modes of inadvertent cloud seeding: expansion of air around aircraft propeller tips as shown observationally (4) and cooling of air over the wings of jet aircraft at cruise speeds as shown from numerical models and empirically (6, 7). Although engine combustion products are not a good source of ice nuclei, additional ice may be produced from combustion.

Because holes and canals were found to expand appreciably and persisted over extended periods, we were left with the conclusion that there must be more to their development and persistence than

solely the operation of the B-F process. The dynamical theory of cloud seeding states that the injection of ice particles into a supercooled cloud layer releases latent heat, creating buoyancy in the ice-affected region and producing or invigorating updrafts. It is plausible that a small-scale and persistent updraft could develop in the ice region with compensating downdrafts on the outside edges, causing the water cloud to erode by evaporation (7).

To support or dismiss the idea that this process plays a role in the development and maintenance of these features, simulations of inadvertent seeding of this supercooled layer were conducted by using the Weather Research and Forecasting (WRF) model (10). The WRF model was configured with 600 by 300 horizontal grid points spaced 50 m apart and 135 vertical levels spaced 150 m apart near the earth's surface, 50 m apart in the kilometer surrounding the depth of the cloud, and 250 m apart well above cloud top. Smoothly

varying vertical spacing was applied between these points. We used the Fort Worth, Texas, rawinsonde data for input thermodynamic and wind conditions. The change in wind speed of 2 m s^{-1} (corresponding to a horizontal wind shear of 0.013 s^{-1}) was specified through the 150-m deep liquid cloud layer.

The model was initialized with an adiabatic cloud liquid water profile. The Thompson cloud scheme (11) was used; it considers processes such as evaporation of droplets and growth by vapor diffusion of ice through the B-F process, release of latent heat, fallout of ice crystals, and other related processes. Radiation and land-surface exchange with the atmosphere were neglected for simplicity. In the simulation, ice production was intentionally disabled for the first 30 simulated minutes. Then, ice crystal concentration was increased to 1000 per liter and held constant for 60 s in a 250- by 250-m region through the depth of the cloud layer so as to simulate ice production by an aircraft penetrating the liquid layer. This concentration is consistent with the concentration of ice crystals measured by research aircraft that have sampled regions of inadvertent ice production by research aircraft (7, 12). From this point forward, no additional ice crystals were introduced.

The model calculations at a snapshot in time are compared visually with a photograph from the ground in Fig. 3, A and B. The simulation exhibits the expected vapor depositional growth of ice and evaporation of water droplets, leading to a hole in the liquid layer (Fig. 3B). The slope of the bottom edge of the snow (which is displaced horizontally about 4 km over a depth of 0.6 km) is consistent with the vertical wind shear of 0.013 s^{-1} and snow fallspeed of 0.6 m s^{-1} .

More quantitative evaluations of the development of the ice and snow field and the vertical air motions are shown for a sequence of times in Fig. 4, left. For clarity, only the snow and vertical velocity fields are shown and not the ice field. Latent heating associated with vapor deposition leads to a 15 cm s^{-1} updraft near the hole center that suspends most of the ice, although some particles are converted to faster-falling snow crystals, which fall through the updraft and produce snow fallstreaks beneath the hole. Downdrafts on the periphery of the hole accelerate evaporation of liquid water, and the hole rapidly widens over time. The spreading rate of the simulated cloud hole is relatively uniform in both wind-parallel and -perpendicular directions. The hole more than doubles in diameter, from 2 to 4.4 km, between 30 and 90 min. This increase is quite similar to the spread rate of the observed holes between 30 and 90 min (fig. S2). However, a more direct comparison between model simulation and observed hole clouds is hindered because the satellite is unable to observe the initial stages of transit of the various aircraft through the supercooled cloud is not known. With no additional ice crystals nucleated, ice and snow begin to dissipate after 90 min.

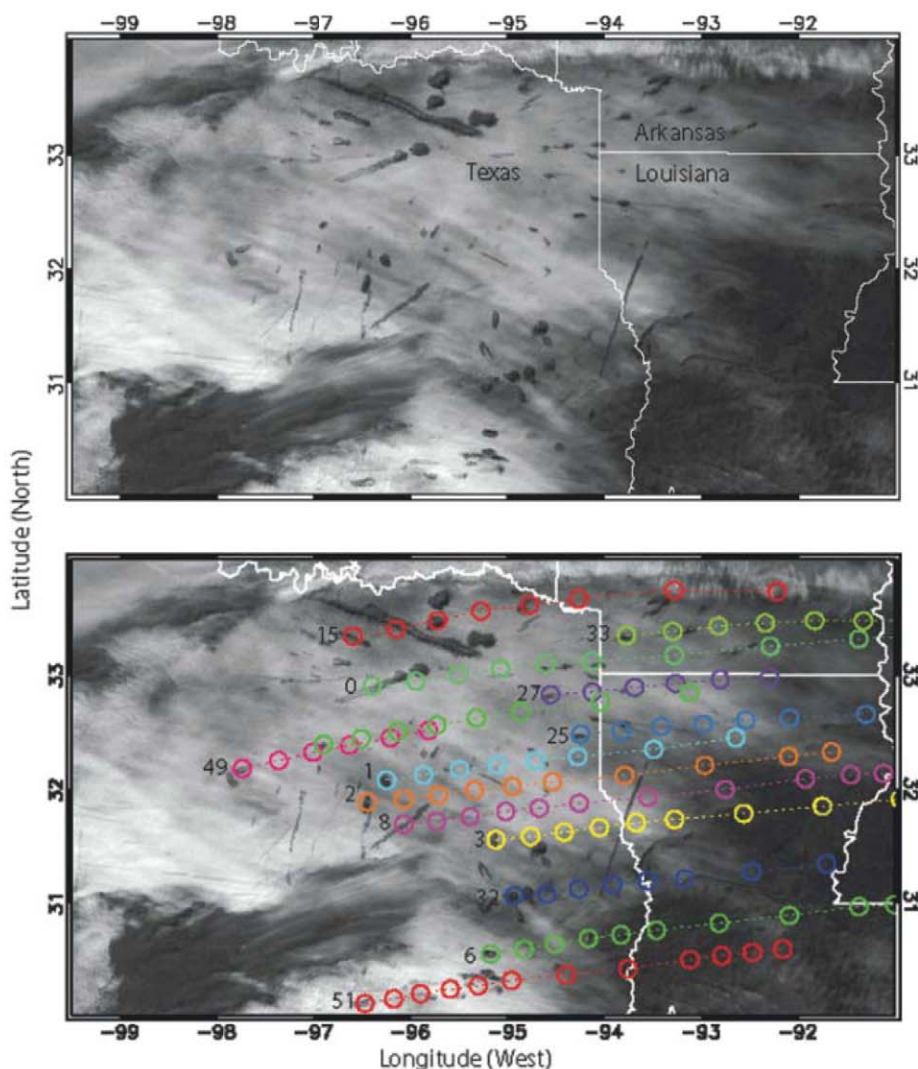
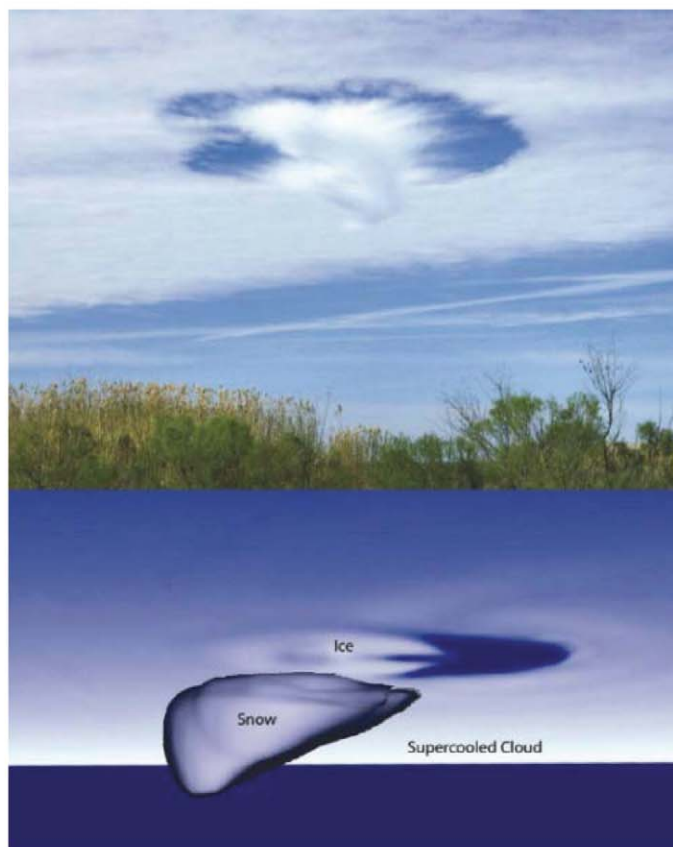


Fig. 2. Imagery from the GOES satellite on 29 January 2007. **(Top)** Circular and linear aircraft-induced holes at 1632 UTC, and **(bottom)** example of paths of multiple holes, with circles indicating the midpoint position of each hole or canal at 15-min intervals from first through last detection. An identifying hole number is given at the beginning time of the first detection of each hole.

Fig. 3. (Top) Photograph of aircraft-induced hole observed on 29 January 2007 as viewed toward the west. [Photograph courtesy of Jafvis] **(Bottom)** Simulated snow fallstreaks at 60 min after the introduction of ice into the cloud layer.



We performed two additional sensitivity tests to understand processes that lead to the hole development and growth. In the first test, latent heating due to vapor depositional growth of ice was turned off, but latent cooling from droplet evaporation was retained. Although the dynamics are weaker in this simulation and there is no clear updraft in the hole center, there are still downdrafts of several centimeters per second on the periphery of the hole driven by cooling from droplet evaporation. This leads to some growth of the hole, but at a reduced rate as compared with the baseline simulation (Fig. 4, right). In the second sensitivity test, all latent heating and cooling was turned off. As a result, the cloud dynamics are very weak, with vertical motions generally less than 1 cm s^{-1} . A hole still develops in this simulation because of ice growth at the expense of liquid water (the B-F process), but the spread of the hole is effectively eliminated. Overall, these tests indicate that interactions between microphysics and dynamics through both latent heating and evaporative cooling are the key to explaining rapid hole growth.

Because propeller and jet aircraft-induced cloud seeding and dynamical effects can ensue after the injection of inadvertent ice into a supercooled layer, potential exists in and around heavily trafficked airports for the generation of precipitation, as illustrated in Fig. 1B. Conditions suitable for inadvertent seeding of clouds were quantified for five major midlatitude and two high-latitude airports: London Heathrow; Frankfurt; Charles De Gaulle, Paris; Seattle-Tacoma; Chicago O'Hare; Yellowknife, Canada; and Byrd Station, Antarctica (13). Colocated data collected from the spaceborne Cloud-Aerosol Lidar and Infrared Pathfinder Satellite Observations (CALIPSO) lidar and CloudSat cloud radar from June 2006 to May 2008 were used to estimate how often supercooled clouds occur within a 100-km radius of selected primary airports in mid- and high latitudes (14). A commercial aircraft will cover this horizontal distance when climbing to about 10,000 feet (3 km), where many of the supercooled cloud layers are noted. Comparative frequencies of occurrence at the six airports are shown in fig. S3.

Taking temperatures of -10°C and below to be conducive to ice production by propeller aircraft and below -20°C for jet aircraft, the former have about a 5 or 6% probability (annual average) of inadvertently seeding clouds, whereas jets have a 2 to 3% probability for these locations. Although the ensuing dynamical effects are situational, our modeling suggests that the generation of precipitation amount and duration would be enhanced through subsequent dynamical effects. Although aircraft might seed these clouds, visible holes will not necessarily be produced if substantial ice is already present, if the cloud layers are thick, or if the dynamics are not favorable for their formation.

Hole-punch clouds induced aerodynamically by propeller and jet aircraft are a signature of a larger cloud process at work: inadvertent seeding

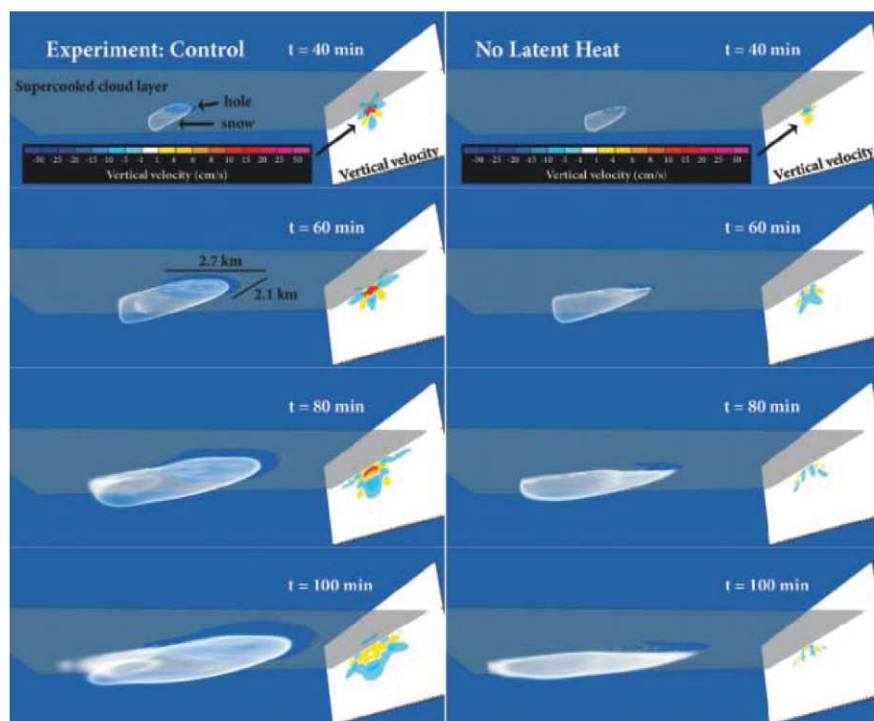


Fig. 4. Modeled fields of cloud (dark gray parallelogram, 14.5 km by 7.5 km, 50 m resolution), snow locations (gray shading), and a vertical slice of averaged vertical velocities (colored contours) located approximately along the wind direction. The model results are shown at 40, 60, 80, and 100 min after model initialization and 10, 30, 50, and 70 min after the introduction of ice. Color bar shows vertical velocity scale. **(Left)** Ice growth with latent heat released. **(Right)** Ice growth with latent heat turned off.

of ice in supercooled clouds at temperatures below about -10 or -20°C . It has already been established that contrails affect the atmosphere primarily at temperatures below -40°C (15). This process extends the envelope for aircraft effects on the atmosphere to warmer temperatures. Inadvertent seeding may not be important globally, but regionally near major airports in midlatitudes during cool weather months it may lead to enhanced precipitation at the ground. Polar clouds are particularly susceptible to the effect, modifying incoming and outgoing radiative fluxes near the surface and therefore local meteorology and climatology.

References and Notes

1. V. C. Schumacher, *Z. Angew. Met.* **57**, 214 (1940).
2. *Weather* **3**, 232 (1948).
3. *Weatherwise* **21**, 1 (1968).
4. A. L. Rangno, P. V. Hobbs, *J. Clim. Appl. Meteorol.* **22**, 214 (1983).
5. A. L. Rangno, P. V. Hobbs, *J. Clim. Appl. Meteorol.* **23**, 985 (1984).
6. K. Gierens, B. Kärcher, H. Mannstein, B. Mayer, *J. Atmos. Sci.* **66**, 217 (2009).
7. A. J. Heymsfield *et al.*, *Bull. Am. Meteorol. Soc.* **91**, 753 (2010).
8. R. S. Sekhon, R. C. Srivastava, *J. Atmos. Sci.* **27**, 299 (1970).
9. The selection of candidate aircraft is available as supporting material on *Science* Online, together with a table detailing aircraft types and numbers.
10. W. C. Skamarock, J. B. Klemp, *J. Comput. Phys.* **227**, 3465 (2008).
11. G. Thompson, P. R. Field, R. M. Rasmussen, W. D. Hall, *Mon. Weather Rev.* **136**, 5095 (2008).
12. W. L. Woodley *et al.*, *J. Appl. Meteorol.* **42**, 640 (2003).
13. The method of quantification is available as supporting material on *Science* Online.
14. D. Zhang, Z. Wang, D. Liu, *J. Geophys. Res.* **115**, D00H13 (2010).
15. H. Appleman, *Bull. Am. Meteorol. Soc.* **34**, 14 (1953).
16. The authors wish to thank contributors to the data used in this study: N. Mirsky, N. Downs, E. Zrubek, M. Carmody, B. Skamarock, J. Tuttle, P. Kennedy, C. Velden, D. Spangenberg, and J. Robaidek. Editing by M. Miller and graphics with particular help from A. Norton, co-developer of VAPOR software, are greatly appreciated. This research was supported by the National Center for Atmospheric Research through NSF, through NASA from grants NNX07AQ85G and NNX10AN18G, and through the FAA Aviation Climate Change Research Initiative.

Supporting Online Material

www.sciencemag.org/cgi/content/full/333/6038/77/DC1

Materials and Methods

Figs. S1 to S3

Table S1

13 January 2011; accepted 19 May 2011

10.1126/science.1202851

Pattern in Escalations in Insurgent and Terrorist Activity

Neil Johnson,¹ Spencer Carran,^{2,3} Joel Botner,⁴ Kyle Fontaine,⁵ Nathan Laxague,¹ Philip Nuetzel,⁵ Jessica Turnley,⁶ Brian Tivnan^{7,8}

In military planning, it is important to be able to estimate not only the number of fatalities but how often attacks that result in fatalities will take place. We uncovered a simple dynamical pattern that may be used to estimate the escalation rate and timing of fatal attacks. The time difference between fatal attacks by insurgent groups within individual provinces in both Afghanistan and Iraq, and by terrorist groups operating worldwide, gives a potent indicator of the later pace of lethal activity.

In 1948, Lewis Fry Richardson found that the number of wars with a given number of fatalities follows an approximate power-law statistical distribution as a function of the number of fatalities (1). Recent research has shown that a similar statistical distribution arises for the number of fatalities in individual clashes and acts of terrorism (2, 3), whereas the relative stability of these distributions over time allows an estimate to be given of the severity of future wars or clashes within an ongoing war (2–4). However, these existing studies say nothing about the operationally relevant questions (5–7) of how the underlying arms race evolves over time, or when fatal attacks might occur. Here, we confront these questions using fatality data obtained on an unprecedented daily scale from the ongoing insurgent war in Afghanistan and the recent one in Iraq. Our data analysis is freely available for public scrutiny: The coalition military fatality data come from the public Web site www.icasualties.org. Our analysis was done with the free down-

loadable tool Open Office, which runs on any computer platform. The supporting online material (SOM) for this paper contains step-by-step instructions together with Open Office worksheets. For Afghanistan, we include fatalities from the start of Operation Enduring Freedom in 2001 until summer 2010, when General Petraeus became commander of the International Security Assistance Force and the U.S.-led surge started. For Operation Iraqi Freedom, the data include fatalities from 2003 until summer 2010, when U.S. military action officially ended. The terrorism results are derived from a recent study, which used the database of the Memorial Institute for the Prevention of Terrorism, comprising the 3143 fatal attacks carried out by the 381 known terrorist groups operating within the period 1968–2008 (8). Suicide bombing data for Hezbollah (1982–1985) and Pakistan militants (1995–2008) comes from the public Web site <http://cpost.uchicago.edu>.

For a wide range of human activities, the time taken to complete a given challenging task decreases with successive repetitions, following an approximate power-law progress curve (8–12). This inspires us to analyze the insurgents' completion of fatal attacks against coalition military forces in a similar way (Fig. 1, A and B). We calculated the best-fit power-law progress curve $\tau_n = \tau_1 n^{-b}$, where τ_n represents the interval between the $(n - 1)$ 'th and n 'th fatal day (one in which the insurgent activity produces at least one

coalition military death), where $n = 1, 2, 3$, etc. b indicates the escalation rate. τ_1 is the time interval between the first 2 days with coalition military fatalities. (For global terrorism, a fatal day is one in which a particular terrorist group produced at least one death anywhere in the world.) Figure 1C shows the best-fit values τ_1 and b for each province in Afghanistan, for all forms of hostile death. The average number of fatalities per fatal attack is fairly constant in a conflict (2, 3, 8), hence it is in insurgents' interest (or that of a particular terrorist group) that the time between fatal days decrease rapidly, and hence b is large and positive, while the opposite is true for the military (or counterterrorism force). The scatter in τ_n in Fig. 1B is typical for real-world tasks (in particular, given the ongoing two-way struggle), and the Pearson rank product-moment correlation coefficient (R^2) is within an acceptable range for social systems (9–14). Although alternative progress curve forms are possible, any such two-parameter progress curve amounts to a nonlinear transformation of the power-law form and hence generates a more complex version of Fig. 1C. An exponential form does not generate systematically better progress-curve fits; R^2 for the power-law form is better by up to 70% for three-quarters of the provinces, including (most importantly) those with the most data points, and only tends to be comparable for the few provinces having sparse datapoints and larger τ_n scatter. We do not consider events with no deaths because they occur almost daily; moreover, the injury statistics are not publicly available. Although the data resolution time scale is 1 day, this is not problematic, because the τ_n values dictating the best-fit progress curve for a given province, or terrorist group, are usually much larger than 1.

Figure 1C reveals a surprising linear relationship between the best-fit progress curve values τ_1 and b for individual provinces. The straight line through the provinces has $R^2 = 0.9$ and is given by the equation $b = m \log_{10} \tau_1 + c$, with best-fit parameter values $m = 0.89$ and $c = -1.22$. Even if one speculated that the τ_1 and b values have to lie somewhere in this range (which, a priori,

¹Department of Physics, University of Miami, Coral Gables, FL 33124, USA. ²Department of Biology, University of Miami, Coral Gables, FL 33124, USA. ³Department of Mathematics, University of Miami, Coral Gables, FL 33124, USA. ⁴Department of Computer Science, University of Miami, Coral Gables, FL 33124, USA. ⁵Department of International Studies, University of Miami, Coral Gables, FL 33124, USA. ⁶Galisteo Consulting Group, Albuquerque, NM 87110, USA. ⁷The MITRE Corporation, McLean, VA 22102, USA. ⁸Complex Systems Center, University of Vermont, Burlington, VT 05405, USA.

they do not), a simple Monte Carlo calculation puts the probability of this linear relationship emerging by chance with a comparable R^2 at less than 1 in 10^6 . Figure 2 shows that the linear relationship extends to a specific weapon [that is, fatalities caused by improvised explosive devices (IEDs)] and to a completely different insurgent conflict (Iraq), as well as to global terrorism and suicide bombings by individual groups. These τ_1 and b values suggest, for example, that common organizational processes underlie all hostile military fatalities in Farah and Kunar, IED military fatalities in Kabul, and fatal terrorist attacks. The fact that Fig. 2 shows larger scatter than Fig. 1C is understandable given its inclusion of events in separate countries and the sparser number of IED fatalities as compared to total hostile fatalities. Although the Afghanistan provinces exhibit an escalation of fatal days throughout the entire data set (that is, decreasing τ_n), the Iraq provinces cease to show pure escalation toward the end of the conflict, where fatalities cease. Because this paper focuses on escalation, the Iraq data points in Fig. 2 correspond to the initial escalation up to the turning point in the cumulative moving average of τ_n . Other reasonable methods for determining a turning point retain the same linear structure as that in Fig. 2.

We considered the possibility that these results derive from contagion or diffusion effects due to proximity. The data points for Kandahar, Kunar, and Farah sit nearby in Fig. 1C, showing that their escalation patterns are almost identical; however, they are widely separated geographically within Afghanistan, with Kandahar in the south, Kunar in the east, and Farah in the west. If fatal days in different provinces were synchronized in calendar time (which they are not), they would sit at the same point in Fig. 1C, but they do not. Likewise, if fatal days in different provinces were independent, then the individual (τ_1, b) points should be scattered randomly across Fig. 1C, but they are not. Comparing Fig. 1C to detailed sociotechnical maps (15), we could not detect a clear systematic relationship between the data point locations and effects such as proximity to Pakistan, density of internally displaced persons, common tribal warlords, or levels of poppy production (16). In terms of increases in troop or insurgent numbers, it would have required a very complex and specific province-dependent increase, combined with a very contrived mathematical relationship to fatalities, to produce the observed patterns. Instead, the calendar times for the n 'th fatal day vary wildly between provinces (for instance, the first recorded military fatality in Paktia was 4 March 2002, whereas in Wardak it was 25 July 2007). Nor are the observed patterns simply linked to an increase in the number of troops and hence to an increase in the number of targets, because monthly troop increases in Afghanistan were almost linear, not a power curve (16, 17). Furthermore, as observed in Iraq after the surge, significant troop increases can actually decrease the military fatality rate.

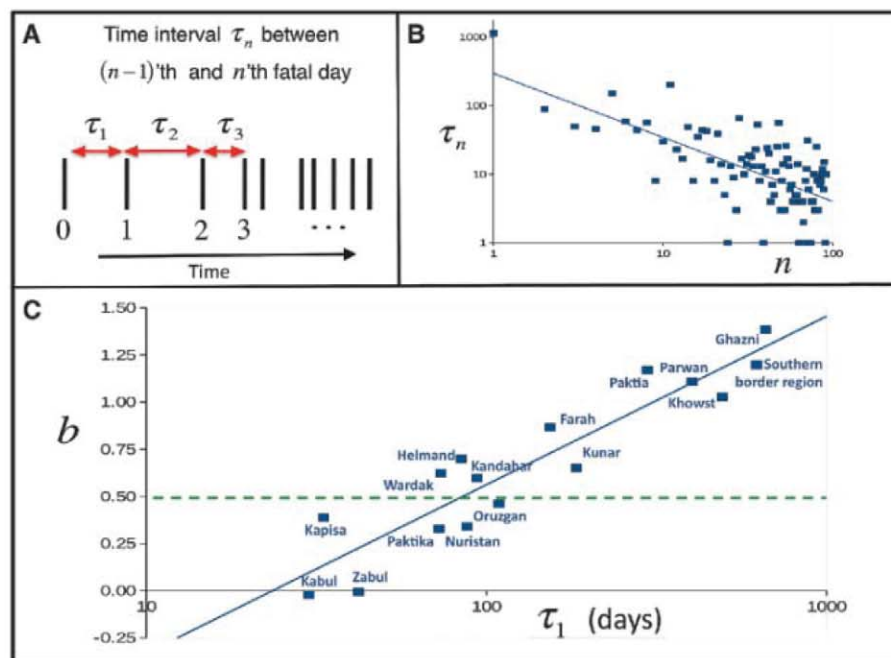


Fig. 1. (A) Schematic timeline of successive fatal days shown as vertical bars. τ_1 is the time interval between the first two fatal days, labeled 0 and 1. (B) Successive time intervals τ_n between days with IED fatalities in the Afghanistan province of Kandahar (squares). On this log-log plot, the best-fit power-law progress curve is by definition a straight (blue) line with slope $-b$ (b is an escalation rate). (C) The solid blue line shows best linear fit through progress-curve parameter values τ_1 and b for individual Afghanistan provinces (blue squares) for all hostile fatalities (all coalition military fatalities attributed to insurgent activity). The green dashed line shows value $b = 0.5$, which is the situation in which there are no correlations. The subset of fatalities recorded in casualties as “southern Afghanistan” is shown as a separate region because of their likely connection to operations near the Pakistan border.

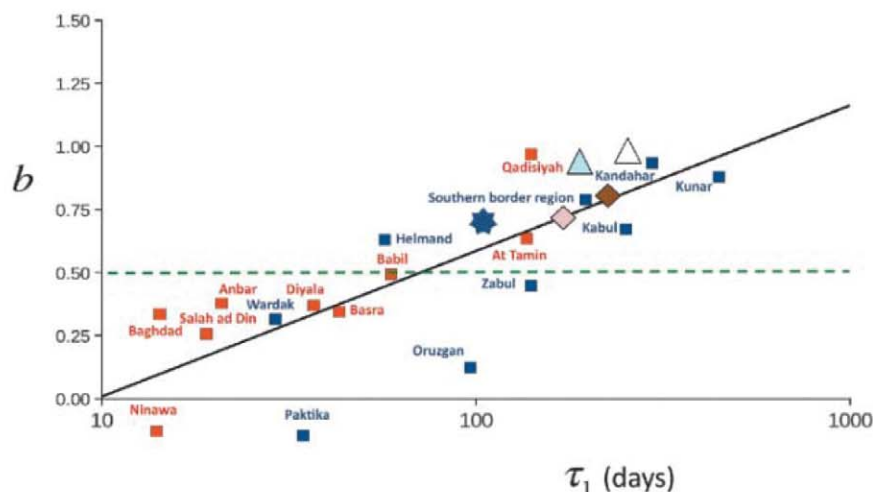


Fig. 2. The solid black line shows the best linear fit through progress-curve parameter values τ_1 and b for IED fatalities in provinces in Afghanistan (blue squares) and Iraq (red squares). Because the frequency of IED fatalities for provinces sitting just below $b = 0$ is low, their b values are relatively uncertain and should be regarded simply as $b \approx 0$. The green dashed line is at $b = 0.5$. These findings are consistent with results for IED data aggregated over all Afghanistan (blue star) and for global terrorism and suicide bombings. Global terrorism: The dark diamond shows the τ_1 and b values deduced from the best-fit progress curve for global terrorist group activity when averaged over all attacks (8); the light diamond is an alternative estimate where τ_1 and b are calculated directly by inserting the time intervals between initial attacks into the progress curve formula (SOM). Suicide bombings: The blue triangle is for Hezbollah suicide attacks, and the white triangle is for suicide attacks within Pakistan (data are from <http://cpost.uchicago.edu/>).

We also analyzed timelines from detailed online reports concerning political events (SOM); however, these timelines represented a poor fit to a progress curve ($R^2 = 0.2$) and produced (τ_1 , b) values ($\tau_1 = 12.4$ and $b = -0.75$), which were unlike those shown in Figs. 1C or 2.

Our broad-brush theory does not require knowledge of specific adaptation or counter-adaptation mechanisms, and hence bypasses issues such as changes in insurgent membership, technology, learning, or skill set, as well as a need to know the hearts and minds of local residents. We regard the escalation of hostilities as representing adaptation and counteradaptation in a way that is analogous to the Red Queen hypothesis of evolutionary biology (18, 19). The traditional story features the Red Queen (which in our context is an insurgency, or terrorist group) running as fast as she can just to stay at the same place, implying that her Blue King opponent (the coalition military or antiterrorism organization) instantaneously and perfectly counteradapts to her advances so that they are always neck and neck (the distance between the two $R = 0$). However, instantaneous and perfect counteradaptation is unrealistic; indeed, complex adaptation-counteradaptation dynamics generated by sporadic changes in circumstances imply that R 's temporal evolution is likely to be so complex that it can be modeled as a stochastic process (20, 21). We do not need to know exactly why R changes at any specific moment, nor do the changes in R have to have the same value, because each change is the net result of a mix of factors [such as learning by experience or changes in personnel and technology (5–7)] for each opponent. When the Red Queen is in the lead ($R > 0$), there will inevitably be fatal days. If her lead increases, the rate of fatal days should also increase, hence for $R > 0$, we take the instantaneous rate of fatal days as proportional to R . As R tends to 0, fatal days become increasingly rare. When $R < 0$, the Blue King holds the lead and there are no fatal days. By definition, provinces with no fatal days do not appear in Figs. 1C and 2 (mathematically, τ_1 becomes infinite and b is undefined). The provinces in Figs. 1C and 2 exhibit escalation and are therefore consistent with an R that is generally positive and increasing over time. For these provinces, significant changes in the Red Queen's lead R are likely to occur around fatal days, making R a function of n : The Red Queen has by definition become successful at that moment and this may stimulate a further increase in R , whereas the Blue King's failure may stimulate an effective counteradaptation effort and hence reduce R . In the simple limiting case where changes in R are statistically independent and have finite variance, the Central Limit Theorem (20) says that the typical magnitude (the root mean square) of the Red Queen's lead R after n steps varies as n^b , where $b = 0.5$ (SOM), which is the random walk result widely used in physics, biology, and economics (20–22). For the more general and realistic case in which changes in R depend on

prior history, research on correlated walks shows that b will deviate from 0.5 but will typically remain in the range $0 \leq b \leq 1.5$ (20–22), in agreement with Figs. 1C and 2. Because the rate is inversely proportional to the time interval, this gives $\tau_n = an^{-b}$, where a is a constant of proportionality. Setting $n = 1$ yields $\tau_1 = a$, hence our theory reproduces the empirical finding that the escalation of fatal days follows an approximate power-law progress curve $\tau_n = \tau_1 n^{-b}$ with typical values in the range $0 \leq b \leq 1.5$. Our theory interprets provinces with b values near 1 as having an ineffective military counteradaptation, so that R persistently increases at every step n , hence $R \propto n^b$ with $b = 1$. This is analogous to the Red Queen moving steadily forward at constant velocity while the Blue King remains stuck at the starting line. If the Red Queen gains momentum, R can start accelerating and hence $b > 1$ as observed for some provinces such as Paktia and Ghazni in Fig. 1C. The fact that b values for IEDs appear to be concentrated between 0 and 1 (Fig. 2) whereas the all-hostile range is from 0 to 1.5 (Fig. 1C) suggests that the coalition military counteradapts to IEDs better than to other threats. Provinces at $b = 0$ (Kabul and Zabul in Fig. 1C) have a constant rate of fatal days, implying that the military is managing to contain further escalation. Similar interpretations can be made for any other data point in Figs. 1C and 2, according to its b value.

The linear relationship between τ_1 and b in Figs. 1C and 2 can be reproduced by adding a coupling between the Red Queen–Blue King arms races in different provinces. This coupling can arise for various reasons: Even though the insurgent groups (Red Queens) operating in two different locations may be unconnected, and even though they inflict military fatalities at different points in space and calendar time, the Blue King opponent is essentially the same for each (the same military coalition), and hence the insurgents in one province may eventually adopt successful tactics from another. On the Blue King side, the widespread use of similar tactics or equipment could generate coupling. For example when MRAPs (Mine Resistant Ambush Protected vehicles) were moved to Afghanistan, the Blue King effectively took on very similar operational characteristics in each country: slow, lumbering movement restricted to certain transport corridors.

To illustrate the potential of our findings, suppose that a quiet region suddenly experiences 2 fatal days. We can estimate the escalation rate b for future fatal days in that region by taking the initial time interval to be τ_1 and reading off the corresponding b value from Fig. 1C or 2. An estimate for the date of the m 'th future fatal day can also be obtained by summing all time intervals $n < m$ using $\tau_n = \tau_1 n^{-b}$. Figure 1B suggests that actual time intervals may exhibit significant scatter around the τ_n estimates; however, their sum (and hence the actual calendar date) will show less variability because positive and nega-

tive errors in τ_n tend to cancel when summed. Inputting only the first data point in Fig. 1B, the error between the predicted and actual time of the ultimate fatal day ($n = 92$, which occurred on 13 May 2010) is less than 25%, which is far smaller than the scatter in individual τ_n values might have suggested. Access to detailed classified data sets would enable future analysis to fully explore this possibility, and may help establish a systematic approach to quantifying an insurgency's momentum, the effectiveness of countermeasures, and that of countermeasure training processes. The fact that Figs. 1C and 2 link progress curves across two current theaters of war and global terrorism may open broader lines of inquiry into group learning, adaptive management strategies, and production metrics associated with modern uprisings, such as those underway in the Middle East. One might argue that analyses of this kind are useless once publicly known, because they can be invalidated by insurgents' free will. However, we believe this will not happen for the same reason that all commuters know that a traffic jam will appear every day at rush hour on a certain route, yet many still end up joining it. External constraints of working hours, school schedules, and finite numbers of direct roads mean that such predictability is hard to avoid. Similarly, the spontaneity of fatal attacks by an insurgency is probably constrained by many factors, including the availability of troop convoys, explosive materials, and sympathy within the local population.

References and Notes

1. L. F. Richardson, *J. Am. Stat. Assoc.* **43**, 523 (1948).
2. J. C. Bohorquez, S. Gourley, A. R. Dixon, M. Spagat, N. F. Johnson, *Nature* **462**, 911 (2009).
3. A. Clauset, M. Young, K. S. Gleditsch, *J. Conflict Resolut.* **51**, 58 (2007).
4. M. Lim, R. Metzler, Y. Bar-Yam, *Science* **317**, 1540 (2007).
5. M. T. Flynn, *Fixing Intel: A Blueprint for Making Intelligence Relevant in Afghanistan* (Center for a New American Security, Washington, DC, 2010).
6. J. Robb, *Brave New War: The Next Stage of Terrorism and the End of Globalization* (Wiley, Hoboken, NJ, 2007).
7. D. Kilcullen, *The Accidental Guerrilla: Fighting Small Wars in the Midst of a Big One* (Oxford Univ. Press, Oxford, 2009).
8. A. Clauset, K. S. Gleditsch, e-print available at <http://arxiv.org/abs/0906.3287v1> (2009).
9. J. M. Dutton, A. Thomas, *Acad. Manage. Rev.* **9**, 235 (1984).
10. L. Argote, D. Epple, *Science* **247**, 920 (1990).
11. S. P. Saraswat, J. T. Gorgone, *Inf. Manage.* **19**, 53 (1990).
12. A. Mottrif et al., *Eur. Urol.* **58**, 127 (2010).
13. N. Ducheneaut et al., in *Proceedings of CHI 2007*, Special Interest Group on Computer-Human Interaction, 28 April to 3 May 2007, San Jose, CA (Association for Computing Machinery Press, New York, 2007).
14. J. Cohen, *Statistical Power Analysis for the Behavioral Sciences* (Lawrence Erlbaum Associates, Hillsdale, NJ, ed. 2, 1988).
15. www.nps.edu/programs/ccs/index.html.
16. A. Belasco, *Troop Levels in the Afghan and Iraq Wars*, 7-5700, R40682 (Congressional Research Service, Washington DC, 2009).
17. International Security Assistance Force, ISAF Troop Numbers 2008–2010, 14 January 2011; as referred to in (23).

18. D. D. P. Johnson, *J. Wash. Acad. Sci.* **95**, 89 (2009).
19. R. D. Sagarin *et al.*, *Nature* **465**, 292 (2010).
20. J. Rudnick, G. Gaspari, *Elements of the Random Walk* (Cambridge Univ. Press, Cambridge, 2010).
21. D. Ben-Avraham, S. Havlin, *Diffusion and Reactions in Fractals and Disordered Systems* (Cambridge Univ. Press, Cambridge, 2000).
22. N. F. Johnson, P. Jefferies, P. M. Hui, *Financial Market Complexity* (Oxford Univ. Press, Oxford, 2003), p. 20.
23. J. Bohannon, *Science* **331**, 1256 (2011).

Acknowledgments: The authors gratefully acknowledge support for this research from the Joint IED Defeat Organization, IDN# N70465, and from The MITRE Corporation and the Santa Fe Institute for their co-hosting of the "Mathematics of Terrorism" workshop. The views and conclusions contained in this paper are those of the authors and should not be interpreted as representing the official policies, either expressed or implied, of any of the above named organizations, to include the U.S. government. We also thank P. Dodds, C. Danforth and A. Clauset for broad discussions

surrounding this topic, L. Amaral for discussions concerning non-Poissonian behavior, and the anonymous reviewers for suggestions.

Supporting Online Material

www.sciencemag.org/cgi/content/full/333/6038/81/DC1
SOM Text
Figs. S1 to S3
SOM Data Analysis

2 March 2011; accepted 26 May 2011
10.1126/science.1205068

Mechanism of RAD51-Dependent DNA Interstrand Cross-Link Repair

David T. Long,¹ Markus Räschele,² Vladimir Joukov,³ Johannes C. Walter^{1*}

DNA interstrand cross-links (ICLs) are toxic DNA lesions whose repair in S phase of eukaryotic cells is incompletely understood. In *Xenopus* egg extracts, ICL repair is initiated when two replication forks converge on the lesion. Dual incisions then create a DNA double-strand break (DSB) in one sister chromatid, whereas lesion bypass restores the other sister. We report that the broken sister chromatid is repaired via RAD51-dependent strand invasion into the regenerated sister. Recombination acts downstream of FANCI-FANCD2, yet RAD51 binds ICL-stalled replication forks independently of FANCI-FANCD2 and before DSB formation. Our results elucidate the functional link between the Fanconi anemia pathway and the recombination machinery during ICL repair. In addition, they demonstrate the complete repair of a DSB via homologous recombination in vitro.

In vertebrate cells, DNA interstrand cross-link (ICL) repair is coupled to DNA replication and involves structure-specific endonucleases, translesion DNA polymerases, recombinases, and numerous proteins mutated in the human disease Fanconi anemia (FA) (1). FA is characterized by genomic instability and cellular sensitivity to DNA interstrand cross-linking agents. A central event in the FA pathway is the ubiquitylation of the FANCI-FANCD2 heterodimer, which activates it

for ICL repair (2, 3). Extensive evidence indicates that homologous recombination (HR) is essential for ICL repair (4–9). However, the precise role of HR in ICL repair remains conjectural, and the functional connection between the FA and HR pathways is unclear.

Using *Xenopus* egg extracts, we established a cell-free system for replication-dependent repair of a plasmid containing a single, site-specific cisplatin ICL (pICL) (Fig. 1A) (2, 10). Upon addition

of pICL to egg extracts, replication initiates at a random site, and two replication forks converge on the ICL (Fig. 1B, i). The leading strand of one fork is then extended to within one nucleotide of the ICL (Fig. 1B, ii). Next, dual incisions surrounding the ICL create a DNA double-strand break (DSB) in one sister chromatid, and translesion DNA synthesis restores the other sister by first inserting a nucleotide across from the adducted base (Fig. 1B, iii), followed by strand extension beyond the ICL (Fig. 1B, iv). Ultimately, 5 to 25% of replicated pICL is fully repaired, as measured by regeneration of a SapI site that was originally interrupted by the cross-link (2, 10). In the absence of ubiquitylated FANCD2, DNA incisions, lesion bypass, and SapI site regeneration are greatly diminished (2). Given the established links between HR and ICL repair and the inefficient removal of the unhooked ICL in egg extracts (10), we postulated that SapI site regen-

¹Department of Biological Chemistry and Molecular Pharmacology, Harvard Medical School, Boston, MA 02115, USA. ²Department of Proteomics and Signal Transduction, Max Planck Institute of Biochemistry, 82152 Martinsried, Germany. ³Department of Cancer Biology, Dana-Farber Cancer Institute, Boston, MA 02115, USA.

*To whom correspondence should be addressed. E-mail: johannes_walter@hms.harvard.edu

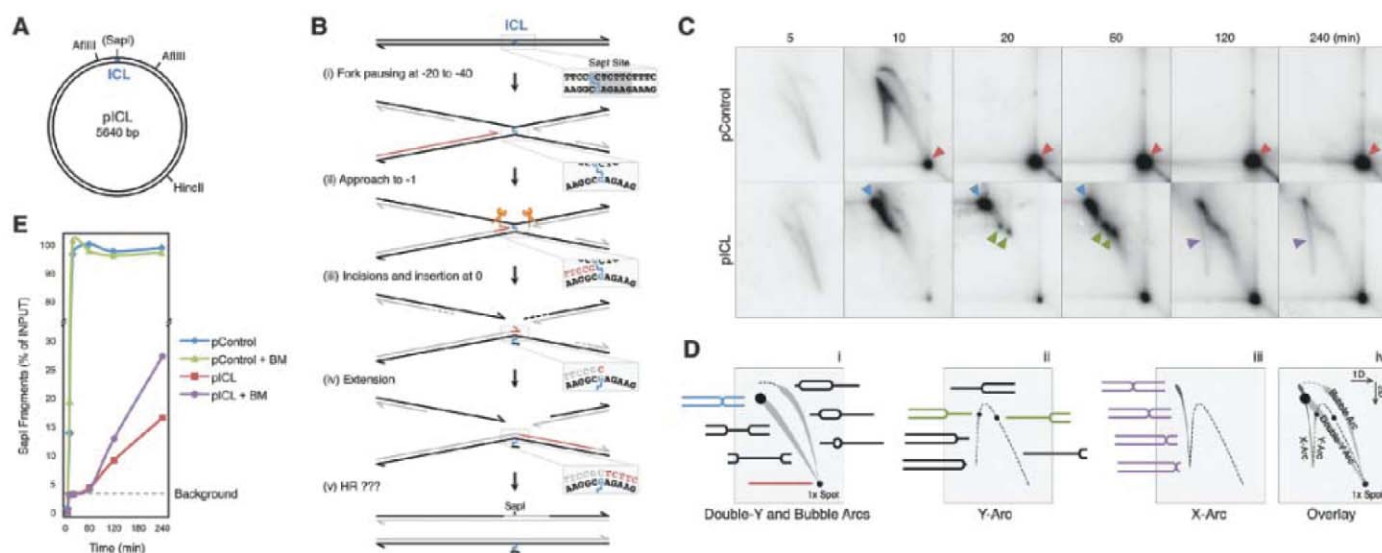


Fig. 1. The X-arc contains intermediates of ICL repair. (A) pICL schematic. (B) Model of ICL repair in *Xenopus* egg extracts (2, 10). (C) pControl or pICL was replicated in egg extract, digested with HincII, and analyzed by 2DGE. Arrowheads, see main text. (D) Cartoon of 2DGE patterns and relevant DNA intermediates. (E) ICL repair of samples from (C) was analyzed under normal and branch migration (+BM) conditions. Background, SapI fragments from contaminating un-cross-linked plasmid. For primary data, see fig. S1, E and F. All graphed experiments were performed at least three times, and a representative example is shown.

eration involves repair of the broken sister chromatid by recombination with the intact sister (Fig. 1B, v).

To look for evidence of HR in ICL repair, pICL or an undamaged control plasmid (pControl) was replicated in egg extract, digested with HincII (Fig. 1A), and analyzed by two-dimensional gel electrophoresis (2DGE) (Fig. 1, C and D) (11). After 5 min, both plasmids generated the expected double-Y and bubble replication intermediates (Fig. 1C and Fig. 1D, i). As replication neared completion, pControl produced unit-sized linear DNA molecules (Fig. 1C, red arrowheads, and Fig. 1D, i), whereas pICL yielded a discrete X-shaped intermediate that results from the con-

vergence of two forks on the ICL (Fig. 1C, blue arrowheads, and Fig. 1D, i). Two simple-Y intermediates also accumulated (3 to 7% of total signal), suggesting that a small number of converging forks undergo aberrant breakage or cleavage (Fig. 1C, green arrowheads, and Fig. 1D, ii). By 60 min, the X-shaped intermediates showed signs of processing, likely due to resection of the nascent lagging strands (10). Even later, the X- and Y-shaped intermediates were replaced by an "X-arc" (Fig. 1C, purple arrowheads, and Fig. 1D, iii). Formation of the X-arc coincided with SapI site regeneration (Fig. 1E, red trace), suggesting that the X-arc contains intermediates of ICL repair.

X-arcs are generally formed when two unit-sized linear molecules are joined by a mobile branch point, such as a Holliday junction or hemicatenane (Fig. 1D, iii) (12). Under conditions that promote resolution of mobile junctions through branch migration (13), the X-arc intermediates of pICL were resolved primarily into the predicted unit-sized linear molecules, whether magnesium was present or not (fig. S1, A to C). Magnesium inhibits migration of Holliday junctions, which implies that the X-arc intermediates contain hemicatenanes. Consistent with this, X-arc intermediates were resistant to cleavage by the Holliday junction resolvase, RuvC (fig. S1D). Exposing replicated pICL to branch migration conditions increased the yield of SapI repair fragments (Fig. 1E, purple trace), further indicating that X-arcs contained intermediates of ICL repair.

If repair of pICL involves HR, inhibiting the RAD51 recombinase should block repair. To test this prediction, we used a ~35-amino acid "BRC" peptide derived from BRCA2 that binds RAD51 and, when supplied at high concentrations, inhibits RAD51 nucleoprotein filament formation (14). As recently reported (15), addition of a BRC^{WT} (where WT is wild type) peptide (fig. S2A) to *Xenopus* egg extracts abolished RAD51 loading onto damaged chromatin (Fig. 2A). Two variants of the peptide that were mutated in one (BRC*) or three (BRC***) amino acids (fig. S2A) were increasingly compromised for RAD51 binding (Fig. 2B) and inhibition of RAD51 loading (Fig. 2A), demonstrating that BRC^{WT} specifically targets RAD51. Without affecting DNA replication (fig. S2B), the BRC peptides inhibited X-arc formation proportional to their effect on RAD51 binding and filament formation (compare Fig. 2, A and B, with Fig. 2C). Thus, X-arc intermediates are RAD51-dependent, indicating

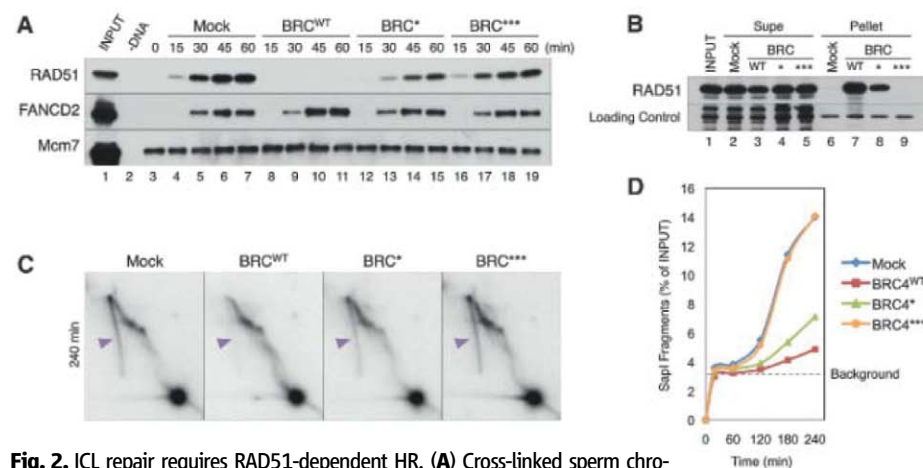


Fig. 2. ICL repair requires RAD51-dependent HR. (A) Cross-linked sperm chromatin was replicated in extract containing buffer (Mock) or the indicated BRC peptide, and chromatin-associated proteins were analyzed by Western blotting. (B) BRC peptides immobilized on glutathione sepharose beads were incubated with egg extract (13), pulled down, and the supernatant (Supe) and pellet blotted for RAD51. (C) pICL was replicated in extract containing buffer (Mock) or the indicated BRC peptide. Samples were digested with HincII and analyzed by 2DGE. Purple arrowheads, X-arc position. (D) Samples from (C) were analyzed for ICL repair as in Fig. 1E.

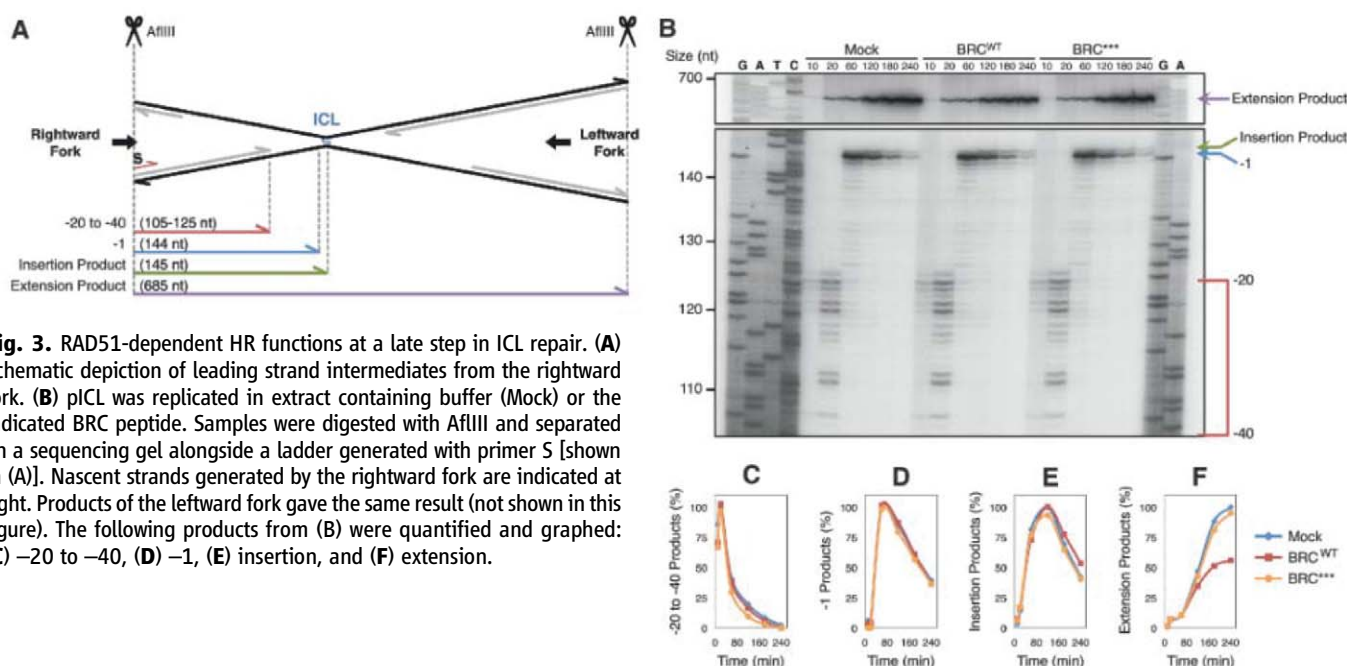


Fig. 3. RAD51-dependent HR functions at a late step in ICL repair. (A) Schematic depiction of leading strand intermediates from the rightward fork. (B) pICL was replicated in extract containing buffer (Mock) or the indicated BRC peptide. Samples were digested with AflIII and separated on a sequencing gel alongside a ladder generated with primer S [shown in (A)]. Nascent strands generated by the rightward fork are indicated at right. Products of the leftward fork gave the same result (not shown in this figure). The following products from (B) were quantified and graphed: (C) -20 to -40, (D) -1, (E) insertion, and (F) extension.

they represent products of HR. Although BRC^{WT} almost completely abolished SapI site regeneration, BRC^* caused intermediate inhibition and BRC^{***} had no effect (Fig. 2D). These results demonstrate that replication-coupled ICL repair requires RAD51-dependent HR. Because dual incisions result in a two-ended DSB (Fig. 1B, iii), recombination likely first yields a double Holliday junction, which is then converted to a mobile hemicatenane.

We next used BRC peptides to investigate which step in ICL repair involves RAD51. Replicating pICL was digested with AflIII (Fig. 1A) and subjected to denaturing gel electrophoresis to examine leading strand products of the rightward and leftward replication forks as they converge on the ICL (Fig. 3A). In the presence of BRC^{WT} , the arrival of leading strands 20 to 40 nucleotides from the ICL (Fig. 3, B and C), the approach of leading strands to the -1 position (Fig. 3, B and D), and nucleotide insertion across from the adducted base (Fig. 3, B and E) were all unaffected. When BRC^{WT} samples were analyzed by native 1D- and 2DGE, there was no change in the rate at which dual-stalled fork structures disappeared (fig. S3, A to D), indicating that DNA incisions were unaffected. In contrast, BRC^{WT} specifically reduced full-length extension products twofold (Fig. 3, B and F), consistent with an absence of

RAD51-mediated restoration of the broken sister chromatid (Fig. 1B, v). Timed addition of BRC peptides to ICL repair reactions indicated that RAD51 completes its repair function late, just before SapI site regeneration (fig. S4, A and B). Additionally, plasmid competition experiments showed that recombination occurred primarily between sister chromatids (fig. S5). Together, the data indicate that RAD51-dependent HR between the broken and intact sister chromatids is a crucial, late step in ICL repair.

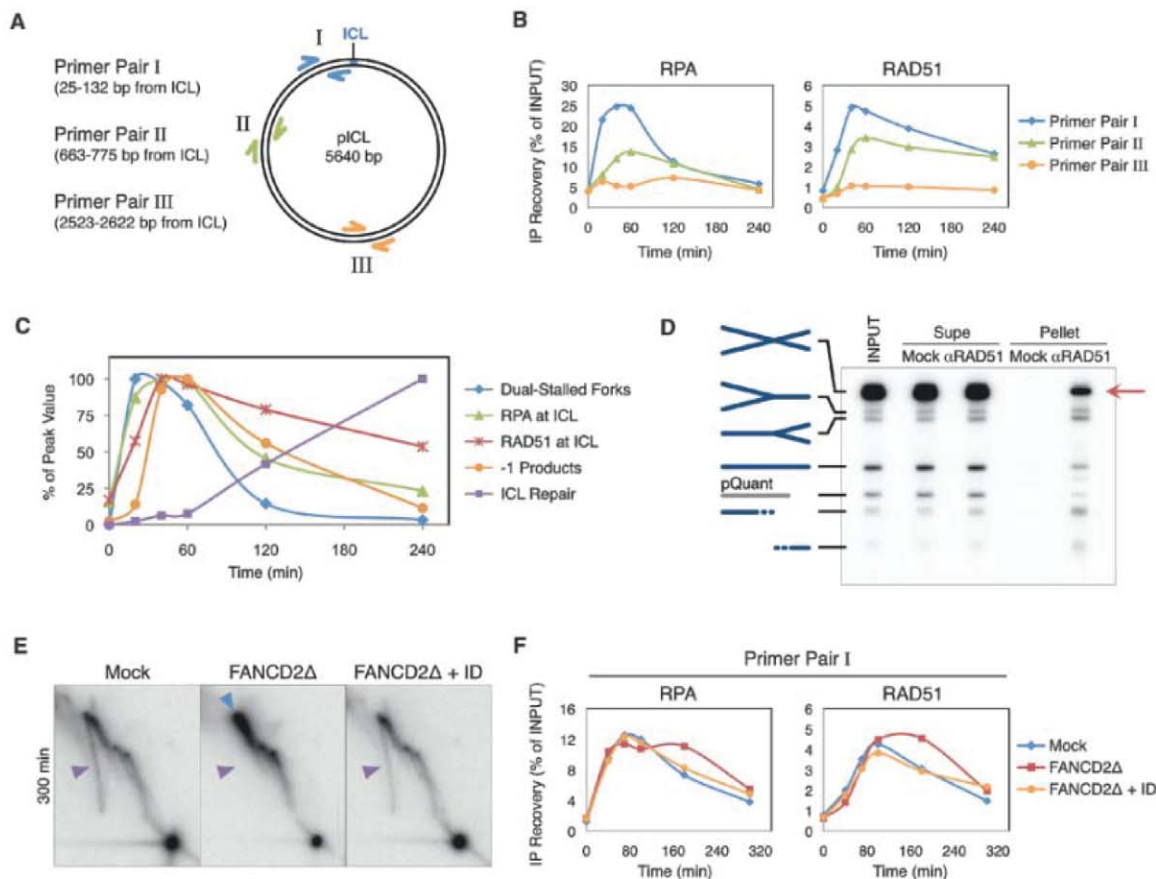
We used chromatin immunoprecipitation (ChIP) to examine the binding of RAD51 and replication protein A (RPA) to three locations on pICL during repair (Fig. 4A). Initially, RPA and RAD51 accumulated near the ICL (Fig. 4B, site I). After a delay, they also bound ~700 base pairs from the ICL (Fig. 4B, site II), likely due to resection of lagging strands (10), but they never accumulated opposite the ICL (Fig. 4B, site III). No RAD51 binding was detected in the absence of replication, on undamaged plasmids, or in the presence of BRC^{WT} (fig. S6A). The timing of RPA binding coincided with the convergence of DNA replication forks at the lesion, followed shortly thereafter by RAD51 binding (Fig. 4C; green, blue, and red traces). When RAD51 binding peaked at 40 min, greater than 90% of the dual-

stalled fork structures remained, indicating that little or no incisions had taken place (Fig. 4C, compare red and blue traces). To rule out the possibility that RAD51 binding at this time was limited to a small number of broken fork intermediates, we immunoprecipitated RAD51 from repair reactions and examined the associated DNA intermediates. Fifty-three percent of DNA associated with RAD51 consisted of intact, dual-stalled fork structures (Fig. 4D, red arrow). Thus, in the context of ICL repair, RAD51 is loaded onto stalled replication forks before DSB formation.

We next examined the connection between the FA and HR pathways. In FANCD2-depleted extracts, the X-arc disappeared, and it was rescued by readdition of recombinant FANCI-FANCD2 (Fig. 4E, purple arrowheads). As expected, the dual-stalled fork structure persisted in the absence of FANCD2 (Fig. 4E, blue arrowhead), consistent with a defect in incisions (2). The data indicate that HR acts downstream of FANCI-FANCD2 during ICL repair, explaining previous epistasis experiments (7). Consistent with some analyses of RAD51 foci [reviewed in (8)], RAD51 binding to ICLs was not reduced in the absence of FANCD2 (Fig. 4F and fig. S7, A to C). Conversely, inhibition of RAD51 function using BRC^{WT} peptide had no effect on FANCD2 recruitment or

Fig. 4. Interplay between the HR and FA pathways.

(A) Schematic of ChIP primer pairs. (B) pICL was replicated and analyzed by RPA and RAD51 ChIP. Controls containing BRC^{WT} peptide, pControl, or lacking DNA replication are shown in fig. S6A. (C) Samples from (B) were also analyzed for the timing of fork convergence, -1 product accumulation, and repair (raw data in fig. S6, B to D). The data were graphed as percentage of peak value and compared with RPA and RAD51 ChIP at site I [from (B)]. (D) pICL was replicated in extract for 40 min and immunoprecipitated with RAD51 antibodies (13). Recovered DNA was digested with HincII and analyzed by agarose gel electrophoresis. Repair intermediates are depicted at left for pICL (blue) and an internal control plasmid, pQuant (gray). Red arrow, see main text. (E) pICL was replicated in mock-depleted egg extract (Mock), FANCD2-depleted extract (FANCD2Δ), or FANCD2Δ extract supplemented with 375 nM FANCI-FANCD2 (FANCD2Δ+ID). Samples were digested with HincII and analyzed by 2DGE. Arrowheads, see text.



See fig. S7E for complete 2D gel time courses. (F) Samples from (E) were analyzed by ChIP using primer pair I. Primer pairs II and III are shown in fig. S7A. IP, immunoprecipitation.

ubiquitylation (Fig. 2A and fig. S7D). Together, our data show that FANCI-FANCD2 acts upstream of HR in the context of replication-coupled ICL repair, but that it is not required for RAD51 recruitment to chromatin. Instead, the requirement for FANCI-FANCD2 in promoting HR can be explained by its role in promoting the incisions that underlie DSB formation (2). The FA pathway may also enhance HR via more direct mechanisms, because FA proteins also stimulate HR in the context of preformed DSBs (6, 7, 9, 16, 17).

Here, we report that in the context of replication-coupled ICL repair, the DSB generated in one sister chromatid through the action of FANCI-FANCD2 is fixed via strand invasion into the intact sister (fig. S8). We find that RAD51 binds efficiently to ICLs before a DSB has been generated (fig. S8, ii). Although lesion bypass likely displaces RAD51 from one sister chromatid, incisions and resection of the other sister creates a new docking site for RAD51, such that both ends of the DSB are coated with the recombinase (fig. S8, iv). The interaction of RAD51 with ICL-stalled forks before DSB formation may function to prevent fork breakage/degradation (5, 15, 18) in favor of regulated incisions and/or to initiate

strand invasion as soon as possible once the DSB has been formed.

A major obstacle impeding our understanding of DSB repair has been the absence of cell-free systems. Combined with ChIP and the ability to inactivate or remove essential proteins, the system described here represents a powerful tool to elucidate the complex mechanism underlying DSB repair.

References and Notes

1. G.-L. Moldovan, A. D. D'Andrea, *Annu. Rev. Genet.* **43**, 223 (2009).
2. P. Knipscheer *et al.*, *Science* **326**, 1698 (2009); 10.1126/science.1182372.
3. W. Wang, *Nat. Rev. Genet.* **8**, 735 (2007).
4. A. J. Deans, S. C. West, *Mol. Cell* **36**, 943 (2009).
5. K. Nakanishi *et al.*, *Nat. Struct. Mol. Biol.* **18**, 500 (2011).
6. K. Nakanishi *et al.*, *Proc. Natl. Acad. Sci. U.S.A.* **102**, 1110 (2005).
7. W. Niedzwiedz *et al.*, *Mol. Cell* **15**, 607 (2004).
8. L. H. Thompson, J. M. Hinz, *Mutat. Res. Fundam. Mol. Mech. Mutagenesis* **668**, 54 (2009).
9. N. Zhang, X. Liu, L. Li, R. Legerski, *DNA Repair* **6**, 1670 (2007).
10. M. Räschele *et al.*, *Cell* **134**, 969 (2008).
11. M. Bzymek, N. H. Thayer, S. D. Oh, N. Kleckner, N. Hunter, *Nature* **464**, 937 (2010).
12. N. P. Robinson, K. A. Blood, S. A. McCallum, P. A. Edwards, S. D. Bell, *EMBO J.* **26**, 816 (2007).

13. Supplementary methods are available as supporting material on Science Online.
14. A. Carreira *et al.*, *Cell* **136**, 1032 (2009).
15. Y. Hashimoto, A. R. Chaudhuri, M. Lopes, V. Costanzo, *Nat. Struct. Mol. Biol.* **17**, 1305 (2010).
16. Y. G. Yang *et al.*, *Carcinogenesis* **26**, 1731 (2005).
17. K. Yamamoto *et al.*, *Mol. Cell. Biol.* **23**, 5421 (2003).
18. S. Lambert, B. Froget, A. M. Carr, *DNA Repair* **6**, 1042 (2007).

Acknowledgments: We thank V. Costanzo for the BRC^{WT} expression construct; T. V. Ho and O. Schärer for instruction on pICL preparation; P. Knipscheer for reagents and helpful discussions; and A. D'Andrea, K. J. Patel, R. Scully, and P. Knipscheer for critical reading of the manuscript. This work was supported by NIH grants GM 080676 and HL098316 and a John and Virginia Kaneb award to J.C.W., Department of Defense Breast Cancer Research Program Award W81XWH-04-1-0524 to V.J., and American Cancer Society postdoctoral fellowship PF-10-146-01-DMC to D.T.L. M.R. made initial observation of X-arcs; V.J. generated x.LRAD51 antibodies; D.T.L. and J.C.W. designed and analyzed experiments; D.T.L. performed experiments; and D.T.L. and J.C.W. prepared the manuscript.

Supporting Online Material

www.sciencemag.org/cgi/content/full/333/6038/84/DC1
Methods
Figs. S1 to S9
References

14 February 2011; accepted 12 May 2011
10.1126/science.1204258

A Key Enzyme in the Biogenesis of Lysosomes Is a Protease That Regulates Cholesterol Metabolism

Katrin Marschner,¹ Katrin Kollmann,¹ Michaela Schweizer,² Thomas Bräulke,^{1*} Sandra Pohl¹

Mucopolidosis II is a severe lysosomal storage disorder caused by defects in the α and β subunits of the hexameric *N*-acetylglucosamine-1-phosphotransferase complex essential for the formation of the mannose 6-phosphate targeting signal on lysosomal enzymes. Cleavage of the membrane-bound α/β -subunit precursor by an unknown protease is required for catalytic activity. Here we found that the α/β -subunit precursor is cleaved by the site-1 protease (S1P) that activates sterol regulatory element-binding proteins in response to cholesterol deprivation. S1P-deficient cells failed to activate the α/β -subunit precursor and exhibited a mucopolidosis II-like phenotype. Thus, S1P functions in the biogenesis of lysosomes, and lipid-independent phenotypes of S1P deficiency may be caused by lysosomal dysfunction.

More than 50 soluble enzymes are targeted to lysosomes in a mannose 6-phosphate (M6P)-dependent manner. The formation of M6P residues on newly synthesized lysosomal enzymes is catalyzed by two multimeric enzyme complexes, *N*-acetylglucosamine (GlcNAc)-1-phosphotransferase and GlcNAc-1-phosphodiester- α -*N*-acetylglucosaminidase, allowing binding of the enzymes to M6P-specific receptors (1). The receptor-enzyme complexes

are then transported to the endosomal compartment, followed by low pH-induced dissociation and delivery of lysosomal proteins to lysosomes and recycling of receptors to the Golgi apparatus. The GlcNAc-1-phosphotransferase comprises a hexameric complex of three subunits ($\alpha_2\beta_2\gamma_2$) with a molecular mass of 540 kD (2). The α and β subunits are encoded by a single gene, *GNPTAB*, and synthesized as a 190-kD precursor protein in a hairpin orientation that contains cytosolic N and C termini and a complex luminal modular structure (3, 4). Mutations in *GNPTAB* cause a severe lysosomal storage disorder, mucopolidosis II (MLII; I-cell disease) (3, 5). The loss of GlcNAc-1-phosphotransferase activity leads to the synthesis of lysosomal enzymes lacking M6P residues,

resulting in missorting and intracellular deficiencies of multiple lysosomal hydrolases, and lysosomal storage of nondegraded material, which are used as diagnostic markers in MLII patients (6). Clinically, these patients are characterized by skeletal abnormalities, chondrodysplasia, cardiomegaly, and motor and mental retardation, leading to early death (6). Cleavage of the α/β -subunit precursor between Lys⁹²⁸ and Asp⁹²⁹ by an unknown protease is a prerequisite for the enzymatic activity of the GlcNAc-1-phosphotransferase complex (7). Treatment with brefeldin A, a drug that disrupts Golgi trafficking, prevents the cleavage of the α/β -subunit precursor, suggesting that this reaction takes place in the Golgi apparatus (8).

To identify the protease responsible for the cleavage, we generated an α/β -subunit precursor miniconstruct that allows its efficient expression, spans the membrane twice, and lacks amino acids 431 to 819 (Fig. 1A). Antibodies to the human β subunit (9) allowed the detection of both the α/β -subunit precursor constructs and the cleaved 45-kD β subunit in baby hamster kidney (BHK) cells (Fig. 1B). Analysis of additional miniconstructs with stepwise deletions showed that 20 amino acids proximal to the cleavage site were required for proper proteolysis (Fig. 1B). Construct 3 was the best substrate and was used for all further experiments. To define structural requirements for efficient cleavage of the α/β -subunit precursor in more detail, we substituted residues Thr⁹²³ to Ser⁹³⁴ (according to the numbering of the full-length precursor) individually with alanines. Arg⁹²⁵, Leu⁹²⁷, and Lys⁹²⁸ were the most critical for cleavage of the phosphotransferase

¹Department of Biochemistry, Children's Hospital, University Medical Center Hamburg-Eppendorf, Hamburg, Germany.

²Department of Electron Microscopy, Center for Molecular Neurobiology, Hamburg, Germany.

*To whom correspondence should be addressed. E-mail: braulke@uke.uni-hamburg.de

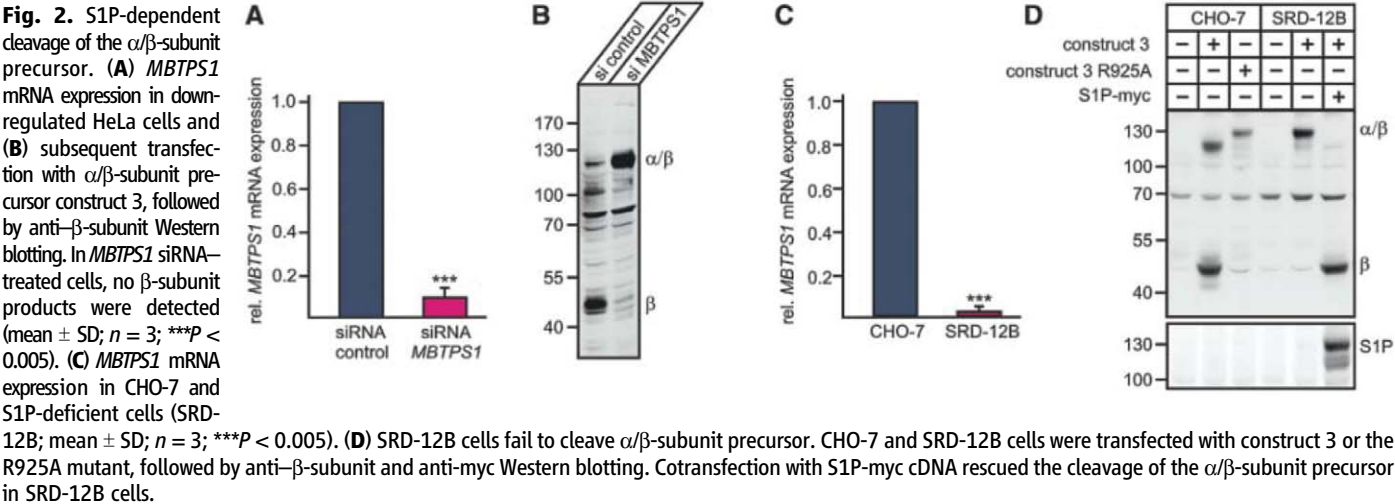
precursor (Fig. 1C and fig. S1). The expression of cleavage-resistant α/β -subunit precursors resulted in a 120/110-kD doublet. Endo H treatment

showed that the 120-kD polypeptide contained complex sugar chains, which are also detectable in mature β subunits. Thus, the α/β -subunit pre-

cursor reaches the mid-Golgi apparatus where these sugar modifications occur (fig. S2).

The residues most critical for the cleavage of the α/β -subunit precursor were found to be homologous to the consensus recognition motif of the Golgi-resident site-1 protease, (R/K)X(hydrophobic)Z↓, where X represents any amino acid and Z preferentially Leu or Thr, but excluding Val, Pro, Glu, Asp, or Cys (Fig. 1D) (10). Site-1 protease (S1P; also known as subtilisin kexin isoenzyme-1, SKI-1), is encoded by the *MBTPS1* gene and is a membrane-bound serine protease (11, 12). The prototypical membrane-bound S1P substrates are the sterol regulatory element-binding proteins SREBP1 and 2, which play a major role in lipid metabolism and cholesterol homeostasis (13). S1P is also responsible for the processing of numerous precursor proteins such as pro-BDNF (brain-derived neurotrophic factor), capsule glycoproteins of arenaviruses, transcription factors [activating transcription factor 6 (ATF6) and members of the cAMP response element-binding protein (CREB) family], and the autocatalytic activation of proS1P (11, 14, 15). To examine whether S1P is responsible for the cleavage of the α/β -subunit precursor, we performed small interfering RNA (siRNA)-mediated down-regulation of *MBTPS1* in HeLa cells, reducing its mRNA level to <10% of that in control cells (Fig. 2A). The subsequent transfection of *MBTPS1* siRNA-treated cells with α/β -subunit precursor construct 3 revealed an almost complete inhibition of its cleavage (Fig. 2B). Next, we overexpressed the α/β -subunit precursor construct 3 and its mutant form, R925A, in Chinese hamster ovary cells (CHO-7) and in S1P-deficient CHO-7 cells, termed SRD-12B (16). The SRD-12B cell line was derived by mutagenesis followed by selection for cholesterol auxotrophy that is resistant to amphotericin. The mutant cells were then rescued by growth in the presence of cholesterol, oleate, and mevalonate and used for cloning of the S1P cDNA by complementation (17). Almost no *MBTPS1* mRNA

Fig. 1. Structural requirements for cleavage of the α/β -subunit precursor of the GlcNAc-1-phosphotransferase. (A) Schematic presentation of α/β -subunit constructs used in this study. Construct 1 shows the full-length α/β -subunit precursor and its domain structure (3). The proposed cleavage site (⁹²⁵RQLK⁹²⁸ ↓) is indicated in red. Constructs 2 to 6 are truncated α/β -subunit precursors missing amino acids 431 to 819/848/888/908/918, respectively. (B) BHK cells were transfected with constructs 1 to 6, followed by anti- β -subunit Western blotting, demonstrating that at least 20 amino acids proximal to the proposed cleavage site are required for cleavage. (C) BHK cells were transfected with construct 3 (wild-type; wt) or construct 3 with single mutations of the proposed cleavage site and analyzed by anti- β -subunit Western blotting. Constructs with mutations R925A, L927A, and K928A show no or reduced amounts of β subunits, indicating reduced cleavage. (D) Sequence alignment of the GlcNAc-1-phosphotransferase α/β -subunit precursor and known S1P substrates. Shading indicates the conserved cleavage consensus motif (R/K)X(hydrophobic)Z↓. Abbreviations for the amino acid residues are as follows: A, Ala; C, Cys; D, Asp; E, Glu; F, Phe; G, Gly; H, His; I, Ile; K, Lys; L, Leu; M, Met; N, Asn; P, Pro; Q, Gln; R, Arg; S, Ser; T, Thr; V, Val; W, Trp; and Y, Tyr.



was detected in SRD-12B cells (Fig. 2C). In CHO-7 cells the α/β -subunit precursor construct was cleaved, but its mutant form, R925A, was not, whereas no cleavage of the α/β -subunit precursor construct was observed in SRD-12B cells. Reexpression of myc-tagged S1P in SRD-12B cells completely rescued the cleavage of the α/β -subunit precursor and the formation of β subunits (Fig. 2D), supporting the role of S1P in the formation of mature GlcNAc-1-phosphotransferase subunits.

To examine the biological importance of S1P for lysosomal targeting, we determined the activities of four lysosomal hydrolases, which were found to be significantly reduced in the SRD-12B cells, with the exception of α -mannosidase. In the culture medium of SRD-12B cells, however, 6- to 10-fold increases of all enzyme activities tested were determined relative to media

of CHO-7 cells, indicating missorting of newly synthesized acid hydrolases (Fig. 3A). In addition, we carried out pulse-chase experiments with [35 S]methionine followed by immunoprecipitation of the lysosomal protease cathepsin Z. In SRD-12B cells, about 72% of the newly synthesized protease was secreted as precursor forms during the 4-hour chase period compared with 28% in CHO-7 cells (Fig. 3B). Finally, anti-M6P immunoblots (18) of cell extracts showed that the formation of M6P residues was strongly impaired in SRD-12B cells compared with CHO-7 cells (Fig. 3C). For comparison, no M6P residues were detectable in embryonic fibroblasts of an MLII mouse model (*Gnptab*^{c.3082insC}) targeting the α/β -subunit precursor substrate of S1P. Chondrocyte morphogenesis and endochondral ossification were severely affected in MLII mice (fig. S3), as was observed for S1P-targeted mice and

the S1P-defective zebrafish *goz* (19, 20). Thus, secondary deficiencies of lysosomal enzymes responsible for degradation of extracellular matrix proteins and glycosaminoglycans may contribute to the cartilage phenotype in S1P-defective animals independent of lipid phenotype (19, 20).

To evaluate the importance of S1P for the function of lysosomes, we examined the proteolytic activation of an endocytosed lysosomal enzyme, arylsulfatase B (ASB), and its lysosomal degradation in SRD-12B cells. These cells internalized similar amounts of [125 I]-labeled ASB precursor in an M6P-dependent manner as control CHO-7 cells, whereas the subsequent proteolytic processing and degradation of [125 I]ASB were impaired and delayed, respectively (Fig. 4A). Ultrastructural analysis of SRD-12B cells revealed the presence of cytoplasmic, membrane-limited vacuoles resembling lysosomal structures and a

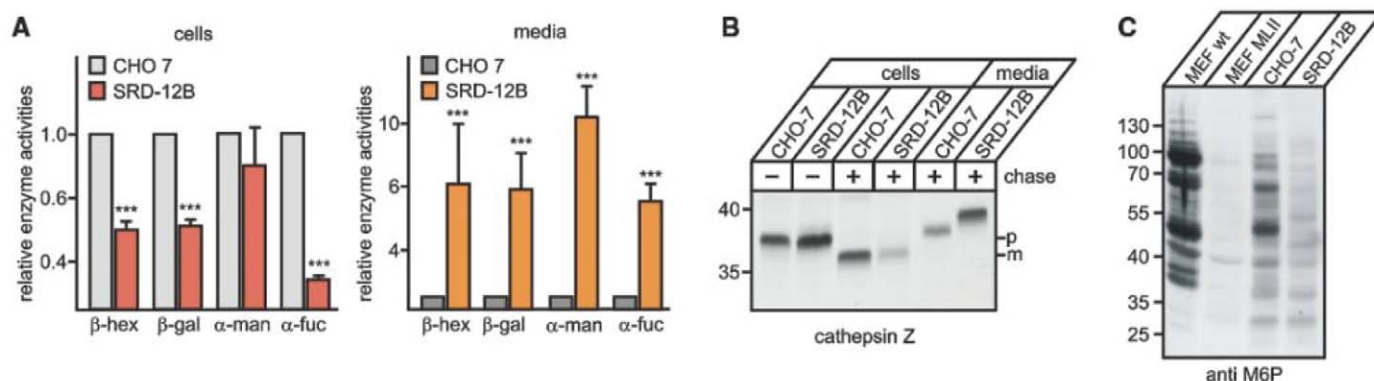


Fig. 3. Lysosomal enzymes are missorted in S1P-deficient cells. (A) The specific activities of the lysosomal enzymes β -hexosaminidase (β -hex), β -galactosidase (β -gal), α -mannosidase (α -man), and α -fucosidase (α -fuc) were measured in cell extracts and conditioned media of CHO-7 and SRD-12B cells. The specific activities in CHO-7 cells were set to 1 (mean \pm SD; $n = 5$; *** $P < 0.005$). The marginal decrease in α -mannosidase activity in SRD-12B cells might be explained by the slow lysosomal turnover of the enzyme present in different proteolytically processed polypeptides in α -mannosidase A and B isoform complexes. The hypersecretion of α -mannosidase into the medium indicated missorting of the newly synthesized enzyme. (B) CHO-7

and SRD-12B cells were labeled with [35 S]methionine for 1 hour and either harvested (–) or chased (+) for 4 hours, followed by immunoprecipitation of the lysosomal protease cathepsin Z from cell extracts and media (p, precursor; m, mature form). In SRD-12B cells, most newly synthesized cathepsin Z was secreted and exhibited decreased electrophoretic mobility due to complex-type oligosaccharides. (C) Cell extracts and media of CHO-7 and SRD-12B cells were analyzed by M6P Western blotting with the scFv M6P antibody fragment (18). Embryonic fibroblasts (MEF) of wild-type (wt) and MLII mice (*Gnptab*^{c.3082insC}) lacking GlcNAc-1-phosphotransferase activity were used as a control (5).

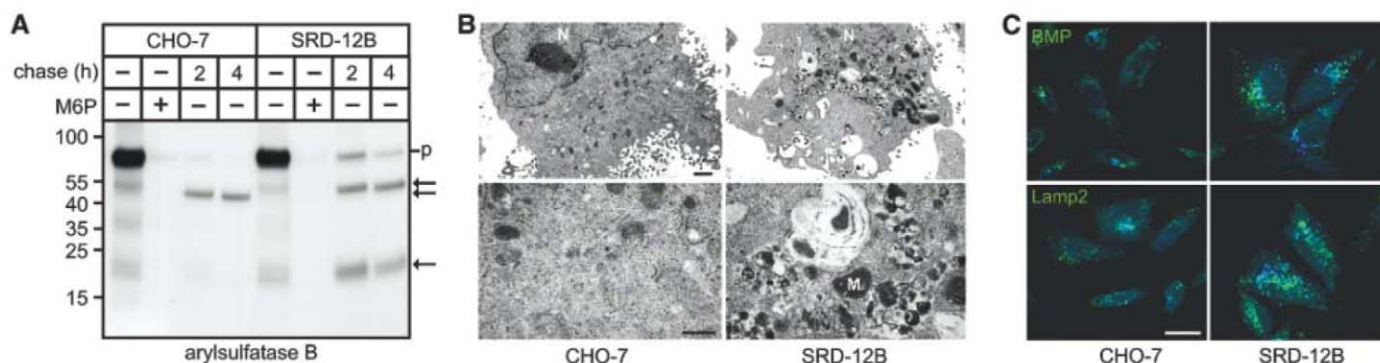


Fig. 4. Impaired enzyme activation and accumulation of storage material in lysosomes of SRD-12B cells. (A) The M6P-dependent endocytosis of [125 I]arylsulfatase B precursor (p) was not affected in SRD-12B cells whereas its subsequent proteolytic activation into mature forms (arrows) was impaired. (B) (Top) Electron micrographs revealed intracellular vacuoles resembling lysosomal structures and electron-dense storage material in SRD-12B cells.

Scale bar, 1 μ m. (Bottom) Higher magnification of CHO-7 and SRD-12B cells. N, nucleus; M, mitochondria. Scale bar, 0.5 μ m. (C) Immunofluorescence microscopy showed accumulation of the lysosomal anionic lipid bis(monoacylglycerol) phosphate (BMP) and unesterified cholesterol stained by filipin (blue) in SRD-12B cells, which is partially colocalized with the lysosomal marker Lamp2 (green). Scale bar, 15 μ m.

prominent accumulation of storage material of high electron density (Fig. 4B and fig. S4). In cells of patients or mice with various lysosomal storage disorders, secondary accumulation of lipids was observed (21). In SRD-12B cells, a variable number showed an accumulation of unesterified cholesterol and a moderate increase in staining intensity of the unusual lysophospholipid bis(monoacylglycerol)phosphate (BMP). Both lipids colocalized partially with the lysosomal marker protein Lamp2 (Fig. 4C and fig. S5). These data indicate that partial deficiencies of lysosomal enzymes in mutagenized and selected SRD-12B cells are sufficient to alter lysosomal functions.

Here we have provided evidence that S1P-mediated cleavage of the α/β -subunit precursor is associated with the activation of GlcNAc-1-phosphotransferase, which is required for proper transport of lysosomal enzymes. The requirement of S1P for activation of the GlcNAc-1-phosphotransferase activity, combined with its established role in lipid metabolism, indicates the importance of S1P for lysosome biogenesis and function. This may have implications for diagnosis of individuals with genetically undefined mucopolysaccharidosis II-like phenotypes such as Pacman dysplasia (22). Moreover, these findings raise the question of beneficial use of S1P inhibitors to reduce the synthesis of cholesterol, low-density lipoprotein

(LDL), and fatty acids in treating cardiovascular disorders or as an antiviral therapy (23–25) owing to their unanticipated deleterious effects on lysosomal function.

References and Notes

1. T. Braulke, J. S. Bonifacio, *Biochim. Biophys. Acta* **1793**, 605 (2009).
2. M. Bao, J. L. Booth, B. J. M. Elmendorf, W. M. Canfield, *J. Biol. Chem.* **271**, 31437 (1996).
3. S. Tiede *et al.*, *Nat. Med.* **11**, 1109 (2005).
4. M. Kudo *et al.*, *J. Biol. Chem.* **280**, 36141 (2005).
5. K. H. Paik *et al.*, *Hum. Mutat.* **26**, 308 (2005).
6. S. Kornfeld, W. S. Sly, in *The Metabolic and Molecular Bases of Inherited Disease*, C. R. Scriver *et al.*, Eds. (McGraw-Hill, New York, 2001), pp. 3421–3452.
7. M. Kudo, W. M. Canfield, *J. Biol. Chem.* **281**, 11761 (2006).
8. K. Kollmann *et al.*, *Eur. J. Cell Biol.* **89**, 117 (2010).
9. S. Pohl *et al.*, *J. Biol. Chem.* **285**, 23936 (2010).
10. A. Elagoz, S. Benjannet, A. Mammabassi, L. Wickham, N. G. Seidah, *J. Biol. Chem.* **277**, 11265 (2002).
11. N. G. Seidah *et al.*, *Proc. Natl. Acad. Sci. U.S.A.* **96**, 1321 (1999).
12. J. Sakai, A. Nohturfft, J. L. Goldstein, M. S. Brown, *J. Biol. Chem.* **273**, 5785 (1998).
13. M. S. Brown, J. L. Goldstein, *Proc. Natl. Acad. Sci. U.S.A.* **96**, 11041 (1999).
14. J. M. Rojek, A. M. Lee, N. Nguyen, C. F. Spiropoulou, S. Kunz, *J. Virol.* **82**, 6045 (2008).
15. J. Stirling, P. O'Hare, *Mol. Biol. Cell* **17**, 413 (2006).
16. R. B. Rawson, D. Cheng, M. S. Brown, J. L. Goldstein, *J. Biol. Chem.* **273**, 28261 (1998).
17. J. Sakai *et al.*, *Mol. Cell* **2**, 505 (1998).
18. S. Müller-Loennies, G. Galliciotti, K. Kollmann, M. Glatzel, T. Braulke, *Am. J. Pathol.* **177**, 240 (2010).
19. K. Schlombs, T. Wagner, J. Scheel, *Proc. Natl. Acad. Sci. U.S.A.* **100**, 14024 (2003).
20. D. Patra *et al.*, *J. Cell Biol.* **179**, 687 (2007).
21. S. U. Walkley, M. T. Vanier, *Biochim. Biophys. Acta* **1793**, 726 (2009).
22. R. A. Saul, V. Proud, H. A. Taylor, J. G. Leroy, J. Spranger, *Am. J. Med. Genet. A* **135A**, 328 (2005).
23. N. G. Seidah, A. Prat, *J. Mol. Med.* **85**, 685 (2007).
24. J. L. Hawkins *et al.*, *J. Pharmacol. Exp. Ther.* **326**, 801 (2008).
25. J. M. Rojek *et al.*, *J. Virol.* **84**, 573 (2010).

Acknowledgments: We thank J. L. Goldstein for providing SRD-12B and CHO-7 cells. Lipoprotein-poor newborn calf serum and human LDL for selection of SRD-12B cells were provided by J. Heeren. We also thank J. Brand and C. Raithore for technical assistance. We are grateful to J. Bonifacio for critical reading of the manuscript and comments, and to K. Duncan for help in editing the manuscript. T. Braulke and S. Müller-Loennies hold a patent on the single-chain antibody fragment for the detection of M6P-containing proteins (International Patent no. PTC/EP2009/060224 and U.S./PTC Application no. 13/057,844). This work was supported by the Deutsche Forschungsgemeinschaft (SFB877/B3, GRK1459).

Supporting Online Material

www.sciencemag.org/cgi/content/full/333/6038/87/DC1

Materials and Methods

Figs. S1 to S5

References (26–30)

16 March 2011; accepted 20 May 2011

10.1126/science.1205677

Long Unfolded Linkers Facilitate Membrane Protein Import Through the Nuclear Pore Complex

Anne C. Meinema,^{1*} Justyna K. Laba,^{1*} Rizqiya A. Hapsari,^{1*} Renee Otten,¹ Frans A. A. Mulder,¹ Annemarie Kralt,² Geert van den Bogaart,^{1†} C. Patrick Lusk,³ Bert Poolman,¹ Liesbeth M. Veenhoff^{1,2‡}

Active nuclear import of soluble cargo involves transport factors that shuttle cargo through the nuclear pore complex (NPC) by binding to phenylalanine-glycine (FG) domains. How nuclear membrane proteins cross through the NPC to reach the inner membrane is presently unclear. We found that at least a 120-residue-long intrinsically disordered linker was required for the import of membrane proteins carrying a nuclear localization signal for the transport factor karyopherin- α . We propose an import mechanism for membrane proteins in which an unfolded linker slices through the NPC scaffold to enable binding between the transport factor and the FG domains in the center of the NPC.

The nuclear envelope (NE) consists of an inner (INM) and outer nuclear membrane (ONM) connected by the pore membrane at sites where the nuclear pore complexes (NPCs) are embedded. The ONM is continuous with the endoplasmic reticulum (ER). NPCs are composed of a membrane-anchored scaffold that stabilizes a cylindrical central channel, in which nucleoporins (Nups) with disordered phenylalanine-glycine (FG)-rich regions provide the selectivity barrier (1). For a membrane protein to move through the NPC, its transmembrane (TM) domains must pass through the pore membrane, while its extraluminal soluble domain(s) must pass through

the NPC by a mechanism yet to be clarified (2–4). Some proteins reach the INM by diffusing through the pore membrane and adjacent lateral channels (5–8) and accumulate by binding nuclear structures (9, 10). Other membrane proteins have a nuclear localization signal (NLS), and binding to transport factors karyopherin- α and karyopherin- β 1 is required to pass the NPC and reach the INM (11, 12). We sought to investigate the mechanism and path of nuclear transport of these integral INM proteins.

We first generated reporters using the *Saccharomyces cerevisiae* homolog of the human LEM domain-containing integral INM protein, Heh2. Heh2 is composed of a LEM domain, a bipartite

NLS (hereafter h2NLS), a linker region (L), two TM segments flanking a luminal domain (LD), and a domain with homology to the C terminus of MAN1 (Fig. 1A) (12). The h2NLS is recognized by Kap60 (also known as Srp1 or Karyopherin- α), the yeast homolog of human Importin- α (12). Similar to Heh2, the reporter protein h2NLS-L-TM, consisting of green fluorescent protein (GFP) fused to amino acids 93 to 378 of Heh2, accumulated specifically at the NE (Fig. 1B). A control lacking the h2NLS, named L-TM, distributed over the NE and cortical ER. Although we could not resolve the INM from the ONM, we used the average pixel intensities at the NE and ER (NE-ER ratio) as a measure of INM accumulation (fig. S2, A and B). We validated this approach by confirming the localization of h2NLS-L-TM to the INM using immuno-electron microscopy (Fig. 1C and fig. S2C). h2NLS-L-TM accumulated 33-fold at the NE (Fig. 1B), whereas L-TM accumulated only 2-fold.

¹Departments of Biochemistry and Biophysical Chemistry, Groningen Biomolecular Sciences and Biotechnology Institute, Netherlands Proteomics Centre, Zernike Institute for Advanced Materials, University of Groningen, Nijenborgh 4, 9747 AG, Groningen, Netherlands. ²Department of Neuroscience, European Research Institute on the Biology of Ageing, University Medical Centre Groningen, Groningen, Netherlands. ³Department of Cell Biology, Yale School of Medicine, New Haven, CT 06519, USA.

*These authors contributed equally to this work.

†Present address: Department of Neurobiology, Max Planck Institute for Biophysical Chemistry, Am Fassberg 11, 37077 Göttingen, Germany.

‡To whom correspondence should be addressed. E-mail: l.m.veenhoff@rug.nl

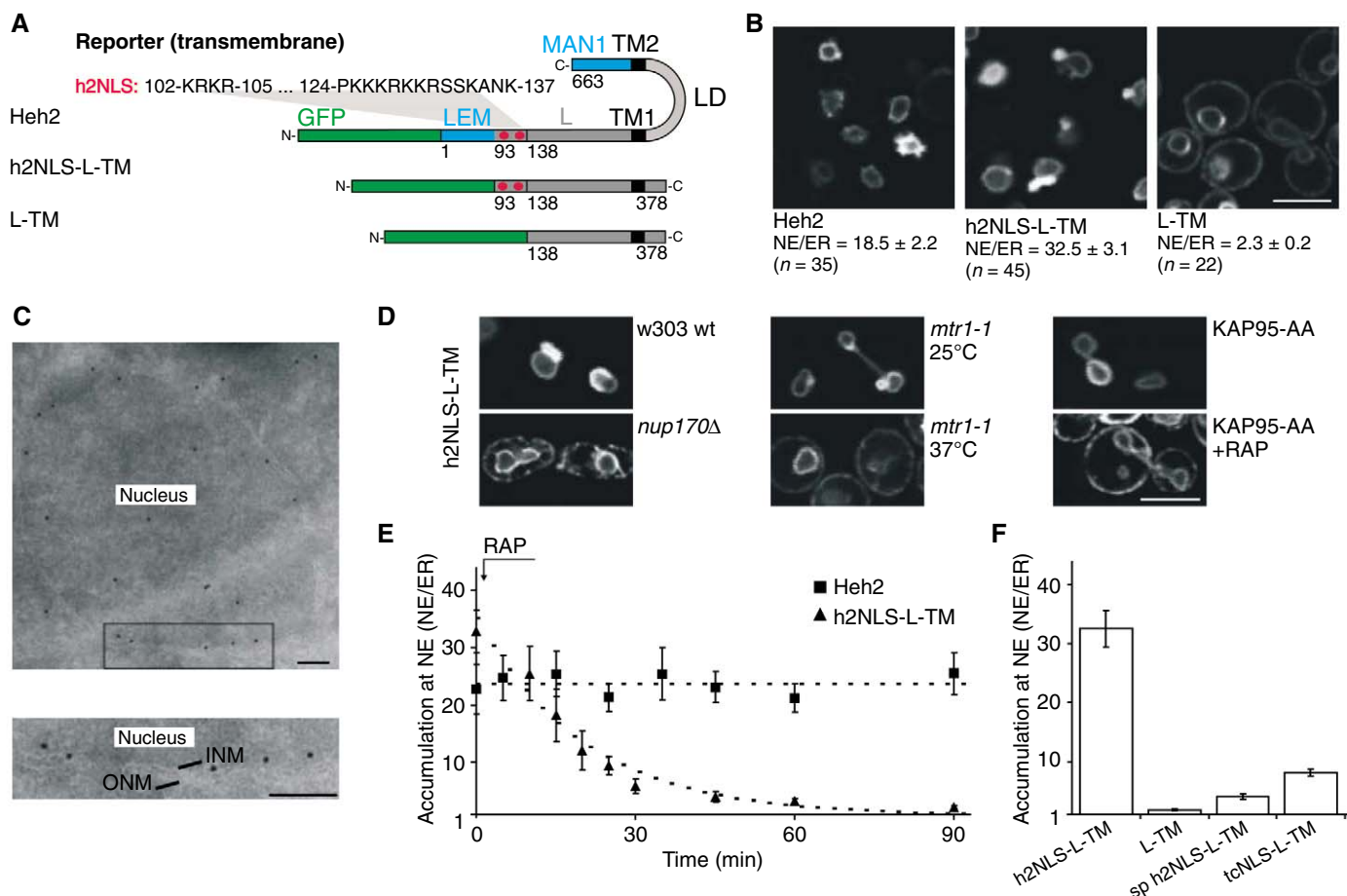


Fig. 1. The NLS-containing domain (h2NLS-L) of Heh2 is sufficient for accumulation at the INM. (A) Representation of Heh2-based GFP-fusion reporter proteins. (B) Confocal fluorescence images of yeast expressing the indicated proteins. Average NE/ER ratios are shown. (C) Immuno-electron micrograph of h2NLS-L-TM in the KAP95-AA strain labeled with antibodies against GFP and 10-nm-diameter gold-conjugated secondary antibody: 64% at the INM ($n = 350$, fig. S1D). (D) h2NLS-L-TM is mislocalized in a *Nup170Δ* strain (left), in a RanGEF

mutant strain (*mtr1-1*) at nonpermissive temperature (middle), and in the KAP95-AA strain upon addition of rapamycin (RAP) (right). (E) The accumulation at the NE of h2NLS-L-TM (▲) and Heh2 (■) in the KAP95-AA strain as a function of time after anchoring of Kap95 (RAP at $t = 0$, $n \geq 13$). (F) The accumulation at the INM of reporter containing a bipartite h2NLS (h2NLS-L-TM), without NLS (L-TM), with single partite NLS (sp h2NLS-L-TM), or with tandem cNLS (tcNLS-L-TM) ($n \geq 32$). SEM is indicated; scale bars: (B and D) 5 μ m and (C) 250 nm.

Transport of h2NLS-L-TM was dependent on the Ran gradient and Nup170, similar to full-length Heh2 (Fig. 1D) (12). To confirm that the import of our membrane reporter was Kap60/95-mediated, we examined the distribution of h2NLS-L-TM in a Kap95 (Karyopherin- β -Importin- β -Rsl1) “anchor away” strain (KAP95-AA) (13). Upon addition of rapamycin, Kap95-FRB was trapped at Pma1-FKBP in the plasma membrane and no longer available for nuclear transport (fig. S2, D to F). Indeed, the accumulation of h2NLS-L-TM at the NE was markedly reduced (+RAP, Fig. 1D). Moreover, INM-localized reporter proteins redistributed to the ONM and ER upon addition of rapamycin, and the nuclear accumulation dropped with a half-time of 14 ± 2.7 min (Fig. 1E). By contrast, the fluorescence intensity of Heh2 at the NE remained unaltered for >90 min. Thus, while Heh2 is bound to nuclear factors, h2NLS-L-TM is fully mobile within the NE-ER network.

The h2NLS is a high-affinity NLS compared to the classical NLS (fig. S3). To assess whether this high affinity is required for import of h2NLS-

L-TM, we replaced the bipartite h2NLS with lower-affinity NLSs: either a single-partite version of the h2NLS that lacked the first KRKR basic region (sp h2NLS) or a tandem classical NLS (tcNLS). Both membrane reporters still accumulated at the INM, but the NE/ER ratios were lower (8.1 and 4.0, respectively) than for h2NLS-L-TM (Fig. 1F), indicating a correlation between the affinity of Kap60 for an NLS and the nuclear accumulation of membrane proteins.

We then examined how the L domain contributes to targeting. The amino acid composition of the L domain and the large Stokes radius (45 Å) of purified recombinant h2NLS-L suggest that it is unstructured (fig. S4, A to C). In addition, nuclear magnetic resonance (NMR) spectra of (unlabeled) h2NLS-L were typical of disordered proteins. The absence of stable secondary and tertiary structure was gauged from a lack of signal dispersion of the backbone amides for h2NLS-L in one-dimensional 1 H-NMR spectra (Fig. 2A, shaded area) and of the side-chain methyl signals in [1 H- 13 C]-HSQC (heteronuclear single-quantum

coherence) spectra (fig. S4D). To evaluate whether the sequence of the linker region contributed to targeting, we replaced the coding regions of the L domain in h2NLS-L-TM with two synthetic sequences, LR1 and LR2. These were generated randomly but had the same relative amino acid abundance as L. LR1 and LR2 are also predicted to be unfolded (fig. S4A). Both h2NLS-LR1-TM and h2NLS-LR2-TM were efficiently transported to the INM in a Kap-dependent manner (Fig. 2B). Systematic truncations of LR1 and LR2 and the original linker (L) resulted in three sets of reporters with variable linker lengths (see tables S2 and S3). The shortest truncations of each linker set did not accumulate at the nucleus (Fig. 2B). Indeed, we observed a marked dependence of INM import on linker length (Fig. 2C). Reporters with a synthetic TM segment and reporters with 1, or all 10 TM segments of an ER protein, Sec61, were also efficiently imported to the INM (Fig. 3). An “NLS-L-TM”-sorting signal could be recognized in Heh1 and, indeed, its NLS-linker-domain, even though lacking

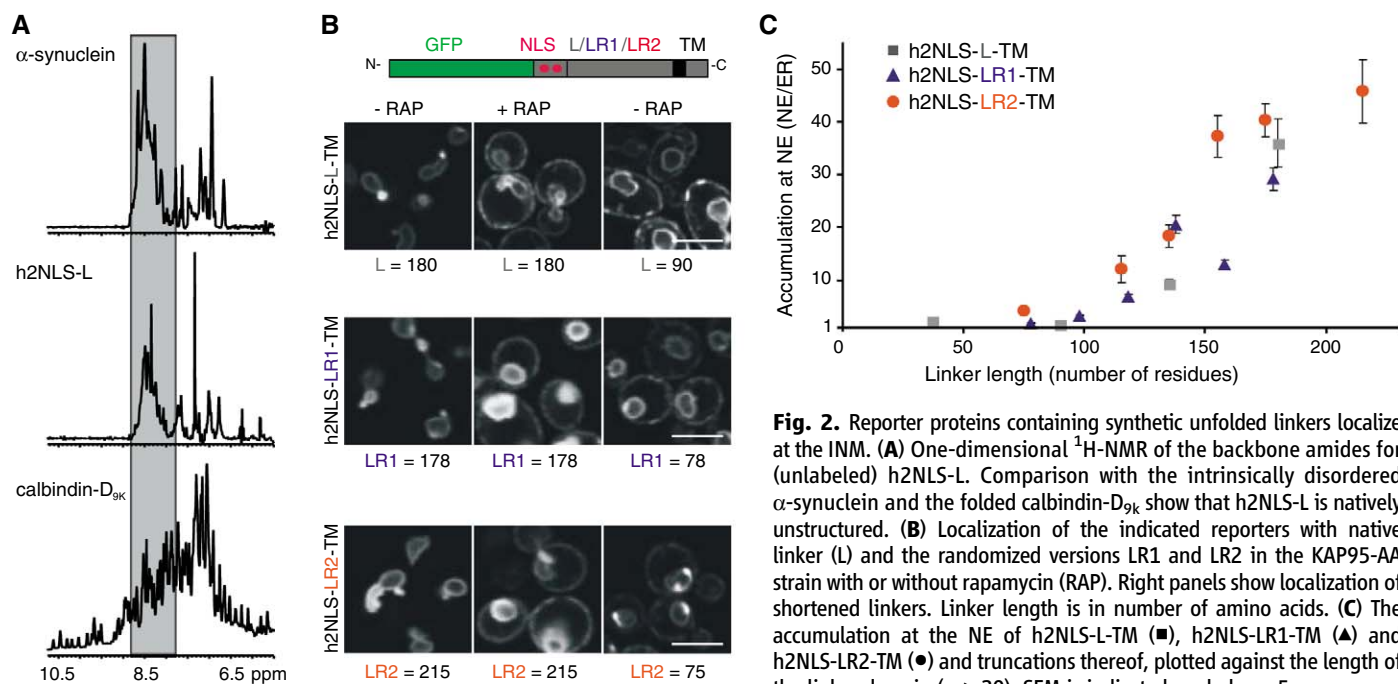


Fig. 2. Reporter proteins containing synthetic unfolded linkers localize at the INM. **(A)** One-dimensional ^1H -NMR of the backbone amides for (unlabeled) h2NLS-L. Comparison with the intrinsically disordered α -synuclein and the folded calbindin-D_{9k} show that h2NLS-L is natively unstructured. **(B)** Localization of the indicated reporters with native linker (L) and the randomized versions LR1 and LR2 in the KAP95-AA strain with or without rapamycin (RAP). Right panels show localization of shortened linkers. Linker length is in number of amino acids. **(C)** The accumulation at the NE of h2NLS-L-TM (■), h2NLS-LR1-TM (▲) and h2NLS-LR2-TM (●) and truncations thereof, plotted against the length of the linker domain ($n \geq 20$). SEM is indicated; scale bars: 5 μm .

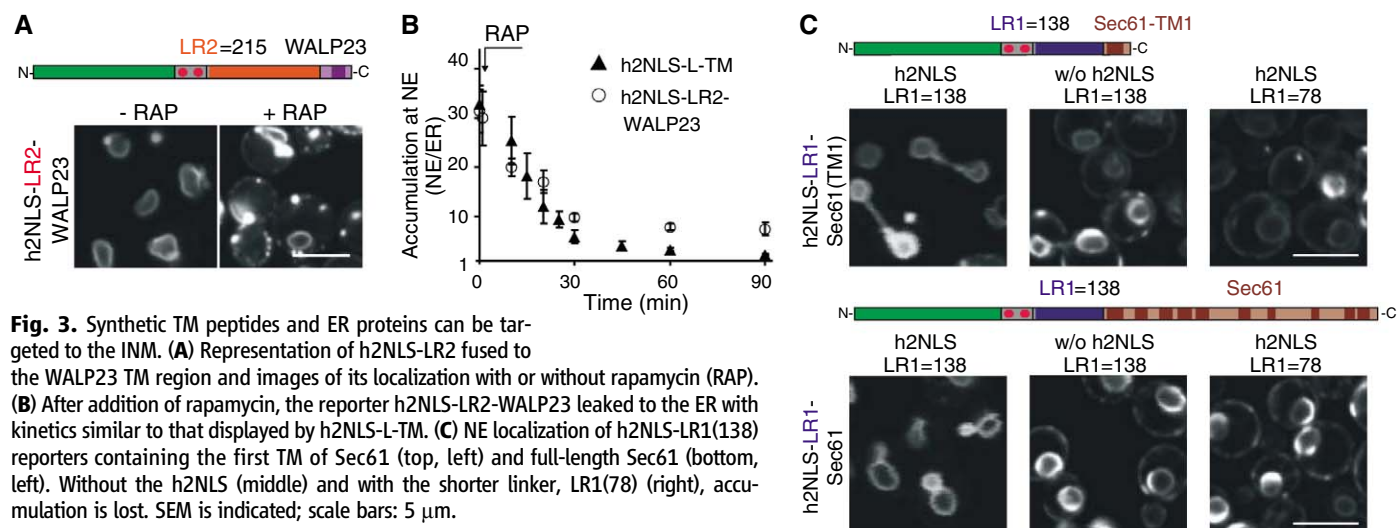


Fig. 3. Synthetic TM peptides and ER proteins can be targeted to the INM. **(A)** Representation of h2NLS-LR2 fused to the WALP23 TM region and images of its localization with or without rapamycin (RAP). **(B)** After addition of rapamycin, the reporter h2NLS-LR2-WALP23 leaked to the ER with kinetics similar to that displayed by h2NLS-L-TM. **(C)** NE localization of h2NLS-LR1(138) reporters containing the first TM of Sec61 (top, left) and full-length Sec61 (bottom, left). Without the h2NLS (middle) and with the shorter linker, LR1(78) (right), accumulation is lost. SEM is indicated; scale bars: 5 μm .

homology to that of Heh2, promoted INM targeting (fig. S5A).

Next, we determined whether the transport of the reporters across the NPC depends on specific FG regions of nucleoporins (14–16). A strain that lacks the GLFG repeats of Nups 100, 145, and 57 (17), which are anchored to both the cytoplasmic and nucleoplasmic halves of the NPC scaffold (18), showed 7.5-fold decreased NE accumulation (SWY2950, Fig. 4A). Minimal effects were seen with single deletions (fig. S5B) and in strains lacking the FG regions from the asymmetric localized Nups (SWY3062, SWY3042), whereas Kap60/95-mediated transport of soluble cargo (tcNLS-GFP) was affected in all three strains.

Our data point toward passage of the extraluminal soluble domains of the membrane pro-

teins through the central channel, which is expected to place few constraints on the bulkiness of these domains. Indeed, membrane proteins with up to 174-kD soluble domains were imported to the INM, although the efficiency decreased with increasing size (Fig. 4B). To further support the suggestion that the extraluminal soluble domains pass through the central channel, we designed experiments to trap the reporters in transit through the NPC. We constructed a strain expressing FRB-tagged FG-Nup Nsp1. The C-terminal FRB tag on Nsp1 is anchored on the pore side of the scaffold of the NPC (16, 18–20). A reporter containing FKBP at its N terminus was expressed to enable rapamycin-dependent trapping at Nsp1-FRB in the NPC (fig. S5C). Addition of rapamycin yielded a punctate stain typical of

NPC-localized proteins; without rapamycin the reporter distributed evenly over the NE (Fig. 4C and fig. S5D). Next, we assessed whether trapping of the reporter at the NPC affected transport. We used a reporter expressed at higher levels (with an additional N-terminal protein A tag) and saw a blockage of INM import and steady increase in fluorescence at the ER from newly synthesized proteins, after rapamycin addition (Fig. 4D and fig. S5E). Trapping of the reporter specifically blocked transport of membrane proteins and not soluble proteins (fig. S5, F and G). Thus, the h2NLS-containing N terminus of the reporter passes where Nsp1 is anchored to the NPC scaffold and within the central channel of the NPC.

Here we have elucidated the NLS-dependent mechanism of membrane protein transport through

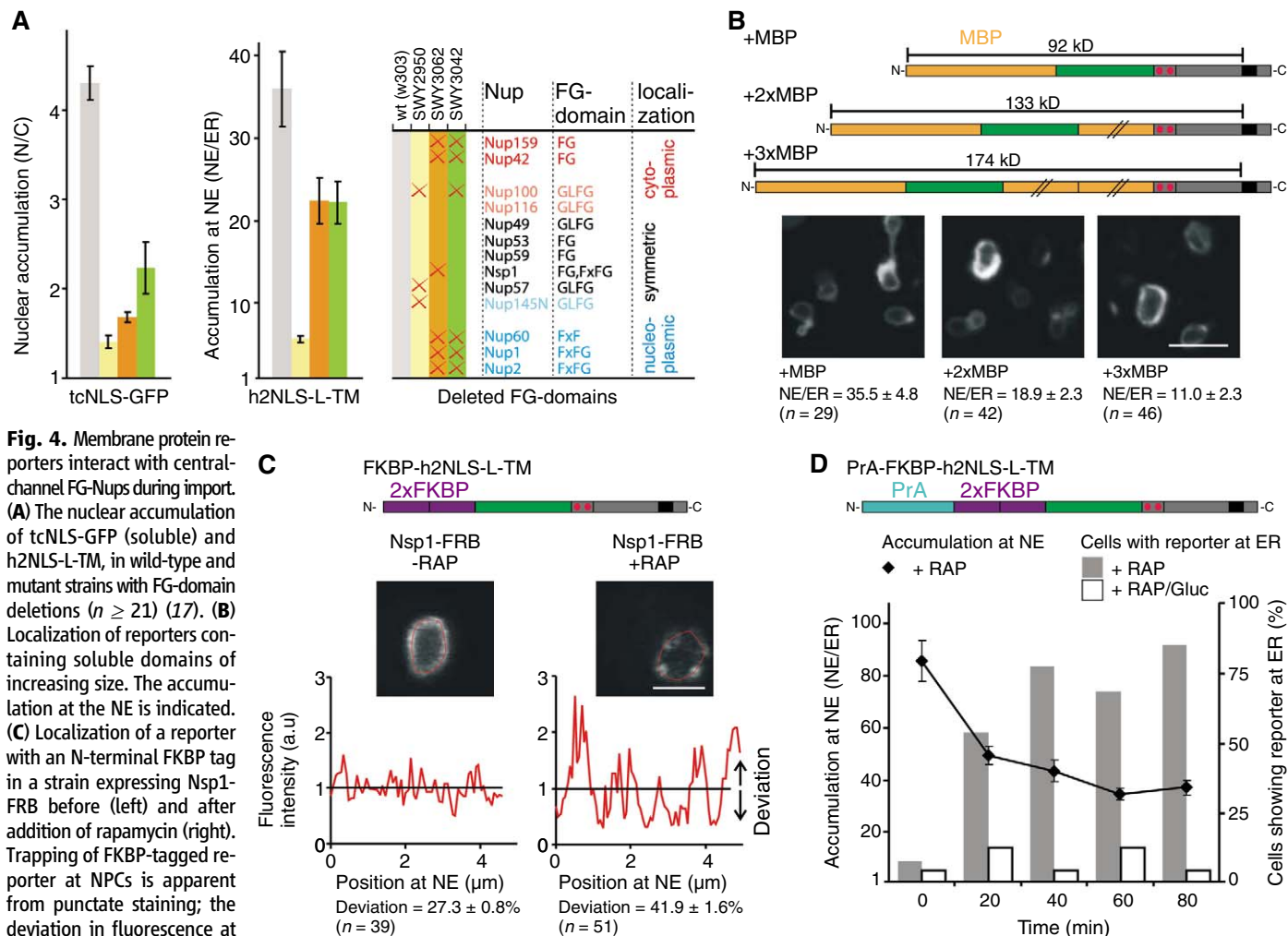


Fig. 4. Membrane protein reporters interact with central-channel FG-Nups during import. **(A)** The nuclear accumulation of tcNLS-GFP (soluble) and h2NLS-L-TM, in wild-type and mutant strains with FG-domain deletions ($n \geq 21$) (17). **(B)** Localization of reporters containing soluble domains of increasing size. The accumulation at the NE is indicated. **(C)** Localization of a reporter with an N-terminal FKBP tag in a strain expressing Nsp1-FRB before (left) and after addition of rapamycin (right). Trapping of FKBP-tagged reporter at NPCs is apparent from punctate staining; the deviation in fluorescence at the NE is higher in the presence of rapamycin. **(D)** Rapamycin-dependent trapping of PrA-FKBP-tagged reporter at Nsp1-FRB blocked import as observed from increased ER-localized reporter. Percentage of cells showing fluorescence at the ER ($n \geq 100$, bars) and

the average NE/ER ratio ($n \geq 13$, symbols) upon addition of rapamycin (RAP, filled bars and \blacklozenge) or glucose (inhibition of reporter synthesis) and rapamycin (RAP/Gluc, open bars). SEM is indicated; scale bars: (B) 5 μ m and (C) 2 μ m.

the average NE/ER ratio ($n \geq 13$, symbols) upon addition of rapamycin (RAP, filled bars and \blacklozenge) or glucose (inhibition of reporter synthesis) and rapamycin (RAP/Gluc, open bars). SEM is indicated; scale bars: (B) 5 μ m and (C) 2 μ m.

the NPC. The Heh2-derived reporter proteins accumulate at the INM, not because they are retained or trapped at the INM, but because Kap60/95-mediated import is faster than export. The signal for targeting to the INM is composed of a natively unfolded linker that spaces the TM segment and a high-affinity NLS. It takes little energy to stretch the linker to allow the NLS, with bound karyopherins, to dodge between the NPC scaffold and the karyopherins to bind the FG-Nups (fig. S6). The proposed transport route implies that, at least transiently, openings must exist between the space immediately aligning the pore membrane and the central channel. At present, structures of the NPC lack the resolution to reveal such conduits, but its plasticity and the overall lattice-like scaffold structure observed in electron microscopy (8, 21, 22) and computational structures (18) are compatible with our model. The transport mechanism described here is likely to exist in parallel with a previously proposed route based on diffusion and nuclear retention (2, 5–7, 9, 10).

References and Notes

- S. R. Wente, M. P. Rout, *Cold Spring Harb. Perspect. Biol.* **2**, a000562 (2010).
- N. Zuleger, N. Korfali, E. C. Schirmer, *Biochem. Soc. Trans.* **36**, 1373 (2008).
- C. P. Lusk, G. Blobel, M. C. King, *Nat. Rev. Mol. Cell Biol.* **8**, 414 (2007).
- T. Ohba, E. C. Schirmer, T. Nishimoto, L. Gerace, *J. Cell Biol.* **167**, 1051 (2004).
- P. Malik et al., *Cell. Mol. Life Sci.* **67**, 1353 (2010).
- B. Soullam, H. J. Worman, *J. Cell Biol.* **130**, 15 (1995).
- W. Wu, F. Lin, H. J. Worman, *J. Cell Sci.* **115**, 1361 (2002).
- J. E. Hinshaw, B. O. Carragher, R. A. Milligan, *Cell* **69**, 1133 (1992).
- J. Ellenberg et al., *J. Cell Biol.* **138**, 1193 (1997).
- C. Ostlund, J. Ellenberg, E. Hallberg, J. Lippincott-Schwartz, H. J. Worman, *J. Cell Sci.* **112**, 1709 (1999).
- Y. Turgay et al., *EMBO J.* **29**, 2262 (2010).
- M. C. King, C. P. Lusk, G. Blobel, *Nature* **442**, 1003 (2006).
- H. Haruki, J. Nishikawa, U. K. Laemmli, *Mol. Cell* **31**, 925 (2008).
- S. Frey, R. P. Richter, D. Görlich, *Science* **314**, 815 (2006).
- R. Peters, *Bioessays* **31**, 466 (2009).
- M. P. Rout et al., *J. Cell Biol.* **148**, 635 (2000).
- L. A. Strawn, T. Shen, N. Shulga, D. S. Goldfarb, S. R. Wente, *Nat. Cell Biol.* **6**, 197 (2004).
- F. Alber et al., *Nature* **450**, 695 (2007).
- N. Schrader et al., *Mol. Cell* **29**, 46 (2008).

- S. M. Bailer, C. Baldof, E. Hurt, *Mol. Cell. Biol.* **21**, 7944 (2001).

- D. Frenkiel-Krispin, B. Maco, U. Aebi, O. Medalia, *J. Mol. Biol.* **395**, 578 (2010).
- Q. Yang, M. P. Rout, C. W. Akey, *Mol. Cell* **1**, 223 (1998).

Acknowledgments: We thank M. C. King, M. P. Rout, and D. J. Slotboom for discussion; V. Krasnikov for help with confocal microscopy; and M. Graham for assistance with immunoelectron microscopy. We thank S. R. Wente, U. K. Laemmli, and M. P. Rout for reagents and strains. This work was supported by funding from the Netherlands Organization for Scientific Research (VIDI fellowship to L.M.V. and F.A.A.M.; Top-subsidy grant 700.56.302 to B.P.). L.M.V. conceived the project. Experiments were performed and analyzed by A.C.M., J.K.L., R.A.H., C.P.L., and A.K. NMR was performed by R.O. and F.A.A.M. G.v.d.B. helped with image analysis. Experiments were designed and the manuscript was written by A.C.M., C.P.L., B.P., and L.M.V.

Supporting Online Material

www.sciencemag.org/cgi/content/full/science.1205741/DC1

Materials and Methods

Figs. S1 to S6

Tables S1 to S3

References

17 March 2011; accepted 10 May 2011

Published online 9 June 2011;

10.1126/science.1205741

No Evidence of Murine-Like Gammaretroviruses in CFS Patients Previously Identified as XMRV-Infected

Konstance Knox,^{1,2} Donald Carrigan,^{1,2} Graham Simmons,^{3,4} Fernando Teque,⁵ Yanchen Zhou,^{3,4} John Hackett Jr.,⁶ Xiaoxing Qiu,⁶ Ka-Cheung Luk,⁶ Gerald Schochetman,⁶ Allyn Knox,¹ Andreas M. Kogelnik,² Jay A. Levy^{5*}

Members of the gammaretroviruses—such as murine leukemia viruses (MLVs), most notably XMRV [xenotropic murine leukemia virus (X-MLV)-related virus]—have been reported to be present in the blood of patients with chronic fatigue syndrome (CFS). We evaluated blood samples from 61 patients with CFS from a single clinical practice, 43 of whom had previously been identified as XMRV-positive. Our analysis included polymerase chain reaction and reverse transcription polymerase chain reaction procedures for detection of viral nucleic acids and assays for detection of infectious virus and virus-specific antibodies. We found no evidence of XMRV or other MLVs in these blood samples. In addition, we found that these gammaretroviruses were strongly (X-MLV) or partially (XMRV) susceptible to inactivation by sera from CFS patients and healthy controls, which suggested that establishment of a successful MLV infection in humans would be unlikely. Consistent with previous reports, we detected MLV sequences in commercial laboratory reagents. Our results indicate that previous evidence linking XMRV and MLVs to CFS is likely attributable to laboratory contamination.

Xenotropic retroviruses, first discovered in mice, have the unusual characteristic of being endogenous to animal species, i.e., integrated into the animal's genome, but not able to reinfect cells from that species. However, as the name (*xenos*, foreign) implies, these vi-

rus can infect cells from other animal species. The xenotropic murine leukemia virus (X-MLV), for example, infects cells from several species including humans but cannot infect many mouse cells (1–3). One particular virus within this group, XMRV (xenotropic murine leukemia virus-related virus), was reported to be present in a subset of human prostate tumors (4) and in blood samples from patients with chronic fatigue syndrome (CFS) (5). Other murine-related gammaretroviruses have also reportedly been detected in CFS patients (6). The infection of humans with these viruses is controversial. Investigators evaluating independent cohorts of CFS patients have failed to detect XMRV or other MLVs (7–12), and contamination of human clinical material (13, 14)

and reagents (e.g., *Taq* polymerase) (15) with mouse DNA containing MLV-like sequences has been reported.

To investigate these discrepancies in a more direct manner, we performed an extensive virological evaluation of blood samples from two human populations with a clinical diagnosis of CFS (16), many of whom had been diagnosed previously as XMRV-infected. The first (P1) consisted of 41 CFS patients ranging in age from 5 to 73 years who came from a private medical practice (Sierra Internal Medicine, Incline Village, Nevada). Twenty-six of the CFS subjects (63%) were female, and 15 (37%) were male; the female median age was 52 years (range 5 to 72 years), and the male median age was 49 years (range 20 to 73 years). These patients were an unselected, sequentially enrolled population submitted for diagnostic testing to the Wisconsin Viral Research Group (WVRG) and were therefore a true cross section of the patients in the medical practice. Thirty-seven of these 41 patients had been tested previously for XMRV infection by the following assays: whole-blood polymerase chain reaction (PCR), serum PCR, or viral XMRV culture with PCR (17). These evaluations were performed by a commercial (VIPDx, Reno, Nevada) or research laboratory [Whittemore Peterson Institute (WPI), Reno, Nevada]. Twenty-six were reported as being XMRV-positive, and 11 were reported as being negative. Blood samples used from this patient cohort were archived diagnostic specimens and, therefore, exempt from Institutional Review Board (IRB) consideration [46.101 (b)(4), Code of Federal Regulations].

The second population (P2) came from the same medical practice, and subjects were selected largely on the basis of a previous positive diagnosis for XMRV infection. This patient cohort included 29 CFS patients, 26 of whom (89.6%) had tested positive for XMRV in at least one of the three virus assays listed above and/or had

¹Wisconsin Viral Research Group, Milwaukee, WI 53226, USA.

²Open Medicine Institute, Mountain View, CA 94040, USA.

³Blood Systems Research Institute, San Francisco, CA 94118, USA.

⁴Department of Laboratory Medicine, University of California, San Francisco, San Francisco, CA 94143, USA.

⁵Department of Medicine, Hematology/Oncology Division, University of California, San Francisco, San Francisco, CA 94143, USA.

⁶Abbott Laboratories, Abbott Park, IL 60064, USA.

*To whom correspondence should be addressed. E-mail: jay.levy@ucsf.edu

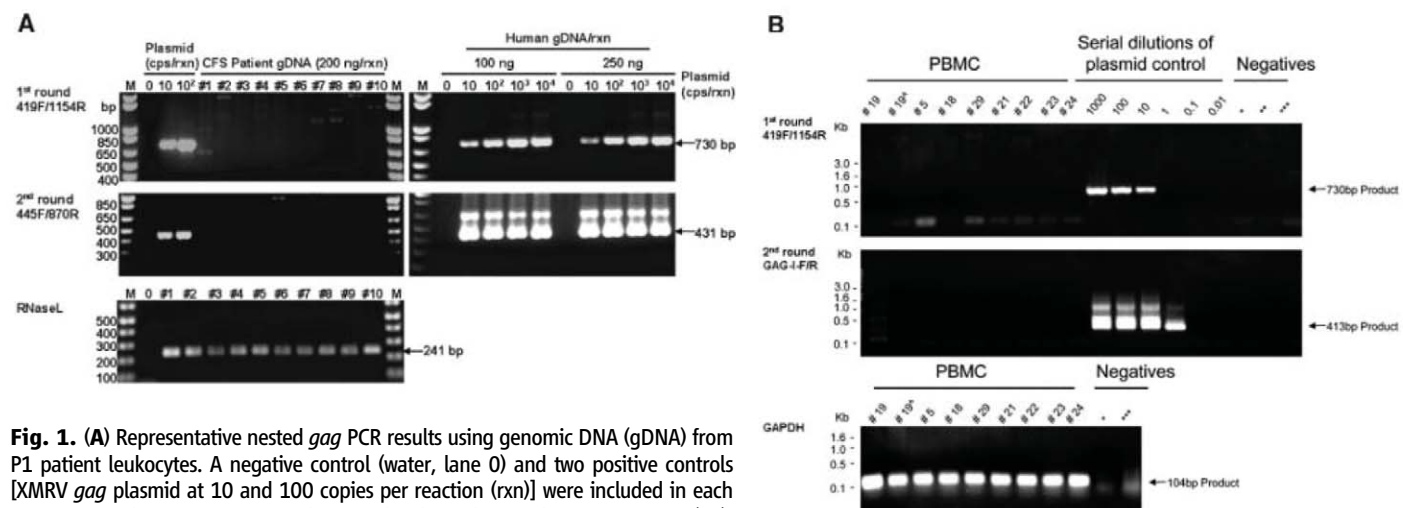


Fig. 1. (A) Representative nested *gag* PCR results using genomic DNA (gDNA) from P1 patient leukocytes. A negative control (water, lane 0) and two positive controls [XMRV *gag* plasmid at 10 and 100 copies per reaction (rxn)] were included in each run. As control, patient DNA was also tested with single-round PCR for RNaseL (17). DNA markers (M) and the positions of expected PCR products are annotated. **(B)** Representative nested RT-PCR results on P2 PBMC samples. Positive and negative controls are shown. Ten-fold serial dilutions of XMRV *gag* plasmid control start at 1000 copies per reaction. Negative controls for each reaction step were tested in triplicate: *RNA/DNA extraction negative control, **RT control, and ***PCR control.

antibodies to XMRV detected in a commercial (VIPDx) or research laboratory (WPI) (5) (table S1). Twenty of the patients (69%) were female and nine (31%) were male with a median age of 52 years. Nine of these subjects were also part of P1 (table S1). Fresh blood samples were used for viral culture and testing (17). For the serum inactivation studies, seven healthy University of California, San Francisco (UCSF) laboratory workers, ranging in age from 21 to 72 years, served as controls. These volunteers were afebrile without signs of any illness. This research received approval of the Human Subjects Committee at the UCSF. All participants signed IRB-approved consent forms.

We initially assessed the peripheral blood leukocytes from the 41 subjects in P1 for XMRV DNA using nested PCR targeting *gag* (primers 419F/1154R and 445F/870R) and *env* (primers 5922F/6273R and 5937F/6198R). The sensitivity

of these PCR assays is at least 10 XMRV genomes per reaction (table S3). No XMRV DNA was detected in any sample (see Fig. 1A for representative data). Notably, a chart review of the 41 patients revealed that 19 had two blood samples drawn on the same day by the same phlebotomist, with one sample submitted to VIPDx and the other to WVRG. For XMRV analysis, VIPDx used diagnostic technologies identical to those utilized in previous studies on XMRV and CFS (5). The chart review indicated that 53% (10 out of 19) of the blood samples were reported by the commercial laboratory as being positive for XMRV DNA. This difference in our results (0 out of 19) versus the chart review results (10 out of 19) was statistically significant ($P < 0.0004$, two-sided Fisher's exact test).

Our failure to detect XMRV DNA in patient population P1 prompted us to undertake a more

extensive study of patient population P2. We used multiple methodologies to evaluate P2 blood samples for the presence of (i) nucleic acids derived from XMRV or MLV; (ii) infectious XMRV and MLV; and (iii) XMRV-specific antibodies (17). Ficoll-Hypaque-purified peripheral blood mononuclear cells (PBMCs) were evaluated by reverse transcription PCR (RT-PCR) procedures directly or after activation with phytohemagglutinin (PHA; 3 μ g/ml for 3 days) with primers and protocols described by others (6) and previously demonstrated to be highly sensitive for detection of XMRV and MLVs (6, 18). In addition, plasma was evaluated by RT-PCR in a similar manner. No MLV was found in the PBMCs or plasma of these 29 CFS patients (Table 1 and Fig. 1B). The positive control consisted of a 730-base pair fragment of XMRV amplified from the prostate cancer cell line, 22Rv1. The assay was able to detect at least 10 copies of XMRV *gag* DNA per reaction; second-round PCR detected 1 to 10 copies per reaction (table S3).

We also investigated whether infectious XMRV or MLV was detectable in the P2 blood samples. The patients' PBMCs were added to duplicate plates of early-passaged mink lung cells to enhance detection of X-MLV and maintained for 5 days (2, 19, 20). The PBMCs were then removed, and the mink lung cells were passaged weekly for 3 weeks. Culture fluids were then evaluated for infectious XMRV or MLV by monitoring the induction of focus formation in the mink S+L- cell line (19, 20), by measuring RT activity in the cell culture fluids (21), and by PCR

Table 1. Summary of assays used to evaluate blood samples from CFS patients in P2. Information about the CFS patients is provided in table S1. Two subjects were studied twice within a 3-month period (table S1) and gave the same results.

Assay	Percent XMRV-positive (n)
PCR analysis of PBMC-derived DNA	0 (0/31)
RT-PCR analysis of patient plasma	0 (0/31)
PBMC culture fluids*	0 (0/19)
Reverse transcriptase assay of supernatants from mink lung cells passaged after PBMC coculture*	0 (0/30)†

*Infectious virus assay: Fluids were tested for infectious virus production by reverse transcriptase and the mink S+L- cell assays (see text) (17). †Insufficient cells were available for these studies from subject no. 24.

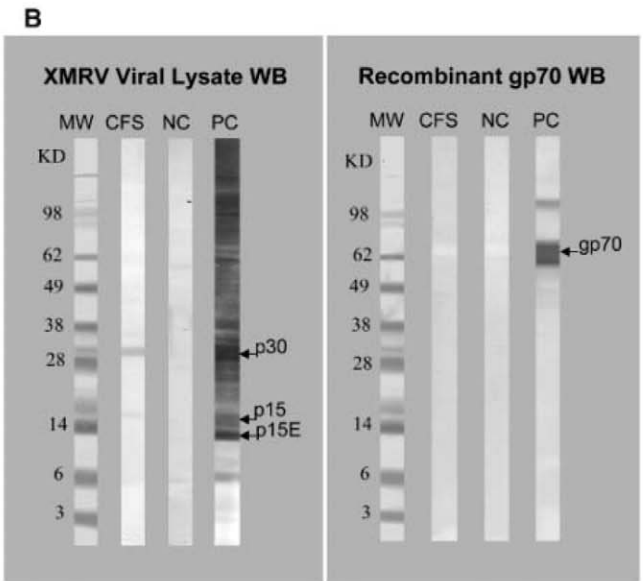
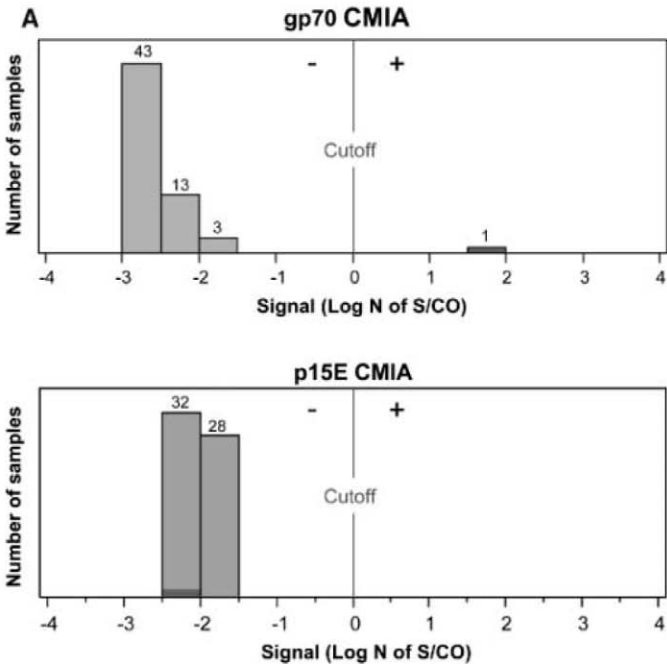


Fig. 2. Evaluation of 60 CFS plasma samples for the presence of XMRV antibodies. (A) Two recombinant protein-based CMIA were used to detect specific antibodies to XMRV gp70 and p15E proteins (17). The x axis represents the CMIA signal in a unit of natural log-transformed ratio of sample signal to the cutoff signal (log N of S/CO). (B) Western blot analysis of gp70 CMIA reactive CFS sample using native XMRV viral proteins and mammalian-expressed recombinant gp70 protein. Sample keys: the gp70 CMIA-reactive (CFS) sample 09-7571, positive control (PC) of XMRV-infected macaque plasma, negative control (NC) of normal blood donor, and molecular mass (MW) markers in kilodaltons (kD).

analysis (11, 18). We also looked for infectious virus in culture fluids from 19 patient PBMCs that had been cultured for 1 to 3 weeks after PHA stimulation. As summarized in Table 1, we did not detect XMRV or MLV in any of the patient samples.

A previous study reported that 50% (9 out of 18) of patients with CFS had plasma antibodies reactive with XMRV (5). We evaluated 60 plasma samples from P1 and P2 patients for the presence of XMRV-specific antibodies by means of two direct-format chemiluminescence immunoassays (CMIA), using either transmembrane p15E or envelope gp70 recombinant proteins of XMRV (22). These assays can detect antibodies to other MLVs. None of the 60 plasma samples from these CFS patients was reactive in the p15E CMIA (Fig. 2A). One of the 60 samples was weakly reactive in the gp70 CMIA with a sample/cut-off (S/CO) value of 5.4 (log N of S/CO = 1.68). However, the plasma was not positive by Western blot (WB) assay with purified XMRV viral lysate as well as recombinant gp70 protein (22) (Fig. 2B). It was therefore considered negative.

Further studies of antiviral responses in the P2 population assessed whether serum samples from these patients could inactivate X-MLV and XMRV. Previous work (23) had indicated that X-MLV is sensitive to inactivation by sera from healthy individuals, most likely by human complement (24–26); conceivably, CFS patient

sera are deficient in this activity. X-MLV and XMRV were mixed with unheated or heated human sera from 7 healthy subjects and 19 CFS patients (17). Both viruses were susceptible to inactivation by unheated, complement-containing sera from both groups; over a 2-log reduction in virus infectivity was noted in several cases. XMRV was less susceptible to inactivation than X-MLV (Fig. 3), most likely a reflection of the passage of XMRV through human cells, which renders the virus less sensitive to human complement (24–26). These results, as well as other reports showing restriction of XMRV replication in human cells (27, 28), suggest that an established MLV infection in humans is unlikely.

Because neither XMRV or MLV sequences or infectious virus could be detected in the blood of the 61 CFS patients in our P1 and P2 populations, we explored whether XMRV and MLV sequences might be present in research reagents used to detect these viruses. While our own studies were under way, other investigators considered the same possibility (29) and reported that mouse DNA and MLV sequences were detectable in reagents and tissues used for RT-PCR (13–15), particularly the mouse monoclonal antibodies (MAbs) in *Taq* polymerase preparations (15). Notably, we detected MLV sequences not only in 3 out of 5 *Taq* polymerases that utilize MAbs, but also in 9 out of 17 other MAbs-containing reagents used in research laboratories (table S2), including antibodies to CD4, CD8, and CD14.

Sequencing of these PCR products revealed a high degree of sequence homology with known MLV sequences from laboratory strains; they most closely resembled the MLV sequences reported by others in the blood of CFS patients (6) (figs. S1 and S2).

Bioreagent contamination, however, does not adequately explain the detection of XMRV by Lombardi *et al.* (5). In this regard, we have found that the DNA sequences of three XMRV proviruses they described are identical to that of VP62, which is the prototype XMRV cloned from prostate cancer tissue (4). Long-term passage of VP62 led to proviruses with accumulated multiple point mutations (fig. S3). As suggested by others (30), independently derived XMRV DNA sequences should show increased genetic diversity compared with the VP62 clone sequence. Therefore, the remarkable conservation of the WPI-XMRV sequences is most consistent with laboratory contamination with the original infectious VP62.

In conclusion, we have found no evidence that XMRV or other murine-like gammaretroviruses are present in blood samples from 43 CFS patients who were previously reported to be infected by XMRV (5, 6). Notably, over a period of several months, seven of our subjects were studied on two occasions; two subjects on three occasions. Because our blood samples were obtained from CFS patients from the same clinical practice that provided the majority of patients described in the early XMRV report (5), differences in the patient cohort or clinical diagnosis cannot account for the discrepancies between our findings and the previous observations. We believe that the detection of MLV in human blood in previous studies (5, 6) reflects contamination of reagents used to assess their presence and/or contamination of human samples during laboratory manipulation of the infectious XMRV clone, VP62 (5). In addition, our studies indicate no antibodies to XMRV and that X-MLV and XMRV are fully or partially inactivated by human serum. The latter finding suggests that these viruses could not readily establish a human infection. Because an activated immune system has been observed in CFS patients (31), the possibility of another infectious agent(s) being associated with this illness merits continued attention.

References and Notes

1. J. A. Levy, *Science* **182**, 1151 (1973).
2. J. A. Levy, *Curr. Top. Microbiol. Immunol.* **79**, 111 (1978).
3. S. Baliji, Q. Liu, C. A. Kozak, *J. Virol.* **84**, 12841 (2010).
4. A. Urisman *et al.*, *PLoS Pathog.* **2**, e25 (2006).
5. V. C. Lombardi *et al.*, *Science* **326**, 585 (2009).
6. S. C. Lo *et al.*, *Proc. Natl. Acad. Sci. U.S.A.* **107**, 15874 (2010).
7. O. Erlwein *et al.*, *PLoS ONE* **5**, e8519 (2010).
8. T. J. Henrich *et al.*, *J. Infect. Dis.* **202**, 1478 (2010).
9. H. C. Groom *et al.*, *Retrovirology* **7**, 10 (2010).
10. P. Hong, J. Li, Y. Li, *Virol. J.* **7**, 224 (2010).
11. W. M. Switzer *et al.*, *Retrovirology* **7**, 57 (2010).
12. F. J. van Kuppeveld *et al.*, *BMJ* **340**, (feb25 1), c1018 (2010).
13. B. Oakes *et al.*, *Retrovirology* **7**, 109 (2010).
14. M. J. Robinson *et al.*, *Retrovirology* **7**, 108 (2010).

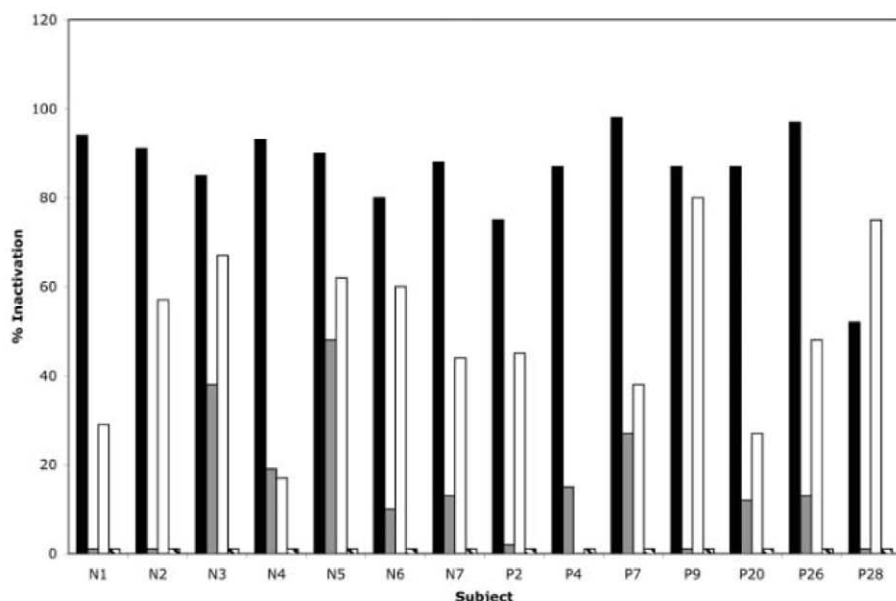


Fig. 3. Effects of human serum on xenotropic MLV and XMRV. Shown is the percent serum inactivation of virus, as measured by induction of focus formation in mink S+L− cells by control untreated X-MLV and XMRV (17). Representative results are shown. Unheated sera from 12 other CFS patients gave similar findings with nearly complete inactivation of X-MLV and partial to high inactivation of XMRV. The X-MLV was obtained from New Zealand Black (NZB) mouse cells and propagated in mink lung cells (20). XMRV was obtained from the human prostate cell line (22Rv1). For the five studies conducted, the control virus titers measured as focus formation in mink S+L− cells were 126, 430, 168, 246, and 208 foci (X-MLV); 84, 376, 208, 284, and 206 foci (XMRV). N, control; P, CFS patient (see table S1); black bars, X-MLV unheated sera; shaded bars, X-MLV heated sera; white bars, XMRV unheated sera; hatched bars, XMRV heated sera.

15. E. Sato, R. A. Furuta, T. Miyazawa, *Retrovirology* **7**, 110 (2010).
16. K. Fukuda *et al.*, *Ann. Intern. Med.* **121**, 953 (1994).
17. Materials and methods are available as supporting material on Science Online.
18. G. Simmons *et al.*, *Transfusion* **51**, 643 (2011).
19. O. E. Varnier, A. D. Hoffman, B. A. Nexø, J. A. Levy, *Virology* **132**, 79 (1984).
20. O. E. Varnier, C. M. Repetto, S. P. Raffanti, A. Alama, J. A. Levy, *J. Gen. Virol.* **64**, 425 (1983).
21. A. D. Hoffman, B. Banapour, J. A. Levy, *Virology* **147**, 326 (1985).
22. X. Qiu *et al.*, *Retrovirology* **7**, 68 (2010).
23. B. Banapour, J. Sernatinger, J. A. Levy, *Virology* **152**, 268 (1986).
24. Y. Takeuchi *et al.*, *J. Virol.* **68**, 8001 (1994).
25. R. P. Rother *et al.*, *J. Exp. Med.* **182**, 1345 (1995).
26. D. M. Takefman, G. T. Spear, M. Saifuddin, C. A. Wilson, *J. Virol.* **76**, 1999 (2002).
27. T. Paprotka *et al.*, *J. Virol.* **84**, 5719 (2010).
28. H. C. Groom, M. W. Yap, R. P. Galão, S. J. Neil, K. N. Bishop, *Proc. Natl. Acad. Sci. U.S.A.* **107**, 5166 (2010).
29. R. A. Weiss, *BMC Biol.* **8**, 124 (2010).
30. S. Hué *et al.*, *Retrovirology* **7**, 111 (2010).
31. A. L. Landay, E. T. Lennette, C. Jessop, J. A. Levy, *Lancet* **338**, 707 (1991).

Acknowledgments: We thank D. Peterson for the referrals of all the subjects evaluated, J. Weismann for coordinating subject participation, I. Livinti for assistance with data management, E. Delwart and J. Fiddes for comments on the manuscript, and K. Peter for help in preparation of

the manuscript. These studies were conducted with support of private funds to the investigators. Patent applications have been filed by Abbott Laboratories relating to detection of XMRV using immunoassays and molecular-based assays.

Supporting Online Material

www.sciencemag.org/cgi/content/full/science.1204963/DC1
Materials and Methods
Figs. S1 to S3
Tables S1 to S3
References

1 March 2011; accepted 16 May 2011

Published online 31 May 2011;

10.1126/science.1204963

Recombinant Origin of the Retrovirus XMRV

Tobias Paprotka,^{1*} Krista A. Delviks-Frankenberry,^{1*} Oya Cingöz,^{3,4*} Anthony Martinez,⁵ Hsing-Jien Kung,^{5,6} Clifford G. Tepper,⁵ Wei-Shau Hu,² Matthew J. Fivash Jr.,⁷ John M. Coffin,^{3,4} Vinay K. Pathak^{1†}

The retrovirus XMRV (xenotropic murine leukemia virus–related virus) has been detected in human prostate tumors and in blood samples from patients with chronic fatigue syndrome, but these findings have not been replicated. We hypothesized that an understanding of when and how XMRV first arose might help explain the discrepant results. We studied human prostate cancer cell lines CWR22Rv1 and CWR-R1, which produce XMRV virtually identical to the viruses recently found in patient samples, as well as their progenitor human prostate tumor xenograft (CWR22) that had been passaged in mice. We detected XMRV infection in the two cell lines and in the later passage xenografts, but not in the early passages. In particular, we found that the host mice contained two proviruses, PreXMRV-1 and PreXMRV-2, which share 99.92% identity with XMRV over >3.2-kilobase stretches of their genomes. We conclude that XMRV was not present in the original CWR22 tumor but was generated by recombination of two proviruses during tumor passaging in mice. The probability that an identical recombinant was generated independently is negligible ($\sim 10^{-12}$); our results suggest that the association of XMRV with human disease is due to contamination of human samples with virus originating from this recombination event.

Murine leukemia viruses (MLVs) are retroviruses belonging to the genus *Gammaretrovirus* that cause cancers and other diseases in mice, and they are divided into the ecotropic, amphotropic, polytropic, and xenotropic classes on the basis of their receptor usage. Xenotropic MLVs cannot infect cells from inbred mice but can infect cells from other spe-

cies, including humans. Xenotropic murine leukemia virus–related virus (XMRV) was isolated from a human prostate cancer (PC) in 2006 and has been reported to be present in 6 to 27% of human PCs (1, 2) and in the peripheral blood of 67% of chronic fatigue syndrome (CFS) patients (3). The assertion that XMRV is circulating in the human population has been challenged by several studies that have failed to detect XMRV in multiple cohorts of PC and CFS patients or healthy controls [reviewed in (4)]. Endogenous xenotropic MLVs can infect human tumors during passage through nude mice (5), and it has been suggested that XMRV may have arisen in this manner (5, 6). In addition, XMRV replication is highly sensitive to human APOBEC3s and tetherin (7–11), which makes it doubtful that XMRV replication occurred efficiently in human peripheral blood mononuclear cells of CFS patients as previously reported (3).

The human PC cell line CWR22Rv1 (hereafter 22Rv1) (12) produces infectious XMRV essentially identical in sequence to that obtained from patients. 22Rv1 contains ≥ 10 proviral copies

per cell (13) and was proposed to have been derived from an XMRV-infected tumor. This cell line was derived from a xenograft (CWR22) that was established from a primary prostate tumor at Case Western Reserve University and serially passaged in nude mice (14, 15). To explore the origin of the virus in 22Rv1 cells, we analyzed various passages of the CWR22 xenograft, as well as a subline of the CWR22 xenograft (2152) from which the 22Rv1 cell line was established (12), and another prostate cancer cell line, CWR-R1, which was also derived from CWR22 (16). Figure 1A traces the timeline of the serial xenograft transplants of CWR22 up to the derivation of the cell lines 22Rv1 and CWR-R1 and indicates (bold letters) the samples that were available for analysis. Nude mouse strain(s) maintained by Charles River (NU/NU) and Harlan Laboratories [Harlan Sprague Dawley (Hsd)] are likely to have been used for in vivo passages of the xenograft (17). DNA samples from passage 3 (777 in Fig. 1A) and an unknown early passage (736) were obtained along with samples from a 7th passage, CWR22-9216R and CWR22-9218R. A xenograft tumor from the early seventh passage was independently propagated at the University of California, Davis, using Hsd nude mice (CWR22-8R and 8L). Total nucleic acid from relapsed androgen-independent tumors (CWR22R) 2152, 2524, 2272, and 2274 and the 22Rv1 and CWR-R1 cell lines was available for analysis (14).

We verified that the xenograft samples (736, 777, 9216R, 9218R, 8R, and 8L) and the 22Rv1 or CWR-R1 cell lines were all derived from the same person by performing short tandem repeat analysis at seven loci (Fig. 1B and fig. S1). The probabilities that the xenografts and the two cell lines have the same allele patterns for these loci by chance are 1.6×10^{-13} and 6.3×10^{-13} , respectively.

To quantify the amount of XMRV DNA in the CWR22 xenografts, we developed a real-time polymerase chain reaction (PCR) primer-probe set that specifically detected XMRV *env* and excluded murine endogenous proviruses present in BALB/c and NIH3T3 genomic DNA (Fig. 1C). We used quantitative PCR of 22Rv1 DNA to estimate 20 proviruses per cell and used the 22Rv1

¹Viral Mutation Section, HIV Drug Resistance Program, National Cancer Institute at Frederick, Frederick, MD 21702, USA. ²Viral Recombination Section, HIV Drug Resistance Program, National Cancer Institute at Frederick, Frederick, MD 21702, USA. ³Department of Molecular Biology and Microbiology, School of Medicine, Tufts University, 150 Harrison Avenue, Boston, MA 02111, USA. ⁴Genetics Program, School of Medicine, Tufts University, 150 Harrison Avenue, Boston, MA 02111, USA. ⁵Department of Biochemistry and Molecular Medicine, University of California, Davis, Sacramento, CA 95817, USA. ⁶Department of Urology, University of California, Davis, Sacramento, CA 95817, USA. ⁷Data Management Services, Inc., National Cancer Institute at Frederick, Frederick, MD 21702, USA.

*These authors contributed equally to this work.

†To whom correspondence should be addressed. E-mail: vinay.pathak@nih.gov

DNA to generate a standard curve. The CWR22 xenografts had significantly fewer copies of XMRV *env* (<1 to 3 copies per 100 cells) compared with the 22Rv1 cells (2000 copies per 100 cells). The CWR-R1 cell line had ~3000 copies per 100 cells, and the NU/NU and Hsd nude mice, thought to have been used to passage the CWR22 xenograft, had 58 and 68 copies per 100 cells, respectively. Because xenograft tumors are expected to contain a mixture of human and mouse cells, we quantified the amount of mouse DNA by analyzing mouse intracisternal A-type particle (IAP) DNA as previously described (18, 19). About 0.3 to 1% of the total DNA from all six xenografts consisted of mouse DNA (Fig. 1D); this result is consistent with the <1 to 3 XMRV *env* sequences per 100 cells detected in the same samples (Fig. 1C).

We characterized XMRV and related sequences in the xenografts, cell lines, and nude mouse strains by PCR and DNA sequencing (Fig. 2). Using primers previously used to clone and sequence XMRV from 22Rv1 cells (8), we determined that all the XMRV proviruses in

the CWR-R1 and 22Rv1 cell lines are identical in sequence (GenBank accession no. FN692043), with the exception of some rare hypermutated proviruses (Fig. 2A and figs. S2 and S3). Next, we developed several primer sets specifically to amplify XMRV sequences and to exclude endogenous murine retroviruses (fig. S2). Primers that specifically amplified XMRV were used to perform PCR on DNA from the late-passage xenografts 2152, 2524, 2272, and 2274; sequencing confirmed the presence of these XMRV sequences in these tumors (Fig. 2A and fig. S3A; boxed in Fig. 1A).

We used the same XMRV-specific primer sets to amplify and sequence DNA from early-passage xenografts (736, 777, 8L, 8R, 16R, and 18R) (Fig. 2B); the results showed that XMRV *env* was present but not *gag* sequences (sequencing coverage summarized in fig. S3), which indicated that the early xenografts did not contain XMRV. However, we did find that early xenografts contained a previously undescribed XMRV-related provirus that we have named PreXMRV-1 (Fig. 2B). The complete sequence of PreXMRV-1 was

determined from the early-passage xenografts, the NU/NU and Hsd strains, and the CWR-R1 cell line (GenBank accession no. FR871849). PreXMRV-1 and consensus XMRV differed by only one base in a 3211-nucleotide (nt) stretch of the genome encoding the 3' half of *pol* and the 5' two-thirds of *env*. In addition, the long terminal repeats (LTRs) were nearly identical; PreXMRV-1 had a single adenine deletion relative to XMRV in a run of six adenines. The two genomes differed by 10% over the remaining 3.5-kb stretch of *gag-pro-pol* and by 9% in a 600-nt stretch at the 3' end of *env*. PreXMRV-1 is replication-defective because of a 16-nt deletion in *gag* and a +1 frameshift mutation in *pol*. Late-passage xenografts 2524 and 2274, but not 2152 and 2272, also contained PreXMRV-1. The detection of low levels of XMRV *env* sequence in the early xenografts (Fig. 1C) can be attributed to the PreXMRV-1 proviruses present in the contaminating mouse DNA. Overall, these results indicate that PreXMRV-1 is an endogenous murine provirus that is present in the NU/NU and Hsd strains, but neither of these strains contains XMRV

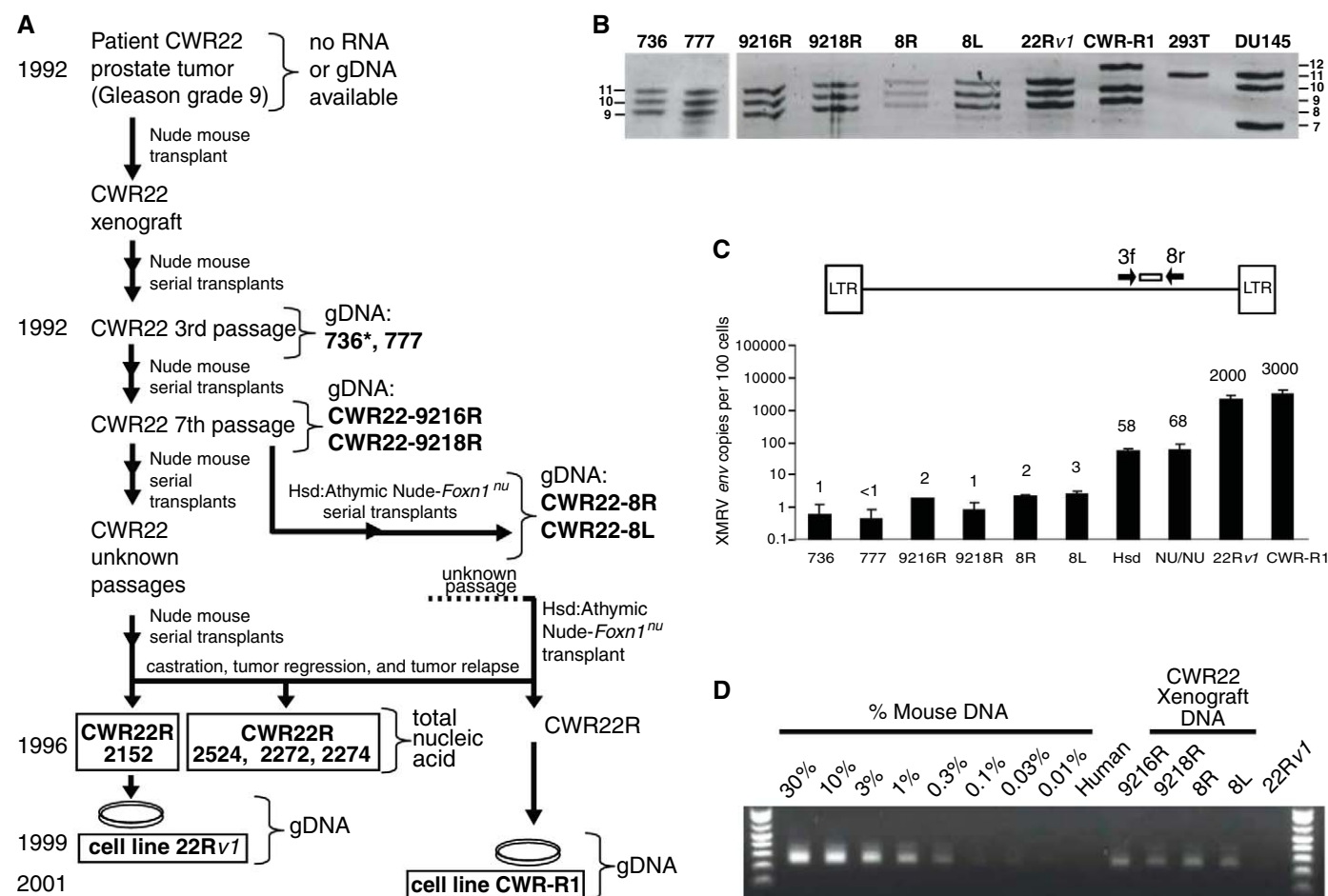


Fig. 1. Characterization of CWR22 xenografts and XMRV-related sequences. **(A)** Genesis of 22Rv1 and CWR-R1 cell lines. Bold letters indicate samples from which genomic DNA (gDNA) or total nucleic acid was available for analysis. XMRV-positive samples are boxed. Asterisk (*) indicates unknown early passage. **(B)** Short tandem repeat analysis. Representative D75280 allele pattern

of xenografts and 22Rv1 and CWR-R1 cell lines, along with analysis of six additional loci (fig. S1). An allelic ladder is shown on left and right of gel. **(C)** Quantitative real-time PCR to detect XMRV *env* sequences. Calculated copies per 100 cells are indicated above each bar. **(D)** IAP assay to quantify the amount of mouse DNA present in the xenograft gDNAs.

(the PCR and sequencing coverage are detailed in fig. S3, A and B).

To screen for the presence of endogenous XMRV in mouse strains, we developed an XMRV-specific PCR assay based on sequence differences in the LTR and *gag* leader regions that excluded all known endogenous murine retroviruses (fig. S2). A survey of 45 laboratory mouse strains and 44 wild mice failed to detect XMRV (fig. S4). In a search for proviruses that might contain XMRV-specific sequence features, we found a second previously undescribed endogenous provirus that we named PreXMRV-2 (Fig. 2C). A portion of PreXMRV-2 corresponds to a 1124-nt sequence of an endogenous provirus from the 129X1/SvJ mouse genome (acc. no. AAHY0159188.1) (6, 20). The sequence of PreXMRV-2 (GenBank accession no. FR871850) revealed that *gag*, *pol*, and *env* reading frames are open and can potentially express functional proteins. A 3.6-kb stretch encompassing the *gag* leader region and *gag-pro-pol*

differs by one base from the consensus XMRV (99.9% identity); in addition, a ~700-nt region of *env* is 99% identical to XMRV; however, the LTRs and the remaining viral genome differ by 6 to 12% from consensus XMRV. Phylogenetic analysis indicates that PreXMRV-1 is grouped with xenotropic viruses, whereas PreXMRV-2 appears to be a recombinant, grouping with polytropic and modified polytropic viruses for certain stretches of its genome (fig. S5).

We screened 15 mouse strains, which included 12 nude mice, for the presence of XMRV, PreXMRV-1, and PreXMRV-2 using XMRV-specific primers, primers that amplified XMRV or PreXMRV-1, and PreXMRV-2-specific primers (Fig. 2D and fig. S2). None of the mouse strains contained XMRV, and only the Hsd and the NU/NU outbred nude strains contained PreXMRV-1 (Fig. 2D and fig. S6). Six of the 15 mouse strains contained PreXMRV-2, but only the NU/NU and Hsd mice contained both PreXMRV-1 and PreXMRV-2

(Fig. 2D and fig. S6). It should be noted that, because the Hsd and the NU/NU are outbred strains, individual mice differ in their endogenous proviruses. NU/NU mice showed variation in the presence of these two endogenous proviruses, and two out of five animals tested contained both (fig. S6). The 22Rv1 cell line contained only XMRV as confirmed by sequence analysis; however, the CWR-R1 cell line contained both XMRV and PreXMRV-1. The CWR-R1 cell line has been reported to contain contaminating mouse cells (21) (and see IAP signal in Fig. 2D), which is likely to be the source of the PreXMRV-1 sequences.

We used the same specific primer sets to determine the distribution of XMRV, PreXMRV-1, and PreXMRV-2 in early and late xenografts (Fig. 2E). None of the early xenografts (736, 777, 9216R, 9218R, 8R, and 8L), but all of the late xenografts (2152, 2524, 2272, and 2274) and both cell lines were positive for XMRV. The primers

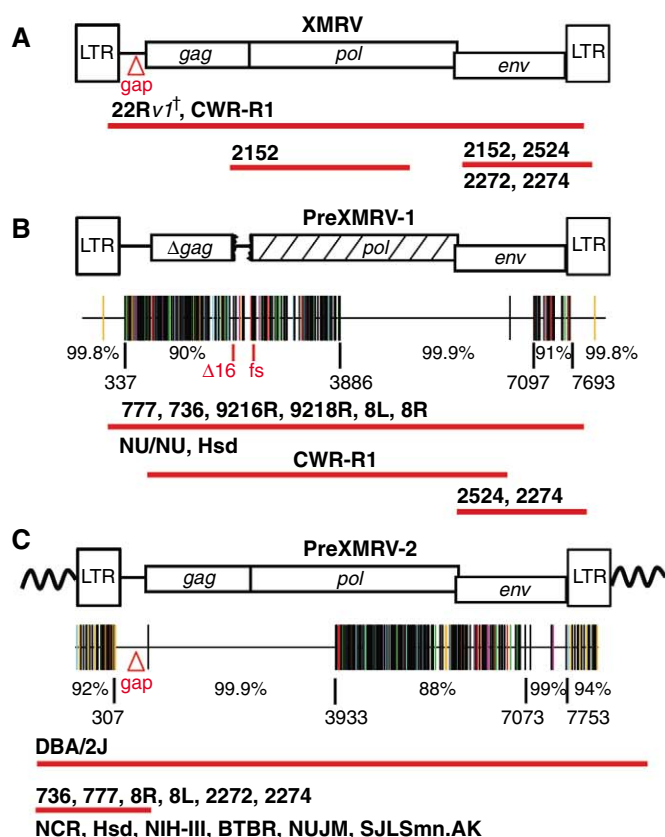


Fig. 2. PCR and sequencing analysis of XMRV and XMRV-related sequences from xenografts, cell lines, and nude mouse strains. Using specific primer sets (fig. S2), cloned PCR products from the xenografts, 22Rv1, CWR-R1, or mouse strains were sequenced. Approximate length and location of sequences determined from samples that were positive for XMRV (**A**), PreXMRV-1 (**B**), and PreXMRV-2 (**C**) are shown as red bars beneath each provirus. Details of primers and numbers of cloned products sequenced are shown in figs. S2 and S3. Hypermut plots (see fig. S3 for details), which indicate nucleotide mismatches relative to XMRV as color-coded vertical lines, are shown for PreXMRV-1 (**B**) and PreXMRV-2 (**C**), together with the percent identity to consensus XMRV for different regions of each provirus [nucleotide numbers refer to the 22Rv1 XMRV sequence (FN692043)]. PreXMRV-1 has a 16-nt deletion (Δ16) in *gag* and a

frameshift (fs) in *pol*, which make it replication-defective, whereas PreXMRV-2 *gag*, *pol*, and *env* reading frames are open. (**D**) Mouse strains and (**E**) xenograft and PC cell lines were analyzed by PCR for the presence of XMRV, PreXMRV-1, and PreXMRV-2. Mouse IAP and human glyceraldehyde-3-phosphate dehydrogenase (GAPDH) serve as positive controls for the presence of mouse and human DNA, respectively. For both (**D**) and (**E**), the primer set used to detect PreXMRV-1 can also detect XMRV. For ease of comparison, the 22Rv1 and CWR-R1 gel lanes from (**E**), which were run in parallel, are duplicated in (**D**). DNAs in (**D**) and (**E**) were all amplified with the same PCR primer master mix. [†]We previously determined the full-length sequence of XMRV from 22Rv1 cells (8). Δ*gap* refers to the 24-bp deletion in the *gag* leader characteristic of XMRV. All mouse strains shown in (**D**) are nudes except for those indicated with an asterisk (*).

used to detect PreXMRV-1 could also detect XMRV; sequencing analysis of the PCR products from all of the early xenografts detected only PreXMRV-1, but both XMRV and PreXMRV-1 were detected from the late xenografts 2524 and 2274 (Fig. 2B). Amplification with PreXMRV-2-specific primers revealed the presence of this provirus in early xenografts 736, 777, 8R, and 8L and late xenografts 2272 and 2274 (Fig. 2, C and E, and fig. S3C). The variable detection level of PreXMRV-2 in the late xenografts could be due to individual differences in the outbred mice, and by extension, in the mouse DNA in these samples.

Comparison of the PreXMRV-1 and PreXMRV-2 sequences revealed that the regions of near identity to XMRV are reciprocal and largely nonoverlapping. We therefore hypothesized that recombination between these two retroviruses resulted in the formation of XMRV. As shown in Fig. 3A, reverse transcriptase template-switching events during minus-strand DNA synthesis can form a recombinant that is essentially identical to the sequences of all of the XMRVs reported to date and that differs from the consensus XMRV by only four nucleotides. The six switching events occurred in 20- to 73-nt stretches that are identical in PreXMRV-1 and PreXMRV-2 (red numbers in Fig. 3A, and fig. S7A). Of the four nucleotide differences between the predicted recombinant and consensus XMRV, only the A>G change at position 790 results in a conservative valine-to-isoleucine amino acid substitution; the other three substitutions are silent. The 22Rv1 and CWR-R1 cell lines, as well as VP42, have an A at position 790, whereas all other XMRV isolates have a G at position 790.

The insertion of an A at position 8092 occurred within a run of six adenines; frameshift mutations commonly occur in such homopolymers during retroviral replication (22). A comparison of the predicted recombinant to the available XMRV sequences is shown in fig. S7B. The available XMRV sequences all have the same six recombination junctions predicted in the hypothetical recombinant and differ from the consensus XMRV by 3 to 14 nt. These differences may be the result of errors during PCR or sequencing or from mutations during the passage of XMRV in another cell line. Phylogenetic analysis supports the predicted recombinant virus as the precursor of the virus in the CWR22 xenografts, the 22Rv1 and CWR-R1 cell lines, and all XMRVs isolated and sequenced from patients (Fig. 3B) (23).

Our findings indicate that virus derived from two previously undescribed murine endogenous retroviruses, PreXMRV-1 and PreXMRV-2, most likely underwent retroviral recombination to generate XMRV during *in vivo* passaging of the CWR22 xenograft in nude mice. Both parental endogenous proviruses were present in some of the nude mouse strains used for *in vivo* passaging of the xenografts; therefore, there were opportunities for this recombinant to form and spread in the tumor cells that were the progenitors of the 22Rv1 and CWR-R1 cell lines. Only six template-switching events, which is close to the average of four template switches per replication cycle (24), are needed to generate a recombinant that is both essentially identical and ancestral to all XMRV sequences characterized to date from cell lines and patients (Fig. 3B). We have estimated the probability that the

exact set of template-switching events occurred independently is 1.3×10^{-12} (fig. S8) (23), which makes it very likely that contamination of human samples with XMRV originating from the relapsed CWR22 xenografts or either of the two cell lines, perhaps through other intermediate cell lines, contributed to its reported association with PC and CFS. Our results and conclusions relate to XMRV detection by isolation of virus of this specific sequence (1–3) and do not directly address detection of antibodies or viral antigens (25, 26) or PCR detection of related but distinct MLV sequences (27). We note, however, that most “XMRV-specific” PCR assays may detect PreXMRV-1 or -2 proviruses in contaminating mouse DNA and that specific detection of XMRV requires the use of primers that flank a crossover site.

The alternative possibility is that recombination between PreXMRV-1 and PreXMRV-2 occurred during mouse evolution, giving rise to an endogenous XMRV provirus that is present in mice and can occasionally infect humans. We think this possibility is remote because analysis of the early xenografts, which contained contaminating nude mouse DNAs, failed to detect XMRV. Furthermore, we were unable to detect XMRV in a screen of 89 inbred and wild-derived mouse strains including 17 individual nude mice (fig. S4) (23).

We conclude that XMRV was generated as a result of a unique recombination event between two endogenous MLVs that took place around 1993–1996 in a nude mouse carrying the CWR22 PC xenograft. Because the probability that the same recombination event could occur independently by random chance is essentially negligible,

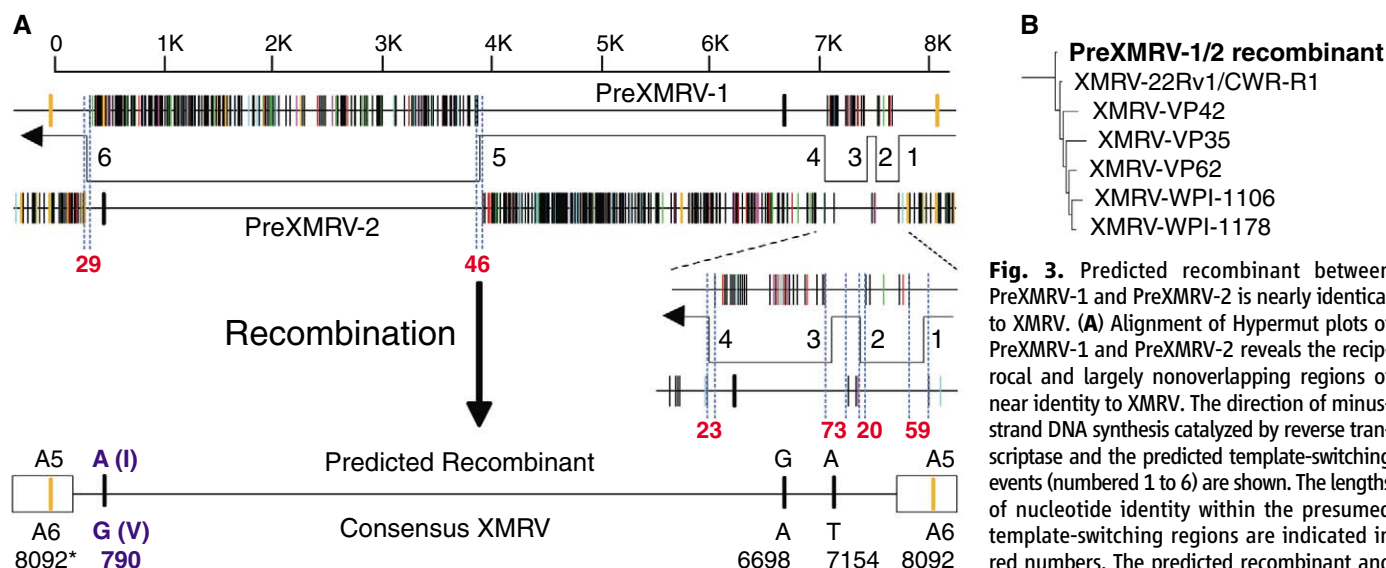


Fig. 3. Predicted recombinant between PreXMRV-1 and PreXMRV-2 is nearly identical to XMRV. **(A)** Alignment of Hypermut plots of PreXMRV-1 and PreXMRV-2 reveals the reciprocal and largely nonoverlapping regions of near identity to XMRV. The direction of minus-strand DNA synthesis catalyzed by reverse transcriptase and the predicted template-switching events (numbered 1 to 6) are shown. The lengths of nucleotide identity within the presumed template-switching regions are indicated in red numbers. The predicted recombinant and the four nucleotide differences with consensus XMRV are shown. The nucleotide numbers refer to numbers of the 22Rv1 XMRV (acc. no. FN692043). Note that nucleotide 8092 is within the U3 region and is present in both LTRs (boxes). A5 and A6 refer to homopolymeric runs of five and six adenines, respectively. The A>G change at 790 results in an isoleucine (I) to valine (V) substitution. **(B)** Phylogenetic tree of all full-length XMRV sequences to date and the predicted recombinant implicates the predicted recombinant as the ancestor of all sequenced XMRV isolates. The tree shown is an enlargement of the XMRV-specific portion of the complete endogenous MLV tree (fig. S5A) (23).

any XMRV isolates with the same or nearly the same sequences identified elsewhere originated from this event (23).

References and Notes

1. R. Schlager, D. J. Choe, K. R. Brown, H. M. Thaker, I. R. Singh, *Proc. Natl. Acad. Sci. U.S.A.* **106**, 16351 (2009).
2. A. Urisman *et al.*, *PLoS Pathog.* **2**, e25 (2006).
3. V. C. Lombardi *et al.*, *Science* **326**, 585 (2009).
4. A. C. Van der Kuyt, M. Cornelissen, B. Berkhout, *Front. Microbiol.* **1**, 147 (2011).
5. R. A. Weiss, *BMC Biol.* **8**, 124 (2010).
6. S. Hué *et al.*, *Retrovirology* **7**, 111 (2010).
7. H. C. Groom, M. W. Yap, R. P. Galão, S. J. Neil, K. N. Bishop, *Proc. Natl. Acad. Sci. U.S.A.* **107**, 5166 (2010).
8. T. Paprotka *et al.*, *J. Virol.* **84**, 5719 (2010).
9. K. Stieler, N. Fischer, *PLoS ONE* **5**, e11738 (2010).
10. H. P. Bogerd, F. Zhang, P. D. Bieniasz, B. R. Cullen, *Virology* **410**, 234 (2011).
11. C. Chaipan *et al.*, *J. Virol.* **85**, 4888 (2011).
12. R. M. Sramkoski *et al.*, *In Vitro Cell. Dev. Biol. Anim.* **35**, 403 (1999).
13. E. C. Knouf *et al.*, *J. Virol.* **83**, 7353 (2009).
14. M. Nagabhushan *et al.*, *Cancer Res.* **56**, 3042 (1996).
15. T. G. Pretlow *et al.*, *J. Natl. Cancer Inst.* **85**, 394 (1993).
16. C. W. Gregory, R. T. Johnson Jr., J. L. Mohler, F. S. French, E. M. Wilson, *Cancer Res.* **61**, 2892 (2001).
17. Materials and methods are available as supporting material on Science Online.
18. B. Oakes *et al.*, *Retrovirology* **7**, 109 (2010).
19. M. J. Robinson *et al.*, *Retrovirology* **7**, 108 (2010).
20. V. Cournaud, J.-L. Battini, M. Sitbon, A. L. Mason, *Proc. Natl. Acad. Sci. U.S.A.* **107**, 15666 (2010).
21. A. van Bokhoven *et al.*, *Prostate* **57**, 205 (2003).
22. V. K. Pathak, H. M. Temin, *Proc. Natl. Acad. Sci. U.S.A.* **87**, 6019 (1990).
23. Further discussion in support of the unique origin of XMRV and its role as the source of XMRV in PC and CFS patients is available as supporting material in Science Online.
24. J. Zhuang, S. Mukherjee, Y. Ron, J. P. Dougherty, *J. Virol.* **80**, 6706 (2006).
25. R. S. Arnold *et al.*, *Urology* **75**, 755 (2010).
26. X. Qiu *et al.*, *Retrovirology* **7**, 68 (2010).
27. S. C. Lo *et al.*, *Proc. Natl. Acad. Sci. U.S.A.* **107**, 15874 (2010).

Acknowledgments: We thank W. Shao for analysis of MLV diversity, and E. Freed and S. Hughes for helpful discussions. This research was supported in part by the Intramural Research Program of the Center for Cancer Research, National Cancer Institute, NIH. The content of this publication does not necessarily reflect the views or policies of the Department of Health and Human Services nor does mention of trade names, commercial products, or organizations imply endorsement by the U.S. government. This work was also supported in part by a Bench-to-Bedside Award to V.K.P., research grant R37 CA 089441 to J.M.C., and R01CA150197 to H.J.K. J.M.C. was a Research Professor of the American Cancer Society with support from the F.M. Kirby Foundation.

Supporting Online Material

www.sciencemag.org/cgi/content/full/science.1205292/DC1
Materials and Methods

Figs. S1 to S8

Table S1

References

1 February 2011; accepted 5 May 2011

Published online 31 May 2011;

10.1126/science.1205292

Predicting a Human Gut Microbiota's Response to Diet in Gnotobiotic Mice

Jeremiah J. Faith, Nathan P. McNulty, Federico E. Rey, Jeffrey I. Gordon*

The interrelationships between our diets and the structure and operations of our gut microbial communities are poorly understood. A model community of 10 sequenced human gut bacteria was introduced into gnotobiotic mice, and changes in species abundance and microbial gene expression were measured in response to randomized perturbations of four defined ingredients in the host diet. From the responses, we developed a statistical model that predicted over 60% of the variation in species abundance evoked by diet perturbations, and we were able to identify which factors in the diet best explained changes seen for each community member. The approach is generally applicable, as shown by a follow-up study involving diets containing various mixtures of pureed human baby foods.

Owing to its many roles in human health (1–3), there is great interest in deciphering the principles that govern the operations of an individual's gut microbiota. Current estimates indicate that each of us harbors several hundred bacterial species in our intestine (4, 5), and different diets lead to large and rapid changes in the composition of the microbiota (6, 7). Given the dynamic interrelationship between diet, the configuration of the microbiota, and the partitioning of nutrients in food to the host, inferring the rules that govern the microbiota's responses to dietary ingredients represents a challenge (8).

Gnotobiotic mice colonized with simple, defined collections of sequenced representatives of the various phylotypes present in the human gut microbiota provide a simplified in vivo model system in which metabolic niches, host-microbe,

and microbe-microbe interactions can be examined by using a variety of techniques (9–12). These studies have focused on small communities exposed to a few perturbations. We used gnotobiotic mice harboring a 10-member community of sequenced human gut bacteria to model the response of a microbiota to changes in host diet. We aimed to predict the absolute abundance of each species in this microbiota on the basis of knowledge of the composition of the host diet. Furthermore, we wanted to gain insights into the niche preferences of members of the microbiota and to discover how much of the response of the community was a reflection of their phenotypic plasticity.

The 10 bacterial species were introduced into germ-free mice to create a model community with representatives of the four most prominent bacterial phyla in the healthy human gut microbiota (fig. S1A) (13). Their genomes encode major metabolic functions that have been identified in anaerobic food webs, including the ability to break down complex dietary polysaccharides not acces-

sible to the host (*Bacteroides thetaiotaomicron*, *Bacteroides ovatus*, and *Bacteroides caccae*); consume oligosaccharides and simple sugars (*Eubacterium rectale*, *Marvinbryantia formatexigens*, *Collinsella aerofaciens*, and *Escherichia coli*); and ferment amino acids (*Clostridium symbiosum* and *E. coli*). We also included two species capable of removing the end products of fermentation: a H₂-consuming, sulfate-reducing bacterium (*Desulfovibrio piger*) and a H₂-consuming acetogen (*Blautia hydrogenotrophica*).

To perturb this community, we used a series of refined diets in which each ingredient represented the sole source of a given macronutrient (casein = protein, corn oil = fat, cornstarch = polysaccharide, and sucrose = simple sugar) and in which the concentrations of these four ingredients were systematically varied (fig. S1, B and C, and table S1). Each individually caged male C57BL/6J mouse was fed a randomly selected diet, with diet switches occurring every 2 weeks ($n = 13$ animals; fig. S1D shows the variation of diet presentation between animals). Shotgun sequencing of total fecal DNA allowed us to determine the absolute abundance of each community member, based on assignment of reads to the various species' genomes, in samples obtained from each mouse on days 1, 2, 4, 7, and 14 of a given diet period (13).

To predict the abundance of each species in the model human gut microbiome given only knowledge of the concentration of each of the four perturbed diet ingredients, we used a linear model

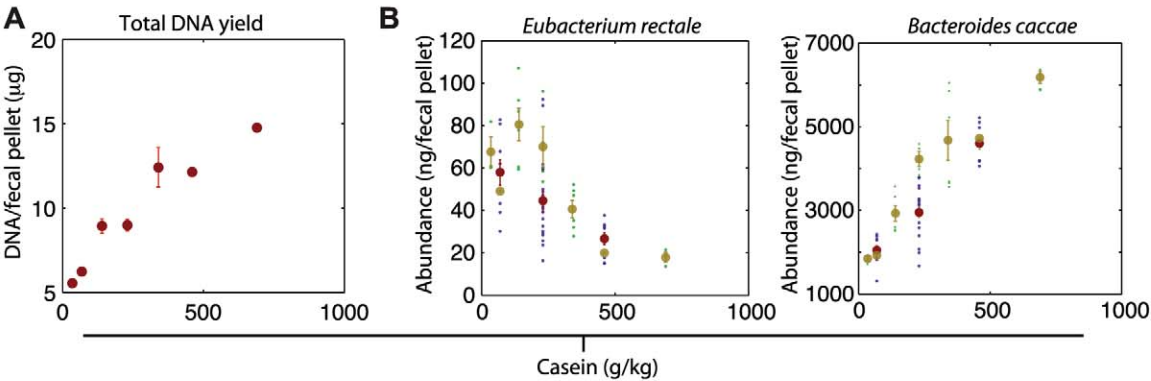
$$y_i = \beta_0 + \beta_{\text{casein}}X_{\text{casein}} + \beta_{\text{starch}}X_{\text{starch}} + \beta_{\text{sucrose}}X_{\text{sucrose}} + \beta_{\text{oil}}X_{\text{oil}} \quad (1)$$

where y_i is the absolute abundance of species i ; X_{casein} , X_{starch} , X_{sucrose} , and X_{oil} are the amounts (in grams per kilogram of mouse diet) of casein,

Center for Genome Sciences and Systems Biology, Washington University School of Medicine, St. Louis, MO 63108, USA.

*To whom correspondence should be addressed. E-mail: jgordon@wustl.edu

Fig. 1. Total community abundance (biomass) and the abundance of each community member can best be explained by changes in casein. **(A)** The total DNA yield per fecal pellet increased as the amount of casein in the host diet increased (shown are mean \pm SEM for each tested concentration of casein). **(B)** Changes in species abundance as a function of changes in the concentration of casein in the host diet were also apparent for all 10 species; seven species (such as *B. caccae*) were positively correlated with casein concentration, whereas the remaining three species (such as *E. rectale*) were negatively correlated with casein concentration. Data points



cornstarch, sucrose, and corn oil, respectively, in a given host diet; β_0 is the estimated parameter for the intercept; and β_{casein} , β_{starch} , β_{sucrose} , and β_{oil} are the estimated parameters for each of the perturbed diet components. Because each mouse underwent a sequence of three diet permutations presented in different order, and each of the diet periods covered all of the 11 possible diets (fig. S1D), we were able to use two of these three diet intervals to fit the model for Eq. 1 (13 mice \times 2 diets per mouse = 26 samples per bacterial species); we then measured our ability to predict the abundance of each bacterial species for the 13 samples in the remaining (third) diet (13). Averaging this cross-validation from all three subsets, the model explained over 61% of the variance in the abundance of the community members (abundance-weighted mean $R^2 = 0.61$; see table S2 for species-specific R^2).

Although the cross-validation provided evidence that the response of this microbiota was predictable from knowledge of these diet ingredients, a more conclusive validation of the model would be its ability to make predictions for new diets. Therefore, we designed six additional diets with new combinations of the four refined ingredients. Using a design similar to the first experiment, eight different 10-week-old gnotobiotic male C57Bl/6J mice harboring the 10-member community were each given a randomized sequence of diets selected from the six new diets (shaded diets L to Q in fig. S1B) or one of the previous diets (fig. S1E). Fitting the model parameters with the data from the first experiment, we were able to explain 61% of the variance in the abundance of the community members on the new diets, showing virtually equivalent results to the cross-validation procedure (table S2).

These results indicate that the linear model explains the majority of the variation in abundance of each organism by using only a knowledge of the species in the community and the concentrations of casein, cornstarch, sucrose, and corn oil in the diet, without having to ex-

from the first and second set of mice given the refined diets (fig. S1, D and E) are shown in purple and green, respectively, and the mean and standard error for all diets at a given concentration of casein are shown in red and tan, respectively.

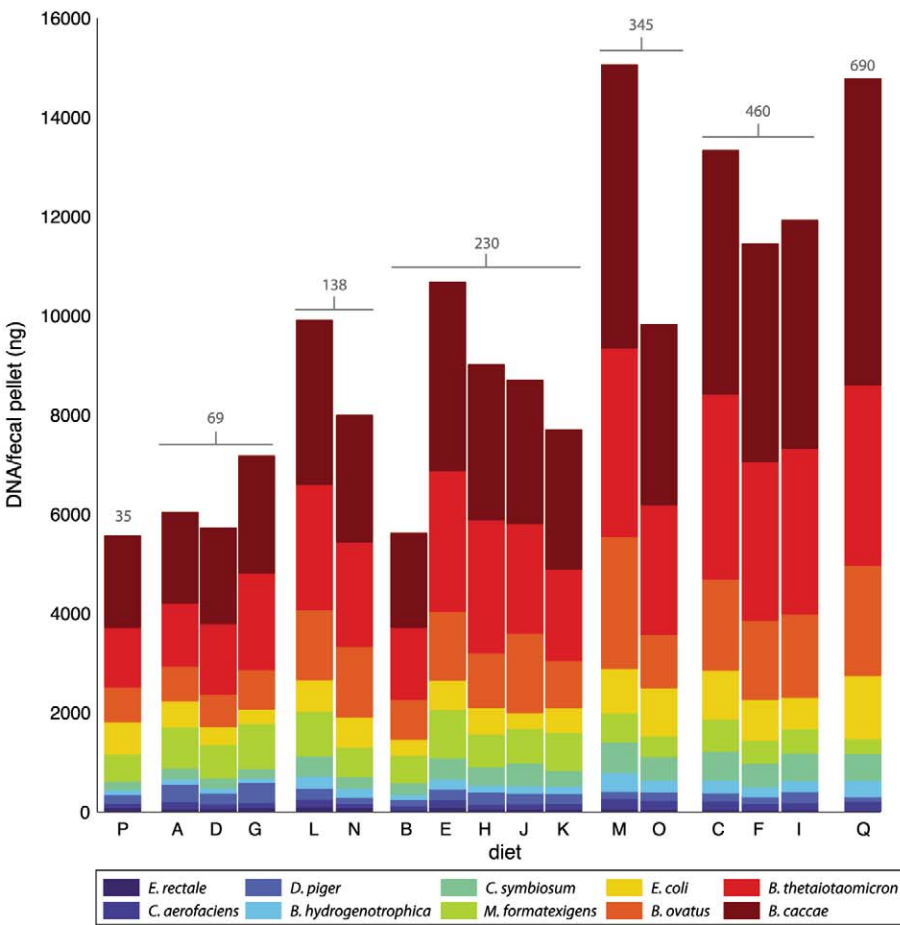


Fig. 2. Mean community member abundance for each diet. The height of each bar indicates the total DNA yield/biomass for a given diet. Casein concentrations (grams per kilogram) for each diet are displayed in gray above each bar. See fig. S1 and table S1 for a description of diets A to Q.

PLICITLY consider the effects of microbe-microbe or microbe-host interactions or diet order. We also tested several other models, including adding interactions between the variables, quadratic terms, and interactions with quadratic terms (13). After correcting for the number of parameters in the model by using Akaike infor-

mation criterion, the linear model was still the best-performing.

To further dissect the community response to these diet perturbations, we needed to infer which set of diet ingredients is associated with the abundance of each community member. Feature selection algorithms assume that the response

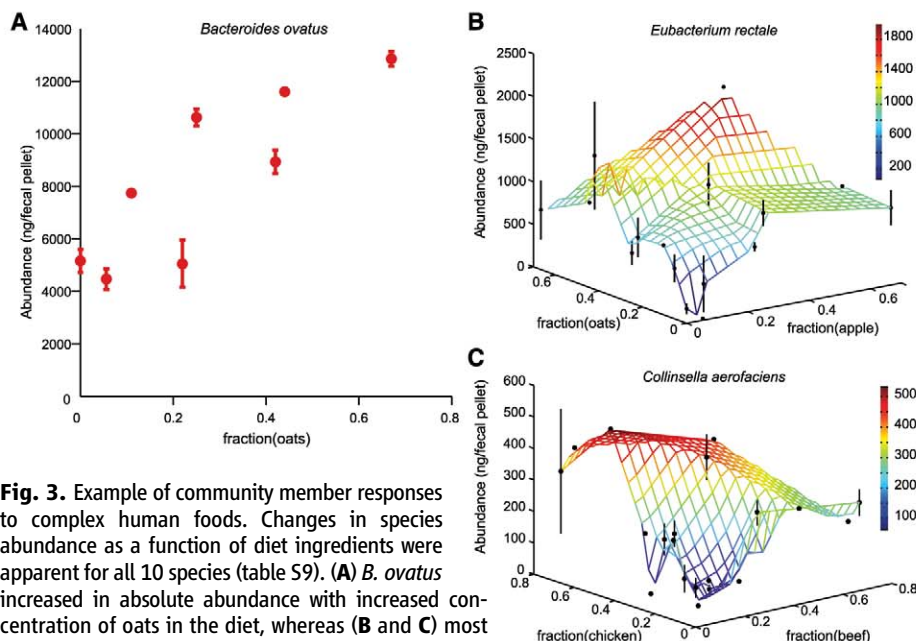


Fig. 3. Example of community member responses to complex human foods. Changes in species abundance as a function of diet ingredients were apparent for all 10 species (table S9). (A) *B. ovatus* increased in absolute abundance with increased concentration of oats in the diet, whereas (B and C) most of the 10 bacterial species (including *E. rectale* and *C. aerofaciens*) responded to multiple ingredients. The mean and standard error for all diets are plotted (no error bars are shown when replicate points are not available). The colored z axis mesh grid on the three-dimensional plots is a triangle-based linear interpolation of the data, with color changes corresponding to the values in the color bar on the right.

variable (in this case, the abundance of each organism) is potentially affected by only a fraction of the variables in the model and use statistical methods to choose the subset of variables that most informatively predict the abundance of each species. Using stepwise regression as a feature selection procedure with the equation above, all species in our 10-member community had the diet variable X_{casein} significantly associated with their abundance (table S3).

E. coli and *C. symbiosum* were the only bacteria with more than one variable significantly associated with their abundance (casein and sucrose for *E. coli*, and casein and starch for *C. symbiosum*). Further exploring this finding, we found casein highly correlated with the yield of total DNA per fecal pellet across all diets (Figs. 1A and 2). A component of casein, presumably amino acids and/or nitrogen, limits the biomass of the community: This resource limitation was observed even for combinations of three additional refined protein and two additional fat sources (soy, lactalbumin, egg-white solids, olive oil, and lard; $n = 9$ different diets given to another group of 9 C57Bl/6J male mice) (fig. S2 and table S4). However, the observed changes in species abundance are not a simple consequence of a constant relative abundance of each community member that is scaled upwards as casein is increased: Three community members (*E. rectale*, *D. piger*, and *M. formatexigens*) decreased in absolute abundance by ~ 25 to 50% from the low- to high-casein diets, even though total community biomass tripled (Fig. 1B, fig. S3, and table S5). Similar changes in species abundance and total com-

munity DNA levels were observed when casein concentrations were altered in gnotobiotic mice harboring a nine- or eight-member subset of the original community (minus *B. hydrogenotrophica* or minus *D. piger* and *B. hydrogenotrophica*) (table S6).

Microbial RNA-seq was used on fecal RNA samples—prepared from mice on each diet (mean = 2.1 ± 0.7 replicates per diet) (table S7) (13)—to determine whether perturbations in diet ingredients correlated with underlying changes in mRNA expression by community members. Each of the 36 RNA-seq data sets was composed of 36-nucleotide-long reads ($3.20 \pm 1.35 \times 10^6$ mRNA reads per sample). Transcript abundances were normalized for each of the 10 species to reads per kilobase per million (RPKM) (14). After correcting for multiple hypotheses, we found no statistically significant changes in gene expression within a given bacterial species as a function of any of the diet perturbations (13). Although community members do not appear to significantly alter their gene expression, they do respond by increasing or decreasing their absolute abundances (Fig. 2), adjusting the total available transcript pool in the microbiota for processing dietary components. For example, as casein levels are increased across the diets *B. caccae* increases its contribution to the gene pool/community transcriptome; so, the number of transcripts per unit of casein remains roughly constant.

Because RNA-seq provides accurate estimates of absolute transcript levels (15), we used transcript abundance information as a proxy to predict the major metabolic niches occupied by each community member. For species posi-

tively correlated with casein, we found high expression of mRNAs predicted to be involved in pathways using amino acids as substrates for nitrogen, as energy and/or as carbon sources. In contrast, the three species that negatively correlated with dietary casein concentration showed no clear evidence of high levels of expression of genes involved in catabolism of amino acids (13). The changes in abundance of the negatively correlated species (such as *E. rectale*) can be explained by competition with another member of the community that increases with casein (fig. S4) (13, 16).

The power of the refined diets we used lies in the capacity to precisely control individual diet variables and to aid data interpretation from more complex diets. To test whether the modeling framework we used generalizes to diets containing food more typically consumed in human diets, we created 48 meals consisting of random combinations and concentrations of four ingredients selected from a set of eight pureed human baby foods (apples, peaches, peas, sweet potatoes, beef, chicken, oats, and rice) (table S8). The meals were administered for periods of 7 days to the same eight gnotobiotic mice that we used for the follow-up refined diet experiments described above and in fig. S1E (13). Each mouse received a sequence of six baby-food diets. The order of presentation of the baby-food diets was varied between animals (table S8) (13). We measured the absolute abundance of each bacterial community member on days 1, 5, 6, and 7 for each diet. Using the linear modeling approach described above (13), we were able to explain over half of the variation in species abundance using only knowledge of the concentrations of the pureed foods present in each meal ($R^2 = 0.62$). We used stepwise regression to identify the type of pureed food (or foods) present in a given mixed meal that was most significantly associated with changes in each bacterial species (Fig. 3 and table S9).

Defining the interrelationship between diet and the structure and operations of the human gut microbiome is key to advancing our understanding of the nutritional value of food, for creating new guidelines for feeding humans at various stages of their life span, for improving global human health, and for developing new ways to manipulate the properties of the microbiota so as to prevent or treat various diseases. The experiments and model described above highlight the extent to which host diet can explain the configuration of the microbiota, both for refined diets in which all of the perturbed diet components are digestible by the host and for human diets whose ingredients are only partially known. These models can now be tested by using larger defined gut microbial communities representing those of humans living in different cultural settings, and with more complex diets, including various combinations of food ingredients that they consume.

References and Notes

- R. E. Ley, P. J. Turnbaugh, S. Klein, J. I. Gordon, *Nature* **444**, 1022 (2006).
- T. A. Clayton, D. Baker, J. C. Lindon, J. R. Everett, J. K. Nicholson, *Proc. Natl. Acad. Sci. U.S.A.* **106**, 14728 (2009).
- R. J. Xavier, D. K. Podolsky, *Nature* **448**, 427 (2007).
- J. Qin *et al.*, *Nature* **464**, 59 (2010).
- P. J. Turnbaugh *et al.*, *Proc. Natl. Acad. Sci. U.S.A.* **107**, 7503 (2010).
- P. J. Turnbaugh *et al.*, *Sci. Transl. Med.* **1**, 6ra14 (2009).
- B. D. Muegge *et al.*, *Science* **332**, 970 (2011).
- J. Handelsman, *DNA Cell Biol.* **27**, 219 (2008).
- J. J. Faith *et al.*, *ISME J.* **4**, 1094 (2010).
- F. E. Rey *et al.*, *J. Biol. Chem.* **285**, 22082 (2010).
- M. A. Mahowald *et al.*, *Proc. Natl. Acad. Sci. U.S.A.* **106**, 5859 (2009).
- A. L. Goodman *et al.*, *Cell Host Microbe* **6**, 279 (2009).
- Materials and methods are available as supporting material on *Science* Online.
- A. Mortazavi, B. A. Williams, K. McCue, L. Schaeffer, B. Wold, *Nat. Methods* **5**, 621 (2008).
- X. Fu *et al.*, *BMC Genomics* **10**, 161 (2009).
- J. M. Chase, M. A. Leibold, *Ecological Niches: Linking Classical and Contemporary Approaches (Interspecific Interactions)* (University of Chicago Press, Chicago, 2003).

Acknowledgments: We are indebted to D. O'Donnell, M. Karlsson, and S. Wagoner for their help with various aspects of gnotobiotic mouse husbandry and to B. Mickelson, I. Mogno, A. Goodman, N. Griffin, H. Seedorf, G. Simon, J. Chase, and B. Cohen for their many helpful suggestions during the course of this work. This work was supported by grants from NIH

(DK30292 and DK70977) and the Crohn's and Colitis Foundation of America. COPRO-seq and microbial RNA-seq data are available in the Gene Expression Omnibus (accession GSE26687). Processed data can be obtained at http://gordonlab.wustl.edu/modeling_microbiota/.

Supporting Online Material

www.sciencemag.org/cgi/content/full/science.1206025/DC1
Materials and Methods
SOM Text
Figs. S1 to S5
Tables S1 to S13
References

24 March 2011; accepted 28 April 2011

Published online 19 May 2011;

10.1126/science.1206025

Oxytocin Selectively Gates Fear Responses Through Distinct Outputs from the Central Amygdala

Daniele Viviani,¹ Alexandre Charlet,¹ Erwin van den Burg,^{1*} Camille Robinet,^{1*} Nicolas Hurni,¹ Marios Abatis,¹ Fulvio Magara,¹ Ron Stoop^{1,2†}

Central amygdala (CeA) projections to hypothalamic and brain stem nuclei regulate the behavioral and physiological expression of fear, but it is unknown whether these different aspects of the fear response can be separately regulated by the CeA. We combined fluorescent retrograde tracing of CeA projections to nuclei that modulate fear-related freezing or cardiovascular responses with in vitro electrophysiological recordings and with in vivo monitoring of related behavioral and physiological parameters. CeA projections emerged from separate neuronal populations with different electrophysiological characteristics and different response properties to oxytocin. In vivo, oxytocin decreased freezing responses in fear-conditioned rats without affecting the cardiovascular response. Thus, neuropeptidergic signaling can modulate the CeA outputs through separate neuronal circuits and thereby individually steer the various aspects of the fear response.

Fear can be severely immobilizing but can also be a major driving force for some of humans' most heroic acts. In both cases,

the internal emotional experience may be similar, although it may lead to substantially different behavioral outcomes (1–3). Studies on human

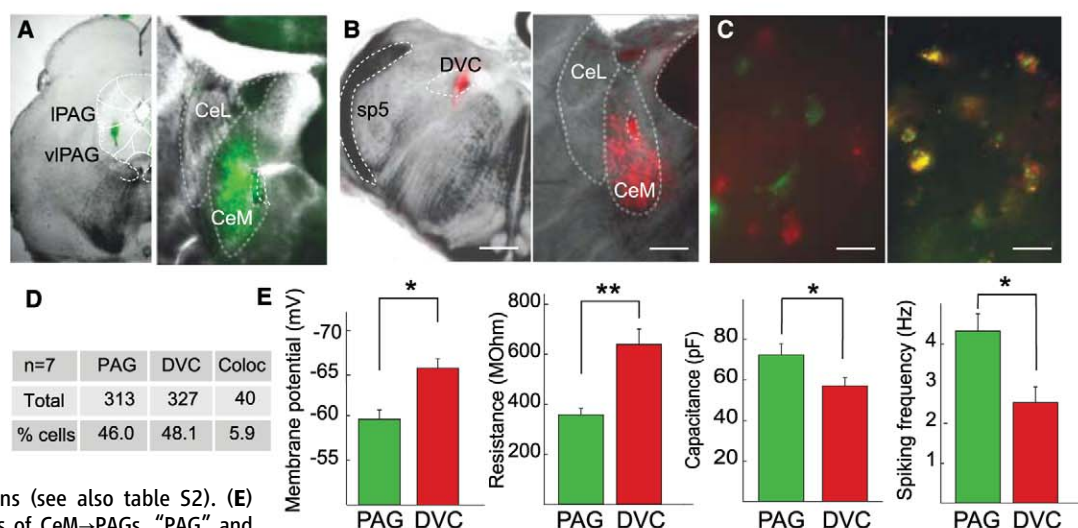
emotions often use autonomic nervous system parameters to assess arousal, because of the role of our internal organs in the emotional state (4, 5). Projections from the central nucleus of the amygdala (CeA) to the hypothalamus and different brain stem nuclei coordinate behavioral and physiological fear expression (6). It has been postulated that different fear responses, characterized by more active or passive behavioral coping strategies, can be triggered by a neuronal switch within the CeA (7). The question thus arises whether fear responses only vary in intensity, or whether different qualities of fear responses exist, reflected in different associations between behavioral and physiological components. We investigated whether a neurophysiological basis for such a distinct regulation could be found in the CeA.

¹Centre for Psychiatric Neuroscience, Department of Psychiatry, Lausanne University Hospital Center, University of Lausanne, CH-1015 Lausanne, Switzerland. ²Department of Physiology, University of Lausanne, CH-1015 Lausanne, Switzerland.

*These authors contributed equally to this work.

†To whom correspondence should be addressed. E-mail: rstoop@unil.ch

Fig. 1. Distinct neuronal populations of the CeM project to PAG and DVC. (A and B) Coronal views of injection sites (A) in PAG of fluorescent green and (B) in DVC of red microspheres (left), corresponding CeM labeling (right). Scale bars: left, 1 mm; right, 500 μ m. IPAG, lateral PAG; vIPAG, ventrolateral PAG; sp5, spinal trigeminal tract. (C) Separately labeled CeM neurons after coinjections of green and red microspheres in respective PAG and DVC (left) versus colabeled neurons after injections of both microspheres in DVC (right, scale bar, 50 μ m). (D) Quantification of colabeled (coloc) CeM neurons (see also table S2). (E) Electrophysiological characteristics of CeM→PAGs, "PAG" and CeM→DVCs "DVC." (* P < 0.05; ** P < 0.01, n = 22 to 43 neurons) Error bars indicate SEM.



Most projections from the CeA to the hypothalamus and brain stem nuclei originate from the medial part of the CeA (CeM) (6). Oxytocin can inhibit neurons in the CeM through its excitatory effects on γ -aminobutyric acid (GABA) inhibitory (GABAergic) projections that originate from the lateral and capsular part of the CeA (8) (henceforth referred to as CeL). The CeL contains distinct neuronal populations (7–10) whose individual activation may differentially regulate active versus passive fear responses (7). Can a similar distinction of neuronal popula-

tions be found in the CeM (10)? Do projections from the CeM to selective targets in the hypothalamus and brain stem arise from distinct neuronal populations and, if so, are these under a specific inhibitory control from the CeL? Such specificity might provide a neurophysiological basis within the CeA to selectively regulate behavioral and physiological components of the fear response.

We first evaluated the target specificity of CeM projections by double fluorescent retrograde tracing of the ventrolateral column of the peri-

aqueductal gray (PAG), which is implicated in the freezing response (6), and the dorsal vagal complex (DVC), which modulates cardiovascular responses (11). We injected green and red fluorescent latex microspheres, respectively, into the PAG and DVC of 3- to 4-week-old Sprague-Dawley rats (12, 13). After allowing 48 hours of retrograde transport, we killed the animals, verified the injection sites (Fig. 1, A and B), and assessed retrograde label in horizontal brain slices of the CeM. Both green and red microspheres were present throughout the CeM (Fig. 1, A and B), yet in separate neurons that were intermingled without any obvious clusters (Fig. 1C and fig. S1). Confocal quantification revealed 5.9% colabeling ($n = 680$ neurons, Fig. 1D, fig. S1, and table S1). Injecting a mixture of green and red microspheres in the DVC resulted in their copresence in all labeled CeM neurons (Fig. 1C), confirming sensitivity to detect colabeling.

We next compared electrophysiological properties by whole-cell recordings from fluorescently labeled PAG- and DVC-projecting neurons (henceforth called CeM→PAGs and CeM→DVCs, respectively). CeM→PAGs ($n = 42$) were, on average, significantly more depolarized (-59.6 ± 1.6 versus -65.4 ± 1.2 mV) and had lower membrane resistance (358 ± 25 versus 640 ± 61 M Ω) and higher membrane capacitance (72.3 ± 5.6 versus 58.5 ± 4.0 pF) than CeM→DVCs ($n = 43$, Fig. 1E). In cell-attached configuration, average basic spiking frequencies of CeM→PAGs ($n = 22$) were significantly higher than CeM→DVCs (4.1 ± 0.5 versus 2.5 ± 0.4 Hz, $n = 28$).

Prompted by these anatomical and electrophysiological differences, we also tested their pharmacological characteristics. Although both projection neurons were similarly excited or inhibited by a range of neuropeptides (table S2), oxytocin—known to increase spontaneous inhib-

Fig. 2. Distinct effects of TGOT on CeM→DVC and CeM→PAG neurons. (A and B) Representative traces of sIPSCs (top) and their average frequencies (bottom) recorded before (control) and after (TGOT) application of (A) CeM→PAGs and (B) CeM→DVCs. (C and D) The same for spontaneous spiking activity (* $F_{2,36} = 8.4$, $P < 0.005$; ** $F_{2,122} = 17.8$, $P < 0.0001$, $n = 20$ to 34 neurons) Error bars indicate SEM.

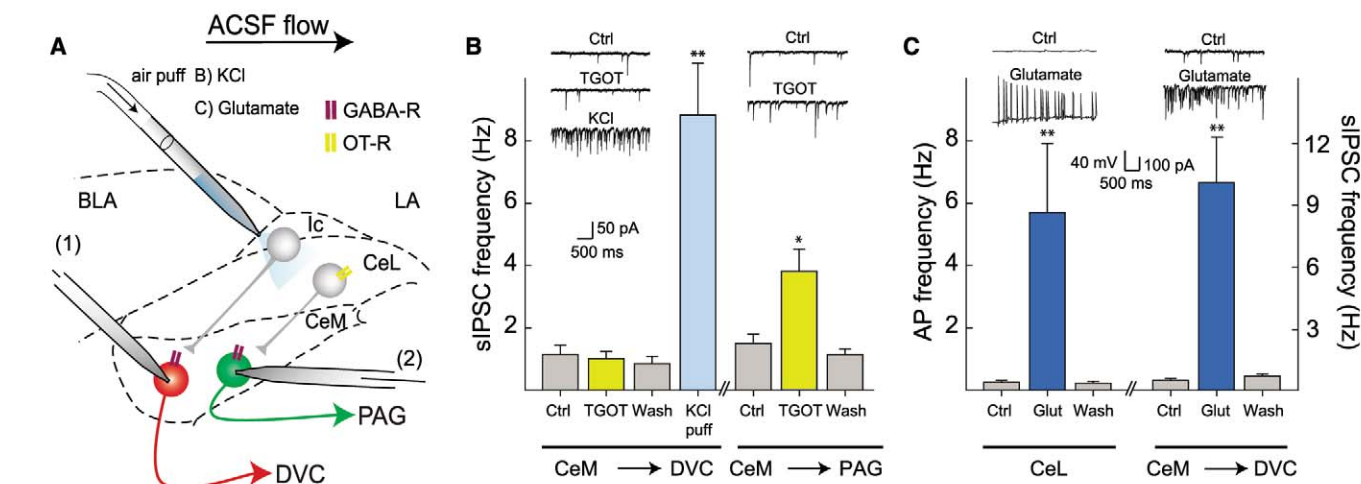
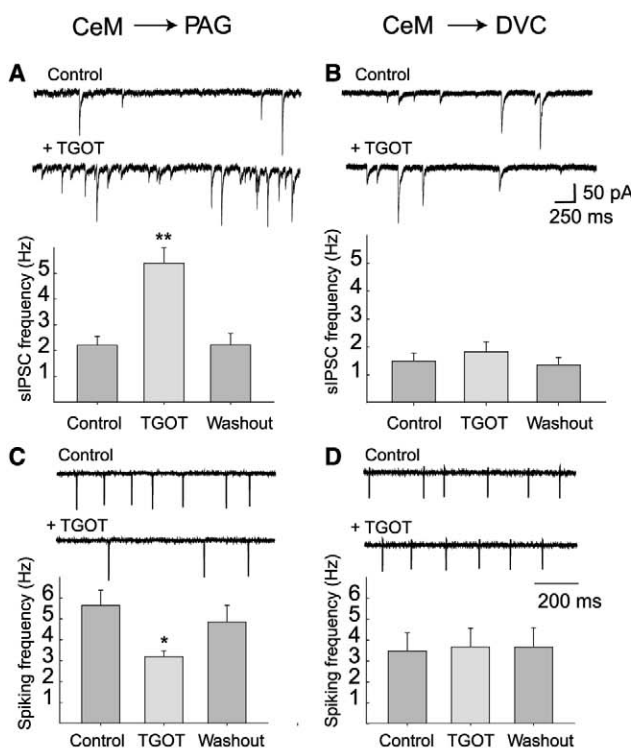


Fig. 3. Local stimulation reveals inhibitory projections on TGOT-insensitive CeM→DVCs. (A) Local perfusion of neurons that project to CeM→DVCs (red) and CeM→PAGs (green) in a horizontal brain slice of the CeA with ACSF flow away from CeM. GABA-R, GABA_A receptor; OT-R, oxytocin receptor; BLA, basolateral amygdala; LA, lateral amygdala; Ic, Intercalated neurons. (B) Average sIPSC frequencies in CeM→DVCs recorded with patch pipette “(1)”

after bath-perfused TGOT followed by locally puffed KCl ($n = 6$), subsequently, in the same slice, in CeM→PAGs recorded with pipette “(2)” after bath-perfused TGOT ($n = 6$). (C) Action potential and sIPSC frequencies in respective CeL ($n = 5$) and CeM→DVC neurons ($n = 5$) after local perfusion with glutamate. (* $P < 0.05$, ** $P < 0.005$) Error bars indicate SEM.

itory postsynaptic current (sIPSC) frequencies of CeM neurons (8) (fig. S2A)—only affected CeM→PAGs. Thus, bath perfusion of the oxytocin agonist [Thr⁴,Gly⁷]-oxytocin (TGOT) specifically and reversibly increased sIPSC frequencies in CeM→PAGs (from 2.2 ± 0.3 to 5.6 ± 0.7 Hz, $n =$

34) (Fig. 2A) but not in CeM→DVCs (from 1.5 ± 0.3 to 1.7 ± 0.2 Hz, $n = 32$) (Fig. 2B) (see also fig. S3). In cell-attached recordings, this translated into a selective inhibition of spontaneous spiking frequencies of CeM→PAGs (from 5.6 ± 0.7 to 3.1 ± 0.2 Hz, $n = 10$) (Fig. 2C) versus

CeM→DVCs (from 3.5 ± 1.0 to 3.7 ± 0.9 Hz, $n = 10$) (Fig. 2D) (8).

To verify whether the failure of TGOT to inhibit CeM→DVCs was caused by the absence of inhibitory projections, we locally depolarized by puffing KCl (35 mM) from a patch pipette (13)

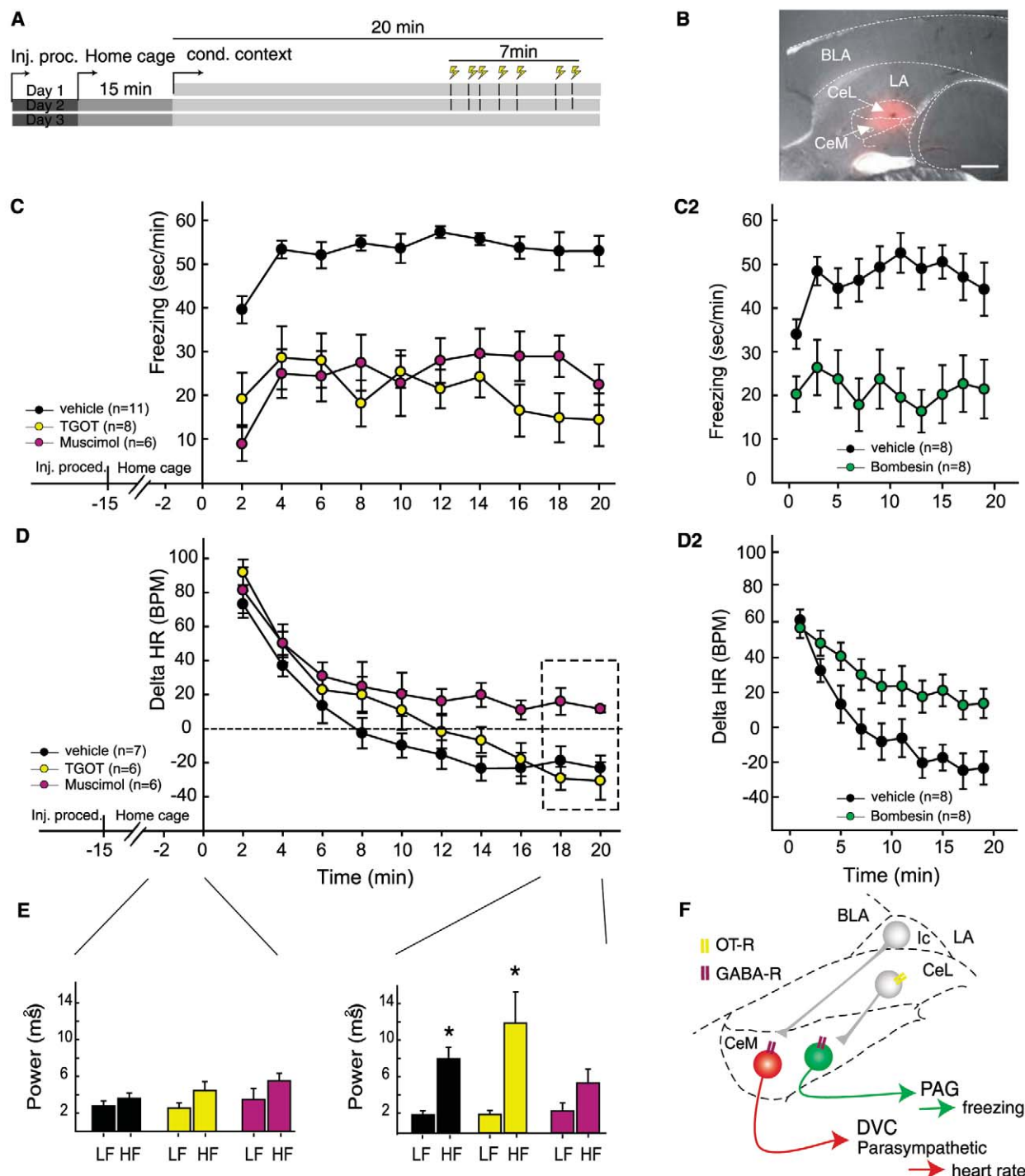


Fig. 4. Differential effects of drugs injected in the CeA on freezing and heart rate during a conditioned fear response. **(A)** Three-day fear-conditioning protocol: Inj. proc, sham injection procedure; yellow lightings, electric shocks. **(B)** Postmortem analysis showing fluorescent muscimol Bodipy diffusion inside the CeA. Scale bar, 1 mm. **(C)** Freezing responses measured on day 3 in the context alone. **(D)** The same for heart rate responses [D

(left): $F_{2,16} = 3.8$, $P < 0.05$; D2: $F_{1,14} = 5.3$, $P < 0.05$]. **(E)** Power spectrum histograms of HRV -2 to 0 min before and 18 to 20 min after placing rats in conditioning context. LF, low-frequency component; HF, high-frequency component. Error bars indicate SEM (* $P < 0.05$). **(F)** Final model illustrating specific TGOT-inhibited freezing through selective inhibition of CeM→PAGs. Abbreviations as in (Fig. 3A).

(Fig. 3A) and simultaneously recorded sIPSCs from CeM→DVCs. Although bath-perfused TGOT did not affect sIPSC frequencies (from 1.2 ± 0.3 to 1.0 ± 0.2 Hz, $n = 6$), rapid increases occurred with KCl puffs at distinct locations in the CeL (from 0.9 ± 0.2 to 8.4 ± 1.6 Hz, $n = 6$) (Fig. 3B). In the same slice, TGOT remained capable of increasing sIPSC frequencies in CeM→PAGs (from 1.5 ± 0.3 to 3.8 ± 0.7 Hz, $n = 6$) (Fig. 3C). Puffing glutamate (Fig. 3C) or bombesin (fig. S4), for which receptors are expressed in the CeL and adjacent intercalated inhibitory neurons, gave similar results, which suggested an activation of inhibitory projections arising from either of these regions [discussed further in (13)].

To investigate how these specific in vitro effects of oxytocin translated in vivo into fear-induced freezing behavior (mediated by the PAG) (6, 14) and cardiovascular changes (modulated by the DVC) (11, 15), we equipped rats with bilateral cannulae for local drug administration into the CeA and implanted radiotelemetric devices to monitor heart rate. To activate the amygdala, we applied a 2-day contextual fear-conditioning protocol (13) that resulted in >90% freezing after conditioning and >80% freezing responses upon reexposure to the context in all vehicle-injected animals (Fig. 4, A and C, and fig. S2B). Bilateral injection of TGOT or GABA_A receptor agonist muscimol decreased these freezing responses to <50% (Fig. 4C). In rats where TGOT had not decreased freezing, the injection sites, identified with fluorescent muscimol (Fig. 4B), were outside the CeA (fig. S5), which confirmed the CeA role in these contextual freezing responses [further discussed in (13)]. Although baseline heart rate before reexposure and the initial elevation in heart rate upon reexposure to the context were similar for all groups [baseline: artificial cerebrospinal fluid (ACSF) 400 ± 10 ; TGOT 394 ± 10 ; muscimol 394 ± 12 beats per min (bpm)] (Fig. 4D), the typical decrease that followed in the second 10-min period was inhibited by muscimol but not by TGOT. Bombesin reduced freezing and prevented the decrease in heart rate (Fig. 4C2 and 4D2) consistent with its inhibition of both CeM→PAGs and CeM→DVCs. Together, these data not only support the selective action of oxytocin on freezing behavior via CeM→PAGs, but also suggest a critical role of CeM→DVC neurons in the control of cardiovascular changes to fearful stimuli. Finally, heart rate variability (HRV) analysis (13) revealed an absence of increase in the high frequency band in the muscimol-treated rats (Fig. 4E), which indicated an inhibition of the parasympathetic activation (13) (table S3 and fig. S7). The failure of TGOT to affect this parasympathetic cardiovascular response is consistent with the absence of TGOT effects on CeM→DVCs (11, 15).

The present findings provide evidence that specific behavioral and physiological components of the fear response are controlled by distinct neuronal populations in the CeM (Fig. 4F). These project to the PAG and the DVC; exhibit

unique electrophysiological characteristics; and despite being spatially intermingled, are selectively modulated by oxytocin through inhibitory projections from the CeL. The functionality of this selectivity was further revealed at the behavioral and physiological level by oxytocin's inhibition of freezing responses without affecting cardiovascular changes. Previous studies have distinguished neuronal populations in the CeL on the basis of expression of CRF or opioids (16) or on mutually inhibitory connections (10). These may play a specific role in the inhibition of CeM→PAGs, and, in combination with the distinct electrophysiological characteristics of CeM neurons, affect further local information processing [see e.g., (17)].

A specific regulation by the CeL of CeM neurons with different projections could have important implications for the mechanisms underlying the expression of fear. Distinct neuronal populations in the CeL are activated or inhibited during the expression of fear (9, 10) and this might represent a switch between active versus passive fear and associated coping strategies (7). Our present findings imply that the CeM differentially controls expressions of the fear response through separate projections to the brain stem. Our findings, instead of supporting a rigid association between behavioral and physiological expressions of fear (1, 2), suggest that these expressions may be specifically controlled by the CeL. This underlines, first, the importance of considering multiple parameters in the correct assessment of fear responses in animals, but it also opens the potential for new therapeutic applications (fig S8). In humans, panic disorder can manifest itself at the visceral level predominantly by increases in heart rate, respiratory rhythm, or gastrointestinal motility (18). While its onset appears to be triggered in the lateral and basal amygdala (19), its specific expression may result from a differential gating within the CeA. Although panic and other anxiety disorders are typically treated with benzodiazepines, future neuropeptide-based therapies might offer a more precise inhibition of their expression.

The amygdala orchestrates behavioral responses to both negative (fearful) and positive (rewarding) salient stimuli (20, 21), although the precise underlying circuits are still unclear. Distinct, intercalated CeL and CeM populations, targeted by projections from the basolateral amygdala (22) and brain stem (11), could play a role in regulating behavioral and physiological expressions associated with different emotions (3–5). Furthermore, the CeA expresses a multitude of neuropeptide receptors that can specifically affect local activity (8, 23–25). Levels of oxytocin and its receptors can vary between individual rats according to genetic background (26), early life experience (27), internal state (28), or environment (24, 29) and have been associated with different degrees of anxiety and fear (27). As we found that oxytocin decreases freezing responses, yet leaves cardiovascular responses unaffected,

this specific regulation could preserve the internal, visceral expression of fear, but alleviate the behavioral inhibition that leads to freezing. Such individual regulation may provide the most adequate reaction in circumstances when a proactive behavioral response is required, while preserving an internal, visceral adaptive response to fear.

References and Notes

1. J. LeDoux, *Cell. Mol. Neurobiol.* **23**, 727 (2003).
2. M. Davis, in *The Amygdala*, J.P. Aggleton, Ed. (Wiley-Liss, NY, 1992), pp. 255–306.
3. S. W. Porges, *Ann. N.Y. Acad. Sci.* **1008**, 31 (2003).
4. E. P. Vianna, D. Tranel, *Int. J. Psychophysiol.* **61**, 70 (2006).
5. P. Rainville, A. Bechara, N. Naqvi, A. R. Damasio, *Int. J. Psychophysiol.* **61**, 5 (2006).
6. J. E. LeDoux, J. Iwata, P. Cicchetti, D. J. Reis, *J. Neurosci.* **8**, 2517 (1988).
7. A. Gozzi et al., *Neuron* **67**, 656 (2010).
8. D. Huber, P. Veinante, R. Stoop, *Science* **308**, 245 (2005).
9. S. Ciochi et al., *Nature* **468**, 277 (2010).
10. W. Haubensack et al., *Nature* **468**, 270 (2010).
11. A. D. Loewy, in *Central Regulation of Autonomic Functions*, A. D. Loewy and K. M. Spyer Eds. (Oxford Univ. Press, New York, 1990), pp. 88–103.
12. L. C. Katz, A. Burkhalter, W. J. Dreyer, *Nature* **310**, 498 (1984).
13. Further information including materials and methods is available as supporting material on Science Online.
14. T. M. da Costa Gomez, M. M. Behbehani, *Brain Res.* **689**, 21 (1995).
15. J. S. Schwaber, B. S. Kapp, G. A. Higgins, P. R. Rapp, *J. Neurosci.* **2**, 1424 (1982).
16. H. E. Day, E. J. Curran, S. J. Watson Jr., H. Akil, *J. Comp. Neurol.* **413**, 113 (1999).
17. E. C. Dumont, M. Martina, R. D. Samson, G. Drolet, D. Paré, *Eur. J. Neurosci.* **15**, 545 (2002).
18. R. A. Sansone, L. A. Sansone, *Psychiatry* **6**, 33 (2009).
19. A. E. Ziemann et al., *Cell* **139**, 1012 (2009).
20. J. J. Paton, M. A. Belova, S. E. Morrison, C. D. Salzman, *Nature* **439**, 865 (2006).
21. K. M. Tye, G. D. Stuber, B. de Ridder, A. Bonci, P. H. Janak, *Nature* **453**, 1253 (2008).
22. K. M. Tye et al., *Nature* **471**, 358 (2011).
23. B. C. Chieng, M. J. Christie, P. B. Osborne, *J. Comp. Neurol.* **497**, 910 (2006).
24. T. J. Sajdyk, A. Shekhar, D. R. Gehlert, *Neuropeptides* **38**, 225 (2004).
25. A. Bisetti et al., *Neuroscience* **142**, 999 (2006).
26. O. J. Bosch, S. L. Meddle, D. I. Beiderbeck, A. J. Douglas, I. D. Neumann, *J. Neurosci.* **25**, 6807 (2005).
27. F. A. Champagne, M. J. Meaney, *Biol. Psychiatry* **59**, 1227 (2006).
28. M. M. McCarthy, C. H. McDonald, P. J. Brooks, D. Goldman, *Physiol. Behav.* **60**, 1209 (1996).
29. M. Waldherr, I. D. Neumann, *Proc. Natl. Acad. Sci. U.S.A.* **104**, 16681 (2007).

Acknowledgments: We thank E. Welker for outstanding scientific advice; H. Markram and R. Perin for expert help with multiple patch recordings; R. Daniel and D. Rainnie for feedback on the manuscript; and O. Bussard, V. Martin, N. Pochon and L. Bonsignore for technical support. Supported by Swiss National Science Foundation grant 3100A0-116462.

Supporting Online Material

www.sciencemag.org/cgi/content/full/333/6038/104/DC1
Materials and Methods
SOM Text
Figs. S1 to S8
Tables S1 to S3
References

30 November 2010; accepted 25 May 2011
10.1126/science.1201043

Following the Crowd: Brain Substrates of Long-Term Memory Conformity

Micah Edelson,^{1*} Tali Sharot,² Raymond J. Dolan,² Yadin Dudai¹

Human memory is strikingly susceptible to social influences, yet we know little about the underlying mechanisms. We examined how socially induced memory errors are generated in the brain by studying the memory of individuals exposed to recollections of others. Participants exhibited a strong tendency to conform to erroneous recollections of the group, producing both long-lasting and temporary errors, even when their initial memory was strong and accurate. Functional brain imaging revealed that social influence modified the neuronal representation of memory. Specifically, a particular brain signature of enhanced amygdala activity and enhanced amygdala-hippocampus connectivity predicted long-lasting but not temporary memory alterations. Our findings reveal how social manipulation can alter memory and extend the known functions of the amygdala to encompass socially mediated memory distortions.

Our memories are often inaccurate. Ubiquitous sources of false recollection are social pressure and interpersonal influence (1–4). This phenomenon, dubbed “memory conformity” (4), is encountered in a variety of contexts, including social interactions, mass media exposure, and eyewitness testimony. In such settings an individual may change veridical recollections of past events to match a false account provided by others (1–6). Although these social influences on memory have been extensively demonstrated (1–5), the underlying neurobiology of this process is unknown.

Conformity may present in two forms, which initially convey similar explicit behavior but are fundamentally different (7, 8). In one type, known as private conformity, an individual’s recollection may genuinely be altered by social influence, resulting in long-lasting, persistent memory errors (1, 4, 5, 7). In such circumstances, even when social influence is removed, the individuals will persist in claiming an erroneous memory as part of their own experience (7, 9). Private conformity could hence be considered a bona fide memory change. In the second type, known as public conformity, individuals may choose to outwardly comply, providing an account that fits that of others, but inwardly maintain certitude in their own original memory. Public conformity can be dispelled when the veracity of the socially transferred information abates (7, 10, 11). Thus, errors induced by public conformity are transient (7, 9) and appear to represent a change in behavior in the absence of lasting alterations to a memory engram.

Although private and public memory conformity are often behaviorally indistinguishable, they reflect different cognitive processes (7, 8). These processes are probably mediated by distinct activation in interconnected brain circuits

previously found to be active in mnemonic functions and social cognition (such as the hippocampal complex, amygdala, and frontal regions) (12–18). Here, we set out to characterize the brain mechanisms that lead to both types of conformity.

Our experimental protocol included four phases spanning a 2-week period (Fig. 1A). Thirty adult participants (12 females, age 28.6 ± 0.8 , mean \pm SEM) viewed an eyewitness-style documentary on a large screen in groups of five. Three days after viewing, participants returned to the lab individually and completed a memory test (test 1). Test 1 served to assess the participants’ baseline accuracy and confidence before the manipulation stage. Four days later, participants returned to the lab and answered the same memory questions while being scanned with functional magnetic resonance imaging (fMRI) (test 2). On this occasion, a manipulation was introduced in an attempt to induce conformity.

Before responding during this test, participants were presented with answers they were led to believe were given by their four fellow co-observers, whose photographs were provided with their corresponding answers (Fig. 1A). In a subset of trials, for which the target participant originally had a confident veridical memory (as identified by test 1), the answers provided by the four co-observers were all false (manipulation condition, 80 questions). In matched control trials, the letter X was presented instead of the co-observers’ answers (no-manipulation condition, 25 questions). Pilot data indicated that the use of manipulation and no-manipulation conditions alone would raise suspicion in the participants’ minds that the answers given by the co-observers were fabricated. Therefore we added credibility trials in which different patterns of co-observer answers were provided (Fig. 1B).

One week later, the participants returned to the lab and were informed that the answers given by the co-observers during the previous fMRI session were in fact determined randomly. This rendered the socially conveyed information previously provided as uninformative. The participants were then requested to com-

plete the memory test again (test 3) based on their original memory of the movie. Finally, the participants were debriefed. Participants with excessive head movements in the scanner or suspected brain pathology and those that indicated suspicion of the manipulation were excluded from the analysis, resulting in a final number of participants (N) = 20.

Our behavioral data revealed that our manipulation induced memory errors (Fig. 2A). Strikingly, participants conformed to the majority opinion in $68.3 \pm 2.9\%$ of manipulation trials, giving a false answer to questions they had previously answered correctly with relatively high confidence. This was not due to forgetting, because in the no-manipulation condition, incorrect answers were given in only $15.5 \pm 1.7\%$ of the questions [Student’s t test (df 19) = 16.9, $P < 10^{-7}$]. When social influence was removed (test 3), participants reverted to their original correct answer in $59.2 \pm 2.3\%$ of the previously conformed trials (transient errors) but maintained erroneous answers in 40.8% (persistent errors). Confidence ratings in persistent and transient errors did not differ either before or after the manipulation stage (Fig. 2B). During the manipulation stage, confidence ratings in transient errors were significantly lower than in persistent errors [t (19) = 6.9, $P < 10^{-5}$]. Differences in confidence levels were controlled for in the fMRI analysis by means of a covariate [supporting online material (SOM)].

Our brain imaging data indicated that at the time of exposure to social influence, distinct brain signatures characterized instances of memory conformity that would result in persistent and transient errors. We first performed analysis on a priori anatomically defined regions of interest (ROIs) selected by virtue of being widely implicated in memory encoding and maintenance (the bilateral anterior hippocampus, bilateral posterior hippocampus, and bilateral parahippocampal gyrus) and in social-emotional processing (bilateral amygdala) (12–25). Brain activity was averaged across all voxels in each ROI for the three conditions of interest (persistent errors, transient errors, and instances when participants did not conform to the erroneous information; i.e., nonconformity). In all regions, except for the left posterior hippocampus, the blood oxygen level-dependent (BOLD) signal was greater during trials that subsequently resulted in persistent memory errors relative to trials that resulted in transient errors or nonconformity (Fig. 3A). No significant difference was found between transient error and nonconformity trials in these regions.

To examine whether other brain regions differentiate between persistent and transient errors, we conducted a whole-brain exploratory analysis. Greater activity during trials resulting in persistent errors versus trials resulting in transient errors was found in four regions, all in the medial temporal lobe (MTL, Fig. 3B): the left amygdala (–22, –8, –10), right hippocampus (28, –22, –12), right parahippocampal gyrus (PHG, 36, –48, –10), and a region bordering the left PHG and occipital

¹Department of Neurobiology, Weizmann Institute of Science, Israel. ²Wellcome Trust Centre for Neuroimaging, Institute of Neurology, University College London, London, UK.

*To whom correspondence should be addressed. E-mail: micah.edelson@weizmann.ac.il

cortex ($-22, -54, -10$), [$P < 0.001$, cluster threshold (k) > 10]. In the opposite comparison (transient versus persistent errors), enhanced activation was found in the bilateral dorsal anterior cingulate cortex (ACC, Brodmann area 32; $-12, 22, 42$; $8, 20, 46$).

A striking activation in both aforementioned analyses was found in the left amygdala. A behavioral control study (SOM) indicated that elevated activation in the amygdala during trials that resulted in persistent errors was not due to heightened emotional arousal during these trials. Nor were these errors related to questions associated with greater emotional content. Rather,

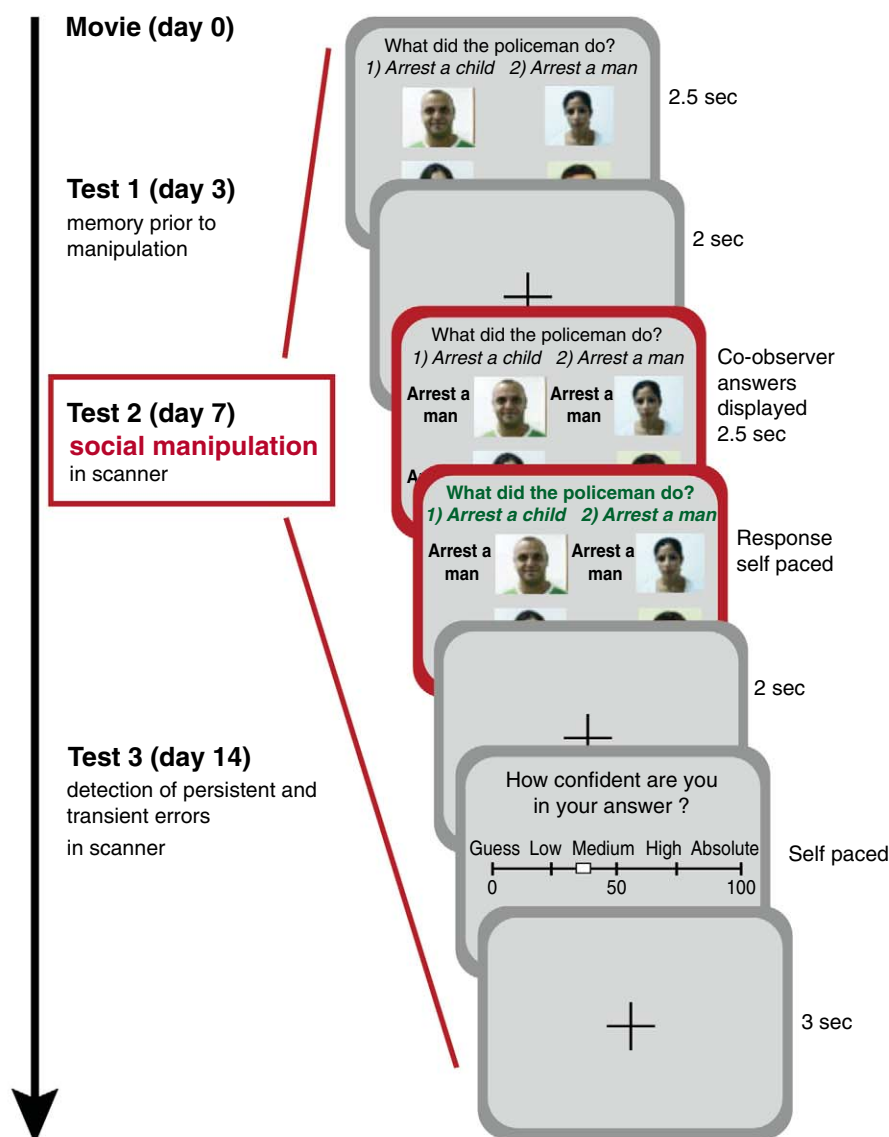
heightened amygdala activation seemed specific to socially induced memory change.

The amygdala plays a key role in social and emotional processing and modulates memory-related hippocampal activity (13–23). It is strategically placed for this function, having rich anatomical connections with the hippocampal complex (the anterior hippocampus in particular) as well as with neocortical areas (13–16, 23, 26). The amygdala is thus a prime candidate for mediating social effects on memory, most likely involving its interactions with other brain regions (13, 14). This consideration motivated us

to carry out a functional connectivity analysis, using a psychophysiological interaction (PPI) approach (27). This analysis showed heightened functional connectivity between the left amygdala and bilateral anterior hippocampus within anatomically defined ROIs, during trials that subsequently resulted in persistent memory errors as opposed to transient errors and nonconformity (Fig. 4A).

We also sought to identify which brain regions responded to the information presented by the co-observers (SOM). To this end, trials in which misleading information was presented

A Protocol



B Experimental conditions

Manipulation



No-manipulation



Credibility



(correct answer = arrest a child)

Fig. 1. Experimental outline. (A) Participants viewed the movie in groups of five and subsequently performed three memory tests individually. Test 1 served to assess the participants' initial memory and confidence before the social manipulation administered in test 2. Test 3 served to identify memory errors that persisted after the social manipulation was removed. For the test 2 scanning session, the question and possible answers were presented for 2.5 s, followed by the fabricated co-observers' answers for

2.5 s. Subsequently, a font color change indicated that the participants were allowed to respond. Finally, confidence ratings were provided. (B) Illustration of the different experimental conditions: the manipulation condition in which all co-observers' answers were incorrect, the no-manipulation condition in which the letter X was displayed instead of co-observers' answers, and the credibility condition in which variable patterns of co-observers' answers were displayed (SOM).

(the manipulation condition) were contrasted with the no-manipulation condition. Five regions (fig. S1A) were identified in the frontal and occipital cortex. Further analysis of brain activity in these regions (fig. S1B) suggests that they are involved in non-mnemonic processes, such as conflict monitoring (28–31) in the face of competing memories (32–34).

Were our findings driven merely by the presentation of additional information regardless of social context? To answer this question, we performed a control fMRI experiment using a non-social medium to convey misinformation (SOM). Participants underwent a similar protocol to that of our main experiment. However, in memory test 2, instead of receiving answers from co-observers, participants were told that the information originated from four different computer algorithms, a common technique used to control for social effects (30). Conformity in this case was significantly lower ($45.3 \pm 4.7\%$) than in the social manipulation described earlier ($68.3 \pm 2.9\%$) but significantly higher than with no manipulation at all ($15.0 \pm 2.4\%$) [$t(38) = 4.2$ and $t(19) = -5.7$, respectively; $P < 0.0002$].

Analysis of BOLD signal in the a priori MTL ROIs revealed an interaction between memory (persistent errors and transient errors) and experimental manipulation (social and nonsocial) in the bilateral amygdala ($P < 0.05$). This interaction was driven by greater activation in trials resulting in persistent memory errors relative to transient errors in the social manipulation, but not in the nonsocial manipulation (Fig. 3A). These results suggest that enhanced activity in these regions is related specifically to socially induced persistent memory errors. In contrast, the right anterior and posterior hippocampus and left PHG revealed a main effect of memory ($P < 0.05$), where there was greater activity during trials resulting in persistent errors relative to transient errors regardless of manipulation type ($P < 0.05$) (Fig. 3A). Thus, the BOLD signal in these regions was associated with long-lasting memory errors irrespective of the medium by which information was conveyed. Results of a functional connectivity analysis between the left amygdala and bilateral anterior hippocampus showed a significant interaction ($P < 0.05$). Heightened connectivity was seen during trials that resulted in persistent errors relative to transient errors, a pattern specific to the social manipulation (Fig. 4B). Our control experiment's results hence indicate that heightened amygdala activation and enhanced connectivity with the hippocampus are specific to socially induced memory changes, whereas hippocampal complex activation differentiates between persistent and transient errors regardless of the source of influence.

Our results indicate that memory is highly susceptible to alteration due to social influence, creating both transient and persistent errors. After over a century of intensive behavioral research into social influences on memory (35), this study now provides a brain account of this phenomenon. Our findings suggest a mechanism by which

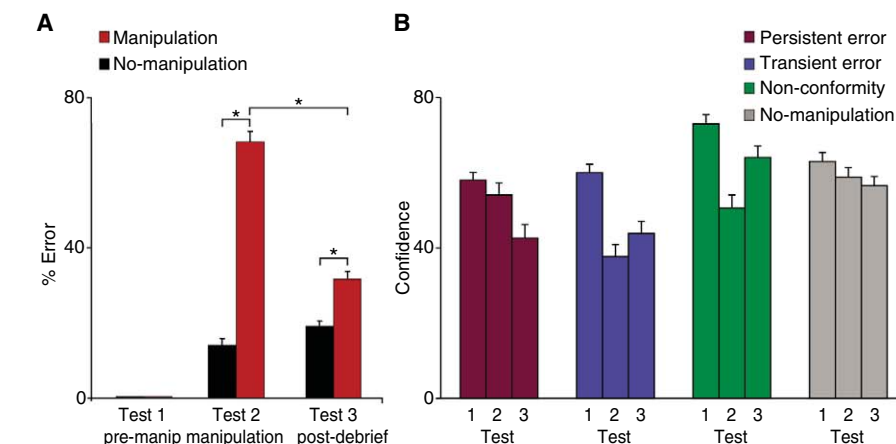


Fig. 2. Behavioral results. (A) Conformity level in the social manipulation condition was 68.3% versus 15.5% in the no-manipulation condition [$t(19) = 16.9$, $P < 10^{-7}$]. In test 3, participants reverted back to their original correct answer in 59.2% of the previously conformed-to events (transient errors) and on 40.8% maintained their erroneous answer (persistent memory error). The error rate was significantly different in test 3 between the manipulation and no-manipulation conditions [$t(19) = 3.7$, $P < 0.002$]. The questions included in the manipulation and no-manipulation trials were those for which participants gave correct answers in test 1 with medium-high confidence. (B) Confidence ratings over time for differential trial types ($*P < 0.002$).

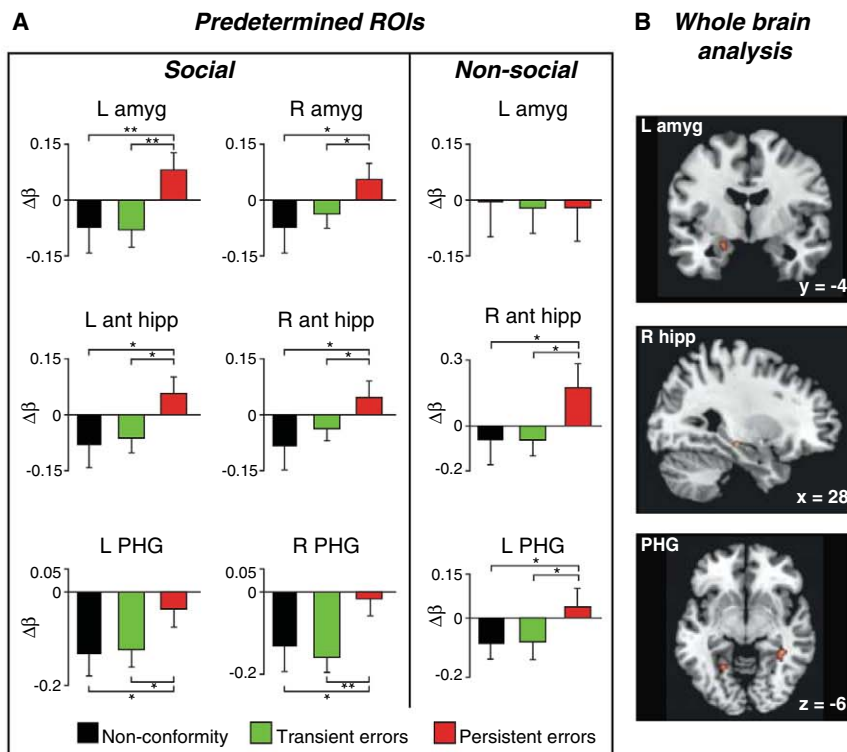
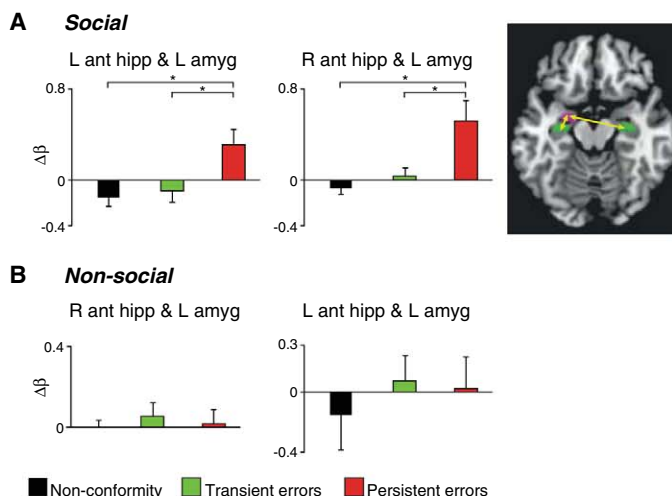


Fig. 3. MTL activation during manipulation predicts long-term socially induced memory errors. (A) BOLD signal in anatomically a priori defined MTL regions. L, left; R, right; In the social manipulation, enhanced activation was found during trials that subsequently resulted in persistent errors relative to all other conditions in the bilateral hippocampal complex and amygdala. In the nonsocial manipulation, this pattern was evident in the hippocampal complex but not in the bilateral amygdala. (B) Whole-brain exploratory analysis in the social manipulation ($P < 0.001$, $k > 10$) revealed greater activity in persistent error versus transient error conditions in the left amygdala, right hippocampus, right PHG, and left PHG bordering on the occipital lobe. All areas also survived small volume correction for multiple comparisons (familywise error < 0.05). The baseline in all figures is the no-manipulation condition ($*P < 0.05$ $**P < 0.005$).

social influence produces long-lasting alterations in memory, and they highlight the critical role of the amygdala in mediating this influence.

Although at the time of social influence on memory overt behavior was indistinguishable, transient and persistent errors nevertheless in-

Fig. 4. Amygdala-hippocampal functional connectivity during manipulation predicts long-term socially induced memory errors. **(A)** Social manipulation. Functional connectivity between the left amygdala and bilateral anterior hippocampus was heightened in the persistent error condition relative to all other conditions. **(B)** Nonsocial manipulation. No condition-dependent difference in functional connectivity between the left amygdala and bilateral anterior hippocampus was found. The baseline in all figures is the no-manipulation condition (* $P < 0.05$). The inset depicts the anatomical ROIs used in the aforementioned analyses.



duced distinct brain signatures. Heightened activation in the hippocampal complex was seen when false information induced a long-lasting change in the participants' memories regardless of social context. The hippocampal complex activation we observed may represent a process of reconsolidation (36) or encoding of new stable representations [e.g., gist (37)]. In contrast, transient changes did not activate areas known to be crucial for memory processing. Our findings provide neurobiological evidence for the classic assertion that private conformity is accompanied by actual changes in beliefs, whereas public displays of conformity are not (7, 8, 10, 38).

Enhanced activation in the bilateral amygdala and heightened functional connectivity with the anterior hippocampus were a signature of long-term memory change induced by the social environment. This indicates that the incorporation of external social information into memory may involve the amygdala's interdependence, in accordance with its special position at the crossroads of social cognition and memory (13, 14, 16).

Multiple formal models have proposed trace attributes that might contribute to memory distortion in different false memory protocols (37, 39–41). These postulated attributes refer, for example, to potential heterogeneity in episodic content and the persistence of memory trace elements. Our laboratory analog to socially induced memory distortion was not intended to distinguish between specific models. However, further exploitation of our protocol, combined with cross-fertilization of behavioral and brain data, might contribute to the refinement of current models and better understanding of the biological and cognitive mechanisms of memory conformity.

Altering memory in response to group influence may produce untoward effects. For example, social influence such as false propaganda can deleteriously affect individuals' memory in political campaigns and commercial advertising (1, 2, 6) and impede justice by influencing eyewitness testimony (2, 4, 5). However, memory conformity may also serve an adaptive purpose, because social learning is often more efficient and accurate than individual learning (42). For this reason, humans may be predisposed to trust the judgment of the group, even when it stands in opposition to their own original beliefs. Such influences and their long-term effects, the neurobiological basis of which we describe here, may contribute to the extraordinary levels of persistent conformity seen in authoritarian cults and societies.

References and Notes

1. M. L. Meade, H. L. Roediger 3rd, *Mem. Cognit.* **30**, 995 (2002).
2. E. F. Loftus, *Learn. Mem.* **12**, 361 (2005).
3. D. L. Schacter, *The Seven Sins of Memory: How the Mind Forgets and Remembers* (Houghton-Mifflin, New York, 2001).
4. D. B. Wright, A. Memon, E. M. Skagerberg, F. Gabbert, *Curr. Dir. Psychol. Sci.* **18**, 174 (2009).
5. J. S. Shaw 3rd, S. Garven, J. M. Wood, *Law Hum. Behav.* **21**, 503 (1997).
6. H. W. Perkins, J. W. Linkenbach, M. A. Lewis, C. Neighbors, *Addict. Behav.* **35**, 866 (2010).
7. E. Smith, D. Mackie, *Social Psychology* (Psychology Press, London, ed. 3, 2007).
8. V. Allen, in *Advances in Experimental and Social Psychology*, L. Berkowitz, Ed. (Academic Press, New York, 1965), pp. 133–170.
9. M. B. Reysen, *Memory* **13**, 87 (2005).
10. S. E. Asch, in *Groups, Leadership and Men*, H. Guetzkow, Ed. (Carnegie Press, Pittsburgh, PA, 1951), pp. 39–76.
11. L. Festinger, *A Theory of Cognitive Dissonance* (Peterson, Evanston, IL, 1957), pp. 99–100.

12. Y. Dudai, *Memory from A to Z. Keywords, Concepts and Beyond* (Oxford Univ. Press, Oxford, 2002).
13. R. Adolphs, *Nat. Rev. Neurosci.* **4**, 165 (2003).
14. E. A. Phelps, *Annu. Rev. Psychol.* **57**, 27 (2006).
15. F. Dolcos, K. S. LaBar, R. Cabeza, *Neuron* **42**, 855 (2004).
16. R. J. Dolan, *Science* **298**, 1191 (2002).
17. K. C. Bickart, C. I. Wright, R. J. Dautoff, B. C. Dickerson, L. F. Barrett, *Nat. Neurosci.* **14**, 163 (2010).
18. K. N. Ochsner, in *Social Neuroscience: People Thinking About People*, J. T. Cacioppo, Ed. (MIT Press, Cambridge, MA, 2005), pp. 245–268.
19. R. N. Cardinal, J. A. Parkinson, J. Hall, B. J. Everitt, *Neurosci. Biobehav. Rev.* **26**, 321 (2002).
20. L. R. Squire, *Neurobiol. Learn. Mem.* **82**, 171 (2004).
21. J. P. Aggleton, *The Amygdala: Second Edition. A Functional Analysis* (Oxford Univ. Press, Oxford, 2000).
22. H. Kluver, P. C. Bucy, *J. Psychol.* **5**, 33 (1938).
23. M. P. Richardson, B. A. Strange, R. J. Dolan, *Nat. Neurosci.* **7**, 278 (2004).
24. Y. Okado, C. E. L. Stark, *Learn. Mem.* **12**, 3 (2005).
25. L. Nadel, M. Moscovitch, *Curr. Opin. Neurobiol.* **7**, 217 (1997).
26. L. Stefanacci, D. G. Amaral, *J. Comp. Neurol.* **451**, 301 (2002).
27. K. J. Friston *et al.*, *Neuroimage* **6**, 218 (1997).
28. R. Cabeza, L. Nyberg, *J. Cogn. Neurosci.* **12**, 1 (2000).
29. E. K. Miller, J. D. Cohen, *Annu. Rev. Neurosci.* **24**, 167 (2001).
30. V. Klucharev, K. Hytönen, M. Rijpkema, A. Smids, G. Fernández, *Neuron* **61**, 140 (2009).
31. D. M. Amodio, C. D. Frith, *Nat. Rev. Neurosci.* **7**, 268 (2006).
32. B. A. Kuhl, N. M. Dudukovic, I. Kahn, A. D. Wagner, *Nat. Neurosci.* **10**, 908 (2007).
33. B. J. Levy, M. C. Anderson, *Trends Cogn. Sci.* **6**, 299 (2002).
34. J. P. Mitchell, C. S. Dodson, D. L. Schacter, *J. Cogn. Neurosci.* **17**, 800 (2005).
35. F. C. Bartlett, *Remembering* (Cambridge Univ. Press, Cambridge, 1932).
36. Y. Dudai, *Annu. Rev. Psychol.* **55**, 51 (2004).
37. V. F. Reyna, C. J. Brainerd, *Learn. Individ. Differ.* **7**, 1 (1995).
38. M. Sherif, *The Psychology of Social Norms* (Harper Collins, New York, 1936).
39. H. L. Roediger 3rd, J. M. Watson, K. B. McDermott, D. A. Gallo, *Psychon. Bull. Rev.* **8**, 385 (2001).
40. J. Arndt, *Psychol. Learn.* **36**, 66 (2010).
41. M. L. Howe, *Psychol. Bull.* **134**, 768, discussion 773 (2008).
42. R. Boyd, P. J. Richardson, in *Social Learning: Psychological and Biological Perspectives*, R. R. Zentall, B. J. Galef, Eds. (Erlbaum, Hillsdale, NJ, 1988), pp. 29–48.

Acknowledgments: M.E. was supported by a Weizmann Institute–UK Grant. T.S. is supported by a British Academy Postdoctoral Fellowship. R.J.D. is supported by a Wellcome Trust Program Grant. Y.D. is supported by the Nella and Leon Benoziyo Center for Neurological Diseases. We thank A. Ben-Yakov, J. G. Edelson, T. Fitzgerald, O. Furman, S. Fleming, D. Levi, M. Guitart-Masip, A. Mendelsohn, U. Nili, A. Pine, J. S. Winston, and N. Wright for helpful comments and the support teams of the Norman and Helen Asher Center for Brain Imaging at the Weizmann Institute and the Imaging Neuroscience & Theoretical Neurobiology unit in the Wellcome Trust Center for Neuroimaging.

Supporting Online Material

www.sciencemag.org/cgi/content/full/333/6038/108/DC1
Materials and Methods
Fig. S1
Table S1
References

31 January 2011; accepted 12 May 2011
10.1126/science.1203557

NEW PRODUCTS: IMMUNODETECTION



MULTIMODAL IMAGING SYSTEM

The new Gel Logic 4000 PRO is a premium, fully automated luminescent, ultraviolet-fluorescent, and radio-isotopic imaging system for the life science research community. Designed for speed and sensitivity, the Gel Logic 4000 PRO can image a wide range of sample formats such as gels (DNA/RNA/protein), membranes (Western, Southern, Northern blots), colony, and microtiter plates. With this system, imaging of blots and plate assays can now be conducted faster than ever before. Additionally, this new Gel Logic is capable of digital radiological imaging of in vitro samples for quantitative analysis of radiolabeled samples. Features include a cooled 4.2 MP scientific grade camera (-29°C), f/0.95 lens, advanced LED lighting, 10 filter positions, and a motorized sample platform for up to 3x zoom and seven prefocused fields of view. This system offers integrated trans-UV, epi-white light, and trans-white light illumination for imaging of protein and DNA based gels. Carestream Molecular Imaging software offers full control over the motorized sample platform and camera system.

Carestream

For info: 877-747-4357 | www.carestream.com

CLEAR-BOTTOMED MICROPLATES

The Krystal UV range of high specification, quartz-bottomed microplates are designed for scientists using assay chemistries which require excitation or detection in the far ultraviolet (UV) spectral region. Precision engineered and assembled, Krystal UV plates provide consistently low background and excellent photometric accuracy down to 220 nm. Manufactured from ultrapure grade black polystyrene, the plates exhibit very low autofluorescence and are resistant to solvents including alcohols, DMSO, and PBS. Available in 96-well format only, Krystal UV quartz bottomed microplates are the perfect choice for high throughput determinations of nucleic acid and/or proteins concentrations at 260/280 nm. Krystal UV quartz bottomed plates precisely conform to SBS/ANSI standards. Their high degree of planar flatness makes them ideal for use with automated plate reading and liquid handling systems.

Porvair Sciences

For info: +44-1372-824290 | www.porvair-sciences.com

MAGNETIC BEAD-BASED IMMUNOASSAYS

New magnetic bead-based multiplex immunoassays for TGF- β , rat cytokines, rat diabetes, and mouse TH17 cytokines are built on Luminex's MagPlex platform to take advantage of the magnetic beads workflow that simplifies assay preparation and reduces variability in results. Magnetic bead-based assays are compatible with both vacuum and magnetic wash stations as well as other Luminex xMAP platforms such as Bio-Rad's Bio-Plex 200 and Bio-Plex 3D systems. The Bio-Plex Pro rat cytokine assays and Bio-Plex Pro rat diabetes assays detect 25 rat cytokines and five rat diabetes biomarkers respectively. Both panels are designed to help researchers investigate mechanisms and quantify biomarkers of diseases, such as cancer, diabetes, Rheumatoid arthritis, cardiovascular, Alzheimer's, and Parkinson's disease, and of those associated with neurological disorders and inflammation. Bio-Plex Pro assays offer many advantages over other xMAP and enzyme-linked immunosorbent assay offerings, including better performance and faster assay run time.

Bio-Rad

For info: 800-424-6723 | www.biorad.com

MULTIPLEX PROTEIN BIOMARKER ANALYSIS

The SignaturePLUS Imaging and Analysis System is designed to meet the cost and performance needs of researchers for accurate, reproducible, and reliable multiplex protein biomarker analysis across preclinical, clinical, and diagnostics applications in all therapeutic areas. The SignaturePLUS system incorporates an advanced CCD imager with custom optics designed specifically for quantitative chemiluminescent protein arrays. Its sleek, compact design uses less than two feet of bench space and includes an integrated iPad user interface with an embedded Mac mini computer that eliminates the need for separate, bulky system components. The SignaturePLUS system also includes the enhanced PROarray Analyst software for fast, accurate, reproducible analysis. Engineered for simple, out-of-the-box setup, the SignaturePLUS system is extremely easy to use and features typical imaging times of less than two minutes per plate. Researchers can choose from Aushon's growing menu of more than 300 validated protein biomarkers for analysis using the new SignaturePLUS system.

Aushon BioSystems

For info: 978-436-6400 | www.aushon.com

CHEMILUMINESCENT WESTERN BLOT DETECTION

The Thermo Scientific Pierce ECL Plus Substrate for Western blotting detection is a highly sensitive, acridan-based reagent used for the chemiluminescent or chemifluorescent horseradish peroxidase detection of immunoblots. The Pierce ECL Plus Substrate detects low picogram level of antigen, which can be visualized on X-ray film or with an imaging system. The long-lasting signal generated using the Pierce ECL Plus Substrate can be detected easily for up to five hours, and up to 20 hours with longer exposure times. The substrate is compatible with both PVDF and nitrocellulose membranes. The substrate is available in two sizes, with reagent sufficient for 250 or 1,000 square centimeters of membrane.

Thermo Fisher Scientific

For info: 800-874-3723 | www.thermoscientific.com/pierce

Electronically submit your new product description or product literature information! Go to www.sciencemag.org/products/newproducts.dtl for more information.

Newly offered instrumentation, apparatus, and laboratory materials of interest to researchers in all disciplines in academic, industrial, and governmental organizations are featured in this space. Emphasis is given to purpose, chief characteristics, and availability of products and materials. Endorsement by *Science* or AAAS of any products or materials mentioned is not implied. Additional information may be obtained from the manufacturer or supplier.

Science Careers

From the journal *Science*



Science Careers Advertising

For full advertising details, go to ScienceCareers.org and click For Employers, or call one of our representatives.

Tracy Holmes

Worldwide Associate Director
Science Careers
Phone: +44 (0) 1223 326525

UNITED STATES & CANADA

E-mail: advertise@sciencecareers.org
Fax: 202-289-6742

Tina Burks

Midwest/West Coast/
South Central/Canada
Phone: 202-326-6577

Elizabeth Early

East Coast & Industry
Phone: 202-326-6578

Marci Gallun

Sales Administrator
Phone: 202-326-6582

Online Job Posting Questions

Phone: 202-326-6577

EUROPE & REST OF WORLD

E-mail: ads@science-int.co.uk
Fax: +44 (0) 1223 326532

Alex Palmer

Phone: +44 (0) 1223 326527

Susanne Kharraz

Phone: +44 (0) 1223 326529

Dan Pennington

Phone: +44 (0) 1223 326517

Lisa Patterson

Phone: +44 (0) 1223 326528

JAPAN

ASCA Corporation

Phone: +81-3-6802-4616
Fax: +81-3-6802-4615
E-mail: careerads@sciencemag.jp

CHINA & TAIWAN

Ruolei Wu

Phone: +86-1367-1015-294
E-mail: rwu@aaas.org

All ads submitted for publication must comply with applicable U.S. and non-U.S. laws. *Science* reserves the right to refuse any advertisement at its sole discretion for any reason, including without limitation for offensive language or inappropriate content, and all advertising is subject to publisher approval. *Science* encourages our readers to alert us to any ads that they feel may be discriminatory or offensive.



ÉCOLE POLYTECHNIQUE
FÉDÉRALE DE LAUSANNE

Tenure Track Assistant Professor in Stem Cell Biology and Regenerative Medicine at Ecole Polytechnique Fédérale de Lausanne (EPFL)

The School of Life Sciences invites applications for an endowed **tenure track assistant professorship in Stem Cell biology and Regenerative Medicine**. We are particularly interested in candidates focusing on the mechanisms of stem cell reprogramming, stem cell plasticity, and disease modeling. A range of research topics within these areas will be considered. Candidates whose projects rely on multidisciplinary approaches are particularly sought.

Candidates will develop an independent and vigorous research program, will be committed to excellence in undergraduate/graduate teaching, and supervise PhD students.

Start-up resources and state-of-the-art research core facilities will be available, within the framework of a campus that fosters very strong interactions between life sciences, basic science, informatics and engineering. Salaries and benefits are internationally competitive.

Applications should be submitted through the Internet on <http://stemcell-search.epfl.ch> and should include the following documents in PDF format: curriculum vitae, publication list, brief statement of research and teaching interests, names and addresses (including e-mail) of at least 3 references. Review of applications will start on **October 1st, 2011**.

Enquiries may be addressed to:

Professor Yann Barrandon
Laboratory of Stem Cell Dynamics
School of life sciences, EPFL
yann.barrandon@epfl.ch

For additional information on EPFL, its School of Life Sciences, please consult <http://www.epfl.ch>, <http://sv.epfl.ch/>

The EPFL School of Life Sciences aims for a very strong presence of women amongst its faculty, and qualified female candidates are strongly encouraged to apply.

The Faculty of Natural Sciences invites applications for a tenured

W3 Professorship for Inorganic and Analytical Chemistry (chair)

(in succession of Prof. Dr. Dr. h. c. mult. Rudi van Eldik)

The successful candidate is expected to represent the field of Inorganic Chemistry in research and teaching at the university. The research interests of the applicant should strengthen current and ongoing activities of the Department of Chemistry & Pharmacy in the area of inorganic molecular synthesis with potential applications in catalysis and/or molecular materials. Based on innovative synthesis concepts, the design, development and application of novel, functional and complex systems are envisioned.

The future chair of Inorganic and Analytical Chemistry will be joining a strongly interdisciplinary environment. The diversity of research currently undertaken by the chemistry faculty is characterized by programs like the Excellence Cluster "Engineering of Advanced Materials", the Graduate School of "Molecular Science" and the DFG Research Initiative 583 "Redox Active Metal Complexes". Active participation in these programs and corresponding follow-up initiatives will be appreciated.

Qualifications of interested candidates include a university doctoral degree, an established record of teaching at the university level and a habilitation or equivalent qualification that may have been gained outside the university or during an Assistant/Associate Professorship.

The University of Erlangen-Nürnberg is committed to a profamily policy and an equal opportunity employer; we also offer encouragement for Dual-Career-Couples. We strongly encourage women to apply in an effort to increase a female representation in research and teaching.

Disabled candidates are given preference if equally qualified.

Application documents (curriculum vitae, photograph, list of publications and teaching activities – in addition as pdf-file with 20 pages maximal on cd –, certified copies of degree documents but no publications) and a brief statement of research interests are due on **August 31, 2011**, the latest and should be mailed to: Dekan der Naturwissenschaftlichen Fakultät, Friedrich-Alexander-Universität Erlangen-Nürnberg, Universitätsstraße 40, D-91054 Erlangen, Germany.

**Friedrich-Alexander-Universität
Erlangen-Nürnberg**



www.uni-erlangen.de



Head of Cell Biology Department and Library Information Scientist positions at Novo Nordisk R&D Center China, Beijing

Novo Nordisk China R&D center is an integrated part of Novo Nordisk's R&D organization. We are seeking innovative and energetic scientists to fill in the open positions described below.

1. Head of Cell Biology Department at Biopharmaceuticals Research China (BRC) (Job Code: BRCCB002-Head of Dept)

BRC is one of the business units in Novo Nordisk China R&D, and is expanding its Protein Engineering & Antibody Development capabilities to leverage its core competencies to support ongoing projects and contribute to the identification of new molecular targets for the treatment of autoimmune diseases.

We are seeking a new Head of Cell Biology department at BRC for setting the direction for the future development of this department with its app. 20 employees. Thus, we are looking for a candidate with a combination of strong personal leadership potential as well as strong insight and documented abilities in directing research and discovery within immunobiology disciplines. Excellent communication skills and the ability to interact constructively with colleagues and peers in an international atmosphere are absolute requirements on top of scientific excellence.

The ideal candidates should optimally have Ph.D. in cell biology, immunology or a related discipline with 5+ years post doctorate experience and solid scientific track-record within immunotechnology or autoimmune diseases. Experienced project and/or people management is a requirement and experience from a biotech/pharmaceutical R&D setting with focus on protein based therapeutics development is strongly preferred.

2. Information Scientist at Novo Nordisk Library (Job code: Lib InfoSci)

We are seeing a Information Scientist to retrieve and analyse scientific information within the company therapy areas (diabetes, haemophilia, inflammation, and human growth hormone)—mainly targeted at R&D China. The position is based and employed in Beijing, yet also a functional member of the Novo Nordisk Library based in Denmark. *The ideal candidates should have a M.Sc. (preferably a Ph.D.) within medicine, biology, biochemistry or similar, must have experience for information searching and communication, and information technology skills within the life science area. This includes experience in handling data, information analysis and utilisation of information within a research environment and experience of searching within specific databases or via STN or Dialog/Datastar on an expert level. Excellent skills in written and spoken Chinese and English is required. Experience from a similar position would be a clear advantage.*

Title and compensation will be commensurate with the individual candidate's qualifications. For detailed information regarding individual position, please send an inquire or application via e-mail to InfoNST@novonordisk.com quoted with the job code in Subject.



University at Buffalo The State University of New York

DIRECTOR POSITION Research Institute on Addictions

The University at Buffalo's Research Institute on Addictions is seeking an outstanding individual with vision, scientific standing, administrative, communications, and leadership qualities to serve as DIRECTOR. Candidates should have a record of excellence in managing an active and nationally/internationally recognized program of addictions research; possess a doctoral degree in behavioral, social or medical science; and demonstrate a broad-based background in research with strong scientific skills in the addictions field. Demonstrated ability to secure extramural funding is essential. Candidates should possess credentials for appointment as full professor. This is a New York State-funded professional position. Salary will be commensurate with qualifications. For more information, visit www.ria.buffalo.edu.

Interested candidates are encouraged to contact:

Nancy J. Smyth, PhD
Chair, Search Committee
Dean, School of Social Work
Email: sw-dean@buffalo.edu
or 716-645-1267

To apply, go to www.ubjobs.buffalo.edu, attach an e-version of your curriculum vitae and a cover letter describing your interest and academic/professional leadership experience.

*UB is an Affirmative Action/
Equal Opportunity Employer.*



THE UNIVERSITY
OF
WISCONSIN
MADISON

FACULTY POSITION IN VETERINARY ONCOLOGY

The Department of Medical Sciences, School of Veterinary Medicine, University of Wisconsin-Madison seeks candidates for the Barbara A. Suran Endowed Chair tenure track faculty position in Veterinary and Comparative Oncology at the rank Associate or Full Professor. Candidates should possess a DVM, PhD, MD or equivalent degree and a record of excellent independent scholarship in basic or clinical research in Veterinary and/or Comparative Oncology. Applicants must have demonstrated a strong commitment to the education of professional students, graduate students, and residents through a history of high quality instruction and service.

The successful candidate will direct independent research in the field of comparative oncology through the administration of the Barbara A. Suran Fund for Oncology Medical Science Research Excellence (Endowed) under the umbrella of the Barbara A. Suran Oncology Research Institute located within the School of Veterinary Medicine. Also, the successful candidate will engage graduate students, residents and veterinary students in classroom and laboratory teaching, and clinical or translational service that advances the mission of the School. Distribution of effort will be 60% research, 30% instruction/clinical service, and 10% university service.

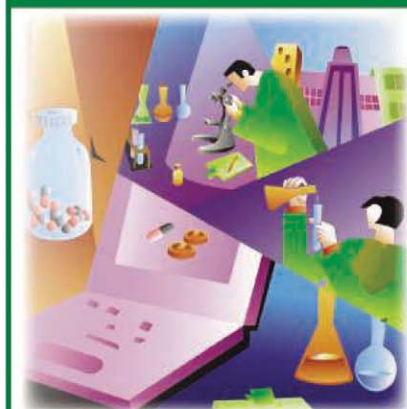
The Department fosters a multidisciplinary approach to research. Ongoing areas of research include comparative oncology, investigational comparative cancer clinical trials through the inclusion of companion animals with cancer, and pharmacogenomics. Established and emerging strengths include explorations of novel chemotherapy and immunotherapy modalities, and investigation of molecular, and functional imaging modalities to better inform the delivery of conformal radiation therapy (e.g., onsite TomoTherapy™). Additionally, through institutional partnerships with the NIH/NCI-designated Carbone Comprehensive Cancer Center, significant collaborative activities are available and expected.

Rank and salary will depend on experience and qualifications. Deadline for receipt of application and reference letters is **August 31, 2011** or until a suitable candidate is identified. Applicants cannot be guaranteed confidentiality. Applicants are invited to submit a curriculum vitae, letter of intent summarizing career goals and current activities, and names and addresses of three references to: **Dr. Mark D. Markel, Chair, Department of Medical Sciences, School of Veterinary Medicine, University of Wisconsin-Madison, 2015 Linden Drive, Madison, WI 53706-1102**. Informal inquiries may be directed to **Dr. Lauren Trepanier (Chair of Search Committee)** at 608-265-9022 or e-mail latrepanier@vetmed.wisc.edu.

*The University of Wisconsin is an
Affirmative Action Equal Opportunity Employer committed to diversity.*

CAREER TRENDS

Running
Your Lab



Download your free copy today at
ScienceCareers.org/booklets

Science Careers

From the journal *Science*



Brought to you by the
AAAS/Science Business Office

Life Inspired.



Tisbe, Patient



Passionate About Our Science and Our People

We're passionate and rigorous about our science. For more than 30 years, Genentech has been at the forefront of the biotechnology industry, using innovative science to develop breakthrough medicines that improve the lives of people with serious or life-threatening diseases. We're also passionate about our people, our most important asset. That's why we offer Genentech employees:

- The chance to make a difference in the lives of patients
- Extraordinary colleagues
- An inclusive environment that encourages diversity
- Highly competitive benefits

Genentech has the following opportunities in our Small Molecule organizations in our South San Francisco, CA, headquarters:

Associate Director, Immune Cell Signaling – Req. #00376671

We are seeking a leader for our Small Molecule Immunology programs with a strong interest and expertise in the discovery of small molecule therapeutics for inflammatory and autoimmune diseases. The candidate will lead research efforts focused on discovering and pursuing new drug targets. As Associate Director, he/she will manage all ongoing and new small molecule therapeutic programs within the Discovery Immunology department and collaborate on associated critical path activities with colleagues in Biochemical Pharmacology.

Associate Director, Biochemical and Cellular Pharmacology – Req. #00376809

We are seeking an Associate Director who will be responsible for overseeing the development, optimization, validation and execution of biochemical and cellular assays to support specific projects as part of both small molecule and biologics drug discovery programs. This position will have oversight and strategic guidance of both small molecule and biologic programs in immunology, infectious disease and neurobiology.

- **Scientist/Sr. Scientist, Process Chemistry**
Req. #00376880
- **Sr. Research Associate, Analytical Chemistry**
Req. #00369381
- **Sr. Scientific Manager, Discovery Analytical Chemistry**
Req. #00376951
- **Scientist/Sr. Scientist, Analytical Chemistry**
Req. #00373324
- **Sr. Research Associate, Analytical Chemistry/QC**
Req. #00375852
- **Sr. Scientific Manager, Analytical Chemistry/QC**
Req. #1000034165

Now a member of the Roche Group, Genentech has multiple medicines on the market for cancer and other serious illnesses. We are an equal opportunity employer and in 2010, we were named “top employer in the biopharmaceutical industry” by Science magazine for the ninth time.

Join us as we continue to tackle medicine's most challenging problems and live a life inspired. For complete position descriptions and to apply, please visit careers.gene.com and enter the Requisition number in the keyword search field.



AAAS is here – helping scientists achieve career success.

Every month, over 400,000 students and scientists visit ScienceCareers.org in search of the information, advice, and opportunities they need to take the next step in their careers.

A complete career resource, free to the public, *Science* Careers offers a suite of tools and services developed specifically for scientists. With hundreds of career development articles, a grants and scholarships database, webinars and downloadable booklets filled with practical advice, a community forum providing real-time answers to career questions, and thousands of job listings in academia, government, and industry, *Science* Careers has helped countless individuals prepare themselves for successful careers.

As a AAAS member, your dues help AAAS make this service freely available to the scientific community. If you're not a member, join us. Together we can make a difference.

To learn more, visit aaas.org/plusyou/sciencecareers

WorldMags





TAMPEREEN TEKNILLINEN YLIOPISTO
TAMPERE UNIVERSITY OF TECHNOLOGY

AT THE LEADING EDGE

Tampere University of Technology (TUT) is an active scientific community of 2,000 employees and more than 10,000 students. The University operates in the form of a foundation and has a long-standing tradition of collaboration with other research institutions and business life. Many of the fields of research and study represented at the University play a key role in addressing global challenges. Internationality is an inherent part of all the University's activities. Welcome to join us at TUT!

www.tut.fi



TENURE TRACK POSITIONS

Physics 1-3 positions, Signal Processing 1-3 positions

Tampere University of Technology in Finland invites applications for six tenure track positions.

1-3 positions are currently available in the field of physics and 1-3 positions in the field of signal processing. Positions can be filled on any level from Assistant Professor to Associate Professor. Positions are open for talented individuals who have the potential to pursue a successful scientific career.

The tenure track system at Tampere University of Technology offers the recruited researchers an opportunity to progress toward the rank of full professor along a predefined career path. This will allow them to devote their time to research and the advancement of their respective fields.

For the complete job advertisements and detailed instructions on how to apply, please visit www.tut.fi/en > Current > Open positions.

The application has to be submitted electronically by 10 p.m. GMT, 15th of September 2011.

Executive Editor – China, Nature Communications

As part of a major strategic move by Nature Publishing Group (NPG) into China, Nature Communications, an innovative online multidisciplinary science journal of NPG, seeks an Executive Editor to head a team of Nature Communications editors to be based in Shanghai, China from early 2012.

Launched in April 2010, Nature Communications publishes high quality research from the breadth of the natural sciences, and has already developed a strong track record in the biological and physical sciences. The journal offers rapid publication in an online environment, with Open Access options.

The Executive Editor, reporting to the Chief Editor in London and with a local reporting line to the head of NPG's publishing operations in China, will play a key role in establishing a presence on the ground for NPG in China.

As well as encouraging high quality submissions of manuscripts to Nature Communications from China and managing the local team of Nature Communications editors in Shanghai, the successful candidate will also play a leading role in encouraging submissions to other Nature journals and NPG publications. This will involve regular visits to key laboratories in China conducting leading edge research and networking with top scientists in China's research community as well as organizing and participating in events and seminars intended to build awareness and understanding of the types of manuscripts NPG is seeking for its journals.


This is a demanding and intellectually stimulating position. Previous experience as an editor for a high quality international science journal is essential and ability to communicate fluently and effectively in Chinese, as well as English, is ideal, although candidates without Chinese language skills, who are prepared to locate in Shanghai, will be considered. Ability to manage a team of editors is also essential and the successful candidate must therefore have excellent communication and interpersonal skills. Candidates with a background in any of the natural sciences will be considered.

The position will require an initial period of training in London with the Nature Communications team for 3-6 months prior to relocation to Shanghai. The salary and benefits will be competitive with a generous relocation package, reflecting the critical importance and responsibilities of this role.

All candidates must be eligible to work in mainland China and must be eligible to spend 3-6 months in the UK for training to be considered for this vacancy.

Application is by CV and covering letter explaining your interest in the post and a Research Highlight piece (600 words) on a recent paper related to your discipline to recruitment@macmillan.co.uk. Please quote reference number NPG/086/11 in the subject header.

Closing date: 14th July 2011

nature publishing group 

Get a Career Plan that Works.

An exceptional career requires insightful planning and management. That's where *Science Careers* comes in. From job search to career enhancement, *Science Careers* has the tools and resources to help you achieve your goals. Get yourself on the right track today and get a real career plan that works. Visit ScienceCareers.org.

Science Careers

From the journal *Science*



ScienceCareers.org



Find My Job

Develop My Career

Research

Track

Navigate

Network

Search





Founded in 1911, The University of Hong Kong is committed to the highest international standards of excellence in teaching and research, and has been at the international forefront of academic scholarship for many years. Ranked 21st among the top 200 universities in the world by the UK's Times Higher Education, the University has a comprehensive range of study programmes and research disciplines spread across 10 faculties and about 100 sub-divisions of studies and learning. There are over 23,400 undergraduate and postgraduate students coming from 50 countries, and more than 1,200 members of academic and academic-related staff, many of whom are internationally renowned.

Tenure-Track Associate Professor/Assistant Professor (2 posts) in the Department of Physics (Ref.: 20110392)

Applications are invited for appointment as Associate Professor/Assistant Professor (2 posts) in the Department of Physics, from as soon as possible. The posts will initially be made on a three-year basis with the possibility of renewal upon mutual agreement. Appointment with tenure will be considered during the second three-year contract.

One position will primarily be in the field of Experimental Condensed Matter Physics, or Atomic, Molecular and Optics, or Quantum Physics. The other position will be in Theoretical Physics including Astrophysics, Condensed Matter Theory, or Computational Physics. Candidates with good qualifications and commitment to high-quality research and excellence in teaching are encouraged to apply.

Annual salaries will be in the following ranges (subject to review from time to time at the entire discretion of the University):

Associate Professor	:	HK\$636,420 – 984,180	(approximately US\$1 = HK\$7.8)
Assistant Professor	:	HK\$484,980 – 749,520	

Applicants should indicate clearly the reference number and which level they wish to be considered for.

A highly competitive salary commensurate with qualifications and experience will be offered. The appointment will attract a contract-end gratuity and University contribution to a retirement benefits scheme, totalling up to 15% of basic salary, as well as leave, and medical/dental benefits. Housing benefits will be provided as applicable. At current rates, salaries tax does not exceed 15% of gross income.

For enquiries of the existing research activities and the specific job requirements, please write to Professor F.C. Zhang, Head of the Department of Physics (e-mail: physhead@hku.hk). Please send an application form together with a curriculum vitae, a detailed publication list, a research plan, and a statement on teaching philosophy to the Appointments Unit (Senior), Human Resources Section, Registry, The University of Hong Kong, Hong Kong. Further particulars and application forms (152/708) can be obtained at <http://www.hku.hk/apptunit/>; or from the Appointments Unit (Senior), Human Resource Section, Registry, The University of Hong Kong, Hong Kong (fax: (852) 2540 6735 or 2559 2058; e-mail: senrapt@hku.hk). Review of applications will start from October 3, 2011 and will continue until the post is filled. Candidates who are not contacted within 3 months from the date of their applications may consider their applications unsuccessful.

The University is an equal opportunity employer and is committed to a No-Smoking Policy



新潟大学

TENURE TRACK PROFESSOR in Biosignaling NIIGATA UNIVERSITY, Japan

The faculty of Medicine at Niigata University invites applications for a tenure track faculty position at the professor level.

This position is located in the Department of Cellular Physiology, which is one of three departments in the Institute of Nephrology, Faculty of Medicine, Niigata University. The screening will be focused on: (a) s/he will be expected to play a core role in the Faculty of Medicine; (b) s/he will be able to develop research to create synergy with the other two departments (Dept. of Structural Pathology and Dept. of Cell Biology).

Applicants must have earned a doctorate within the last 10 years and also, have been engaged in research in other institution(s).

JPY 9 million Start-up, JPY 3 million Research funds per year, Employment expense salary as a postdoctoral fellow will be provided.

The successful candidate will commit research activities. However, for the purpose of training to develop skills in students education, the active participation in educational activities will be recommended.

In accordance with the University Regulations, salary will be commensurate with experience and qualifications.

Appointment term will be from December, 2011 to March, 2016. If a successful candidate is recognized to have achieved a certain level in the mid-term evaluation performed at the end of FY2013, s/he will be promoted to tenured professor of the same department from April, 2014.

The application deadline is **17:00 on August 8, 2011 (JST)**.

For further information and application forms, visit http://www.niigata-u.ac.jp/tenure_track/english/recruitment/information.html

Research and Academic Inquiry:

Prof. Michihiro IGARASHI (tarokaja@med.niigata-u.ac.jp)

Other inquiries and applications: Office for Development of Young Researchers (tenure-t@adm.niigata-u.ac.jp)

Call for applications for the positions of Research Scientist / Technical Scientist Permanent position, RIKEN, JAPAN

RIKEN has openings for research scientists and technical scientists at the following laboratories.

[RIKEN Advanced Science Institute]

Advanced Device Laboratory

http://www.riken.jp/engn/r-world/info/recruit/k110916_e_asi.html

Condensed Molecular Materials Laboratory

http://www.riken.jp/engn/r-world/info/recruit/k110916_e_asi_2.html

[RIKEN Nishina Center for Accelerator-Based Science]

Quantum Hadron Physics Laboratory

http://www.riken.jp/engn/r-world/info/recruit/k110916_e_rnc.html

Radioactive Isotope Physics Laboratory

http://www.riken.jp/engn/r-world/info/recruit/k110916_e_rnc_2.html

Spin-Isospin Laboratory

http://www.riken.jp/engn/r-world/info/recruit/k110916_e_rnc_3.html

Accelerator Applications Research Group

http://www.riken.jp/engn/r-world/info/recruit/k110916_e_rnc_4.html

[RIKEN Spring-8 Center]

Research Infrastructure Group

http://www.riken.jp/engn/r-world/info/recruit/k110916_e_rsc.html

[Conditions] A tenured fulltime position until RIKEN's retirement age of 60. However, the applicant may be offered instead a five-year fixed-term employment contract depending on the selection results. In this case, the employee can move to a tenured position after undergoing a successful review to be held at the end of the first 3 years of employment. Annual salary and other conditions of the fixed-term contract position are the same as for the tenured position. Salary shall be determined on an annual basis subject to the applicant's experience and performance. These and other provisions are in accordance with RIKEN regulations.

[Application] The required documents differ according to the laboratory. Refer to the each URL mentioned above for more details.

[Deadline] 5pm on Friday, September 16, 2011 (Japan Standard Time)

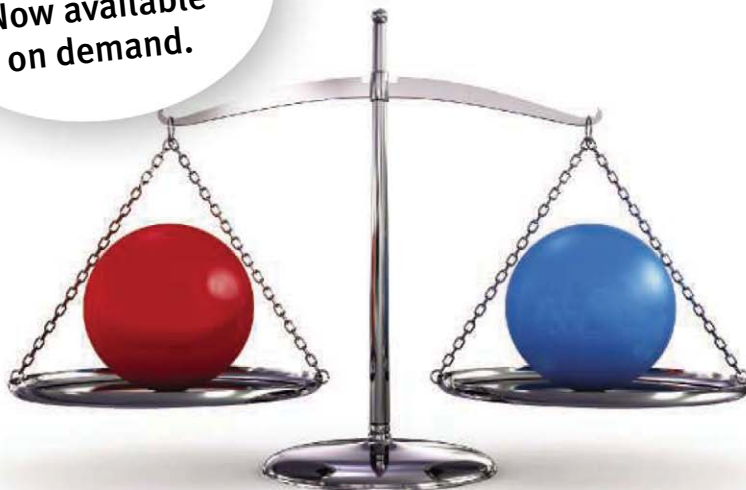
[Start of Employment] April 1, 2013 or later, but negotiable.

[Submitting Documents and Making Inquiries] Research Affairs Section, Advanced Research Promotion Division, RIKEN, 2-1 Hirosawa, Wako, Saitama 351-0198 Japan
E-mail: rps-saiyo (please add "@riken.jp" to complete the address) Email attachments and telephone calls cannot be accepted. When you mail your application, please send as certified mail so that there will be a record of delivery. Please write in red on the front of the envelope, the name of the laboratory you are applying for.

<http://www.riken.jp/engn/r-world/info/recruit/index.html>



WEBINAR
Now available
on demand.



FACTS & FICTION

Careers in Industry and Academia

Trying to figure out the next step in your career? Join us for a roundtable discussion that will look at facts and fiction surrounding academic and industry career options for PhD-level scientists. Get some nuts and bolts advice on how to research career options, what questions to ask, and how to best prepare for various careers.

- Do industry and academic careers require different skill sets?
- Do industry jobs have better compensation? Less autonomy?
- Do academic scientists have less work/life balance?

For answers view our roundtable discussion for free at:

ScienceCareers.org/webinar



Produced by the *Science*/AAAS Business Office.



NOMINATIONS ARE INVITED
for the prestigious
InBev-BAILLET LATOUR HEALTH PRIZE
of € 250,000
(Two hundred and fifty thousand euros)

Theme for 2012 : **Neurosciences**

Previous winner : **Peter H. Seeburg, Germany**

This annual award is intended to recognize outstanding scientific achievements in biomedical research and/or their practical applications for human health and to encourage the laureate in the pursuit of his/her career. Exceptionally, the Prize may be shared between two persons who have collaborated over a long period. The laureate will be selected by an international Jury in February 2012.


The Prize is open to scientists of all nationalities who have not received in their own name an equivalent Prize rewarding the work that is submitted. The themes for the following years will be : Cancer; Cardiovascular Diseases, Metabolic Disorders, Infectious Diseases and Immunology.

Deadline for nominations : September 30th, 2011

Nominations must be submitted in an envelope marked "Confidential" to the Secretary General of the Fund for Scientific Research-FNRS, rue d'Egmont 5, BE - 1000 Brussels, Belgium and postmarked no later than **September 30th, 2011.**

Regulations and nomination forms can be obtained by e-mail from chantal.mairesse@frs-fnrs.be

Science Careers is the forum
that answers questions.




Science Careers is dedicated to opening new doors and providing timely answers to the career questions that matter to you.

Science Careers Forum:

- » Relevant Career Topics
- » Timely Advice and Answers
- » Community, Connections, and More!

Visit the forum and join the conversation today!

Your Future Awaits.



ScienceCareers.org

AWARDS

Origin of Life Research Award

\$50,000 AWARD FOR BEST PROPOSAL
\$2 Million Potential Research Funding

The sponsor named below is offering an award of \$50,000 for the best original proposal pertaining to the study of the origin of life on Earth, including an outline of work to be performed in support of the proposal. All submissions will be reviewed by a panel of scientific experts.

Submissions that are deemed highly meritorious by the reviewing panel will be eligible for additional research funding of up to \$2,000,000 over a multi-year period, at the discretion of the sponsor.

Submissions accepted from July 1 to December 31, 2011.

To learn more or to make a submission, visit our website.

Harry Lonsdale
Sponsor

www.originlife.org





Nontraditional Careers: Opportunities Away From the Bench Webinar

Want to learn more about exciting and rewarding careers outside of academic/industrial research? View a roundtable discussion that looks at the various career options open to scientists and strategies you can use to pursue a nonresearch career.

Now Available On Demand
www.sciencecareers.org/webinar

Produced by the
 Science/AAAS Business Office.



POSITIONS OPEN



DIRECTOR

The Louis J. Fox Center for Vision Restoration of UPMC and the University of Pittsburgh, a collaborative project of UPMC Eye Center and the University of Pittsburgh's McGowan Institute for Regenerative Medicine

The Fox Center seeks a scientist or clinician-scientist with an established research program in tissue engineering, tissue regeneration, nerve regeneration, or neuroprotection. Interest in vision research is required. We are in need of an individual who will be at the associate professor level, tenured or tenure stream, and in receipt of peer-reviewed funding. Successful applicants will have the desire to build a premier comprehensive ocular regeneration center. The candidate should be a creative thinker who can foster collaboration and develop consensus as well as motivate and align others towards a single goal. Demonstrated supervisory skills are required.

The Louis J. Fox Center for Vision Restoration of UPMC and the University of Pittsburgh, a joint program of the UPMC Eye Center and the McGowan Institute for Regenerative Medicine, was established as the world's first comprehensive, multidisciplinary research and clinical program dedicated to regenerative ophthalmology. The University of Pittsburgh School of Medicine is consistently ranked among the nation's leading medical schools, enjoying unparalleled growth in its clinical, research and academic missions. The McGowan Institute for Regenerative Medicine is internationally recognized for research and clinical translation of regenerative medicine-based therapies. UPMC is a large, diversified, multi-hospital tertiary care medical institution and is consistently ranked among the top healthcare institutions in the nation.

Send curriculum vitae and cover letter to:

Joel S. Schuman, M.D., FACS
 Eye & Ear Foundation Professor and Chairman
 Department of Ophthalmology
 University of Pittsburgh School of Medicine
 203 Lothrop Street, Suite 816
 Pittsburgh, PA 15213
 Fax: 412-647-5119
 E-mail: schumanjs@upmc.edu

The University of Pittsburgh and UPMC are Affirmative Action/Equal Opportunity Employers.

MICROBIOLOGIST—Chicago State University (CSU), a public urban university in Chicago, Illinois, is seeking applications for a tenure-track position as **ASSISTANT PROFESSOR** of Biology. The successful candidate is expected to teach microbiology and other related courses at the introductory and advanced levels. Other responsibilities will include engaging undergraduate and graduate students in research and attracting extramural funding. The ability to teach introductory zoology and interest in aquaponics is considered a plus. Preference will be given to candidates having post-doctoral and teaching experience.

A letter of application, curriculum vitae, statements of teaching philosophy and research interests should be uploaded to **website: <http://www.csu.edu>**, click on quick links and choose HR/Jobs at CSU. Three reference letters should be sent electronically in PDF format to the address below:

Microbiology Search Committee
 E-mail: bhome@csu.edu
 Department of Biological Sciences
 Chicago State University
 WSC 310
 9501 S. King Drive
 Chicago, IL 60628

The subject line should read microbiology search. Review of applications will begin June 1, 2011, and continue until the position is filled. *Chicago State University is an Affirmative Action/Equal Opportunity Employer.*

POSITIONS OPEN



PH.D. and POSTDOCTORAL positions at the RiboCORE center for multidisciplinary ribosome research.

We welcome applications from excellent candidates with interest or experience in: Fast kinetics, structural biology, molecular genetics and evolution, systems biology, computational chemistry, and single molecule biophysics.

Please see **website: <http://www.icm.uu.se/ribocore>** for application procedures.

TENURE-TRACK FACULTY POSITIONS Physiology

The Department of Physiology at Wayne State University (WSU) School of Medicine invites applications for TWO tenure-track **ASSISTANT/ASSOCIATE PROFESSOR** positions. We seek energetic individuals with research interests in the areas of molecular, cellular, systems, translational physiology, and/or biophysics to strengthen and complement ongoing programs in the Department (**website: <http://physiology.med.wayne.edu>**). The Department is currently under new development of its strong multidisciplinary research programs.

Startup packages and salaries are highly competitive. Candidates are expected to establish active extramurally funded research programs and participate in teaching medical/graduate students. Candidates must hold Ph.D., M.D., or equivalent and apply with curriculum vitae, detailed research plan, and names and contact information of three references to **e-mail: wsuphysiologyfacultysearch@med.wayne.edu**. Review of applications will begin after August 1, 2011 and continue until positions are filled.

WSU offers 350 academic programs through 14 schools and colleges to over 31,000 students in metropolitan Detroit. The Detroit metro area combines cosmopolitan attractions with lovely suburban communities as part of a national technology hub. WSU School of Medicine is a state-of-the-art research environment, and is rated by the Carnegie Foundation in the top one third of all U.S. Research Institutions. WSU was also ranked in Scientist Magazine, 2009 as one of the Top 40 Best Places to Work among all U.S. Academic Institutions. *WSU is an Equal Opportunity/Affirmative Action Employer.*

We deliver customized job alerts.



www.ScienceCareers.org

MARKETPLACE

Promab Biotechnologies Inc.
Custom Monoclonal Antibody \$4,200

>3,000 CLONES WILL BE SCREENED

1-866-339-0871

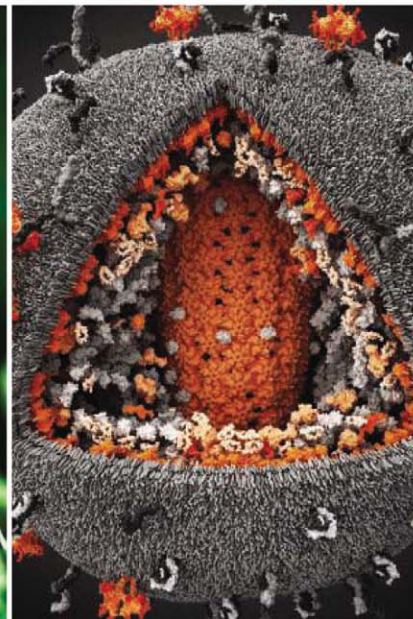
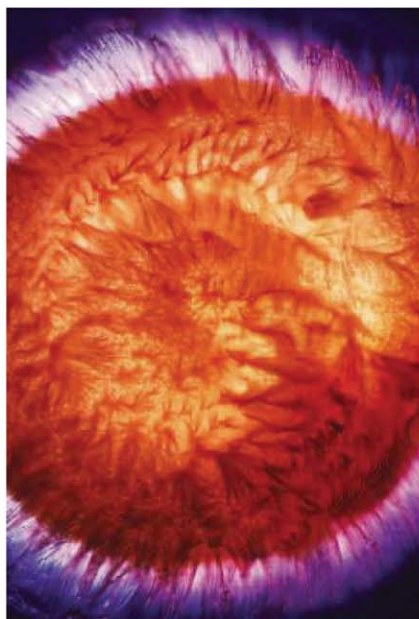
www.promab.com info@promab.com

INTERNATIONAL SCIENCE & ENGINEERING
VISUALIZATION CHALLENGE

CALL FOR ENTRIES

ENTRY DEADLINE: SEPTEMBER 30, 2011

SCIENCE AND ENGINEERING'S MOST POWERFUL STATEMENTS
ARE NOT MADE FROM WORDS ALONE



NEWS of exciting changes to this year's Challenge!

Now you can:

- Submit your entries online
- Read what the judges think about the entries
- Vote for your favorite entry – People's Choice
- Share your favorite entries on Facebook and Twitter



COMPLETE ENTRY INFORMATION:
WWW.NSF.GOV/NEWS/SCIVIS

The National Science Foundation (NSF) and the journal *Science*, published by the American Association for the Advancement of Science, invite you to participate in this year's Challenge. The competition recognizes scientists, engineers, visualization specialists, and artists who produce innovative work in visual communication. Winning entries will be published in *Science* and *Science Online*, and will be displayed on the NSF web site.

Award Categories

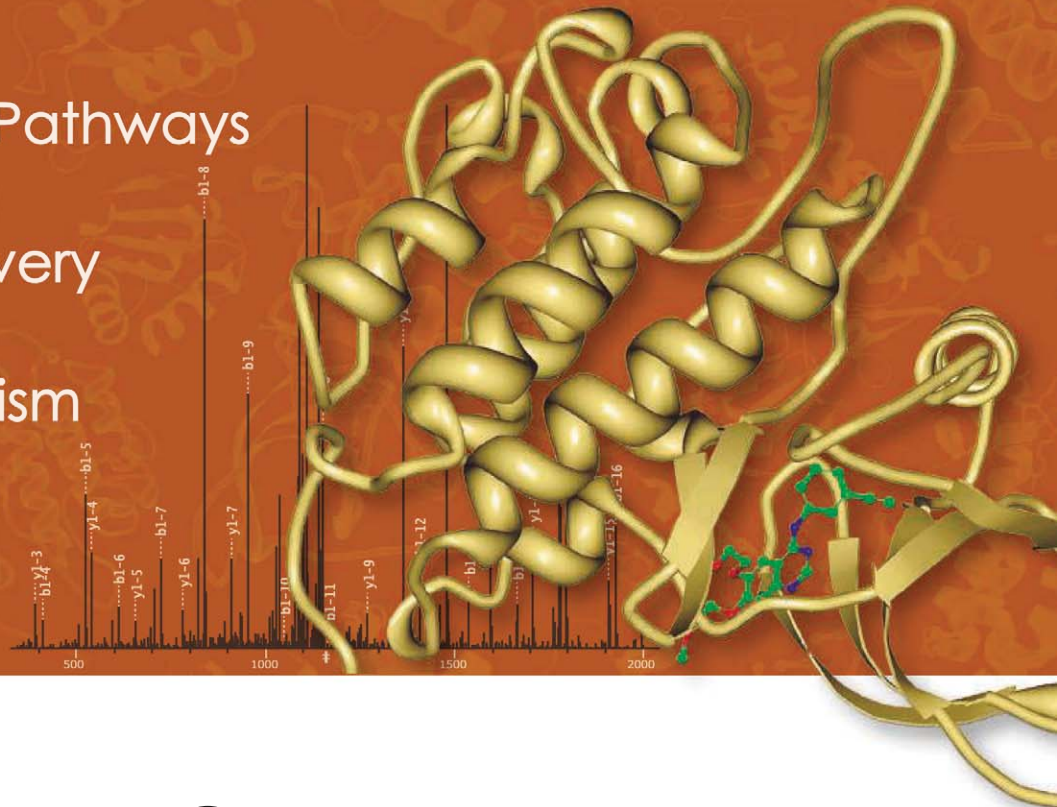
- Photography
- Illustrations
- Informational Posters and Graphics
- Videos
- Interactive Video Games



Profile Signaling Pathways

Biomarker Discovery

Explore Mechanism
of Action

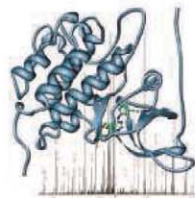


PTMScan[®] Proteomics Services

from Cell Signaling Technology

PTMScan[®] Proteomics Services employ patented methodologies for antibody-based peptide enrichment combined with tandem mass spectrometry for quantitative profiling of post-translational modifications (PTMs).

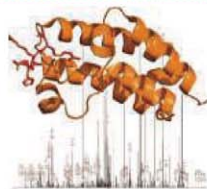
Visit www.cellsignal.com/proteomics
or contact ptmscan@cellsignal.com
for more information.



PhosphoScan[®] Services provide a powerful strategy for kinome-wide phosphoproteomics employing phospho-motif antibodies to direct analysis to the relevant regions of the kinome.



UbiScan[®] Service is a sensitive method utilizing a unique ubiquitin-branch antibody for ubiquitinated sequence identification and the most comprehensive profiling analysis of cellular ubiquitin pathways.



AcetylScan[®] Service provides comprehensive qualitative and quantitative analysis of protein acetylation using proprietary acetylated-lysine antibodies optimized for AcetylScan[®].

for quality products you can trust...

www.cellsignal.com



Cell Signaling
TECHNOLOGY[®]